A N N U A L R E P O R T

2012

and list of publications

Bayerisches Forschungsinstitut
für Experimentelle Geochemie und Geophysik
Universität Bayreuth

Bayerisches Geoinstitut
Universität Bayreuth
D-95440 Bayreuth
Germany

Telephone: +49-(0)921-55-3700
Telefax: +49-(0)921-55-3769
e-mail: bayerisches.geoinstitut@uni-bayreuth.de
www: http://www.bgi.uni-bayreuth.de

Staff and guests of the Bayerisches Geoinstitut in **July 2012**:

Die Mitarbeiter und Gäste des Bayerischen Geoinstituts im **Juli 2012**:

First row, from left (1. Reihe, v. links) Xingcheng Liu, Hongzhan Fei, Mattia Giannini, Ruifang Huang, Dickson Ojwang, Oles Savchuk, Catherine McCammon

Second row, from left (2. Reihe, v. links) Stefan Keyssner, Nobuyoshi Miyajima, Anna Spivak, Yuan Li, Florian Heidelbach, Riko Iizuka, Asiye Shabestari, Tiziana Boffa Ballaran, Gertrud Gollner, Ana Cernok, Hoda Mohseni, Madeleine Humphreys

Third row, from left (3. Reihe, v. links) Ryosuke Sinmyo, Christopher Beyer, Sven Linhardt, Petra Buchert, Huiyang Gou, Tomoo Katsura, Antje Vogel, Dan Frost, Dave Rubie, Ahmed El Goresy, Ulrike Trenz

Fourth row, from left (4. Reihe, v. links) Lydia Kison-Herzing, Yoichi Nakajima, Mainak Mookherjee, Nico Walte, Huaiwei Ni, Clemens Prescher, Stephan Blaha, Alexander Kurnosov, Detlef Krauße, Stefan Übelhack

Fifth row, from left (5. Reihe, v. links) Matteo Masotta, Egor Zakharchenko, Leonid Dubrovinsky, Jellie de Vries, Gleb Parakhonskiy, Gerd Steinle-Neumann, Raphael Njul, Svyatoslav Shcheka, Andreas Audétat, Oliver Rausch, Hans Keppler

Absent (Es fehlten) Vladislav Alexandrov, Valerio Cerantola, Ganna Dinius, Martha Evonuk, Heinz Fischer, Corinne Frigo, Kurt Klasinski, Kanchana Kularatne, Davide Novella, Mezhoura Oussadou, Sergey Ovsyannikov, Martha Pamato, Giacomo Pesce, Henri Samuel, Hubert Schulze, Natalia Solopova, Vincent Soustelle, Dmytro Trots, Vojtěch Vlček

Contents

Foreword

The main research aims of the Bayerisches Geoinstitut are to understand the structure, composition, dynamics and evolution of the Earth's interior. These aims are addressed through the experimental study of the chemical and physical properties of Earth materials. In addition, first-principles computational approaches are used to understand material properties at extreme conditions that cannot be achieved experimentally. The methods employed at the Geoinstitut overlap strongly, therefore, with those used in physics, chemistry and material science.

Many projects described in this Annual Report were performed using equipment directly available at the Geoinstitut. However, a number of projects also employed intense synchrotron X-ray sources such as the ESRF. In addition to synchrotron sources, there is increasing recognition of the importance of neutron facilities in high pressure research. Neutron beams are particularly useful for determining the structural and crystallographic environment of light elements such as hydrogen, which cannot be probed using X-rays. In November 2012, the BGI successfully installed a multi-anvil press with six independently acting 800 tonne hydraulic rams at the neutron source FRM II in Garching. This apparatus will open up completely new scientific possibilities, such as allowing the *in situ* determination of the structure and properties of water-bearing phases at high pressures and temperatures.

A remarkable development in high pressure technology was made at the Bayerisches Geoinstitut in the past year. A significant extension of the pressure attainable in the diamond anvil cell (DAC) was achieved to over 600 GPa (over 6 Megabar). This was made possible through the use of a double-stage DAC with inner nanocrystalline diamond anvils. Another interesting technical development was the modification of a hydrothermal DAC for the measurement of the electrical conductivity of fluids. This cell will extensively expand the range of pressure at which such measurements can be performed.

One of the remarkable scientific results of the previous year concerns Si diffusion in the mineral forsterite, an end member of olivine, the most important mineral in the upper mantle. Previous rock deformation studies have shown that traces of water can significantly weaken forsterite and olivine. New experiments at the Geoinstitut indicate, however, that the dependence of the Si-self diffusion coefficient on the water content of forsterite is much smaller than previously accepted. This may mean that the influence of water on the strength of olivine, and therefore on mantle convection, is much smaller than previously assumed.

Last year, Prof. Dave Rubie was awarded an ERC Advanced Grant to fund a five-year project entitled "The Accretion and Early Differentiation of the Earth and Terrestrial Planets" (*ACCRETE*). The aim of this project is to investigate the formation of the Earth during the early history of the solar system. In 2012, five young colleagues have joined the BGI as part

of this project, and have started to tackle the essential problems concerning the formation of the Earth and planets, both experimentally and theoretically.

In December 2011 Dan Frost was offered the Professorship in Experimental Geosciences at the Bayerisches Geoinstitut. To the delight of his colleagues he subsequently accepted this offer and started the position in October 2012.

From the yearbooks of the Bayerisches Geoinstitut it is evident that the institute has continuously developed to offer a scientifically excellent and flexible working environment for our researchers. We have, at the same time, strived successfully to attract the most talented scientists to Bayreuth and to strengthen our international cooperation. This would not have been possible without the steady help and support of the late President of the University of Bayreuth, Prof. Rüdiger Bormann. We are deeply saddened by his sudden death and will always honour his memory.

On behalf of my colleagues, I would like to thank the Free State of Bavaria as represented by the *Bayerisches Staatministerium für Wissenschaft, Forschung und Kunst* as well as the *Kommission für Geowissenschaftliche Hochdruckforschung* for their continuing support and strong commitment to the Bayerisches Geoinstitut. We also gratefully acknowledge the generous support from external funding agencies, in particular the *Alexander von Humboldt Foundation*, the *European Union* and the *German Science Foundation*, which have also contributed greatly to the development and success of the Institute.

Bayreuth, March 2012 Tomoo Katsura

Vorwort

Das wichtigste Ziel des Bayerischen Geoinstituts ist es, die Struktur, Zusammensetzung und Dynamik des Erdinnern zu verstehen. Hierzu dienen experimentelle Untersuchungen der chemischen und physikalischen Eigenschaften von Geomaterialien unter hohem Druck und hoher Temperatur. Quantenmechanische *ab initio*-Berechnungen erlauben das Verständnis von Materialeigenschaften unter extremen Bedingungen, die bisher im Labor noch nicht erreichbar sind. Die am Geoinstitut angewandten Methoden überschneiden sich daher stark mit denen in Physik, Chemie und Materialwissenschaft.

Viele der in diesem Jahresbericht beschriebenen Projekte wurden mit Apparaturen direkt am Bayerischen Geoinstitut durchgeführt. Viele Projekte nutzten jedoch auch die sehr intensive Röntgenstrahlung von Synchrotron-Quellen wie der ESRF. Zusätzlich zu Synchrotron-Einrichtungen hat die wissenschaftliche Bedeutung von Neutronenquellen in der Hochdruck-forschung stark zugenommen. Neutronenstrahlen sind besonders nützlich, um die Strukturen und kristallographische Umgebung von leichten Elementen wie Wasserstoff zu untersuchen, die mit Röntgenstrahlen kaum lokalisiert werden können. Im November 2012 hat das Bayerische Geoinstitut erfolgreich eine mit sechs unabhängig voneinander steuerbaren Kolben ausgestattete Multi-Anvil-Presse an der FRM II-Neutronenquelle in Garching installiert. Diese Apparatur wird völlig neue Möglichkeiten eröffnen, um beispielsweise die Strukturen und Eigenschaften von wasserhaltigen Phasen bei hohen Drücken und Temperaturen *in situ* zu untersuchen.

Eine wichtige Entwicklung in der Hochdrucktechnologie gelang im vergangenen Jahr am Bayerischen Geoinstitut. Der mit Diamantstempelzellen zugängliche Druckbereich konnte auf über 600 GPa (über 6 Megabar) ausgedehnt werden. Dies war möglich durch die Verwendung von inneren Stempeln aus nanokristallinem Diamant in einer zweistufigen Diamantstempel-zelle. Das Bayerische Geoinstitut hält damit gegenwärtig den Weltrekord in der Erzeugung des höchsten statischen Drucks. Eine andere interessante technische Entwicklung ist eine modifizierte Diamantstempelzelle für die Messung der elektrischen Leitfähigkeit von Fluiden. Mit dieser Zelle kann der experimentell zugängliche Druckbereich für solche Messungen um mindestens eine Größenordnung erweitert werden.

Ein bemerkenswertes wissenschaftliches Resultat lieferten Messungen der Si-Diffusion in Forsterit, dem wichtigsten Mineral im oberen Mantel. Frühere Deformationsexperimente zeigten, dass Spuren von Wasser die Festigkeit von Forsterit und Olivin drastisch verringern. Bei neuen Untersuchungen am Geoinstitut wurde nun festgestellt, dass die Abhängigkeit des Si-Selbstdiffusionskoeffizienten vom Wassergehalt in Forsterit viel geringer ist als bisher angenommen. Dies könnte bedeuten, dass der Einfluss von Wasser auf die Festigkeit von Olivin und damit auf die Konvektion im Mantel nur gering ist.

In 2011 erhielt Prof. Dave Rubie ein ERC Advanced Grant für ein fünfjähriges Forschungsprojekt mit dem Titel “The Accretion and Early Differentiation of the Earth and

Terrestrial Planets" (*ACCRETE*). Ziel dieses Projektes ist es, die Entstehung der Erde während der Frühgeschichte des Sonnensystems zu untersuchen. In 2012 wurden in diesem Projekt fünf junge Wissenschaftler am Bayerischen Geoinstitut eingestellt, um die frühe Entwicklung der Erde sowohl mit experimentellen als auch mit theoretischen Methoden zu untersuchen.

Dan Frost erhielt im Dezember 2011 den Ruf auf die Professur für Experimentelle Geowissenschaften am Bayerischen Geoinstitut. Zur großen Freude seiner Kollegen hat er diesen Ruf angenommen und die Professur im Oktober 2012 angetreten.

Aus den Jahresberichten des Bayerischen Geoinstituts ist ersichtlich, dass sich das Institut kontinuierlich weiterentwickelt hat, um Wissenschaftlern hervorragende Arbeitsbedingungen und ein flexibles Umfeld zu bieten. Wir haben uns gleichzeitig mit Erfolg bemüht, die besten Wissenschaftler nach Bayreuth zu berufen und unsere internationalen Kooperationen zu verstärken. Dies wäre nicht möglich gewesen ohne die stetige Hilfe und Unterstützung des Präsidenten der Universität Bayreuth, Prof. Rüdiger Bormann. Wir sind daher durch seinen plötzlichen Tod tief getroffen und werden ihm stets ein ehrendes Andenken bewahren.

Wie in den vorangegangenen Jahren möchte ich auch im Namen meiner Kollegen dem *Freistaat Bayern*, vertreten durch das *Bayerische Staatsministerium für Wissenschaft, Forschung und Kunst*, der *Hochschulleitung der Universität Bayreuth*, als auch der *Kommission für Geowissenschaftliche Hochdruckforschung* der *Bayerischen Akademie der Wissenschaften* danken für ihre fortwährende Unterstützung und ihre enge Verbundenheit mit dem Bayerischen Geoinstitut. Wir sind auch sehr dankbar für die großzügige Förderung durch externe Geldgeber, insbesondere durch die *Alexander von Humboldt-Stiftung*, die *Europäische Union* und die *Deutsche Forschungsgemeinschaft*, die ebenfalls wesentlich zur Entwicklung und zum Erfolg des Bayerischen Geoinstituts beigetragen haben.

Bayreuth, im März 2013 Tomoo Katsura

1. Advisory Board and Directorship

1.1 Advisory Board

The *Kommission für Geowissenschaftliche Hochdruckforschung der Bayerischen Akademie der Wissenschaften* advises on the organisation and scientific activities of the institute. Members of this board are:

Prof. Dr. G. BREY	Institut für Geowissenschaften der Johann Wolfgang Goethe-Universität, Frankfurt am Main
Prof. Dr. U. CHRISTENSEN	Max-Planck-Institut für Sonnensystemforschung, Katlenburg-Lindau
Prof. Dr. R. KNIEP	Institut für Chemische Physik fester Stoffe der Max-Planck-Gesellschaft, Dresden
Prof. Dr. H. PALME	Institut für Mineralogie und Geochemie der Universität zu Köln
Prof. Dr. M. RIEDERER (Chairman)	Julius-von-Sachs-Institut für Biowissenschaften, Würzburg
Prof. Dr. R. RUMMEL (Vice Chairman)	Institut für Astronomische und Physikalische Geodäsie der TU München
Prof. Dr. E. SALJE, FRS, FRSA	Department of Earth Sciences, University of Cambridge
Prof. Dr. H. SOFFEL	Emeritus, Institut für Allgemeine und Angewandte Geophysik der Universität München

The Advisory Board held meetings in Bayreuth (20.04.2012) and in Munich (16.11.2012).

1.2 Leadership

Prof. Dr. Hans KEPPLER (Director until 30.09.2012)
Prof. Dr. Tomoo KATSURA (Director from 01.10.2012)
Prof. Dr. Dan FROST (from 01.10.2012)

2. Staff, Funding and Facilities

2.1 Staff

At the end of 2012 the following staff positions existed in the Institute:

- Scientific staff *: **12**
- Technical staff: **13**
- Administrative staff: **2**
- Administrative officer: **1**

* Including a tenure-track junior professorship in geodynamic modeling initially funded by *Stifterverband für die Deutsche Wissenschaft* for 6 years.

During 2012, 24 scientific (220 months) positions were funded by grants raised externally by staff members of the institute. In addition 9 long-term scientific positions (76 months) were funded by the resources of the BGI Visiting Scientists' Programme (see Sect. 8) which also supported short-term visits for discussing future projects or presenting research results (see Sect. 6). Positions for 5 Ph.D. students and 1 co-ordinator were funded under the BGI International Graduate School under the Elitenetzwerk Bayern "Structure, Reactivity and Properties of Oxide Materials" (see Sect. 4). 5 scientists (39 months) were supported by personal grants (stipends).

2.2 Funding

In 2012, the following financial resources were available from the Free State of Bavaria:

- Visiting Scientists' Programme: 239.000 €
- Consumables: 489.000 €
- Investment Funding: 341.000 €

The total amount of national/international external funding (*"Drittmittel"*) used for ongoing research projects in 2012 was 2.325.000 € (Positions: 1.256.000 €; equipment, consumables and travel grants: 1.069.000 €).

	positions	**equipment, consumables, travel grants**	**total**
• ENB	253.000 €	205.000 €	458.000 €
• AvH	96.000 €	7.000 €	103.000 €
• DFG	449.000 €	84.000 €	533.000 €
• EU	272.000 €	64.000 €	336.000 €
• BMBF	118.000 €	633.000 €	751.000 €
• Stifterverband	55.000 €	42.000 €	97.000 €
• Others	13.000 €	34.000 €	47.000 €
			2.325.000 €

(ENB = Int. Graduate School „Oxides“ in the Elite Network of Bavaria; AvH = Alexander von Humboldt Foundation; DFG = German Science Foundation; EU = European Union; BMBF = Federal Ministry of Education and Research; Stifterverband = Stifterverband für die Deutsche Wissenschaft; Others: DAAD, University of Bayreuth, Universitaet Bayern e.V., Industry)

In the following list only the BGI part of the funding is listed in cases where joint projects involved other research institutions. Principal investigators and duration of the grants are listed in brackets. Total project funding refers to the funding over the entire duration of this project.

Funding institution	**Project, Funding**	**Total Project Funding**
BFHZ	Bayerisch-Französisches Hochschulzentrum Travel grant (H. Samuel) "The influence of plate tectonics on Earth's mantle thermal evolution and stirring efficiency" Total funding:	1.480 €
BMBF - DESY	05K10WC1 (L.S. Dubrovinsky – 7.10 - 6.13) "Verbundprojekt: Kernresonante Streutechniken: Entwicklung von Messplätzen zur Charakterisierung von Nanostrukturen, molekularen Schaltern, biologischen Mikroproben und Materie unter extremen Bedingungen mit kernresonanten Streutechniken. Teilprojekt 1" Total funding:	529.670 €
BMBF	05K12WC1, (L.S. Dubrovinsky – 8.12 - 7.15) "Single crystal crystallography at extreme pressures and variable temperatures" Total funding:	448.000 €
BMBF	05K10WC2 (H. Keppler – 7.10 - 6.13) "Aufbau einer Hochdruckpresse vom Multi-Anvil-Typ für TOF-Neutronenbeugung und Neutronen-Radiographie am FRM II" Total funding:	2.050.078 €
DAAD	(D.J. Frost – 1.12 - 12.12) "Volatiler Elemente im Erdmantel" Travel funds:	5.954 €
DFG	AU 314/1-2 (A. Audétat – 7.11 - 6.12) "Fraktionierung von Schwefel, Kupfer und Gold in zweiphasigen Fluiden" Positions: E 13/2, 12 months 28.050 € Consumables and travel funding: 27.700 € Overhead: 6.800 €	62.550 €
DFG	Bo 2550/4-1 (T. Boffa Ballaran, F. Langenhorst – 2.10 - 1.12) "Crystal chemistry of hibonite as indicator for oxygen fugacities during solar nebula condensation" Positions: E 13/2, 24 months 56.100 € student assistant (57 h/month) 24 months 19.050 € Consumables and travel funding: 22.000 € Overhead: 19.400 €	116.550 €

DFG	Bo 2550/4-2 (T. Boffa Ballaran, F. Langenhorst – 2.12 - 1.14) "Crystal chemistry of hibonite as indicator for oxygen fugacities during solar nebula condensation" Positions: E 13/2, 24 months 56.500 € Consumables and travel funding: 25.000 € Overhead: 16.300 €	97.800 €
DFG	Du 393/7-1 (L.S. Dubrovinsky, N.A. Dubrovinskaia – 6.09 - 5.12) "Elasticity of iron and iron-based alloys at conditions of the Earth's and planetary cores" Positions: student assistant (80 h/month), 36 months 23.895 € Consumables and travel funding 42.017 € Publication costs 1.500 € Overhead: 18.600 €	86.012 €
DFG	EV 166/1-1 (M. Evonuk – 11.10 - 10.13) "Core formation in Terrestrial planets via global Rayleigh-Taylor destabilization" 1 position: E 13, 36 months 179.100 € Consumables and travel funding: 6.727 € Publication costs 2.250 € Overhead: 37.100 €	225.177 €
DFG	GO 315/21-1 (A. El Goresy, L. Dubrovinsky – 11.12 - 10.14) "Mineralogical, REE and ^{146}Sm-^{142}Nd isotopic systematics of the earliest solar condensates in unequilibrated Enstatite chondrites" Consumables and travel funding: 3.000 € Publication costs 1.500 € Overhead: 900 €	5.400 €
DFG	KE 501/8-1 (H. Keppler – 8.09 - 2.12) "Untersuchungen der Kristallisationskinetik und Gefüge-entwicklung von Basalten mit einer neuartigen Moissanit-Sichtzelle" 1 position: E 13, 24 months 119.400 € Consumables and travel funding: 27.690 € Publication costs 800 € Overhead: 32.200 €	180.090 €
DFG	KE 501/9-1 (H. Keppler – 2010 - 2013) "Noble gases in silicate perovskite: Solubility, dissolution mechanism and influence on the equation of state" 1 position: E 13, 36 months 179.100 € Consumables and travel funding: 15.000 € Overhead: 38.300 €	232.400 €

DFG	KO 3958/1-1 (N. de Koker, D.C. Rubie, D.J. Frost – 12.10. - 11.13) "Combining experimental and computational approaches to determine high P and T thermal conductivity of $CaGeO_3$ and $MgSiO_3$ perovskite" Positions: E 13, 20 months 99.500 € student assistant (57 h/month) 6 months 4.760 € Consumables and travel funding: 6.000 € Overhead: 22.000 €	132.260 €
DFG	KO 3958/2-1 (N. de Koker, G. Steinle-Neumann – 2.11. - 1.14) "Thermal and electrical conductivity of iron at planetary core conditions from ab initio computations" Positions: E 13, 36 months 179.100 € student assistant (79 h/month) 12 months 7.965 € Consumables and travel funding: 9.000 € Publication costs: 2.250 € Overhead: 41.100 €	239.415 €
DFG	Mc 3/16-2 (C.A. McCammon, L.S. Dubrovinsky – 10.09 - 9.12) "High-pressure high-temperature ^{57}Fe Mössbauer spectroscopy in laser-heated diamond anvil cells: Applications for the mineralogy of Earth's lower mantle and core" Positions: student assistant (80 h/month), 36 months 23.895 € Equipment, consumables and travel funding: 30.000 € Overhead: 15.400 €	69.295 €
DFG	Mc 3/17-1 (C.A. McCammon, L.S. Dubrovinsky – 1.10 - 12.12) "Iron-bearing minerals in Earth's lower mantle and coremantle boundary: Development and application of a synchrotron Mössbauer source" Positions: student assistant flat rate 18.000 € Equipment, consumables and travel funding: 51.935 € Overhead: 14.000 €	83.935 €
DFG	OV 110/1-1 (S.V. Ovsyannikov – 7.11 - 6.13) "Structural and electronic properties of sesquioxides at high pressures and temperatures: new forms, new insights and new possible applications" Positions: E 13, 24 months 119.400 € Consumables and travel funding: 14.000 € Overhead: 26.500 €	159.900 €

DFG	RU 1323/2-1 (D.C. Rubie, D.J. Frost, H. Palme – 4.10 - 3.12) "Conditions, timescales and cosmochemical evolution during the early accretion of terrestrial planets" Positions: E 13/2, 24 months 56.100 € Consumables and travel funding: 16.750 € Overhead: 15.100 €	87.950 €
DFG	RU 1323/2-2 (D.C. Rubie, D.J. Frost, H. Palme – 6.12 - 5.14) "Conditions, timescales and cosmochemical evolution during the early accretion of terrestrial planets" Positions: 56.500 € Consumables and travel funding: 40.000 € Publication costs: 1.500 € Overhead: 19.600 €	117.600 €
DFG	SA 2042/2-1 (H. Samuel – 10.10 - 9.13) "The effect of continental plates on convective stirring efficiency" Positions: E 13/2, 36 months 84.150 € student assistant (57 h/month) 12 months 9.525 € Consumables and travel funding: 9.464 € Overhead: 21.200 €	124.339 €
DFG	SA 2042/3-1 (H. Samuel – 10.11 - 9.14) "Convective mixing in magma chambers" Positions: ¾ E13, 36 months and funds for student assistants 142.500 € Consumables and travel funding: 7.000 € Publication costs: 2.250 € Overhead: 30.400 €	182.150 €
DFG	STE 1105/6-2 (G. Steinle-Neumann, H.-P. Bunge – 9.10 - 8.13) DFG SPP 1375 (SAMPLE) "Mineralogical and Dynamic Origin of the South African Superplume" Positions: ¾ E13, 36 months 134.325 € Consumables and travel funding: 7.200 €	141.525 €
DFG	STE 1105/8-1 (S. Gilder/LMU München, G. Steinle-Neumann, R. Egli and N. Petersen/LMU München – 2.11 - 1.14) DFG SPP 1488 (PlanetMag) "How pressure influences the magnetic properties of titanomagnetite and iron with implications for magnetic anomalies and core fields" Budget (G. Steinle-Neumann): Positions: ¾ E13, 36 months 134.325 € Travel funding: 9.250 €	BGI funding: 143.575 €

EU	European Research Council (ERC) Advanced Grant No. 227893 (D.J. Frost – 2.09 - 1.14) "Deep Earth elastic properties and a universal pressure scale DEEP" Positions, equipment, consumables and travel funding maximum EU contribution:	2.079.888 €
EU	European Research Council (ERC) Advanced Grant No. 290568 (D.C. Rubie - 5.12 - 4.17) “Accretion and Early Differentiation of the Earth and Terrestrial Planets ACCRETE” Positions, consumables and travel funding:	1.826.200 €
EU	Marie Curie – International Incoming Fellowship Grant No. 302637 (A. Rosenthal – 10.12 - 10.14) FATEMANTLE Fellowship, consumables and travel funding	167.370 €
Stifter-verband	Stifterverband für die Deutsche Wissenschaft Junior-Professur Geodynamische Modellierung Positions: W1, 72 months 245.200 € Consumables and travel funding: 120.000 €	365.200 €
Industry	Industrial grants (L.S. Dubrovinsky)	30.000 €

2.3 Laboratory and office facilities

The institute occupies an area of

ca. 1350 m^2	laboratory space
ca. 480 m^2	infrastructural areas (machine shops, computer facilities, seminar room, library)
ca. 460 m^2	office space

in a building which was completed in 1994.

2.4 Experimental and analytical equipment

The following major equipment is available at the Bayerisches Geoinstitut:

I. High-pressure apparatus
- 6x800 tonne independently acting-anvil press (25 GPa, 3000 K)
- 5000 tonne multianvil press (25 GPa, 3000 K)
- 1200 tonne multianvil press (25 GPa, 3000 K)
- 1000 tonne multianvil press (25 GPa, 3000 K)
- 500 tonne multianvil press (20 GPa, 3000 K)
- 500 tonne press with a deformation DIA apparatus
- 4 piston-cylinder presses (4 GPa, 2100 K)
- Cold-seal vessels (700 MPa, 1100 K, H2O), TZM vessels (300 MPa, 1400 K, gas), rapid-quench device
- Internally-heated autoclave (1 GPa, 1600 K)
- High-pressure gas loading apparatus for DAC

II. Structural and chemical analysis
- 1 X-ray powder diffractometer
- 1 X-ray powder micro-diffractometer
- 1 X-ray powder diffractometer with furnace and cryostat
- 2 automated single-crystal X-ray diffractometers
- High-brilliance X-ray system
- Single crystal X-ray diffraction with super-bright source
- 1 Mössbauer spectrometer (1.5 - 1300 K)
- 3 Mössbauer microspectrometers
- 2 FTIR spectrometers with IR microscope
- FEG transmission electron microscope, 200 kV analytical, with EDS and PEELS
- FEG scanning electron microscope with BSE detector, EDS, EBSD and CL
- 3 Micro-Raman spectrometers with ultraviolet and visible lasers
- Tandem-multipass Fabry-Perot interferometer for Brillouin scattering spectroscopy
- JEOL JXA-8200 electron microprobe; fully-automated with 14 crystals, 5 spectrometer configuration, EDX, capability for light elements
- 193 nm Excimer Laser-Ablation ICP-MS
- ICP-AES sequential spectrometer

Water content determination by Karl-Fischer titration
GC/MS-MS for organic analyses
Confocal 3D surface measurement system

III. *In situ* determination of properties

Diamond anvil cells for powder and single crystal X-ray diffraction, Mössbauer, IR, Raman, optical spectroscopy and electrical resistivity measurements up to at least 100 GPa
Facility for in situ hydrothermal studies in DAC
Externally heated DACs for in situ studies at pressures to 100 GPa and 1200 K
1-atm furnaces to 1950 K, gas mixing to 1600 K, zirconia fO2 probes
1-atm high-temperature creep apparatus
Gigahertz ultrasonic interferometer with interface to resistance-heated diamond-anvil cells
Heating stage for fluid inclusion studies
Impedance/gain-phase analyser for electrical conduc-tivity studies
Apparatus for in situ measurements of thermal diffusivity at high P and T
Laser-heating facility for DAC
Portable laser heating system for DAC

IV. Computational facilities

9 node linux cluster (2x3.0 GHz Xeon Woodcrest Dual Core, 8 Gb memory), InfiniBand
8 node linux cluster (16x2.83 GHz Xeon 5440 Quad Core, 64 Gb memory), InfiniBand
32 TB mass storage

The Geoinstitut is provided with well equipped machine shops, an electronic workshop and sample preparation laboratories. It has also access to the university computer centre.

3. Research Overview:
The carbon cycle in Earth's interior and the formation of diamonds (D.J. Frost)

The availability of carbon at planetary surfaces is vital for the evolution and sustainability of life. The Earth's mantle, the region of the interior comprised of silicate minerals that extends to a depth of 2900 km, hosts by far the largest reservoir of carbon on Earth. Carbon is exchanged between the surface and the interior as a result of volcanism and the processes of plate tectonics. A major limb of the carbon cycle passes through the interior and due to the size of the internal reservoir, it has had an enormous potential to influence the surface availability of carbon throughout geological time. The Earth's first carbon dioxide-rich atmosphere, for example, degassed from the interior in the earliest phase of our planet's history. In order to understand how carbon is transported, stored and expelled from the interior, we need information on the forms in which carbon exists under various conditions. When bonded to oxygen in the form of carbon dioxide, carbon behaves as a volatile element lowering the melting temperatures of rocks and forming melts and gases, which can migrate and rise out of the mantle. On the other hand, it can also form solid phases such as diamond and graphite where it is not bonded to oxygen and remains solid to extreme temperatures unattained in the Earth. In this form it can remain fixed in the mantle for billions of years. Here I describe the results of some current research at the Geoinstitut to investigate the conditions in the Earth where carbon changes its geochemical behaviour by reacting with oxygen. These results not only bear on the way that carbon is extracted to the surface by melting within the Earth but also on the formation mechanism of diamonds. By obtaining a better understanding of the role of the Earth's interior in the carbon cycle, we can ultimately constrain the extent to which the interior may have influenced the surface availability of carbon and gain some insight into whether the net exchange of carbon is well balanced or whether it is dominated by movement of carbon in one particular direction, either into or out of the interior.

The term carbon cycle is normally used to describe the exchange of carbon between the Earth's atmosphere, biosphere and hydrosphere. This cycle is essential to the habitability of the Earth because a major part of it involves the complimentary exchange of carbon and oxygen between plants and animals. As shown in Fig. 1, the yearly flux of carbon between these surface reservoirs is of similar magnitude to the size of the reservoirs themselves. As carbon exchanges so rapidly, the concentrations in each reservoir are closely linked. The annual growth cycle of plants, for example, causes a yearly variation in the amount of CO_2 in the atmosphere by approximately 2 %. CO_2 is also a major atmospheric greenhouse gas: CO_2 absorbs and reradiates heat back towards the Earth's surface that would otherwise be lost to space. This links atmospheric CO_2 concentrations to Earth's climate. Some greenhouse warming is important for the Earth because calculations show that without any CO_2 in the atmosphere average surface temperatures would be -18 °C. Since the industrial revolution, however, levels of CO_2 in the atmosphere have risen by close to 20 %, raising the prospect of global warming. A pressing concern is that increasing temperatures may ultimately cause a so called "tipping point", whereby an irreversible event occurs that perturbs Earth's carbon cycle to an extent that it cannot be brought back into the current balance. Due to the complexity of

the carbon cycle, such events are hard to predict, but that such events can occur is supported by geological evidence found in sedimentary rocks. Extreme variations in Earth's climate in the past have been attributed to fluctuations in atmospheric CO_2. Over such geological time frames, however, the exchange of carbon between the Earth's interior will also have a major influence on the availability of carbon at the surface.

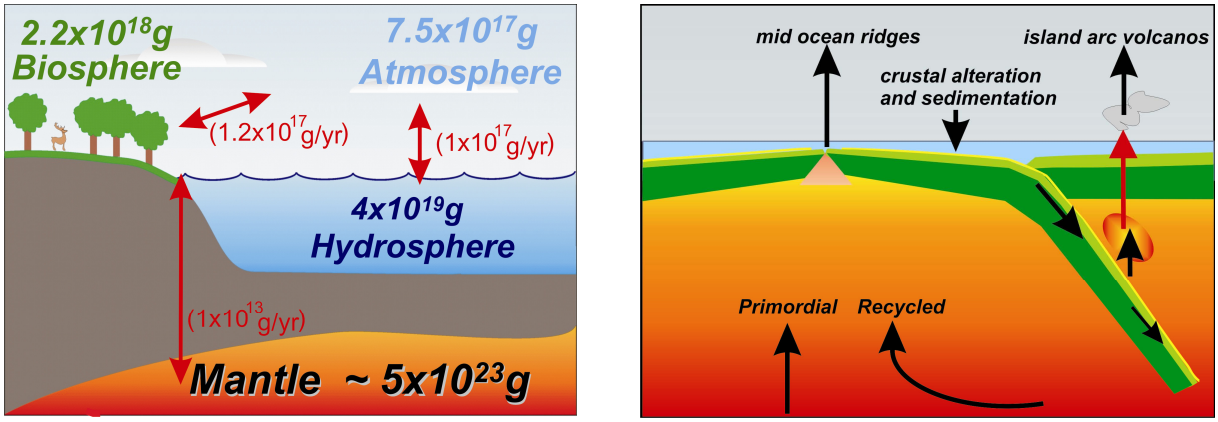

Fig. 1: **(left)** The amount of carbon in each surface reservoir is shown in grams with the yearly exchange between the reservoirs given in brackets in grams per year. The mantle is the Earth's largest carbon reservoir. **(right)** Carbon is out gassed from the mantle through eruptions at mid ocean ridges where the oceanic crust is formed. Alteration and sedimentation causes carbon to be fixed into the crust. Subduction of the crust returns carbon to the mantle. Some of the carbon leaves the subducting crust and is returned to the surface in island arc volcanoes, such as those that surround the Pacific Ocean. But some carbon is subducted further into the mantle to form a deep limb of the carbon cycle. Some proportion of the mantle's carbon has been recycled from the surface but a large proportion is primordial, present in the Earth since its formation.

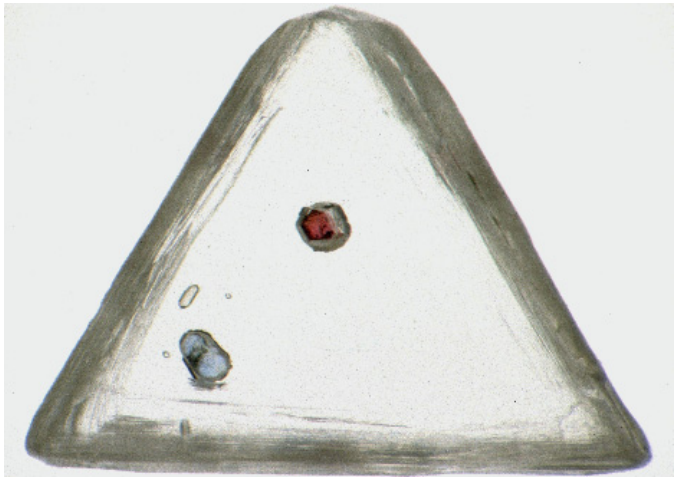

Fig. 2: Diamonds are formed at depths greater than 150 km in the mantle. As they form they can trap inclusions of mantle minerals that can provide information on the conditions of diamond formation. This diamond, which has a form described as a Macle that arises from twinning, contains inclusions of a red garnet and an unusual blue-colored olivine. The redox conditions, crystal chemistry and optical spectroscopy of the blue olivine are being investigated in collaboration with Steve Jacobsen (Northwestern), Bill Bassett and Elise Skalwold (Cornell), and John Koivula (Gemological Institute of America). The diamond measures approximately 5-mm in the longest dimension. Photomicrograph by John Koivula (GIA).

Figure 1 also shows an estimate for the amount of carbon in Earth's mantle which is many orders of magnitude more than the entire near surface reservoirs. Mantle carbon is degassed to the surface as carbon dioxide during volcanic eruptions, such as at mid ocean ridges, where basalt magma creates new oceanic crust, and through island arc volcanoes that occur at subduction zones. During its residence time at the surface the carbon content of the oceanic crust is raised due to interaction with the hydrosphere and biosphere, through alteration by sea water and by the deposition of carbon-bearing sediments such as limestone, formed from the shells of sea creatures. At subduction zones slabs of oceanic lithosphere, comprising both the oceanic crust and part of the underlying mantle, dip back into the Earth's interior, returning this crustal carbon to the mantle. Subduction is part of the Earth's internal convective cooling cycle, whereby cold lithospheric material sinks back into the mantle. As the subducting lithospheric slab heats up in the interior, volatiles are driven off that may include carbon-bearing species. These volatiles are implicated in the source of island arc magmas and through the eruption of such magmas carbon from the slab may be returned to the surface on a relatively short time scale. On the other hand if carbon species remain below their melting or decarbonation temperatures, it is possible that a portion of carbon remains in the slab and is subducted into the deep mantle.

Volcanism and subduction are the mechanisms by which carbon is exchanged between the mantle and the surface forming a further arm of the carbon cycled through the interior. But the current yearly flux of carbon in this exchange is small compared to the size of the main surface reservoirs. For this reason exchange with the interior can only affect the surface availability of carbon over geological time scales. However, the Earth's first atmosphere was likely dominated by CO_2 that degassed from the interior. In addition, fluctuations in surface carbon availability in the past seem to have been coupled to plate tectonic cycles that would imply that mantle carbon exchange has been an important factor over Earth's history. A major question is whether the exchange of carbon between the surface and interior is in balance or if there is a tendency for a net flux of carbon into or out of the interior which over geological time will either deplete or augment the surface reservoir. Another important question is how much of the mantle's carbon is actually recycled from the surface and how much is primordial, *i.e.*, present in the mantle since Earth formed.

To understand the role of the Earth's mantle in the global carbon cycle we need to appreciate how carbon is stored in the interior and how it is transported. In particular, the behaviour of carbon during melting processes is important for determining the rate and extent to which it is extracted from the interior. The form in which carbon exists in subducting slabs will determine the depth in the mantle to which carbon is returned in the subduction process.

Here I review the results of some recent studies performed at the Geoinstitut to understand the stability of carbon-bearing phases in the Earth's interior. A particular emphasis is to determine conditions in the Earth where carbon exists in so called reduced forms, such as diamond or graphite where it is not bonded to oxygen, and where it exists in oxidised forms

bonded to oxygen as either carbon dioxide (CO_2) or carbonate minerals ($MgCO_3$) or melts. Reactions where carbon is transformed between oxidised or reduced forms, so called redox reactions, must be balanced by complimentary redox reactions that either provide or consume oxygen. In the Earth these complimentary reactions likely involve ferrous (Fe^{2+} as in FeO) and ferric (Fe^{3+} as in Fe_2O_3) iron components in mantle silicate minerals. The main goal of the studies described here has been to understand this interaction between carbon and iron-bearing minerals and to understand how redox processes caused by the passage of carbon-bearing liquids might be recorded in mantle rocks and influenced by them.

Diamonds have formed from redox processes in the mantle, and by studying the types of rocks in which diamonds are found we can gain some insight into the types of fluids and melts which carry carbon in the mantle. The liquids from which diamonds are formed are not preserved in the rocks in which they are found. These liquids are transient, they travel through rocks and alter their chemical composition but evidence for the composition of the liquid is removed in the mantle by recrystallisation. However, some evidence for the nature of these liquids is recorded by the redox state of mantle rocks which can be determined from an analysis of the ferric and ferrous iron contents of mineral phases.

The forms that carbon takes in the Earth

Evidence exists that carbon takes numerous forms in the interior. Carbon dioxide is the main carbon-bearing species to leave the mantle, which degasses during volcanic eruptions as the magma approaches the surface. At depths greater than 60 km CO_2 will react with mantle silicate minerals to produce carbonate minerals in a reaction, which in simplified terms, can be written as,

$$\underset{\text{clinopyroxene}}{CaMgSi_2O_6} + \underset{\text{olivine}}{2Mg_2SiO_4} + 2CO_2 = \underset{\text{orthopyroxene}}{2Mg_2Si_2O_6} + \underset{\text{dolomite}}{CaMg(CO_3)_2} \qquad [1]$$

where clinopyroexene, olivine and orthopyroxene are typical minerals of the mantle and dolomite is a carbonate mineral that is found as a type of limestone at the surface but is also present inside the Earth as a host for carbon. Mantle xenoliths, which are pieces of the lithospheric mantle brought to the surface in volcanic eruptions, are known, in rare instances, to contain carbonate minerals. Carbonate minerals melt at quite low temperatures in the mantle. The presence of carbonate, therefore, lowers the melting temperature of the mantle creating melts at conditions where normal volatile-free mantle would remain solid.

In addition to carbonates, diamonds and graphite are found in mantle xenoliths. At shallow depths the formation of graphite is controlled by the reduction reaction,

$$CO_2 = C + O_2 \qquad [2]$$

Reduction describes the loss of oxygen from a compound, the opposite of oxidation. Whether this reaction occurs at a given pressure and temperature will depend on the availability of oxygen which we can describe using a term called the oxygen fugacity or fO_2. The behaviour of a gas in a chemical reaction should theoretically be proportional to the pressure of the gas. However, in reality this is almost never the case, so to account for this deviation the behaviour of a gas is defined to be proportional to the fugacity rather than the pressure. Fugacity is the effective pressure exerted by a real, rather than a theoretical, gas. Low values of fO_2 define reducing conditions where little oxygen is available and where graphite forms, whereas at higher fO_2 CO_2 will be stable. Because fO_2 varies a lot it is usually described using a base 10 logarithmic value.

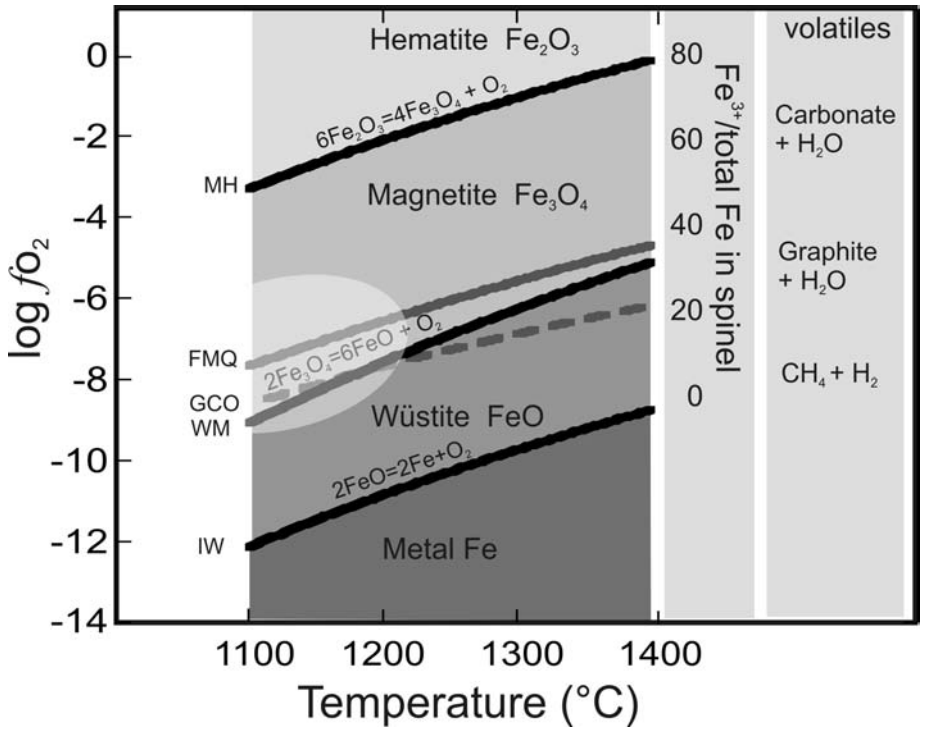

Fig. 3: The stability of iron and iron oxides as a function of fO_2 calculated at 20 kbars *i.e.*, the pressure at approximately 60 km depth. At low fO_2 iron metal is stable but as fO_2 increases and the reaction labelled IW (iron-wüstite) is crossed, oxygen reacts with iron to produce the mineral wüstite *i.e.*, FeO. At higher oxygen fugacities the WM (wüstite-magnetite) reaction is crossed and the mixed iron 2+ and 3+ oxide, magnetite, is formed and at the highest fO_2 hematite forms (above MH) where all iron is in the 3+ oxidation state. If both iron oxides at a reaction are present, equilibrium occurs and the fO_2 is fixed or buffered along the particular black curve. Other reactions given in the text are FMQ and GCO. The fO_2 of mantle rocks at these conditions is indicated by the bright partial ellipse. In the mantle these simple iron oxides are not present but iron-bearing minerals such as spinel go through a gradual transition from being Fe^{2+} dominated at low fO_2 to Fe^{3+} dominated at high fO_2. The Fe^{3+} content of the mineral spinel as a percentage of total iron (*i.e.*, Fe^{2+}+Fe^{3+}) is shown on the right hand scale. The volatile elements carbon and hydrogen will also form different solid and liquid phases as a function of fO_2 at this depth in the mantle. These are indicated on the far right hand side.

fO_2 is a useful way of determining the conditions where redox reactions occur. There is no free oxygen in the mantle but individual oxidation or reduction reactions can be defined in terms of an fO_2. In Fig. 3 for example the fO_2 where the reduction of graphite to form carbon dioxide occurs, *i.e.*, equation [2], is shown. This reaction defines a specific fO_2 for a given pressure and temperature, the equivalent oxidation reaction would occur at the same fO_2. This reaction is described using an acronym GCO because it describes the equilibrium between Graphite and Carbon diOxide. At oxygen fugacities above the GCO curve CO_2 will be stable but below this curve graphite will be stable.

In addition to GCO the stability of iron metal and iron oxides is also shown in Fig. 3 as a function of fO_2. At low fO_2 iron is stable as metal but at higher fO_2 it becomes oxidised into two oxidation or valence states. As it bonds with oxygen it loses electrons to oxygen and takes on a positive ionic charge or valence. Ferrous iron has lost two electrons, as in FeO or the mineral wüstite, and can be said to be in the 2+ oxidation state *i.e.*, Fe^{2+}. Most minerals in the mantle are dominated by ferrous iron. Ferric iron, however, is more oxidised. It has lost 3 electrons (Fe^{3+}) as in Fe_2O_3 or the mineral hematite. In addition, there is a mixed valence iron oxide, called magnetite, $Fe^{2+}Fe^{3+}{}_2O_4$. As shown in Fig. 3 curves can be drawn (IW, WM, MH) which describe the oxygen fugacities where these iron oxides transform. The reactions define the stability fields of iron metal and the iron oxides. As fO_2 increases, the oxidation state of the stable iron oxide increases.

Absolute values of fO_2, defined by mineral reactions, increase with pressure and temperature. However, these dependencies are normally sub-parallel to one another and by subtracting an absolute value for a particular reaction, a normalised, relative scale can be produced which is not so dependent on pressure and temperature. For this purpose the FMQ reaction shown in Fig. 3 is often used. FMQ stands for fayalite magnetite quartz and it refers to the fO_2 defined when all phases in the reaction,

FMQ $\quad 3Fe_2SiO_4 + O_2 = 2Fe_3O_4 + 3SiO_2$ [3]
fayalite magnetite quartz

are present. The normalised value is generally indicated as $\Delta\log fO_2$ (FMQ), where the value of FMQ therefore becomes zero. Upper mantle rocks are generally in the range FMQ ±2 log units as shown by the shaded partial elipse in Fig. 3.

In reality things are more complicated than this because rocks do not contain pure iron oxides, instead ferric and ferrous iron are present as components in mineral phases. In upper mantle rocks at depths < 100 km for example magnetite, Fe_3O_4, exists as a component in the mineral spinel as part of a mixture or solid solution, the composition of which varies between Fe_3O_4 and $MgAl_2O_4$. However, just like the pure oxides, the proportion of ferric iron in a mantle mineral will depend on the fO_2 and by calibrating this dependence it is possible to measure the fO_2 of mantle rocks by measuring the ferric and ferrous iron proportions. The amount of ferric iron in the mineral spinel as a percentage of the total iron content of the mineral is shown in the right hand scale of Fig. 3. If the fO_2 of the mantle is low the ferric iron content of spinel will also be low.

The forms in which volatile elements exist and their consequent behaviour will also be influenced by the fO_2, as shown on the right hand bar of Fig. 3. At high fO_2, above the GCO curve carbon will exist as CO_2 but as indicated in reaction [1] at high pressure in the mantle CO_2 will react with silicate minerals to produce carbonate minerals or melts. At lower fO_2 carbonates will reduce to produce graphite while at very low fO_2 H_2O and graphite will react to produce the gas methane, CH_4. The behaviour of carbon therefore changes with fO_2. By examining the fO_2 of mantle rocks we can get some idea of the likely form in which carbon was stable. Rocks containing iron minerals which have very low ferric iron contents and therefore record low fO_2 would have been in equilibrium with CH_4. Minerals rich in ferric iron would record an oxidation state consistent with the existence of carbonate melts. This is important because gases and liquids are transient in the mantle and are rarely preserved in the rocks we get from the mantle. We can only piece evidence together from the ferric and ferrous iron contents in the minerals as to the nature of the carbon-bearing phase that would have been present. Diamond could in principle be formed from carbonate or methane in the mantle. But diamonds found in rocks which record an fO_2 of -5 log units below FMQ, for example, must have formed from a methane-rich gas phase.

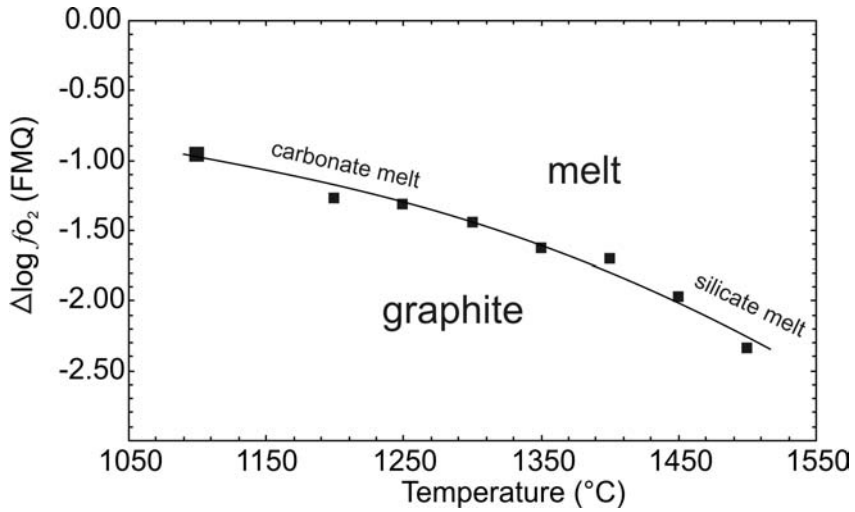

Fig. 4: Two important forms of carbon in the mantle are graphite and carbonate liquid. The oxygen fugacity will determine which of these phases exists, with graphite forming at low oxygen fugacity and carbonate liquid at higher values. The experimental results shown in the figure were performed to determine the oxygen fugacity between these two forms of carbon. At higher temperatures silicate minerals will also start to melt and contribute silicate to the liquid, which will evolve towards a silicate melt. Due to the dilution of the carbonate liquid component with silicate melt at high temperature the fO_2 will deviate to lower values (Stagno and Frost 2010).

On the other hand carbonate minerals might be reduced to form diamond in the mantle through the reaction,

$MgSiO_3 + MgCO_3 = Mg_2SiO_4 + C + O_2.$ [4]
enstatite magnesite olivine graphite/diamond

But this is unlikely to be the case because multiple growth rings can be detected in diamonds that indicate intermittent periods of diamond crystallisation from a mobile carbon source *i.e.*, a liquid (Wiggers de Vries *et al.*, 2011). However molten carbonate liquids might also reduce to produce diamonds in a similar reaction to [4]. Figure 4 shows the fO_2 determined in high-pressure experiments for the equilibrium between a carbonate liquid and graphite at 3 GPa (Stagno and Frost 2010). The fO_2 defined by the coexistence of graphite and carbonate liquid deviates to lower levels with increasing temperature. This is because with increasing temperature more silicate starts to be present in the liquid which evolves with temperature from a carbonate liquid to a silicate melt at high temperatures. The more silicate material that is present in the liquid, the lower the fO_2, because the carbonate component in the liquid becomes diluted. The more dilute the carbonate component the lower the fO_2 is at which graphite will form from the liquid. At higher pressures the same relationship is found for diamond. In these experiments many other dilutants were tested such as P_2O_5 and H_2O and in all instances as the carbonate is diluted the fO_2 at which graphite forms is decreased. The fO_2 therefore again provides information on the amount of carbonate present in the liquid from which graphite or diamonds formed.

The formation of diamonds and the oxygen fugacity of the cratonic mantle

The outer surface of the Earth is called the lithosphere and is broken up into tectonic plates which move over a softer region of the mantle called the asthenosphere. The lithosphere is comprised of the crust and an underlying section of the uppermost mantle called the lithospheric mantle. The lithospheric mantle is rigid compared to the underlying softer asthenosphere, which deforms to allow plates to move over it. Diamonds are found in xenoliths, rocks of the lithospheric mantle brought to the surface by magma. Diamond-bearing xenoliths, however, are only found in eruptions which occurred in the oldest continental crust called cratonic crust. Cratonic crust and lithosphere formed in the eon called the Archean which ended 2.5 billion years ago.

The cratonic lithosphere is particularly thick and extends deep enough for the roots to descend into the diamond stability field, which occurs at depths greater than 150 km. Diamonds are not found in xenoliths from younger lithosphere as it does not generally extend beyond 100 km. Diamond-bearing xenoliths are found in kimberlite magmas, a rare volatile rich magma of which there are no recently erupted examples. Diamond-bearing kimberlites erupted generally more than 50 million years ago. As shown in Fig. 5, kimberlitic magmas are likely produced by melting of the asthenosphere but they pass through a section of the lithosphere which extends into the diamond stability field. At depths where diamonds form the main mantle rocks are garnet peridotites, ultramafic rocks containing the mineral garnet in addition to olivine, orthopyroxene and clinopyroxene. At shallower depths garnet transforms to the mineral spinel as shown in Fig. 5. Garnet peridotite, Fig. 6, is generally only found as kimberlite xenoliths erupted in cratonic lithosphere. Diamonds must form from liquids which most likely pass into the lithosphere from the asthenophere. But what type of liquids form diamonds and what is the origin of these liquids?

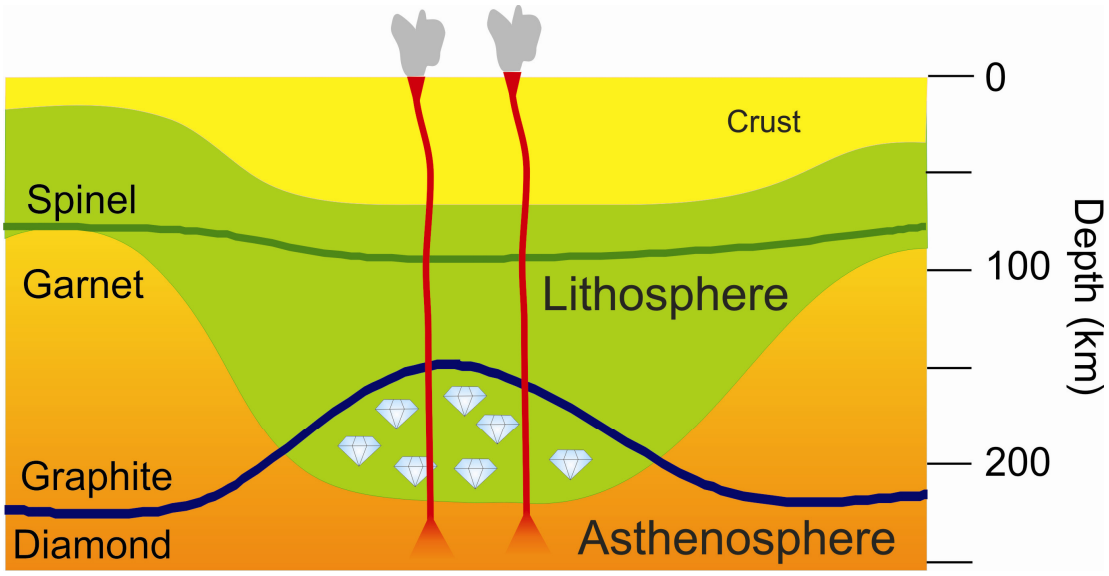

Fig. 5: Cratonic lithosphere contains the oldest crust on Earth. It forms the central sections of continents such as south Africa, north America and Siberia and formed in the Archean, at least 2.5 billion years ago. Diamonds are only found in such crust because the cratonic lithosphere extends into the diamond stability field. Kimberlite magmas likely form in the asthenosphere and rise through the cratonic lithosphere bringing pieces of the mantle, called xenoliths, to the surface. On extremely rare occasions, these mantle xenoliths contain diamonds. Diamond-bearing xenoliths are often composed of garnet peridotite. Garnet is formed at depths above approximate 70 km in the mantle from a transformation involving the mineral spinel.

Fig. 6: An example of a garnet peridotite mantle xenolith. Such rocks form the majority of the cratonic lithospheric mantle at depths greater than 100 km. Large rounded red garnets are surrounded mainly by light green olivine, darker green orthopyroxene and mint green clinopyroxene. By examining the composition of these minerals and particularly the ferric and ferrous iron content of garnet, the oxygen fugacity at which the rock last equilibrated can be determined.

As described in the previous section, in order to understand the types of liquids from which diamonds formed we need to get an estimate for the fO_2 of mantle rocks. Oxygen fugacites can be estimated by measuring the distribution of ferric and ferrous iron in mantle minerals.

By examining an fO_2-sensitive reaction between mineral components in a rock, the fO_2 at which the rock last equilibrated can be determined. The reaction,

$$2Ca_3Fe_2Si_3O_{12} + 2Mg_3Al_2Si_3O_{12} + 4FeSiO_3 = 2Ca_3Al_2Si_3O_{12} + 4Fe_2SiO_4 + 6MgSiO_3 + O_2$$
garnet garnet orthopyroxene garnet olivine orthopyroxene [5]

for example, involves the reduction of the Fe^{3+}-bearing component $2Ca_3Fe_2Si_3O_{12}$ in garnet, which is named after the mineral andradite. As all components are always present in the minerals of the rock, [5] constitutes an equilibrium rather than a reaction. By determining the amounts of each of these components in the minerals the fO_2 can be calculated for the rock using a thermodynamic calculation that must be calibrated using high-pressure and -temperature experiments (Stagno *et al.* 2013). To determine the proportion of the garnet andradite component requires measuring the ferric and ferrous iron contents using Mössbauer spectroscopy.

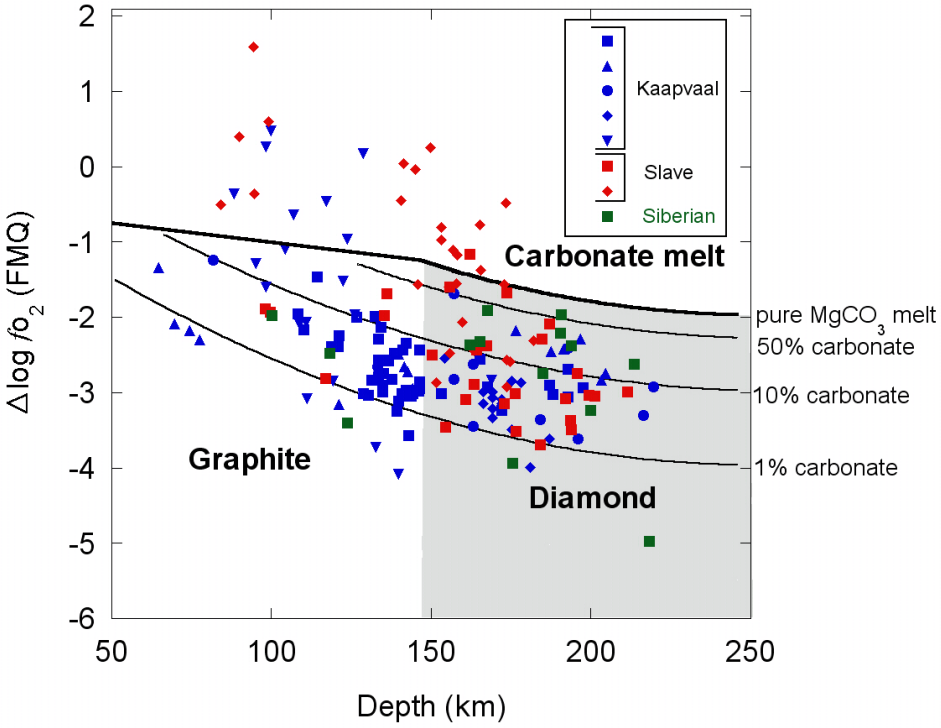

Fig. 7: Log fO_2 (normalized to the FMQ buffer) calculated for mantle cratonic xenoliths and plotted as function of depth. The shaded region indicates the diamond stability field with respect to pressure and fO_2. The bold curve marking the upper fO_2 stability of diamond, indicates the fO_2 where diamond would transform to pure $MgCO_3$ melt. At depths shallower than 150 km carbonate would be solid and the curve becomes linear. Lighter curves show the carbonate concentration of melts that would be in equilibrium with diamond at oxygen fugacities below the level where pure carbonate melt could be stable. These melts would have to be diluted with another component such as H_2O or silicate melt. It can be observed that the majority of the reported mantle xenoliths would coexist with melts characterized by relatively low carbonate concentrations, mainly in the range 1-10 % carbonate (Stagno *et al.* 2013).

Figure 7 shows oxygen fugacities for cratonic lithospheric mantle xenoliths determined using equilibrium [5] and plotted as a function of depth. The xenoliths come from different regions of diamond-bearing cratonic lithosphere, such as the Kaapvaal craton in south Africa, the Slave craton in Canada and the Siberian craton. The diamond stability field is also indicated by the shaded region. This region is delimited at 150 km by the transformation of diamond to graphite and at high oxygen fugacities by the transformation, by oxidation, of diamond to carbonate melt. Only at oxygen fugacities along this thick solid curve can diamonds have formed from pure carbonate melts and most rocks are below this curve. Most rocks would be in equilibrium with liquids which only contained dilute carbonate components. The thinner black lines mark the amounts of carbonate in the liquids that would be in equilibrium with diamond in these mantle rocks. It can be seen that most rocks lie between 1 and 10 % carbonate, implying that the liquids from which diamonds formed mainly contained something else and carbonate was a relatively small component. But what was the major component?

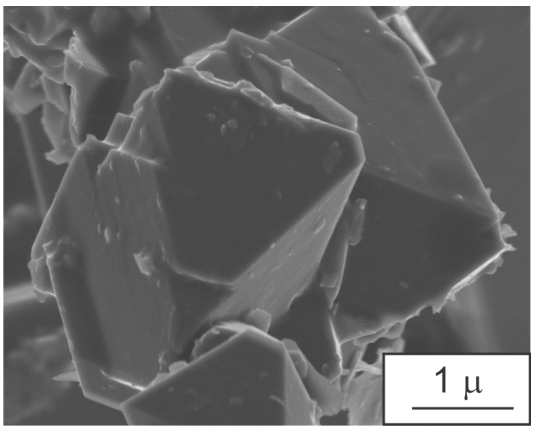

Fig. 8: A scanning electron microscope image of a diamond formed in a high-pressure experiment at 60 kbars and 1200 °C from a liquid dominated by H_2O. The diamond crystal has grown in the shape of an octahedron, which is typical of many natural diamonds. Diamond nucleation is normally kinetically inhibited at the conditions and time scale of the experiment but water-rich liquids appear to act as a suitable catalyst for diamond growth (Bureau *et al.* 2012).

One possibility would be that diamonds formed from water-rich liquids that contained a minor amount of carbonate or CO_2. This is quite plausible because recent experiments have shown that diamonds can form from such water dominated fluids. Figure 8 shows an example of a diamond formed from a water-rich liquid during a high-pressure experiment at the Geoinstitut (Bureau *et al.* 2012). The diamond is very small because the growth rate is extremely slow, however, that the diamond formed at all is quite remarkable as its crystallisation is normally kinetically inhibited at such conditions. The experiments indicate that water-rich liquids can act as a catalyst for diamond growth; a catalyst is an agent that speeds a reaction, in this instance bringing diamond to crystallize in the time scale of a laboratory experiment.

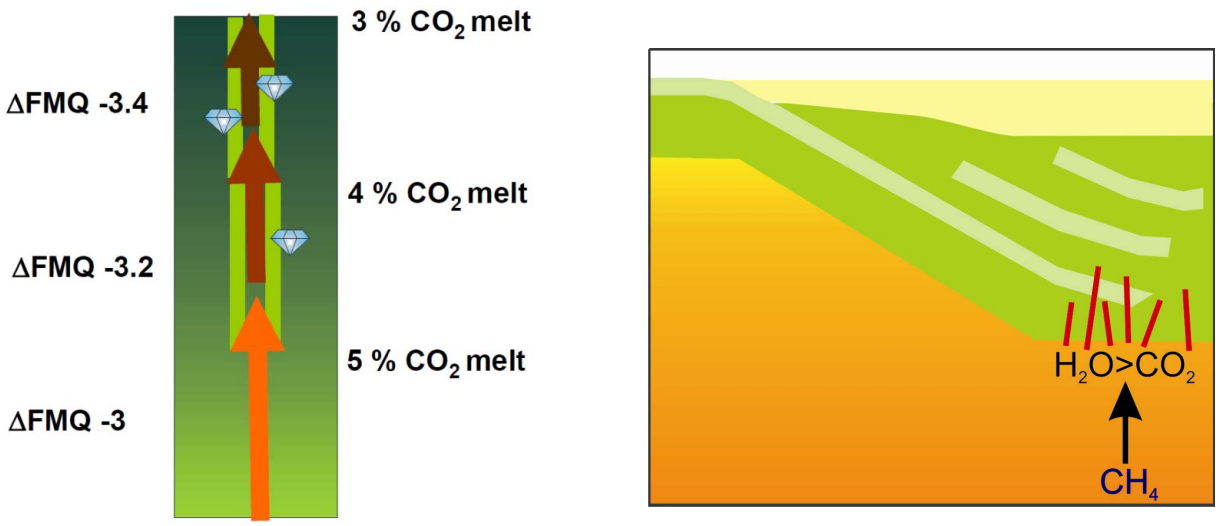

Fig. 9: (left) The formation of diamonds along a redox gradient in mantle rocks. The CO_2 or carbonate content of mantle melts has to approach equilibrium with the redox state of the wall rocks through which the melt vein passes. As the fO_2 of the wall rocks decreases, the CO_2 content of the melt must decrease, which is achieved through the precipitation of diamond. As diamond forms by reduction of CO_2 in the melt, ferrous iron in the minerals of the wall rocks is oxidised. (right) The cratonic lithosphere was likely thickened as a result of under-plating by subducted lithosphere. However, the formation of the melts from which diamonds formed likely had nothing to do with subduction, as the carbon appears to come from the deeper mantle. Reducing conditions in the deep asthenospheric mantle > 300 km will stabilise methane, CH_4, in the mantle. Up welling low density CH_4 will be oxidised in the shallower mantle at conditions below the lithosphere to create H_2O. H_2O melts the mantle and infiltrates the lithosphere.

Studies on the water contents of minerals from cratonic xenoliths do not support the passage of water-rich liquids in the lithosphere because the water contents are well below the levels expected for equilibrium with water-rich liquids (Peslier *et al.* 2010). Another possibility is that diamond forming melts were quite rich in silicate material and that the amount of H_2O and CO_2 in the magmas was actually relatively low. The compositions estimated for some kimberlite magmas seem to correspond to plausible liquids from which diamonds could have grown, as they are estimated to be mainly silicate melts with only around 5 wt.% of both H_2O and CO_2 (Sparks *et al.* 2009). Diamonds did not form from the kimberlite melts that brought them to the surface, as diamonds are known to have formed billions of years before this event. However, kimberlites are examples of melts that can be stable within the lithosphere and they match also the volatile element concentrations required by fO_2 determinations of lithospheric rocks.

Figure 9 (left) demonstrates how diamonds may be formed from CO_2-bearing silicate magmas in the lithospheric mantle. Analyses of diamond-bearing mantle xenoliths demonstrate that diamonds form along lineations that can be interpreted as ancient melt pathways or veins

(Anand *et al.* 2004). As shown in Fig. 7 the fO_2 of lithospheric rocks is heterogeneous and gradients in fO_2 exist on the scale of meters or smaller. The carbonate or CO_2 content of a melt passing through a rock should adjust in order for it to approach equilibrium with the redox state of the wall rock. The amount of CO_2 in the melt in equilibrium with the wall rock needs to decrease if the fO_2 of the silicate wall rock decreases. Melts passing along a gradient of decreasing fO_2 will, therefore, precipitate diamonds in order for the CO_2 content of the melt to decrease. As this occurs ferrous iron in minerals of the wall rock will be oxidised. Over time the wall rocks will become oxidised until a level where the CO_2 melt content is in equilibrium with the rock and diamond precipitation will stop. This helps to explain why diamonds form in growth phases where only a small amount of diamond is added in each phase. It is quite likely that some melts entering the rock also contain too little CO_2 to be in redox equilibrium with the wall rocks. Under these circumstances preexisting diamond layers will be dissolved. Periods where diamond layers have been clearly redissolved are recorded in many diamonds (Wiggers de Vries *et al.*, 2011).

As shown in Fig. 9 (right) the thickening of the cratonic lithosphere was likely related to subduction of multiple sections of lithosphere that under plated the original lithosphere. However, the magmas from which diamonds themselves formed are unlikely to be related to subduction type processes. This can be ascertained by looking at the carbon isotopic composition of diamonds. Carbon comprises two stable isotopes, the dominant ^{12}C and ^{13}C. Carbon from the Earth's mantle is lower in ^{13}C, compared to the carbonate rocks brought into the mantle in subduction zones. Most diamonds are ^{13}C poor indicating that the carbon had a so called primordial mantle origin (Cartigny 2005). It was not recycled from the Earth's surface into the interior at a subduciton zone. For this reason the carbon in the melts that formed diamond likely originated from the deeper asthenospheric mantle. Possibly due to the up welling of low density methane, CH_4, from a more reduced deeper asthenosphere (Frost and McCammon 2008). CH_4 which does not lower the melting temperature of rocks would oxidise to H_2O in the asthenosphere just below the lithosphere. H_2O, however, does depress the melting of rocks and would create melts which then invade the overlying lithosphere. This flux of deeper reduced volatiles that are oxidised in the shallower asthenosphere may help to soften the asthenospheric mantle as water-bearing minerals are weaker. This may enable the lithospheric mantle to flow over the weaker asthenosphere, aiding the process of plate tectonics.

Mantle melting and the extraction of carbon from the interior

At mid ocean ridges tectonic plates move apart from each other and asthenospheric mantle flows upwards mainly in the solid state to fill the space created. As it up-wells the decompression experienced by mantle rocks causes them to melt and create basaltic magma, which rises to the surface and forms new oceanic crust. The mantle does not melt completely but only partially because the rocks contain many different mineral components which tend to enter melts at different temperatures. The temperature where a rock starts to melt is called the

solidus and where it is completely molten is called the liquidus. The solidus temperature of rocks increases with pressure, so a decrease in pressure at approximately the same temperature can cause mantle rocks to start melting. During decompression, rocks that are free of volatile elements will start to partially melt at approximately 60 km. However, the presence of carbon as carbonate lowers the solidus temperature of mantle rocks, which means up welling carbonate-bearing mantle would start to melt at depths of approximately 300 km (Fig. 10). Most of the melting that forms basalt magma would still occur at depths shallower than 60 km, but low degree carbon-rich melts would be formed much deeper and they would contain the entire carbon content of the rock (Dasgupta and Hirschmann 2006). As indicated in Fig. 10, melts produced at depth beneath a mid ocean ridge become focused into the main basaltic melting region. The solid mantle itself will at some point flow sideways as the

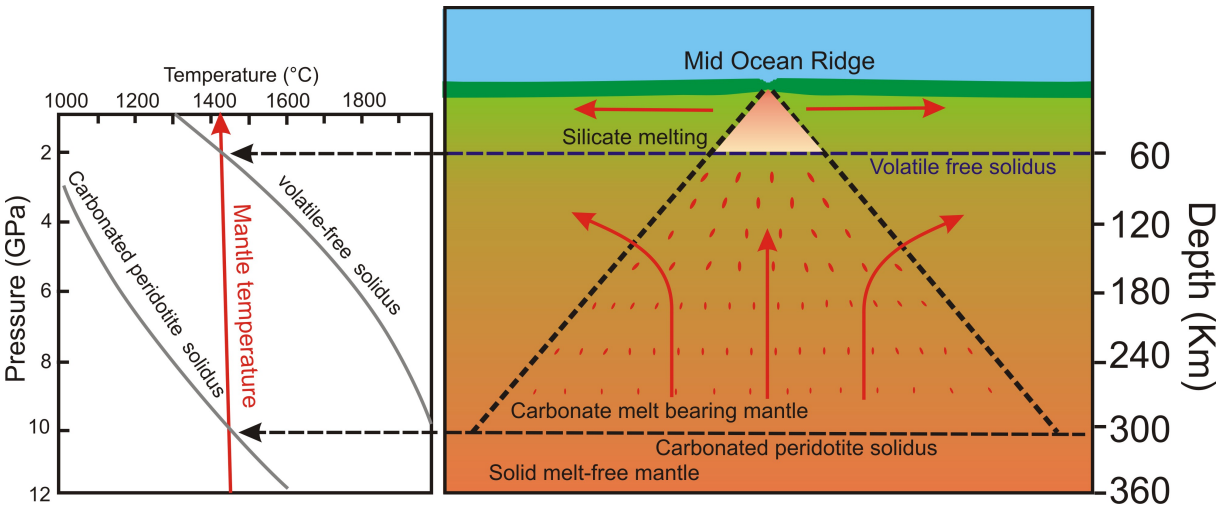

Fig. 10: A simple model for the extraction of carbonate melts from the mantle. If carbonate minerals are present in up welling mantle beneath mid ocean ridges, they will lower the melting temperature (solidus) of the mantle rocks and cause melting to commence at approximately 300 km. The diagram on the left shows how the mantle solidus is depressed in the presence of carbonate, compared to the volatile free solidus The resulting small degree carbonate melts will rise and be focused in the zone where silicate melting occurs to produce basaltic magma *i.e.*, < 60 km. In this way carbon will be stripped from a much larger volume of the mantle, *i.e.*, between the dashed diverging black lines, compared to that from which basaltic magma is extracted, *i.e.*, the pink triangle at the very top. Red lines show the flow direction of the solid mantle. This model takes no account of the redox state of the mantle, however, and the possibility that diamond rather than carbonate may be stable at depth.

oceanic plates move apart, but the melt produced within a certain zone, (indicated by dashed diverging lines in Fig. 10), will be drawn to the surface, mixed with basaltic magma and erupted. This model has important implications because it implies that the CO_2 erupted with basalt magma at mid ocean ridges has been extracted from a much larger volume of mantle than the basaltic magma itself. It would also mean that carbon is efficiently stripped from large volumes of mantle beneath ridges, implying that the carbon content of the mantle may

be relatively low. This model assumes, however, that carbon beneath ridges is hosted by carbonate minerals at depths of 300 km and this is not necessarily the case. If the fO_2 of the mantle is low enough, diamond may instead be stable at this depth. Diamond cannot be extracted by melting and will therefore fix carbon in the mantle, preventing a large extraction of carbon to the surface. In order to determine which scenario is more likely we need to determine whether diamond or carbonate melts will be stable and for this we need to make some estimate for the plausible range of fO_2 of the asthenospheric mantle. We have no direct samples of the asthenospheric mantle. All mantle samples come from the lithosphere and although they once formed the asthenosphere they have undergone melt extraction since this time. However, by mixing the composition of a melt depleted lithosphere with that of the extracted basalt, an estimate for the composition of the original asthenosphere can be obtained. From this composition it is clear that at depths > 80 km the asthenosphere would be mainly composed of garnet peridotite (Fig. 6).

Equilibrium [5], the same one used to determine the fO_2 of the cratonic lithosphere, can be used to estimate the fO_2 of the asthenospheric mantle (Fig. 11). Because we have no direct evidence for the amount of ferric iron as a percentage of the total iron content ($Fe^{3+}/\Sigma Fe$) of the asthenosphere, the calculation has been made for a range of values, but ultimately at shallow depth the fO_2 of the mantle should be consistent with the range estimated for mid ocean ridge basalts (MORB) as they inherit their fO_2 from the mantle source. With increasing depth beneath a mid ocean ridge the mantle will become more reducing. Conversely on decompression during upwelling, the mantle will experience a relative oxidation. This change in fO_2 results solely from the effect of changing pressure and temperature on the ferric and ferrous iron components in equilibrium [5].

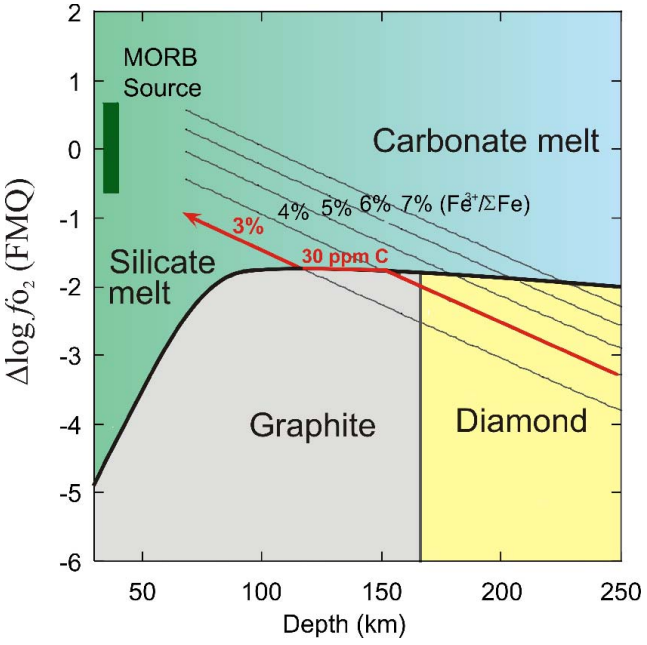

Fig. 11: The stability fields of carbon-bearing phases in upwelling mantle, compared to the fO_2 of the asthenospheric mantle. Below 100 km the stability field of melts is expanded to low fO_2 as the carbonate content becomes diluted by silicate melt. Curves for the fO_2 of the mantle are plotted as a function of the bulk rock $Fe^{3+}/\Sigma Fe$ content (finer diagonal gray lines). The red lines indicate a typical path that the up welling mantle will take if it contains initially 30 ppm carbon and 4 % $Fe^{3+}/\Sigma Fe$. Melting commences at the depth where the fO_2 of the mantle passes into the carbonate melt field. At this point graphite or diamond will oxidise to form melt. The green square indicates the fO_2 of the mid ocean ridge basalt (MORB) source (Stagno et al. 2013).

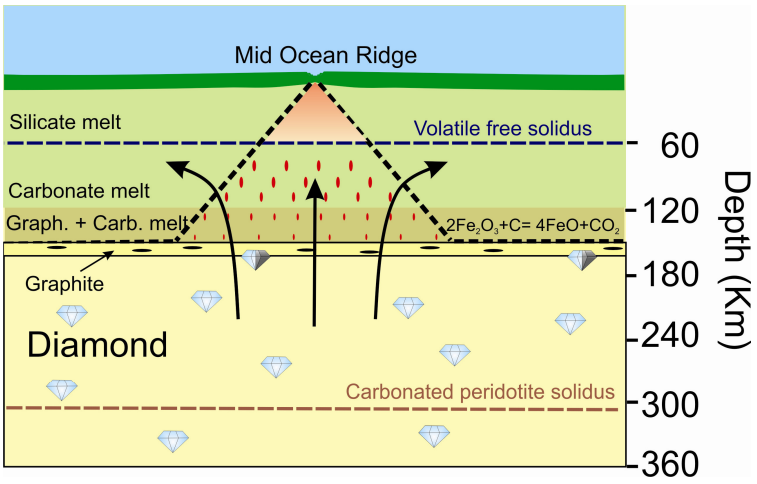

Fig. 12: The consequences of the path followed by the black line in Fig. 11 are shown in cartoon form. At depth the fO_2 of the mantle is in the diamond stability field and only rises into the carbonate melt field at approximately 150 km. At this point graphite is oxidised through the reduction of ferric iron in silicates. This redox melting process limits the amount of carbon extracted from the mantle.

What is important, however, is to examine how this range of asthenospheric fO_2, controlled by iron redox reactions, would interact with carbon redox reactions. Figure 11 also shows a solid curve which indicates the fO_2 at which graphite or diamond transforms to carbonate melt. By 250 km even the most ferric iron-rich mantle composition is in the diamond stability field so carbonate melting should not take place at 300 km depth as previously proposed. If we assume a typical mantle carbon estimate of 30 ppm (parts per million or 0.03 wt.% of the mantle rock) and an initial $Fe^{3+}/\Sigma Fe$ content of 4 %, then as shown as the highlighted curve in Fig. 11, below approximately 160 km carbon would be in the diamond stability field. As the mantle decompresses the diamond would transform to graphite but at only approximately 150 km would the fO_2 of the decompressing mantle reach the level where carbonate melt would form. At this point the first carbonate-rich melt would be produced, 150 km shallower than where the carbonate solidus would be crossed. Melting would therefore start as a result of a redox reaction and we refer to this as redox melting. At 150 km only an infinitesimally small amount of melt would be produced. It would take a further 40 km of decompression before all the graphite in the mantle would be oxidised to carbonate melt. This is because the reaction that has to occur, which can be simplified as,

$$\underset{\text{graphite}}{C} + \underset{\text{silicate}}{2Fe_2O_3} = \underset{\text{melt}}{CO_2} + \underset{\text{silicate}}{4FeO} \qquad [6]$$

is driven to the right hand side only as pressure is decreased. This means that oxidation of graphite occurs over a pressure, *i.e.*, depth, interval. During this interval graphite is oxidised as ferric Fe in silicates is reduced. As this occurs the fO_2 of the mantle will be buffered *i.e.*, constrained to lie along the near constant fO_2 curve for the equilibrium between graphite and

coexisting carbonate melt. After 30 ppm of graphite has been oxidised the remaining mantle has an $Fe^{3+}/\Sigma Fe$ content 1 % lower *i.e.*, it drops from 4 to 3 %. After all the graphite has oxidised the fO_2 of the mantle will rise again and eventually reach levels compatible with those recorded in MORB basalts. This redox melting behaviour is shown in the cartoon in Fig. 12.

As a result of redox reactions with iron-bearing minerals, carbon will be hosted at depth in the mantle as graphite and then diamond with carbonates only forming at depths shallower than 200 km. Even when carbonate melts form, a large depth interval is required for the redox reaction forming carbonate melt to go to completion. This redox melting process therefore significantly reduces the volume of mantle from which carbon can be extracted to the surface and means that the extraction process is controlled by the ferric/ferrous ratio of the mantle (Stagno *et al.* 2013). For oxidised mantle, rich in ferric iron, melting would occur at greater depth but for reduced mantle, poor in ferric iron, melting would only extract carbon from relatively shallow depths. This relationship between the fO_2 or more specifically the oxidation state of iron in the mantle and the extraction of carbon has likely had an important influence on the evolution of the Earth.

During the formation of the Earth, the metallic core separated from the silicate mantle. As a result, the fO_2 of the mantle was very low due to the presence of liquid Fe metal. Low fO_2 in the Earth's early history would have helped to keep carbon within the Earth's interior as it would have been immobilised as graphite or diamond. This may have prevented the accumulation of a particularly thick CO_2 atmosphere as occurred on Venus.

Basalt magmas associated with hot spots, such as those which formed the Hawaiian chain of islands, appear to come from mantle sources enriched in carbon. Hot spots form from hot up welling plumes from the deep mantle. Some estimates for the carbon content of hot spot mantle are up to 500 ppm (Dasgupta and Hirschmann 2010). In the deep mantle this carbon must be in the form of diamond, so a significant amount of ferric iron must be reduced to oxidise diamond to carbonate in the up welling plume, as in reaction [7]. In order to convert 500 ppm of diamond to carbonate the initial mantle $Fe^{3+}/\Sigma Fe$ content would have to drop by 15 % of total iron. This would imply that hot spot or plume type mantle is not only richer in carbon but is also enriched in ferric iron by an enormous amount. However, because this mantle is richer in ferric iron, it will also start to oxidise diamond to carbonate melt at a much greater depth, extracting carbon from the mantle over a larger depth interval. This means that rather than plume type mantle being enriched in carbon it may just be more oxidised, *i.e.*, contain more ferric iron, and this increases the depth of the column from which carbon is extracted from the mantle.

This may have had implications for the extraction of CO_2 from the mantle in the past. The initial opening of oceanic basins, such as the Atlantic, were associated with enormous phases of mantle melting that appear to have been caused by large mantle plumes. If these plumes

were more oxidised they would have started the extraction of carbon at a greater depth, extracting more carbon from the mantle which would also encourage a greater amount of silicate melting to occur. The oxidation state of iron in the deeper mantle may have consequently influenced the amount of melting and carbon extraction from the interior.

Summary and outlook

The fO_2 of the mantle, which for the main part is synonymous with the ferric and ferrous iron contents of silicate minerals, influences the form that carbon takes in the interior. By examining the fO_2 of diamond-bearing mantle rocks it is possible to place constraints on the types of liquids from which diamonds formed, even though these liquids are no longer preserved in the rocks. Melts with a significant silicate component but sub-equal proportions of CO_2 and H_2O provide a good match to the types of melts from which diamonds form.

Carbon extraction from the mantle beneath mid ocean ridges will occur through a redox melting process where carbon is present as diamond or graphite at depths deeper than 150 km but becomes oxidised to form carbonate melt only at shallower depths. Redox melting curtails the volume of mantle from which carbonate melts can be extracted and helps to keep carbon in the mantle.

The mantle source of hot spot magmas, which rises in plumes possibly from the very base of the mantle, seems to be enriched in ferric iron. This will cause carbonate melting to start at greater depths beneath the surface, which will lead to the extraction of carbon from a larger volume of mantle. This focuses more carbon towards the surface, even if the mantle source is not particularly enriched in carbon. Large amounts of plume activity in Earth's past may have had a profound effect on the amount of carbon exchanged between the mantle and the surface.

While here I have examined the carbon cycle in normal mantle peridotite rocks, the subduction of carbon will mainly occur in portions of the oceanic crust, which is mainly made of more silica-rich basalt *i.e.*, the partial melting product of peridotite rocks. Carbonates and organic carbon may be deposited in the oceanic crust as a result of alteration and sedimentation. As oceanic crust subducts it transforms in a series of metamorphic reactions to produce a rock called an eclogite. Eclogites are important for the subduction of carbon into the Earth. A critical aspect is to determine if carbonates in eclogites would be expected to melt or dissolve in fluids during the early stages of subduction and rise back towards the surface in island arc eruptions or if they may become reduced to graphite and diamond and be subducted into the deep mantle. Eclogitic xenoliths are also found in kimberlitic eruptions from cratonic lithosphere and diamonds are more regularly found in eclogites than peridotites, although eclogites make up only a small proportion of xenoliths. The exploration of carbon redox reactions for eclogites, of which there is currently little understanding, is therefore of particularly great interest not only to the carbon cycle but for the formation of diamonds in the Earth.

References

Anand M, Taylor LA, Misra KC, Carlson WD, Sobolev NV (2004) Nature of diamonds in Yakutian eclogites: views from eclogite tomography and mineral inclusions in diamonds. Lithos 77:333-348.

Bureau H, Langenhorst F, Auzende A-L, Frost DJ, Esteve I, Siebert J (2012) The growth of fibrous, cloudy and polycrystalline diamonds. Geochimica et Cosmochimica Acta 77:202-214.

Cartigny P (2005) Stable isotopes and the origin of diamonds. Elements 1:79-84.

Dasgupta R and Hirschmann MM (2010) The deep carbon cycle and melting in Earth's interior. Earth and Planetary Science Letters 298, 1-13.

Dasgupta R, Hirschmann MM (2006) Melting in the Earth's deep upper mantle caused by carbon dioxide. Nature 440, 659-662.

Frost DJ, McCammon CA (2008) The redox state of the Earth's mantle. Annual Review of Earth and Planetary Science 36, 389-420.

Sparks RSJ, Brooker RA, Field M, Kavanagh J, Schumacher JC, Walter MJ, White J (2009) The nature of erupting kimberlite melts. Lithos 112, 429-438.

Stagno V, Frost DJ (2010) Carbon speciation in the asthenosphere: Experimental measurements of the redox conditions at which carbonate-bearing melts coexist with graphite or diamond in peridotite assemblages. Earth and Planetary Science Letters 30, 72-84.

Stagno V, Ojwang DO, McCammon CA, Frost DJ (2013) The oxidation state of the mantle and the extraction of carbon from Earth's interior. Nature 493, 84-88.

Peslier AH, Woodland AB, Bell DR, Lazarov M (2010) Olivine water contents in the continental lithosphere and the longevity of cratons. Nature 467, 78-81.

Wiggers de Vries DF, Drury MR, de Winter DAM, Bulanova GP, Pearson DG, Davies GR (2011) Three dimensional cathodoluminescence imaging and electron backscatter diffraction; tools for studying the genetic nature of diamond inclusions. Contributions to Mineralogy and Petrology 161, 565-579.

Next page:

New experimental high-pressure station of the Bayerisches Geoinstitut at the Research Neutron Source Heinz Maier-Leibnitz (FRM II) in Garching/Munich. This project is funded by the German Ministry of Education and Research (BMBF) in the program "Condensed Matter Research".
A: Arrival of the large press weighing 50 tonnes in Garching; **B:** Installation of the base frame/positioning stage to allow three-dimensional alignment of the press into the highly focused neutron beam; **C:** Installation of the 2400 tonne (load capacity) press onto the base frame; **D:** Final set-up of the experimental station with the associated hydraulic system.

Nächste Seite:

Neuer Hochdruck-Messplatz des Bayerischen Geoinstituts an der Heinz Maier-Leibnitz Forschungsneutronenquelle in München-Garching. Dieses Projekt wird im Rahmen der Verbundforschung mit Mitteln des BMBF im Programm „Erforschung kondensierter Materie" gefördert.
A: Ankunft der 50 Tonnen schweren Großpresse in Garching; **B:** Einbringen des Unterbaus/ Positioniertisches zur dreidimensionalen Anpassung der Presse an den stark gebündelten Neutronenstrahl; **C:** Montage der Presse mit einer Presskraft von 2400 Tonnen auf ihrem Unterbau; **D:** Endgültiger Aufbau des Experimentier- und Messplatzes mit dem zugehörigen Hydrauliksystem.

A

B

C

D

4. Forschungsprojekte

4.1 Struktur und Dynamik der Erde und Planeten

Die frühe Geschichte unseres Sonnensystems bestimmte die Anfangsbedingungen (Temperatur, Zusammensetzung, Größe, …) der Entwicklung eines jeden Planeten von vor Milliarden Jahren bis heute. Dieser Zusammenhang erlaubt es, die frühe Entwicklung der Erde und anderer terrestrischer Planeten anhand von Laborexperimenten und der gegenwärtigen Zusammensetzung der Planeten abzuleiten. Auf ähnliche Weise ermöglicht die Kombination von thermodynamischen Eigenschaften von Mineralen und geodynamischen Modellen ein besseres Verständnis der dynamischen Prozesse im Inneren der Planeten. Die drei Beiträge dieses Kapitels bauen auf diesem Prinzip auf, in dem dynamische Simulationen mit geochemischen oder petrologischen Daten verknüpft werden.

Im ersten Beitrag dieses Kapitels wird die Bildung von Planeten durch N-Körper-Simulationen untersucht. In solchen Modellen wird die Kernbildung durch wiederholte gravitative Instabilitäten simuliert und die Verteilung chemischer Elemente innerhalb der Planeten nach Erkenntnissen aus geochemischen Experimenten berechnet. Unterschiede zwischen den Simulationen und den Beobachtungen für Merkur machen deutlich, dass bestehende Modelle zur Planetenentwicklung verbesserungswürdig sind.

In diesem Zusammenhang fällt dem Verständnis von Schmelzprozessen im Verlauf der Planetenentstehung eine Schlüsselrolle zu, um die Verteilung chemischer Elemente zwischen dem Metallkern und dem Silikatmantel in Planeten zu bestimmen. Der zweite Beitrag zielt darauf ab, Skalierungsbeziehungen zwischen der Größe von Einschlagskörpern (Meteoriten) und dem Schmelzvolumen in Protoplaneten zu bestimmen.

Die Erde unterscheidet sich von den anderen terrestrischen Planeten durch die Plattentektonik. Subduktion von Lithosphäre ins Erdinnere spielt eine entscheidende Rolle in der langfristigen thermischen und chemischen Entwicklung unseres Planeten. Der letzte Beitrag in diesem Kapitel nutzt ein thermodynamisches Modell, um Entgasungsprozesse von Wasser und Kohlendioxid in einer abtauchenden Lithosphärenplatte zu bestimmen. Dabei wird die Lithosphäre in drei Lagen unterteilt, die aus verschiedenen Gesteinsarten aufgebaut werden. Die Ergebnisse zeigen, dass die Abgabe von Wasser und Kohlendioxid auf den darüberliegenden Mantel beschränkt ist, und dass flüchtige Bestandteile in Subduktionszonen tief in den Erdmantel transportiert werden können.

4.2 Geochemie

Fraktionierungsvorgänge, die während der Akkretion der Erde stattfanden, sind aufgrund der Vielzahl an involvierten Prozessen generell schwierig zu interpretieren. Besonders wertvolle Informationen ergeben Untersuchungen an stabilen Isotopensystemen, da viele

Hochtemperatur-Prozesse nur wenig Auswirkung auf die Verteilung eines bestimmten Isotops zwischen zwei Reservoiren haben. Der erste Beitrag dieses Kapitels beschreibt, wie Si-Isotope möglicherweise während der Bildung des Erdkerns fraktionierten. Es zeigt sich, dass die Isotopensignatur von Silizium im Erdmantel höchstwahrscheinlich durch die Anreicherung von isotopisch leichtem Silizium im Erdkern zustande kam. Da der Umfang dieser Fraktionierung mit zunehmenden Druck und Temperatur abnimmt, kann der maximale Druck, unter dem diese Fraktionierung auftrat, abgeschätzt werden. Die zwei folgenden Beiträge befassen sich mit dem Thema, inwiefern die Anwesenheit von leichten Elementen wie Silizium die Fraktionierung anderer Elemente in den Erdkern ermöglicht haben könnte. Es werden die Bedingungen untersucht, bei denen mäßig volatile Elemente wie Blei und Zinn sich im Erdkern anreichern. Es stellt sich heraus, dass die gleich starke Verarmung dieser Elemente im Erdmantel auf die Präsenz von Schwefel im Erdkern hinweist. Demgegenüber zeigt die zweite Studie, dass eine Anwesenheit von Silizium in der den Kern bildenden Schmelze einen starken Einfluss auf die Verteilung von Wolfram zwischen Mantel und Kern gehabt hätte, nicht jedoch auf die Verteilung zahlreicher anderer Elemente.

Drei weitere Untersuchungen befassen sich mit der Aufschmelzung von Mantelgesteinen unter hohem Druck. Im ersten Beitrag werden Ergebnisse des vereinfachten Systems MgO-SiO_2 präsentiert. Mit diesen Daten können thermodynamische Modelle entwickelt werden, die Schmelzbildung über einen bestimmten Druck- und Temperaturbereich im tiefen Erdmantel erklären. In der nächsten Studie wird der Einfluss von Wasser auf Schmelzbeziehungen in demselben binären System untersucht. Die dritte Arbeit befasst sich mit der Zusammensetzung wasserhaltiger Schmelzen, welche bei geringem Aufschmelzungsgrad entstehen, wie z. B. durch Druckentlastung in Tiefen >150 km. Diese Schmelzen ähneln bezüglich ihrer Zusammensetzung einem wasserreichen, Kimberlit-ähnlichen Gesteinstyp, der in alten Krustenregionen vorkommt.

Eklogite sind metamorphe Gesteine, die sich im Erdmantel aus subduzierten Basalten bildeten. Der Oxidationszustand eklogitischer Gesteine steht im Fokus der nächsten beiden Beiträge. Eklogitische Mantelxenolithe führen häufiger Diamanten als peridotitische Mantelxenolithe. Der erste Beitrag versucht, den Ursachen dieses Phänomens durch Bestimmungen der Sauerstofffugazität in eklogitischen Gesteinen auf die Spur zu kommen, da dieser Parameter die Bildung von Diamanten aus kohlenstoffhaltigen Schmelzen stark beeinflusst. Der zweite Beitrag untersucht die Veränderungen im Redoxzustand eklogitischer Gesteine, welche als Folge von Plattensubduktion partiell aufgeschmolzen werden. Der Beitrag von Beyer und Frost beschreibt im Detail die ersten Schritte in der Entwicklung eines thermodynamisch robusten Geobarometers für Eklogite. Es wurden Hochdruck-Experimente durchgeführt, um den Einfluss der Jadeitkomponente auf den Ca-Tschermak-Gehalt von mit Granat koexistierendem Klinopyroxen zu messen. Das weiterentwickelte Barometer wurde dann gegen einen vorhandenen umfangreichen Satz experimenteller Daten getestet. Die Ergebnisse zeigen eine gute Übereinstimmung zwischen erwarteten und gemessenen Werten.

Drei weitere Beiträge widmen sich der Speicherung von flüchtigen Bestandteilen im Erdmantel. Die gegenwärtige Erdatmosphäre ist durch eine markante Abreicherung an Xenon im Vergleich zu anderen Edelgasen charakterisiert. Shcheka und Keppler haben experimentell die Löslichkeit von Edelgasen in $MgSiO_3$-Perowskit bestimmt. Sie haben herausgefunden, dass Argon und Krypton in hohem Masse kompatibel sind, während Xenon inkompatibel ist. Das bedeutet, dass die Edelgassignatur der neuzeitlichen Atmosphäre das Ergebnis einer Vermischung zwischen einem kleinen Überrest der Ursprungsatmosphäre und einer aus dem unteren Erdmantel entgasten Ar- und Kr-reichen Komponente ist. Die nächste Studie befasst sich mit der Löslichkeit von Stickstoff in Mineralen des oberen Erdmantels. Die Ergebnisse zeigen eine starke Abhängigkeit vom Redoxzustand auf und implizieren, dass der gegenwärtige obere Mantel eine potentielle Speicherkapazität für Stickstoff besitzt, die den N-Gehalt der modernen Atmosphäre um ein ca. 40-faches übertrifft. Außerdem könnte die Kristallisation des Magmaozeans zu einer Fraktionierung von N/Ar und N/C in der frühen Atmosphäre geführt haben. Die letzte Studie erforscht, wie viel Fluor und Chlor in den Mineralen Ringwoodit und Wadsleyit eingebaut werden können. Es zeigt sich, dass diese beiden Minerale mindestens zehn mal mehr F und Cl speichern können als Olivin, was bedeutet, dass die Übergangszone nicht nur ein wichtiges Reservoir für Wasser, sondern auch für Halogene darstellen könnte.

Die nachfolgende Studie von Solopova *et al.* erforscht die Stabilität von Na_2CO_3 unter Bedingungen, die vom oberen bis in den unteren Mantel herrschen. Die Resultate implizieren, dass Na_2CO_3 über den größten Teil des oberen Mantels und der Übergangszone als Schmelze vorliegen würde, sich aber im mittleren unteren Erdmantel in Diamant und O_2 aufspalten würde. Liu *et al.* befassen sich mit der Aufteilung von Kupfer zwischen Mantelmineralen und wasserführender Silikatschmelze als Funktion von Druck, Temperatur und Sauerstoff-fugazität. Normalerweise wird angenommen, dass Sulfide die Cu-Verteilung kontrollieren; es konnte jedoch gezeigt werden, dass auch Silikatminerale einen erheblichen Einfluss auf den Cu-Gehalt von Teilschmelzen haben können.

Die nächsten zwei Beiträge beschäftigen sich mit Prozessen in der Erdkruste. Yang und McCammon verwenden publizierte Daten über Seltene Erden-Elemente in Zirkonen, um die Entwicklung der Sauerstofffugazität fO_2 vom Hadaikum bis zur Gegenwart zu rekonstruieren. Sie fanden einen auffälligen Trend zu mehr reduzierenden Werten in Zirkonen mit einem Alter > 3,6 Ga. Dies lässt vermuten, dass die kontinentale Kruste zu jener Zeit reduzierender war, und dass dies eventuell mit einem reduzierenderen Mantel und einer reduzierenderen Atmosphäre im Zusammenhang steht. Kularatne und Audétat untersuchen experimentell die Löslichkeit von Rutil in wasserhaltigen felsischen Magmen, da diese Ergebnisse wichtig für die Anwendung der Titan-in-Quarz- und Titan-in-Zirkon-Thermo(-baro)meter sind. Bisher verfügbare Löslichkeitsmodelle zu TiO_2 liefern widersprüchliche Ergebnisse. Die Autoren wenden eine neue Methode an, um die langsame Diffusion von Ti bei niedrigen Temperaturen zu überwinden. Die erhaltenen Ergebnisse stimmen mit einer vorangegangenen experimentellen Untersuchung überein und unterstützen die Stichhaltigkeit der jüngsten Re-Kalibrierung des Ti-in-Quarz-Thermobarometers.

Die zwei abschließenden Beiträge dieses Kapitels stehen im Zusammenhang mit der Bildung von Erzlagerstätten. Tan *et al.* untersuchen die Herkunft von Metallen in gangförmigen Goldlagerstätten Ost-Chinas. Mafische, alkalihaltige Gänge, die räumlich und zeitlich mit der Erzbildung im Zusammenhang stehen, weisen eine ungewöhnliche, nicht-radiogene Blei-Isotopen-Zusammensetzung auf, die mit derjenigen des Erzes identisch ist. Dieser und weitere Befunde liefern einen deutlichen Hinweis darauf, dass die Metalle dieser Lagerstätte aus mafischen Magmen stammen, die bei der Teilaufschmelzung des alten Lithosphärenmantels entstanden. Lerchbaumer und Audétat untersuchen Schmelz- und Fluideinschlüsse in schwach mit Molybdän mineralisierten Graniten und vergleichen ihre Ergebnisse mit Daten von wirtschaftlich Mo-mineralisierten Graniten, um die lagerstättenbildenden Prozesse zu identifizieren. Es zeigt sich, dass die Mo-Konzentration in Fluiden und Schmelzen von geringerer Bedeutung ist als der Wirkungsgrad, mit dem diese aus großräumigen Magmenkammern extrahiert und in kleineren Volumen akkumuliert wurden.

4.3 Mineralogie, Kristallchemie und Phasenübergänge

Kristall- und Schmelzstrukturen sind druck- und temperaturabhängig, aber auch beeinflusst durch Sauerstofffugazität und chemische Zusammensetzung. Weitere Forschungsarbeiten für ein besseres Verständnis der Prozesse, die das dynamische Kräftespiel im Erdinneren sowie die physikalischen Eigenschaften der Materialien kontrollieren, werden im Folgenden beschrieben. Dieses Kapitel präsentiert neue Forschungsarbeiten, mit denen das Verhalten unterschiedlicher Materialien geklärt werden soll. Es ist in vier Themenfelder unterteilt: *Kristallstruktur*, *Elektronenstruktur*, *Kompressionsverhalten* und *Phasenstabilität*.

Die ersten acht Beiträge sind auf das Gebiet *Kristallstrukturen* ausgerichtet und darauf, wie chemische und physikalische Eigenschaften Kristallstrukturen beeinflussen. Röntgenbeugungsanalysen an Einkristallen aus Silikatperowskit des unteren Erdmantels wurden mit Hilfe von Synchrotronstrahlung in einer laserbeheizten Diamantstempelzelle (DAC) durchgeführt. Das eingesetzte Laser-Heizsystem arbeitet doppelseitig und ist transportabel. Die Beugungsmessungen zeigen keinen Spinübergang von Eisen, der aus chemischen Austauschreaktionen zwischen den A- und B-Gitterstellen resultieren könnte. Ein ähnlicher methodischer Ansatz mit Kompression von $CaIrO_3$ als Analogon für $MgSiO_3$-Post-Perowskit, offenbart ungewöhnliche Eigenschaften, deren Deutung für ein besseres Verständnis des Kompressionsmechanismus relevant sein könnte. Die Raman-Spektroskopie stellt in Verbindung mit der DAC-Technik eine leistungsfähige Methode dar, um druckabhängige Strukturveränderungen zu erkennen. Mit dieser Methode wurden Karbonate aus der $MgCO_3$- und $FeCO_3$-Mischkristallreihe untersucht, um deren mögliches Schicksal im unteren Erdmantel zu verstehen. Mit einer ähnlichen Studie für die Majorit-Knorringit-Mischkristallreihe wurde ein wichtiger Durchbruch im Verständnis der kristallchemischen Eigenschaften der Reihe erzielt. Die vier folgenden Beiträge befassen sich mit analytischen elektronenmikroskopischen Untersuchungen von Ringwoodit, Hibonit, Diamanten in

Meteoriten und großen $MgSiO_3$-Perowskit-Einkristallen. Transmissionselektronenmikroskopische Untersuchungen (TEM-ALCHEMI) zur Eisenverteilung in Ringwoodit im System Mg_2SiO_4-Fe_2SiO_4 zeigen Gitterplatzverteilungen; Bestimmungen des Valenzzustands und der Gitterstellenbelegung von Titan im Hibonit ergeben nützliche Hinweise auf die Sauerstofffugazität zur Zeit der Kondensation des Sonnennebels. Diamanten in Ureiliten wurden wahrscheinlich durch chemische Kondensation aus der Dampfphase gebildet; die geringe Fehlstellendichte in Einkristallen aus $MgSiO_3$-Perowskit, die mit einer TEM-Messmethode (*weak-beam dark field imaging*) identifiziert wurde, zeigt, dass diese Kristalle sich für Verformungsuntersuchungen sehr gut eignen.

Die physikalischen Eigenschaften von Schmelzen im Erdmantel und im äußeren Erdkern können die chemische und thermische Entwicklung der Erde ganz erheblich beeinflussen. Einige dieser Eigenschaften werden durch die *Elektronenstruktur* bestimmt, wobei experimentelle und theoretische Ansätze sich mit dem Spinzustand von Eisen in Silikatgläsern und mit elektronischen Transporteigenschaften von flüssigem Aluminium unter extremen Druckbedingungen befassen. Der Spinzustand von Eisen kann durch eine druckbedingte Verdichtung einer Silikatschmelze beeinflusst werden, aber es wurden in einem eisenführenden Silikatglas bis zu Drücken von 84 GPa keine Hinweise auf einen Spinübergang von *High-Spin* nach *Low-Spin* gefunden. In einem zweiten Beitrag wird das Verhalten von flüssigem Aluminium unter extremen Druckbedingungen als freies Elektronen-Metall beschrieben. Daraus ist abzuleiten, dass sich Aluminiumschmelzen für Fallstudien zu elektronischen Transporteigenschaften eignen.

Druck ist nicht nur in den Geowissenschaften eine bedeutende Variable, sondern auch in den angewandten Materialwissenschaften. Unter dem Oberbegriff *Kompressionsverhalten* wird in zwei Studien der Einfluss von Druck auf Materialien wie Quarzglas bzw. komplexes zeolithähnliches Material mit Hilfe der *in situ*-Röntgenbeugung und der Ultraschall-Interferometrie untersucht. Das Verhalten der Hydroxyl-Spezies in Mineralen des Erdmantels wurde anhand von OH-führendem $MgSiO_3$-Akimotoit untersucht, der bei Hydratisierung deutliche Veränderungen in seinen physikalischen Eigenschaften aufweist. Eine Studie über Wadsleyit und Ringwoodit bei hohen Drücken und Temperaturen, bei der die *in situ*-Infrarot-Spektroskopie zum Einsatz kommt, führte zu neuen Erkenntnissen über den Bindungszustand von Wasser im Erdmantel.

Phasenübergänge gehören zu den drastischsten Reaktionen einer Kristallstruktur auf Druck. Nahezu jegliches Material ist davon in einem gewissen kritischen Druck- und Temperaturbereich betroffen. Im letzten Unterthema dieses Kapitels, *Phasenstabilität*, werden in zwei Beiträgen die Phasenbeziehungen einer neuen Eisenoxidphase, Fe_4O_5, bei hohem Druck und hoher Temperatur dargelegt, die sich auf elektronenmikroskopische Untersuchungen und auf Röntgenbeugungsanalysen stützen. Eine Raman-spektroskopische Untersuchung eines druckbedingten Phasenübergangs in Coesit liefert neue Einsichten in die Polymorphie von Quarz und in Amorphisierungsprozesse.

4.4 Physikalische Eigenschaften von Mineralen

Geophysikalische und geochemische Untersuchungen liefern uns indirekte Hinweise auf das Erdinnere; ihre Interpretation beruht fast gänzlich auf direkten experimentellen Messungen physikalischer und chemischer Eigenschaften unter den relevanten Druck- und Temperaturbedingungen im Labor.

Das Verständnis seismischer Profile des Erdinneren anhand von elastischen Eigenschaften von Mantelmineralen ist der erste Schritt auf dem Weg zu einer Charakterisierung der Struktur unseres Planeten. Es überrascht daher nicht, dass auch im vergangenen Jahr am Bayerischen Geoinstitut große Anstrengungen unternommen wurden, sowohl Kompressibilität als auch Schallwellengeschwindigkeiten in unterschiedlichen Materialien zu bestimmen. Diese Untersuchungen sind Thema der ersten sechs Beiträge dieses Kapitels. Kompressibilitätsuntersuchungen an kristallinem Granat mit komplexen Zusammensetzungen und an einer neuen aluminiumreichen Phase (NAL) sollen Erkenntnisse über die Eigenschaften von Basalten, die in den unteren Erdmantel subduziert werden, erbringen.

Der mögliche chemische Ursprung seismischer Geschwindigkeitsanomalien im unteren Erdmantel an der Kern/Mantel-Grenze wird dadurch untersucht, dass man Veränderungen in den Wellengeschwindigkeiten in polykristallinen $MgSiO_3$-Perowskiten, die sowohl Fe^{3+} als auch Al enthalten, unter hohem Druck misst. Dazu wird eine Kombination aus Röntgenbeugungs- und Ultraschall-Messungen in Verbindung mit einer Synchrotron-Strahlungsquelle benutzt. Außerdem wurde der komplette elastische Tensor von Fe^{2+}-haltigen $MgSiO_3$-Perowskiten bei unterschiedlichen Drücken mit Hilfe der am BGI vorhandenen Kombination aus Brillouin-Streuung und hochauflösender Röntgendiffraktometrie bestimmt. Des Weiteren wurden vor kurzem Schallwellengeschwindigkeiten an (Mg,Fe)O mit inelastischer Kernstreuung (NIS) bestimmt, die zu widersprüchlichen Ergebnissen führten. Ein am ESRF in Grenoble durchgeführtes Experiment – mit einer am BGI synthetisierten und charakterisierten Probe – ergab, dass die Diskrepanz dieser Ergebnisse darauf beruht, dass die NIS-Messungen die lokale Umgebung des Fe in der Probe erfassen, während die Brillouin-Spektroskopie die Gesamtprobe untersucht.

Immer noch offen ist die Frage, ob Laborexperimente, die entweder bei recht hoher Frequenz oder statisch ausgeführt wurden, dazu genutzt werden können, die Geschwindigkeiten seismischer Wellen zu interpretieren, oder ob Dispersion berücksichtigt werden muss, d. h. die elastischen Eigenschaften frequenzabhängig sind. Eine Zusammenstellung von Kompressions- und Schermoduli für MgO aus der Literatur, die mit unterschiedlichen Methoden gemessen wurden, lassen keinen klaren Trend als Funktion der Frequenz erkennen. Somit lassen sich zur Interpretation seismologischer Daten die Elastizitätsmoduli zumindest für MgO einsetzen.

Die elastischen Eigenschaften sind nicht die einzigen physikalischen Eigenschaften, die herangezogen werden können, um die Struktur des Erdinneren zu erklären. Im Labor

gewonnene Ergebnisse zur elektrischen Leitfähigkeit liefern zum Beispiel wichtige Informationen darüber, wie die die Leitfähigkeit eines Minerals von der chemischen Zusammensetzung und der Temperatur beeinflusst werden. Mit diesen Informationen lassen sich Messergebnisse zur elektromagnetischen Induktion interpretieren, die auf Temperatur und Eisengehalt viel sensibler reagiert, als seismische Daten. Erkenntnisse zur elektrischen Leitfähigkeit eines Fe- und Al-reichen $MgSiO_3$-Perowskits, die im siebten Beitrag vorgestellt werden, zeigen, dass das $Fe^{3+}/\Sigma Fe$-Verhältnis und nicht lediglich der Gesamt-Eisengehalt die Leitfähigkeiten im Bereich des mittleren Erdmantels signifikant beeinflusst.

Seit den frühen Arbeiten von Ringwood ist die Verwendung analoger Phasen eine leistungsfähige Methode, um Materialeigenschaften zu erfassen, deren Druck- und Temperatur-Stabilitätsfelder nur schwer zugänglich sind. Der Einsatz von Fluoriden mit einer Post-Perowskit-Struktur stellt zum Beispiel ein brauchbareres Analogon für $MgSiO_3$-Post-Perowskit dar als $CaIrO_3$- oder $CaPtO_3$-Materie. Im letzten Beitrag wird die Bestimmung von Struktur und magnetischem Übergang von $NaCoF_3$ mit Hilfe der Neutronenstrahl-Pulverdiffraktometrie beschrieben.

4.5 Fluide, Schmelzen und ihre Wechselwirkung mit Mineralen

Die Erdatmosphäre ist letztlich das Produkt der Entgasung des Erdmantels durch Vulkanismus. Die Entmischung von flüchtigen Bestandteilen aus Magmen ist gleichzeitig die Ursache für alle Arten von explosiver vulkanischer Tätigkeit. Ein wesentlicher Schritt ist hier die Bildung und das Wachstum von Gasblasen, die letztlich das Magma zerreißen können. Bisher konnten diese Prozesse nur mit klassischen Quench-Experimenten untersucht werden, bei denen lediglich die Textur der Probe nach dem Experiment, aber nicht die Entwicklung des Gefüges während des Experimentes untersucht werden kann. Der erste Beitrag in diesem Abschnitt des Jahresberichts beschreibt Experimente, in denen Keimbildung und Wachstum von Blasen im Magma erstmals *in situ* bei hoher Temperatur beobachtet wurden. Diese Experimente zeigen unter anderem, dass direkte Koaleszenz – und nicht Ostwald-Reifung, wie oft angenommen – der Hauptmechanismus für das Wachstum der Blasen ist.

Zwei Beiträge in diesem Abschnitt beschäftigen sich mit der Freisetzung von flüchtigen Bestandteilen bei vulkanischen Eruptionen, und zwar von Schwefel und Stickstoff. In oxidierten sauren Silikatschmelzen ist oft der größte Teil des Schwefels als Anhydrit $CaSO_4$ gebunden, so dass er während der kurzen Zeitskala einer plinianischen Eruption nicht in die Gasphase abgegeben werden kann. Es wird hier gezeigt, dass die Stabilität von Anhydrit durch das Löslichkeitsprodukt von CaO und SO_3 in der Schmelze gut beschrieben werden kann und dass dieses Löslichkeitsprodukt sehr stark mit der Temperatur zunimmt. Die Daten zur Verteilung von Stickstoff zwischen wässrigen Fluiden und granitischen oder basaltischen Schmelzen sind die ersten, die jemals unter den für vulkanische Systeme typischen Druckbedingungen gemessen wurden. Hierzu mussten spezielle Methoden für die Elektronen-

Mikrosonde entwickelt werden, um sehr niedrige Konzentrationen von Stickstoff in abgeschreckten Gläsern quantifizieren zu können.

Die letzten beiden Beiträge dieses Abschnitts untersuchen das Verhalten von Wasser im oberen Mantel. Die Verteilungskoeffizienten von Wasser zwischen Mantelmineralen und Silikatschmelzen wurden bei 6 GPa gemessen und ergaben einen Gesamt-Verteilungskoeffizienten von Wasser zwischen Peridotit und Schmelze von 0.018. Zusammen mit weiteren experimentellen Daten lassen diese Experimente vermuten, dass wasserhaltige Schmelzen in einer Tiefe von 180 km im oberen Mantel nicht stabil sind. Schließlich wurde die Lage der kritischen Kurve im System H_2O-H_2 für den oberen Mantel auskartiert. Die Daten zeigen, dass Entmischung zwischen Wasser und Wasserstoff sowohl im heutigen Mantel als auch im sehr viel heißeren Mantel zur Zeit des Archaikums auftreten kann. Entgasung von fast reinem Wasserstoff aus dem reduzierten Mantel könnte eine frühe, reduzierte Atmosphäre auf der Erde stabilisiert haben.

4.6 Rheologie und Metamorphose

In den Geowissenschaften versteht man unter Rheologie die Untersuchung der Fließeigenschaften von Gesteinsmaterialien unter Druck- und Temperaturbedingungen des Erdinneren. Diese Eigenschaften tragen zum Verständnis globaler Deformationsprozesse wie der Mantelkonvektion bei. Das Studium der Metamorphose befasst sich mit den Phasenübergängen, die in Gesteinen unter den veränderten Druck- und Temperaturbedingungen während solcher Fließprozesse stattfinden. Die hier vorgestellten Beiträge sind exzellente Beispiele dafür, wie die experimentelle Untersuchung mikroskopischer Eigenschaften kleiner Proben zu einem besseren Verständnis der großmaßstäblichen Eigenschaften der dynamischen Erde führen kann.

Die ersten drei Beiträge beschäftigen sich mit der möglichen Verringerung der Festigkeit von Olivin, dem wichtigsten Mineral des oberen Mantels, durch den Einbau geringer Mengen von Wasser. Frühere Laborstudien legten nahe, dass der hydrolytische Festigkeitsabfall von Olivin für die Existenz der Asthenosphäre verantwortlich sein könnte, einer weichen Lage im oberen Mantel, die den Mechanismus der Plattentektonik ermöglicht. Durch die Messung der Eigendiffusion von Si und O als Funktion des Wassergehalts zeigen die Autoren, dass Wasser eine deutlich geringere Festigkeitsreduktion von Olivin bewirkt als bisher angenommen wurde, wodurch die Rolle von Wasser für die Entstehung der Astenosphäre in Frage gestellt wird. Im dritten Beitrag werden erste Ergebnisse einer Studie präsentiert, in der die Mobilität von Versetzungslinien beim Einbau von Wasser in Olivin untersucht wurde.

Ein weiterer wichtiger Aspekt der Deformation von polykristallinen Aggregaten ist die Ausbildung einer kristallographischen Vorzugsorientierung (Textur), die die beobachtete seismische Anisotropie z. B. im oberen Mantel und nahe der Kern/Mantel-Grenze erklären kann. Im vierten Beitrag wird die Textur von experimentell verformten Lawsonit präsentiert,

einem wasserhaltigen Mineral, das bei Hochdruckmetamorphose in subduzierten Lithosphärenplatten entsteht. Die Autoren präsentieren Hinweise auf die Bildung einer Deformationstextur, allerdings erfordert die Komplexität des Systems weitere Untersuchungen. Auf dem Weg der Platten tiefer in den Mantel hinein werden durch Phasenübergänge dichte, wasserhaltige Magnesiumsilikate erzeugt. In dem folgenden Beitrag wird eine TEM-Untersuchung zu den Versetzungen in einer solchen Phase („superhydrous B“) präsentiert, die bei der Deformation unter hohem Druck gebildet wurden. Mit Deformationsprozessen im noch tieferen Erdmantel beschäftigt sich der sechste Beitrag, bei dem es um die Verformung von $CaIrO_3$ geht, einem strukturellen Analogon für die Hauptphasen (Mg, Fe)SiO_3-Perowskit und Post-Perowskit des unteren Mantels. In der Studie wird gezeigt, dass deformierter $CaIrO_3$-Perowskit eine deutliche Textur aufweist, wenn er in seiner orthorhombischen Kristallstruktur indiziert wird. Die Autoren zeigen, dass die erwartete seismische Anisotropie mit der gemessenen Anisotropie nahe der Kern/Mantel-Grenze kompatibel ist.

Viele Gesteinsproben des oberen Mantels weisen eine Pyroxenbänderung auf, die als Resultat von Deformation und Reaktion des Olivins mit einer reaktiven Schmelze interpretiert wird. Im siebten Beitrag wurde dieses Zusammenspiel in einem Olivinaggregat mit einer Si-übersättigten Schmelze untersucht. Die Autoren konnten die Entstehung der Bänderung zum ersten Mal simulieren und deren Orientierung erklären. Für den achten Beitrag wurde das Deformationsverhalten koexistierender metallischer und silikatischer Schmelzen in einer Olivinmatrix untersucht, um mögliche Mechanismen der Kern/Mantel-Differenziation während der Planetenentstehung zu untersuchen. Die Autoren zeigen die relative Immobilität der Metallschmelzen im Verhältnis zu den Silikatschmelzen während der Deformation, was eine Segregation erschwert und die Notwendigkeit großräumiger Aufschmelzung zur effizienten Schmelzextraktion bestätigt. Im letzten Beitrag werden durch detaillierte Untersuchungen des metamorphen Phasengefüges drei unterschiedliche Episoden in der geologischen Geschichte zweier Marsmeteoriten rekonstruiert.

4.7 Materialwissenschaften

Die Mehrheit der materialwissenschaftlichen Forschungsprojekte am Bayerischen Geoinstitut beschäftigt sich mit der Synthese ultraharter Materialien sowie mit Untersuchungen eines weiten Bereichs von physikalischen und chemischen Eigenschaften dieser Materialien. Die Ausstattung des Instituts ist für diese Forschungsziele aufgrund des großen Spektrums an experimentellen Hochdruck-Apparaturen, die zur Synthese ultraharter Materialien erforderlich sind, ideal. Auch die vorhandenen analytischen Einrichtungen für chemische Analysen, Röntgenbeugung und spektroskopische Untersuchungen sind hervorragend. Um physikalische und chemische Eigenschaften der Materialien bei Drücken und Temperaturen jenseits der experimentellen Zugänglichkeit zu erkunden, werden rechnergestützte Methoden angewandt. Die hier präsentierten Ergebnisse behandeln Oxide, Boride, Nitride, Bor sowie $BiFeO_3$ mit unterschiedlichen Fe-Wertigkeiten.

Der erste Beitrag präsentiert Bestimmungen der Schmelztemperatur von kubischem Bornitrid (BN) bei Drücken bis zu 1000 GPa durch Molekulardynamik-Simulationen. Kubisches BN ist ein ultrahartes Material mit Eigenschaften, die denen von Diamant ähnlich sind und ist daneben ein potentieller Druckstandard bei Experimenten mit Diamantstempelzellen. Bisher war es lediglich möglich, die Schmelztemperatur experimentell bei Drücken von maximal 10 GPa zu bestimmen. Eine wichtige Erkenntnis ist, dass oberhalb von 500 GPa (0,5 TPa) die Schmelztemperatur von kubischen BN bei steigendem Druck abnimmt, sodass die Neigung der Kurve von positiv auf negativ wechselt. Ursache für dieses Verhalten könnte sein, dass die BN-Schmelze oberhalb von 500 GPa durch druckbedingte strukturelle Veränderungen eine höhere Dichte aufweist als die feste Phase.

Das Kompressionsverhalten von V_2O_3 wurde bis 33 GPa untersucht. Diese Verbindung zeigt einen Halbleiter-Metall-Übergang unterhalb von 150-160 K, der in Verbindung mit einer deutlichen thermodynamischen Instabilität steht. Die Instabilität äußert sich durch einen Strukturwandel und durch einen um einige Größenordnungen veränderten elektrischen Widerstand. Neue Ergebnisse der Kompressionsuntersuchungen deuten auf einen niedrigeren Kompressionsmodul als bisher angegeben – was eventuell durch eine nicht-hydrostatische Belastung beeinflusst wurde. Das Kompressionsverhalten von V_2O_3 mit Korundstruktur weicht von dem Verhalten anderer 2:3-Oxide ab, was ein Hinweis auf andere ungewöhnliche physikalische und chemische Eigenschaften sein kann.

Boride stellen eine Materie mit potentiell ultrahartem Charakter dar. Zwei Beiträge über MnB_2 and FeB_4 folgen hier. In Experimenten und durch atomistische Berechnungen wurden Struktur, Stabilität und Kompressionsmodul von MnB_2 bestimmt – mit dem Ergebnis, dass dieses Material nicht als superhart bezeichnet werden kann. Die zweite Studie beschreibt sehr detaillierte Untersuchungen der Kristallstruktur von FeB_4 anhand von Experimenten mit einem Einkristall; das Kompressionsverhalten wurde bei Drücken bis zu 38 GPa bestimmt. Der Kompressionsmodul ist im Vergleich zu den meisten anderen Boriden hoch und stimmt mit dem hohen Härtegrad dieses Stoffs überein.

Im Anschluss wird das Ramanspektrum eines Einkristalls aus α-Bor bei Drücken bis 36 GPa and Temperaturen bis 473 K beschrieben. Die beiden das Kapitel abschließenden Beiträge präsentieren Ergebnisse (1) zu texturellen und elektronischen Eigenschaften von OsB_2, einem potentiell harten Material, wie atomistische Berechnungen ergaben und (2) über Eigenschaften von $BiFeO_3$, einem Material mit verschiedenen Fe-Wertigkeiten, anhand von Proben, die bei unterschiedlichen Bedingungen bis 19 GPa und 1100 °C synthetisiert wurden.

4.8 Methodische Entwicklungen

Die Entwicklung neuartiger theoretischer Ansätze und experimenteller Methoden und die Beurteilung ihres Potentials sind eine faszinierende wissenschaftliche Herausforderung, die

manchmal zu unerwarteten, bahnbrechenden Ergebnissen führen kann. Derartige innovative Leistungen sind notwendig, um fundamentalen Fortschritt zu erzielen und auf einem wissenschaftlichen Arbeitsfeld zur Spitze zu zählen. Die thematische Vielfalt der methodischen Arbeiten im vorliegenden Abschnitt zeigt sehr gut die breite Ausrichtung der Forschung des Bayerischen Geoinstituts.

Die thermodynamische Beschreibung der physikalischen Eigenschaften schafft eine solide Ausgangsbasis für die Analyse der Prozesse im tiefen Erdinneren. Der erste Beitrag dieses Kapitels präsentiert ein im Geoinstitut entwickeltes neuartiges, flexibles und erweiterbares Software-Paket, das die Berechnung von Phasengleichgewichten und deren thermodynamischer Eigenschaften auf Basis der Eigenschaften von einzelnen Mineralen erlaubt.

Der zweite rechnergestützte Beitrag stellt eine neue Methode vor, wie ein skalares Feld in eine Strömung bewegt wird, z. B. in geodynamischen Simulationen. Die Methode basiert auf dem Konzept, eine Wellengleichung zweiter Ordnung an Stelle der Advektionsgleichung erster Ordnung zu lösen, wodurch Transport ohne numerische Diffusion erreicht wird. Hier wird ein multi-dimensionaler Ansatz durch Aufspaltung der Advektionsgleichung in die verschiedenen Richtungen eingeführt, und deren Lösung wird analysiert. Dieser Ansatz erweist sich als leistungsfähig und bemerkenswert erfolgreich in der Reproduktion analytischer Ergebnisse.

Wasserhaltige Fluide spielen eine entscheidende Rolle bei der Metasomatose und für chemischen Transport im Erdmantel. Die Lösungseigenschaften wasserhaltiger Fluide als Funktion des Drucks sind nur mäßig bekannt. Sogar elementare Daten, wie z. B. die dielektrische Konstante von Wasser, die Dissoziationskonstante von Wasser sowie der Dissoziationsgrad von Salzen und Säuren unter Druckbedingungen des Erdmantels, wurden bisher nicht bestimmt. All diese Parameter sind im Prinzip über die Bestimmung der elektrischen Leitfähigkeit zugänglich. Eine neue Methode, bei der eine hydrothermale Diamantstempelzelle zur Anwendung kommt, ermöglicht die Bestimmung elektrischer Leitfähigkeiten von Fluiden bei Temperaturen bis 900 °C und Drücken bis mindestens 7,5 GPa, was bisherige Experimente um eine Größenordnung übersteigt.

Präzise Spannungsmessungen sind eine Grundvoraussetzung für die Bestimmung rheologischer Eigenschaften von Materie bei Verformungsexperimenten unter erhöhten Drücken und Temperaturen. Der vierte Beitrag widmet sich Untersuchungen des piezoelektrischen Effekts – Ladungsverschiebung als Reaktion auf Druckbelastung – eines Kristalls als neuem Ansatz für diese seit langem ungelöste Fragestellung. Die Verwendung von Quarz- und $GaPO_4$-Kristallen hat erste, vielversprechende Ergebnisse bei Raumtemperaturen geliefert, jedoch sind weitere technische Entwicklungen erforderlich, um die Methode auch für höhere Temperaturen einzusetzen.

Von ähnlich großer Wichtigkeit wie Spannungsmessungen in Verformungsexperimenten ist die genaue Druckbestimmung in Experimenten mit Diamantstempelzellen. Am einfachsten wird der Druck durch Fluoreszenz-Verschiebung von Eichmineralen bestimmt: Üblicherweise werden Rubin oder Sm-haltiger Yttrium-Aluminium-Granat (Sm:YAG) verwendet. Fluoreszenz-Verschiebungen sind sekundäre Druckanzeiger, weil sie mit Hilfe von Zustandsgleichungen aus Schockwellenexperimenten kalibriert werden; ihre Verwendung außerhalb der Kalibrierungsbedingungen kann zu großen Ungenauigkeiten in den Druckbestimmungen führen. Die Kombination aus Brillouin-Spektroskopie zur Bestimmung der elastischen Konstanten mit Röntgenbeugungsverfahren zur Bestimmung der Dichte ermöglicht eine von Eichmineralen unabhängige Druckbestimmung, die mit der Fluoreszenzverschiebung korreliert werden kann. Dadurch wird die Fluoreszenz von Sm:YAG zu einem primären Druckstandard aufgewertet.

Die drei das Kapitel abschließenden Beiträge behandeln Fortschritte im technischen Design von Diamantstempelzellen (DAC). Der experimentelle Aufbau zur Bestimmung inelastischer Kernstreuung an der Europäischen Einrichtung für Synchrotronstrahlung in Grenoble (ESRF) erfordert in Kombination mit einer doppelseitigen Laserheizung bauliche Veränderungen der DAC und der Laserheizung, um ein gleichzeitiges Beheizen und Bestrahlen der Probe zu ermöglichen.

Diamanten werden in der DAC typischerweise in einer Metallhalterung montiert, die herkömmlich eine konische oder polygonale Form aufweist. Hier wird ein neues Stempel-Design mit einem Diamant mit kugelförmiger Krone und einer Halterung mit einer halbkugelförmigen Aussparung präsentiert. Es wird gezeigt, dass diese Bauart signifikante Vorteile für die Herstellung des Halterungssystems sowie für die Ausrichtung der Zelle erbringt. Die gleichmäßige Unterstützung des Diamanten erlaubt auch einen größeren Öffnungswinkel der Zelle für Experimente.

Unter statischem Druck durchgeführte Experimente spielen eine wichtige Rolle bei Untersuchungen von Phasenübergängen, chemischen Prozessen sowie des Einflusses von Kompression auf die Textur von Feststoffen. DAC-Experimente waren bisher auf Druckbereiche unter ca. 400 GPa beschränkt. Um den Druckbereich zu erweitern, wurden nano-kristalline Diamanten als Druckstempel-Material für die inneren Komponenten einer zweistufigen DAC eingesetzt. Der letzte Beitrag dieses Kapitels berichtet über derartige Experimente mit Rhenium, bei denen Drücke von mehr als 600 GPa erzielt wurden.

4. Research Projects

4.1 Earth and Planetary Structure and Dynamics

The early accretion history of our solar system set up the initial conditions (thermal state, composition, size…) from which each planet has evolved for billions of years until the present. Such a strong link allows one to use laboratory constraints on element partitioning and the present day composition of the Earth and the other terrestrial planets to infer the very early dynamic history of planetary evolution. Similarly, combining thermodynamic formalism with geodynamic models allows one to better constrain the deep dynamics of planetary interiors and their long-term evolution. The three contributions to this chapter follow these approaches.

The opening contribution combines the accretion history provided by N-body simulations with a multi-stage model of core formation to compute the abundances of chemical elements in the resulting planetary bodies. Compositional differences between the model and the observations on Mercury's mantle suggest that current models of accretion history need to be revised.

In that context a good knowledge of melting processes during the early accretion history is a key to better constraining the partitioning of chemical elements between metallic cores and silicate mantles of planets. The second contribution focuses on determining scaling laws for the melt volume produced upon impact as a function of impact parameters.

Plate tectonics sets the Earth apart from the other terrestrial planets in our solar system, and subduction plays a fundamental role in the long-term thermo-chemical evolution of the Earth. The final contribution in this chapter uses a thermodynamic model to better understand the devolatilization reactions in a subducting multi-component slab. The results of the thermodynamic modeling show that while the volatile loss into the mantle wedge and arc source regions are moderate, subducting slabs may efficiently recycle volatiles into the Earth's deep mantle.

a. *Early differentiation of the terrestrial planets – combining accretion and core formation models (D.C. Rubie, J. de Vries, D.J. Frost and A.K. Vogel, in collaboration with D. O'Brien/Tucson, A. Morbidelli/Nice, F. Nimmo/Santa Cruz and H. Palme/Frankfurt)*

Earth, Mars, Venus and Mercury accreted on a timescale of 10-100 million years through a series of violent collisions with smaller bodies (planetesimals and embryos). This process is studied numerically using N-body simulations in which up to 40 planetary embryos and 1500 planetesimals, initially distributed in a disk that extends outwards from the Sun, collide to form the terrestrial planets. The classic dynamical models of terrestrial planet formation, starting from a disk of planetesimals extending from the Sun to the current orbit of Jupiter, typically produce 3-5 planets in the terrestrial zone with orbits comparable to the actual ones

of the Solar System. However, model planets located near 1.5 AU are systematically much more massive than Mars. The large Earth/Mars mass ratio seems to require a strong depletion of solid mass beyond ~ 1 AU. The recently published "Grand Tack" model explains such a depletion by coupling the early orbital migration of the giant planets with the terrestrial planet's accretion process. In the model it is assumed that, when the giant planets formed in a proto-planetary disk still dominated by gas, Jupiter first migrated towards the Sun and then, as a consequence of the formation of Saturn, reversed its migration and spiralled back outwards. If the reversal (or tack) of Jupiter's migration occurred when the planet was at ~ 1.5 AU, the region beyond ~ 1 AU would have been strongly depleted by the passage of Jupiter. The Grand Tack simulations produce terrestrial planets on orbits consistent with those in the solar system within 30-50 Ma (Fig. 4.1-1), and they explain why Mars is ~ 10 times smaller than the Earth and is formed ~ 10 times faster. Thus, the Grand Tack model is so far the most successful model of terrestrial planet formation from the dynamical point of view. To test the Grand Tack and other accretion models further, we are now applying geochemical constraints by combining the accretion simulations with bulk chemistry and models of core-mantle differentiation.

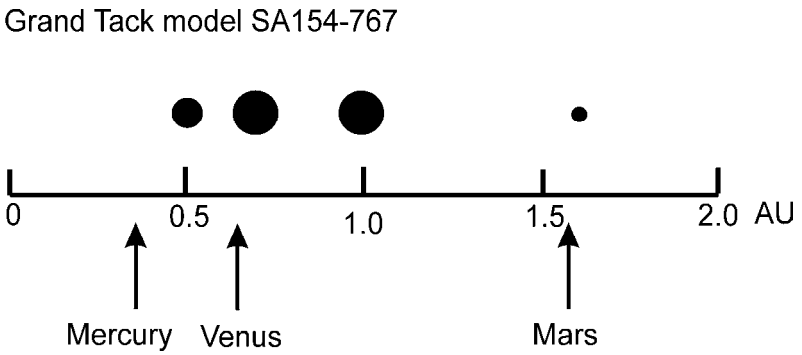

Fig. 4.1-1: The final four planets in Grand Tack simulation SA154_767 with the actual locations of Mercury, Venus and Mars indicated by arrows. The masses of the two outer planets are comparable to the masses of Earth and Mars. However, the inner planet has a mass greater than Mercury's mass by a factor of ~ 10.

The high energy of impacts during planetary accretion was sufficient to cause large-scale melting and deep magma ocean formation which facilitated the segregation of molten metal and silicate. Planetary cores thus formed in a multistage process that was inseparable from accretion. In order to better understand the formation and early differentiation of the terrestrial planets, we are integrating a multistage core-formation model with accretion simulations. A primary aim is to determine if a model Earth-like planet, at ~ 1 AU, can be accreted with a mantle composition identical to that of the Earth. Thus, constraints on model parameters are the compositions of the Earth's primitive mantle and, to a lesser extent, the mantles of Mars and Mercury which are believed to be FeO rich and FeO-poor respectively. In order to satisfy these constraints, we use a least-squares minimization to optimize 4 model parameters. Based

on specified bulk compositions, a combination of rigorous mass balance and thermodynamic element partitioning models is used to determine the compositions of chemically-equilibrated metal and silicate. This approach enables the evolving mantle and core compositions of all accreting bodies to be determined continuously. Elements currently considered include Si, O, Ni, Co, W, Nb, Cr, Ta and V.

In order to satisfy the model constraints, accretion has to be heterogeneous, with embryos and planetesimals originating in the inner part of the solar system (*e.g.*, < 1.8 AU) having highly reduced (oxygen-poor) compositions and those from further out being more oxidized. Metal-silicate equilibration pressures are high (*e.g.*, ~ 0.75 × evolving core-mantle boundary pressures). The model enables estimates of (1) the extent to which the metallic cores of impactors emulsify and equilibrate in a magma ocean and (2) the fraction of magma oceans that are involved in the equilibration process for both impacting planetesimals and embryos. Best results are obtained when the fraction of silicate mantle/magma ocean that interacts chemically with the metallic cores of impactors is limited and lies in the range of 0.003 to 0.1, depending on the size of the impactor and magma ocean depth. The degree of incomplete metal equilibration depends on the extent to which the impactor's mantle participates in the re-equilibration process.

The evolution of composition of the Earth-like planet at 1 AU in the Grand Tack simulation (Fig. 4.1-1) is shown in Fig. 4.1-2. The SiO_2 content of the mantle decreases progressively due to the dissolution of Si into the metallic core whereas the FeO content progressively increases. Final concentrations of all elements considered can be matched well with those of the Earth's mantle. The final composition of the core includes ~ 7.5 wt.% Si, 3 wt.% O and 2 wt.% S.

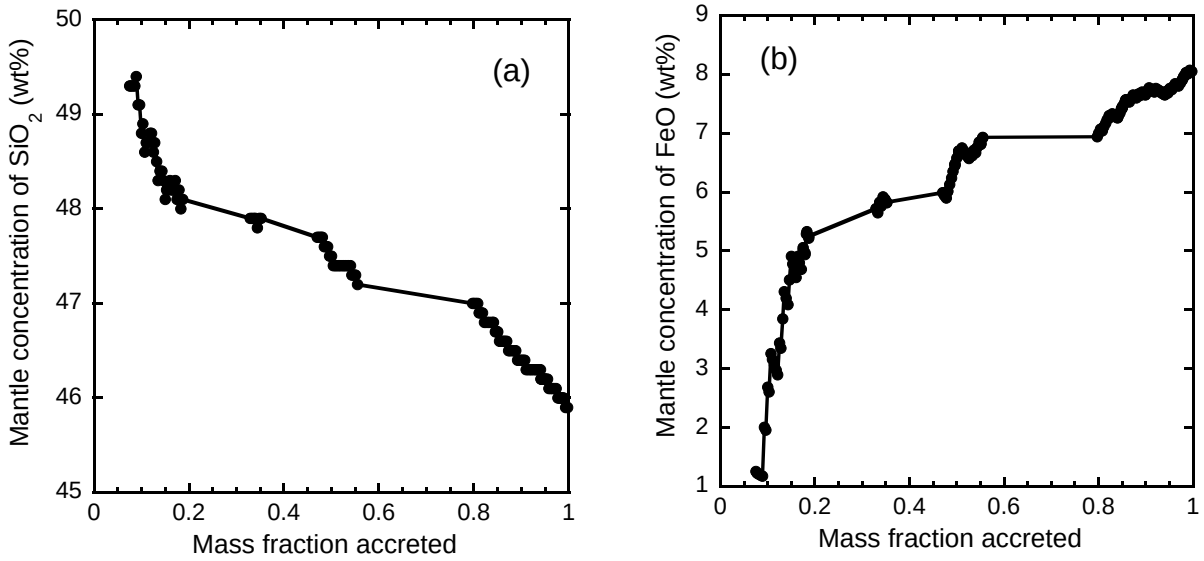

Fig. 4.1-2: The evolution of the SiO_2 (a) and FeO (b) contents of the mantle of the Earth-like planet of (located at 1 AU) during accretion.

For Grand Tack simulation SA154_767 the final FeO content of the outer planet is ~ 17 wt.% and is close to the likely composition of the Martian mantle. However the inner planet has a final mantle FeO concentration of ~ 9 wt.%, which is considerably higher than the likely FeO content of Mercury's mantle (2-4 wt.%). This comes on top of the problem mentioned above that the mass of the inner planet is greater than that of Mercury by a factor of ~ 10. Modifications of the Grand Tack model are thus required before it can fully predict the masses and compositions of all the terrestrial planets simultaneously.

b. *Melting due to impacts on growing proto-planets (J. de Vries and D.C. Rubie, in collaboration with F. Nimmo/Santa Cruz and H.J. Melosh/West Lafayette)*

As presented in the previous section (4.1.a), N-body simulations for the origin of planets in our solar system are now able to predict the formation of four terrestrial planets with locations and masses that are broadly consistent with those of Mercury, Venus, Earth and Mars (except for Mercury, for which the mass is generally too large in the simulations). As also discussed there, understanding the differences between the rocky planets hinges on models of their compositional evolution. These models determine the change in mantle composition through core-mantle differentiation, using calculations of metal-silicate element partitioning. This requires knowledge of the temperature and pressure conditions in the magma oceans that result from impacts, as partition coefficients can depend strongly on these parameters. We use modelling of impact cratering processes to provide these conditions by determining the amount of melting caused by the energy of each collision in N-body simulations.

We have calculated the shock pressure in the planetary embryo from the impact parameters (projectile velocity, impact angle, mass, radius). Comparing this pressure to melting pressures determined from high-pressure shock experiments gives an indication of the amount of melting. However, the propagation of the shock wave through the embryo, and therefore the pressure in the material, depends on several parameters, such as impact angle and material properties. Slower decay of the shock wave will result in higher pressures in the interior of the embryo, resulting in a larger melt volume.

To take this into account, full 3-D models of planetary collisions are required. However, as these models are computationally very time consuming, it is not feasible to use them for determining the melting caused by the several hundreds of impacts (~ 400-500) that result from N-body modelling. Therefore, a parameterised model is used, where the impact is approximated by a point impact with pressure waves spreading radially from the point of first contact. This results in a hemispherically-shaped melt region. For a vertical (head on) impact, this is a reasonable approximation. However, most impacts are not vertical, with the most likely impact angle being 45°. The melt region has been shown to become more asymmetrical when the impact angle is further from the vertical. Scaling of the melt region from our parametrised models is therefore required to determine the depth of the melt pool, which gives the approximate pressure at which the materials from the colliding bodies will equilibrate. This scaling will be done based on comparisons with 3D studies that use a similar

parameter space to the outcome of the N-body models that are used as input for our melt volume calculations (Fig. 4.1-3).

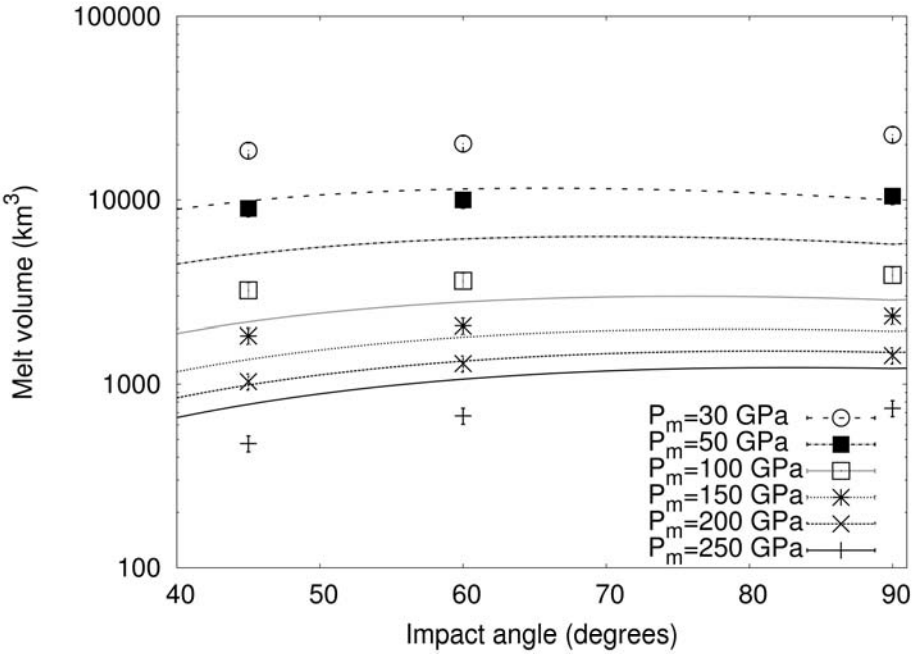

Fig. 4.1-3: Melt volume as a function of impact angle (head on is 90°). The lines indicate the melt volume from our calculations for different melting pressures. Symbols are data from 3D simulations by Pierazzo and Melosh (Icarus, 145, p.252, 2000). Scaling dependent on the melting pressure is required to fit the 3D data.

c. *Devolatization reactions in a three-component subducting slab (D. Dolejš/Prague, Z. Chemia/Copenhagen and G. Steinle-Neumann)*

The volatile budget of a subducting slab is of primary importance for the physical and rheological properties of the slab and the understanding of volatile cycling through the overlying mantle wedge that in turn causes partial melting and magmatic activity. A subducting slab can be approximated by a three-layer lithology: The basaltic oceanic crust (BOC) is extracted from the mantle at mid-ocean ridges, underlain by the complementary depleted harzburgite mantle (SHB). On the top, the lithological sequence is completed by a sedimentary layer (GLOSS). The different layers contain the major volatiles H_2O and CO_2 to a different extent, and experience a different devolatilization history as different phase assemblages become stable along the subduction path.

For the three lithologies we use different initial volatile contencentrations: globally compiled measurements with 7.29 wt.% H_2O and 3.01 wt.% CO_2 for the sediments, and 2.68 wt.% H_2O and 2.95 wt.% CO_2 for the basaltic crust. For the serpentinized harzburgite the range of hydration is highly variable both laterally and vertically. Full hydration of depleted peridotite prior to subduction is achieved at 13.4 wt.% H_2O, which is probably appropriate for the

basalt-harzburgite interface. The hydration is expected to linearly decrease to zero with depth, and as a consequence we assume an average 50 % of maximum hydration, *i.e.*, 6.8 wt.% H_2O. In the harzburgite layer, no CO_2 is assumed to be present.

The separation of the slab into these three chemically distinct layers allows for an accurate evaluation of phase equilibria and associated devolatilization reactions. We performed phase equilibrium calculations using the internally consistent thermodynamic dataset in the system SiO_2-TiO_2-Al_2O_3-FeO-MgO-CaO-Na_2O-K_2O-H_2O-CO_2 with non-ideal solid solution models and an aqueous-carbonic fluid phase. Computations were carried out by Gibbs energy minimization with the Perple_X code, monitoring the prograde mineral assemblages and the volatile content of the three slab components (Fig. 4.1-4).

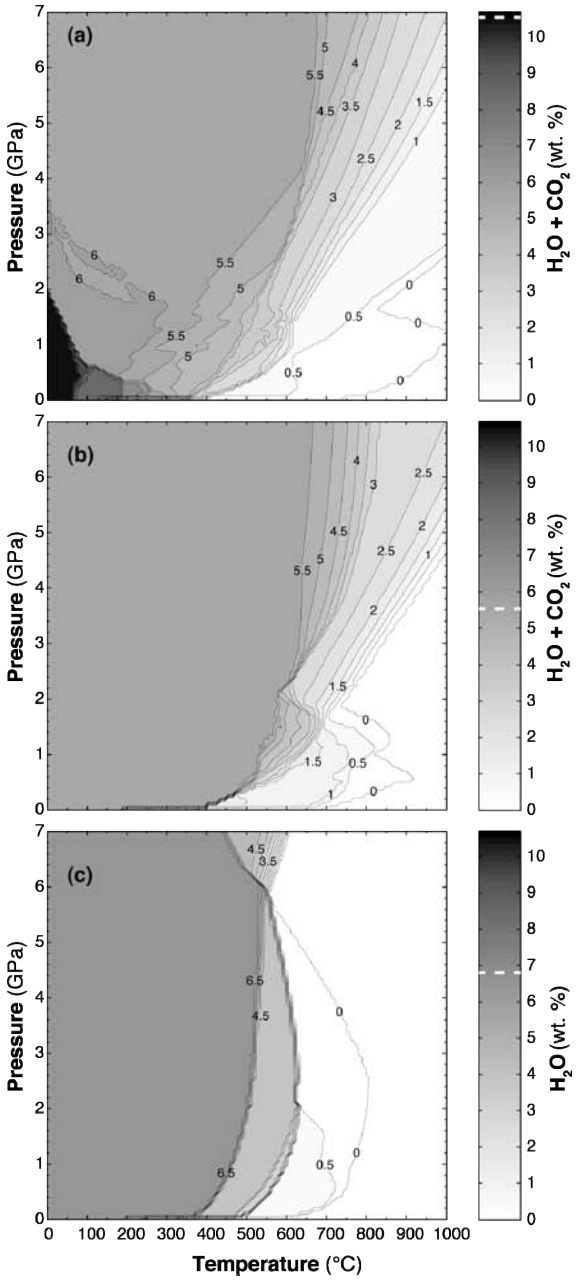

Fig. 4.1-4: Volatile content of the sediment (a), basalt (b) and harzburgite (c) layers as a function of pressure and temperature. The initial volatile content of the different lithologies is indicated in the scale bar by the white dashed lines.

The sediments (Fig. 4.1-4a) devolatilize already at low temperature (50-100 °C) from a level of 10 wt.% down to ~ 6 wt.% due to the breakdown of zeolites and other Ca-bearing aluminosilicates to carbonate-bearing blueschist assemblages. The volatile budget decreases marginally between 100 and 500 °C due to the wide stability of phengite- and lawsonite-bearing blueschists; negligible dehydration occurs as a result of exchange equilibria between alkali amphibole and omphacite. Devolatilization continues above ~ 570 °C by lawsonite breakdown according to the following equilibria:

3 lawsonite = 1 grossular + 2 kyanite + 1 quartz + 6 H_2O (1)

3 lawsonite + 3 diopside = 2 grossular + 1 pyrope + 3 quartz + 3 H_2O (2)

The complete lawsonite breakdown leads to ~ 3.2 wt.% H_2O + CO_2 in the sediments. Higher degrees of devolatilization are probably not attained during subduction. Extremely hot slab geotherms would further intersect the carbonate breakdown by

1 dolomite + 1 coesite = 1 diopside + 1 CO_2, (3)

followed by phengite breakdown to kyanite and K-feldspar.

Moderate H_2O and CO_2 contents in partially altered oceanic crust and harzburgitic mantle cause these lithologies to remain fluid-undersaturated during subduction until the amphibolite/eclogite facies has been reached. For the basaltic oceanic crust, devolatilization commences with the transformation of chlorite to pyrope and a free fluid phase at 520-660 °C (Fig. 4.1-4b), leaving ~ 1.3 wt.% H_2O and no CO_2 in the rock through the following reaction:

1 clinochlore + 1 amesite + 4 quartz = 3 pyrope + 4 H_2O (4)

The blueschist assemblage transforms by divariant breakdown of chlorite, clinozoisite and sodic amphibole to garnet and omphacite-rich clinopyroxene, producing carbonate-bearing lawsonite eclogites with accessory talc. The volatile-bearing phases decompose by divariant equilibria into the volatile-free eclogite assemblage as follows: talc to orthopyroxene at 4.8-5.9 GPa, lawsonite + silica to garnet + omphacite in the range of 650-840 °C (Eqs. 1 and 2), and complete breakdown of the carbonate in excess of 1000 °C and 4.7 GPa:

6 aragonite + 1 pyrope = 3 diopside + 1 grossular + 6 CO_2. (5)

With initially 2.68 wt.% of H_2O and 2.95 wt.% of CO_2 BOC remains fluid-undersaturated until 520-660 °C at 0.5-0.7 GPa. At higher temperatures the devolatilization pattern is identical to that of the sediments (Fig. 4.1-4a) and is mainly determined by the breakdown of lawsonite as outlined above. As for the sediments, the devolatilization is predicted to remain incomplete along characteristic subduction geotherms.

The partially serpentinized harzburgite initially consists of a peridotite assemblage (olivine, clinopyroxene) that is incompletely transformed to chlorite, serpentine (antigorite), and brucite as a function of degree of hydration. With 6.5 wt.% H_2O, the harzburgite contains 41.8 wt.% olivine, 4.0 wt.% clinopyroxene, 44.8 wt.% antigorite, 6.2 wt.% chlorite, and 3.1 wt.% brucite at 250 °C and 0.5 GPa. In order of increasing temperature, dehydration reactions are dominated by brucite, antigorite and chlorite breakdown (discussed below) and also occur along boundaries of a large stability field of phase A at < 500 °C and high pressures (Fig. 4.1-4c). At 450-520 °C, brucite decomposes to olivine + free fluid phase (1.9 wt.%) leaving 4.9 wt.% H_2O in chlorite and antigorite. At 520-630 °C, antigorite breaks down according to

1 antigorite = 14 forsterite + 20 enstatite + 31 H_2O, (6)

leading to 6.3 wt.% fluid and ~ 0.5 wt.% H_2O in chlorite-bearing peridotite. In contrast to the sediments and the oceanic crust, the harzburgites become completely dehydrated at > 700-800 °C by chlorite breakdown to an aluminous phase (anorthite, spinel, or garnet as a function of pressure), olivine and orthopyroxene, as follows:

1 clinochlore + 2 enstatite = 2 forsterite + 1 pyrope + 2 H_2O. (7)

Along colder slab geotherms, all dehydration equilibria intersect with the chlorite-garnet reaction near 520 °C and 6.2 GPa (Fig. 4.1-4c).

Our phase equilibrium models illustrate that (i) the release of H_2O and CO_2 during subduction is discontinuous and episodic, mainly driven by zeolite and lawsonite dehydration, while contributing to an increasing abundance of garnet and omphacite. Breakdown of carbonates (aragonite and/or dolomite) and of phengite is probably not attained during standard subduction geotherms, hence the oceanic lithosphere probably remains partially hydrated and carbonated beyond the magmatic arc; (ii) in contrast to the sediments, the initial volatile budget of the oceanic crust and of the harzburgitic upper mantle is much lower and these lithologies remain fluid-undersaturated until ~ 3 GPa. Consequently, H_2O activity differs substantially at the subducted sediment-oceanic floor interface, and any fluids released from the sediments may be locally consumed by rehydration of mafic and ultramafic lithologies to eliminate these $a(H_2O)$ gradients. This implies that the fluid loss from igneous-sedimentary melanges at initial and moderate stages of subduction may be even lower than predicted by sediment devolatilization. Overall, our calculations demonstrate that the subducting lithologies may loose much less volatiles into the mantle wedge and arc source regions, but may efficiently recycle them into the Earth’s deeper interior.

4.2 Geochemistry

Interpreting evidence for fractionation events occurring during Earth's accretion is difficult given the large number of other processes that have introduced chemical diversity within all planetary bodies. For this reason stable isotopic studies can be particularly useful as many high-temperature processes have little effect on the distribution of a particular isotope between two reservoirs. The first study in this section examines how Si isotopes may have fractionated during the process of core formation. It is found that the silicon isotopic signature of Earth's mantle likely derived from the partitioning of isotopically lighter Si into the core. However, because the extent of this fractionation decreases with pressure and temperature, additional constraints can be placed on the plausible maximum pressure at which this fractionation event was likely to have occurred. The next two studies examine how the presence of light elements such as silicon may have influenced the partitioning of other elements into the core. The first examines the conditions at which moderately volatile elements such as lead and tin may have separated to the core and finds that the similar depletions of these elements in the mantle are consistent with core forming liquids also containing sulphur. Whereas the second study shows that the presence of silicon in core forming metal would have strongly influenced the partitioning of tungsten between mantle and core, but would have had little affect on many other elements.

The next three studies examine melting of mantle rocks at high pressures. The first reports results to determine melting phase relations of the MgO-SiO_2 binary system at high pressure. Using such data thermodynamic models can be developed that can explain melting in the deep mantle under a range of pressures and temperatures. Similarly the following study looks at the effect of water on melting relations in the same binary with the same objective in mind. The final melt study is aimed at determining the composition of small degree hydrous melts that might form at depths greater than 150 km during decompression melting of the mantle. The melts formed are found to be very similar in composition to a type of water-rich kimberlitic rock, a rare enigmatic igneous rock emplaced in regions of ancient crust.

The oxidation state of eclogitic rocks, which are metamorphic rocks formed in the mantle from subducted basalt, forms the focus of the next two studies. Proportionately more diamonds are found in eclogitic xenoliths than in more typical mantle peridotite rocks. The first study attempts to understand this by determining the oxygen fugacity of these rocks, a parameter that would strongly influence the formation of diamonds from carbon bearing melt phases. The second study examines the changes in redox state occurring when eclogitic rocks partially melt during subduction. The following contribution by Beyer and Frost details the first steps in developing a thermodynamically sound geobarometer for eclogites. They perform high-pressure experiments to assess the influence of the jadeite compound on the Ca-Tschermak content of clinopyroxene coexisting with garnet. The refined barometer was then tested against a large set of available experimental data, with results showing good agreement between predicted and measured values.

The next three contributions deal with the storage of volatiles in the Earth's mantle. The modern atmosphere is characterized by a strong depletion in Xe relative to other noble gases. Shcheka and Keppler have experimentally determined the solubilities of noble gases in $MgSiO_3$ perovskite and found that Ar and Kr are highly compatible whereas Xe is not. This implies that the noble gas signature of the modern atmosphere is the result of mixing between a small residue of primary atmosphere and an Ar- and Kr-rich component supplied by degassing of the lower mantle. The following study has examined the solubility of nitrogen in upper mantle minerals. The results show a strong dependence on redox state and imply that the current upper mantle has a potential nitrogen storage capacity ~ 40 times the amount present in the modern atmosphere and that the crystallization of a magma ocean may have caused fractionation of N/Ar and N/C in the early atmosphere. The final study on mantle volatiles explores the capacity of ringwoodite and wadsleyite to store F and Cl . It is found that these two minerals can store at least an order of magnitude more F and Cl than olivine, which means that the transition zone may not only be a major reservoir of water, but also of halogens.

The next study by Solopova *et al.* examines the stability of Na_2CO_3 at conditions ranging from the upper to the lower mantle. They find that Na_2CO_3 would be present as a liquid throughout most of the upper mantle and transition zone, but would decompose into diamond and O_2 in the middle of the lower mantle. The following study by Liu *et al.* looks at the partitioning of Cu between mantle minerals and hydrous silicate melt as a function of pressure, temperature and oxygen fugacity. Traditionally it is considered that sulphides control Cu partitioning but it is found that silicate minerals could also have a significant impact on the Cu content of partial melts.

The final contributions in this section deal with crustal processes. Yang and McCammon used published rare earth element data in zircons to reconstruct the evolution of fO_2 in the continental crust from the Hadean to present. They find a conspicuous trend toward more reducing values in zircons with ages > 3.6 Ga. This suggests that the continental crust was more reducing at that time, and that this may be linked to a more reducing mantle and atmosphere. Kularatne and Audétat experimentally re-examined rutile solubility in hydrous felsic magmas because these data are crucial for the application of Ti-in-quartz and Ti-in-zircon thermo(-baro)metry, but available TiO_2 solubility models return inconsistent results. They used a new method to overcome the slow diffusion of Ti at low temperature. The results are in agreement with a previous experimental study and support the validity of a recent re-calibration of the Ti-in-quartz thermobarometer.

The last two contributions deal with the formation of ore deposits. Tan *et al.* have investigated the origin of metals in a vein-type gold deposit in eastern China. They find that mafic alkaline dikes that are spatially and temporally associated with ore formation have an unusually non-radiogenic lead isotopic composition that is identical to that of ore minerals. The findings

provide strong evidence that the metals in this deposit originate from mafic magmas produced by partial melting of old lithospheric mantle. Lerchbaumer and Audétat examine melt and fluid inclusions in weakly molybdenum mineralized granites and compare the results with data obtained from ore-related granites to identify the ore formation processes. It turns out that the Mo concentration in fluids and melts is less important than the efficiency by which they are extracted from large magma chambers and accumulated.

a. *Silicon isotope fractionation between metal and silicate at high-temperature, high-pressure conditions – Implications for Earth's core (J. Kempl/Amsterdam, in collaboration with D.J. Frost, P.Z. Vroon/Amsterdam, P. Kowalski/Jülich and W. van Westrenen/Amsterdam)*

In the past, constraints on the conditions that were prevalent during the formation of Earth's metallic core have been obtained from experimental studies on the partitioning of siderophile elements between metal and silicate. Due to the advent of multi-collector (MC) ICP-MS techniques it has become possible in recent years to approach the question of Si incorporation into Earth's core by studying the distribution of Si stable isotopes between metal and silicate at high-pressure and -temperature conditions. Here, we report results of a high-pressure, high-temperature study into the fractionation of isotopes of silicon between metal and silicate.

Silicon has three stable isotopes: ^{28}Si, ^{29}Si and ^{30}Si. Variations in silicon isotopic composition are expressed using the delta notation relative to reference material NIST RM 8546, with $\delta^{30}Si = (^{30}Si/^{28}Si_{sample} / {}^{30}Si/^{28}Si_{standard})$ x 1000 (unit: per mil). The average $\delta^{30}Si$ isotopic signature of samples from the Bulk Silicate Earth (BSE) and lunar samples is approximately -0.29 ‰ (± 0.1 ‰, $2_{S.D}$), slightly higher than the average $\delta^{30}Si$ for primitive meteorites, -0.48 ‰ (± 0.2 ‰, $2_{S.D}$). The resulting difference in Si isotopic composition $\Delta^{30}Si_{BSE\text{-}Chondrites} = \delta^{30}Si_{BSE} - \delta^{30}Si_{Chondrites}$ = 0.19 ‰ (± 0.1, $2_{S.D.}$) has been explained by equilibrium metal-silicate Si isotope fractionation during core formation at high temperatures and high pressures, driven by the different chemical bonding environment of Si in silicate mantle rocks and in metallic liquid.

Translation of these results into corresponding core Si concentrations requires knowledge of Si equilibrium isotope fractionation factors between silicate and iron-rich metal at high-temperature and high-pressure conditions. To date, these have mostly been derived from theoretical calculations, suggesting that the Si concentration in the outer Earth's core could comprise between 2.5 wt.% and 16.8 wt.% Si - a range that is even larger than estimates of the Si content of the core derived from Si elemental partitioning data (1-11 wt.%).

To expand the currently available experimental data set on Si isotopic fractionation between metal and silicate, high-pressure and high-temperature experiments were performed in the BGI 1000 and 1200 ton multianvil devices. Time series were performed to assess the kinetics

and absolute amount of Si isotope fractionation at 9 GPa and ~ 2150 °C in MgO capsules. Run products, consisting of silicate melt and a sphere of Si-bearing metal alloy (Fig. 4.2-1), were chemically analysed by electron microprobe at VU University Amsterdam. Samples were micro drilled and metal and silicate were separated by hand picking. Sample aliquots were chemically digested, purified and diluted for Si isotope analyses on a Thermo-Finnigan MC-ICPMS at VU University in Amsterdam.

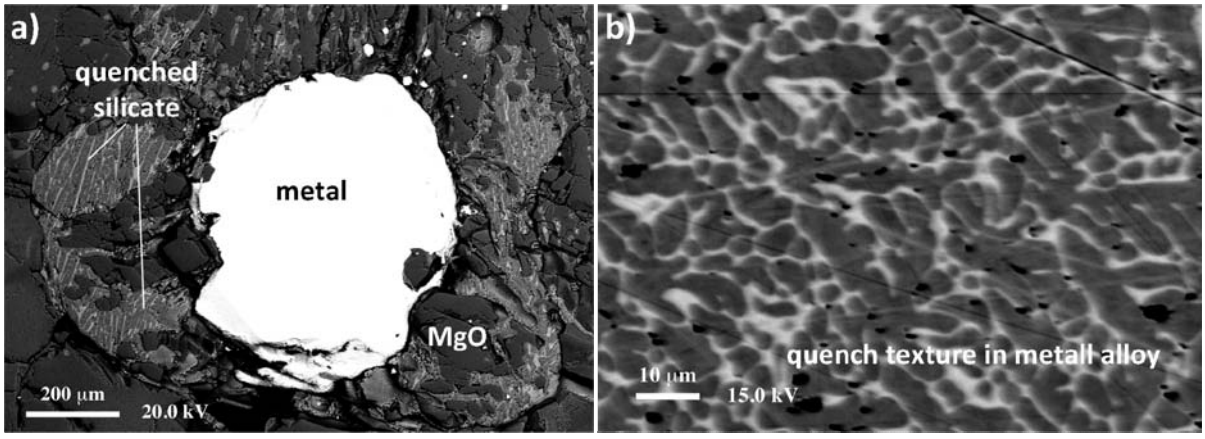

Fig. 4.2-1: Typical run products of high-pressure multianvil experiments at 9 GPa and 2100 °C after 30 minutes. Quench textures in silicate and metal indicate that both phases were molten.

Based on electron microprobe analyses of Fe and FeO concentrations in metal and the MgO capsule, respectively, we calculate oxygen fugacities of our experiments to be ranging between -4 and -6 log units below the iron-wüstite (IW) buffer. Our time series results show that Si isotopic equilibrium is reached after 30 minutes at the pressure and temperature conditions, resulting in a Si concentration of up to 8.8 wt.% in the metal phase. At equilibrium, $\delta^{30}Si_{metal}$ = -0.77 ‰ for the metal, and 0.19 ‰ for the silicate. As expected, the silicate is concentrating the heavier isotopic fraction due to stronger chemical bonding, whereas the metal is enriched in the lighter Si isotope fraction.

Data collected at different temperatures can be compared based on the inverse T^2 dependence displayed by Si isotope fractionation between metal and silicate *i.e.*,

$$\Delta^{30}Si_{silicate-metal} \approx \frac{1}{T^2}$$

Our data can be combined with literature data spanning the range 1-9 GPa and 1800-2150 °C. We rescale existing experimental results to a fixed temperature and determine the first pressure dependence of Si equilibrium isotope fractionation between metal and silicate (Fig. 4.2-2).

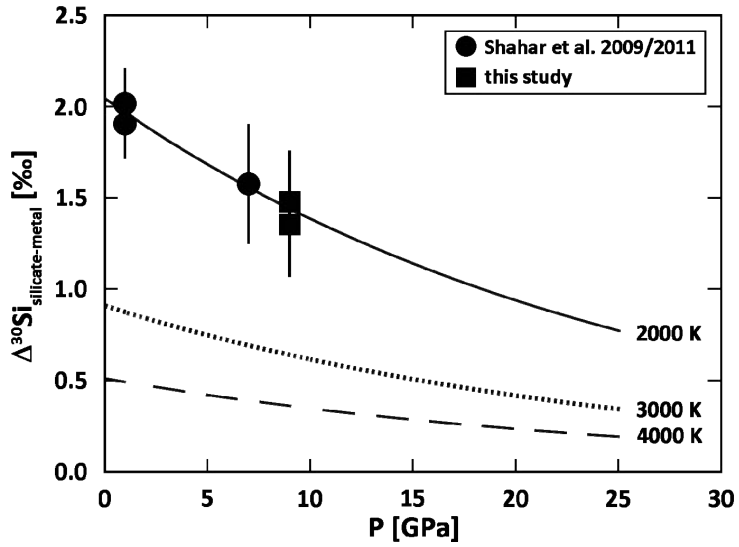

Fig. 4.2-2: The pressure dependence of Si isotope fractionation between metal and silicate at different temperatures calculated on the basis of existing experimental data (Shahar *et al.* 2009, EPSL, 288, 228-234; Shahar *et al.* 2011, Geochim. Cosmochim Acta. 75, 7688-7697).

A negative pressure dependence raises estimates of the Si content of Earth's core. If core-mantle equilibration occurred at 25 GPa and 2500 K, the model shown in Fig. 4.2-2 implies that the core contains between 11 and 29 wt.% Si depending on the value of $\Delta^{30}Si_{BSE\text{-}Chondrites}$. Higher core formation pressures and temperatures would raise these estimates even further. To improve the accuracy of this model, experimental data are required at even higher pressure conditions. In particular the change in Si coordination in silicate phases at higher pressures may influence the isotopic fractionation.

b. *New metal/silicate partitioning data for the siderophile elements Pb, Ag, Sn and Au in S-free and S-bearing compositions (A.K. Vogel, D.C. Rubie, D.J. Frost and A. Audétat, in collaboration with H. Palme/Frankfurt)*

The Earth accreted in the early Solar System through numerous collisions with smaller bodies (planetesimals and embryos). The energy that was released by these collisions caused large-scale melting and was thus sufficient to create one or more deep global magma oceans. The segregation of metal from silicate to form the Earth's metallic Fe-rich core and silicate mantle was greatly facilitated by magma ocean formation and is believed to have occurred during the initial 100 My of the solar system. The geochemistry of the Earth's mantle combined with experimental determinations of how elements partition between metal and silicate provide important insights into the processes and conditions of core formation.

Siderophile elements partition preferentially into the metal phase during the separation of liquid metal from liquid silicate to form the Earth's core, which means that these elements

have been partially depleted from the mantle. To date most partitioning studies have concentrated on refractory siderophile elements such as Ni, Co, W and Mo. However, it is also important to study the partitioning behaviour of volatile siderophile elements. These are depleted in the Earth's mantle because of their failure to condense at the high temperatures in the inner part of the solar system. However, additional depletions have also resulted from core formation.

It is well known that the Earth's core contains light elements. Based on the mantle depletion of S compared to other similarly volatile non siderophile elements, an estimate can be made that there is approximately 2 wt.% S in the core. However the presence of S is known to have a significant influence on the partitioning behaviour of a range of other elements and can therefore influence the geochemical outcome of core-mantle segregation.

The distribution of an element between metal and silicate is described by its partition coefficient which is the ratio of the concentration of the element in the metal to its concentration in the silicate. Normalizing the partition coefficient of any element of interest to the partition coefficient of iron (taking also the valence state of the element of interest into account) yields the so called exchange coefficient K_D, with the advantage that this parameter is independent of oxygen fugacity.

We report new partitioning data for the volatile elements Pb and Sn and the moderately volatile elements Au and Cu. Experiments have been performed in a multianvil apparatus at 11 GPa and temperatures between 2264 K and 2707 K. The oxygen fugacities have been determined to range between -1.8 and -2.5 log units relative to the iron-wüstite buffer. We have also investigated the influence of S on the partitioning of these elements.

The starting compositions consisted of Fe or FeS together with 1 wt.% of the pure element or the oxide of the element of interest and a peridotitic silicate. Metal and silicate powders were contained in a MgO capsule with a layer of metal sandwiched between two layers of silicate. Successful experiments resulted in the formation of a liquid metal sphere surrounded by silicate that quenches to skeletal olivine quench crystals. The use of MgO capsules results in the formation of ferropericlase which was analysed in order to determine oxygen fugacities relative to the iron-wüstite buffer. All metal and ferropericlase compositions were obtained with an electron microprobe, whereas the silicate phases were analysed with a laser ablation inductively coupled plasma mass spectrometer.

We found no significant temperature dependence to the partitioning of Pb, Sn and Cu within the experimental temperature range at 11 GPa, whereas Au shows a decrease in siderophility with increasing temperature (Fig. 4.2-3; Fig. 4.2-4). Furthermore Au is clearly the most siderophile element with absolute logarithmic exchange coefficient values between 2.5 and 4. The addition of 14-17 mol.% S causes a decrease in siderophile behaviour for the moderately volatile element Au and the volatile element Sn by about half a logarithmic unit. Partitioning of the moderately volatile element Cu and the volatile element Pb are unaffected by S.

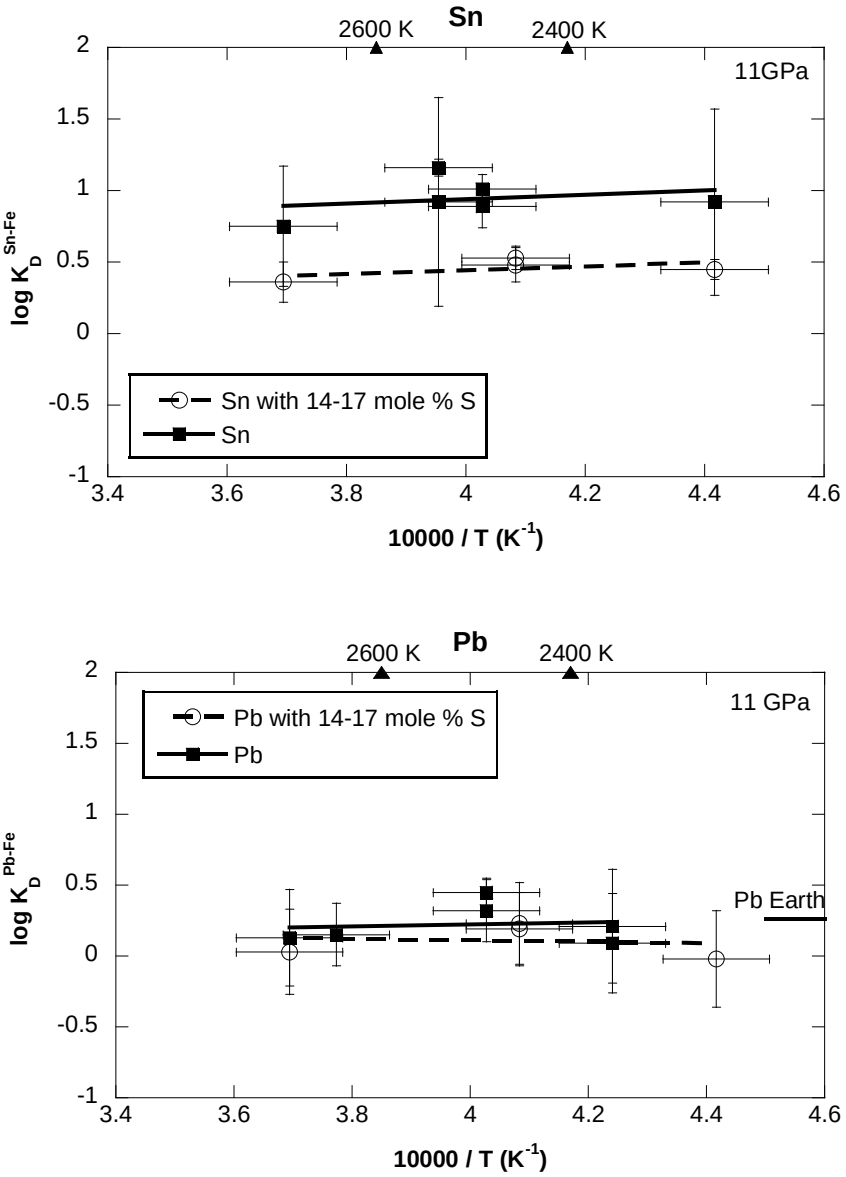

Fig. 4.2-3: The logarithmic exchange coefficients (K_D) of Pb and Sn are plotted against inverse temperature (in K^{-1}). Unfilled symbols show S bearing experiments.

The volatile elements Pb and Sn (Fig. 4.2-3) are depleted in the Earth's mantle by approximately the same amount, which requires similar exchange coefficient values during core formation. However, in our experiment the absolute values for both elements differ by half a logarithmic unit. The addition of 14-17 mol.% S, however, equalizes both partitioning trends within the error bars. Furthermore the absolute exchange coefficient values of Pb (with and without S) are in good agreement with the actual mantle abundances of this element. On the other hand, for Cu there is a discrepancy of about 1.5 logarithmic units between the partitioning data and its current mantle abundance based on the current experimental conditions. These results show that the experimentally covered pressure – temperature range is insufficient to explain the conditions that prevailed during the separation of the Earth's

core. Thus it is necessary to cover a wider pressure and temperature range and additionally take ideas of multistage core formation scenarios or inefficient core formation into account.

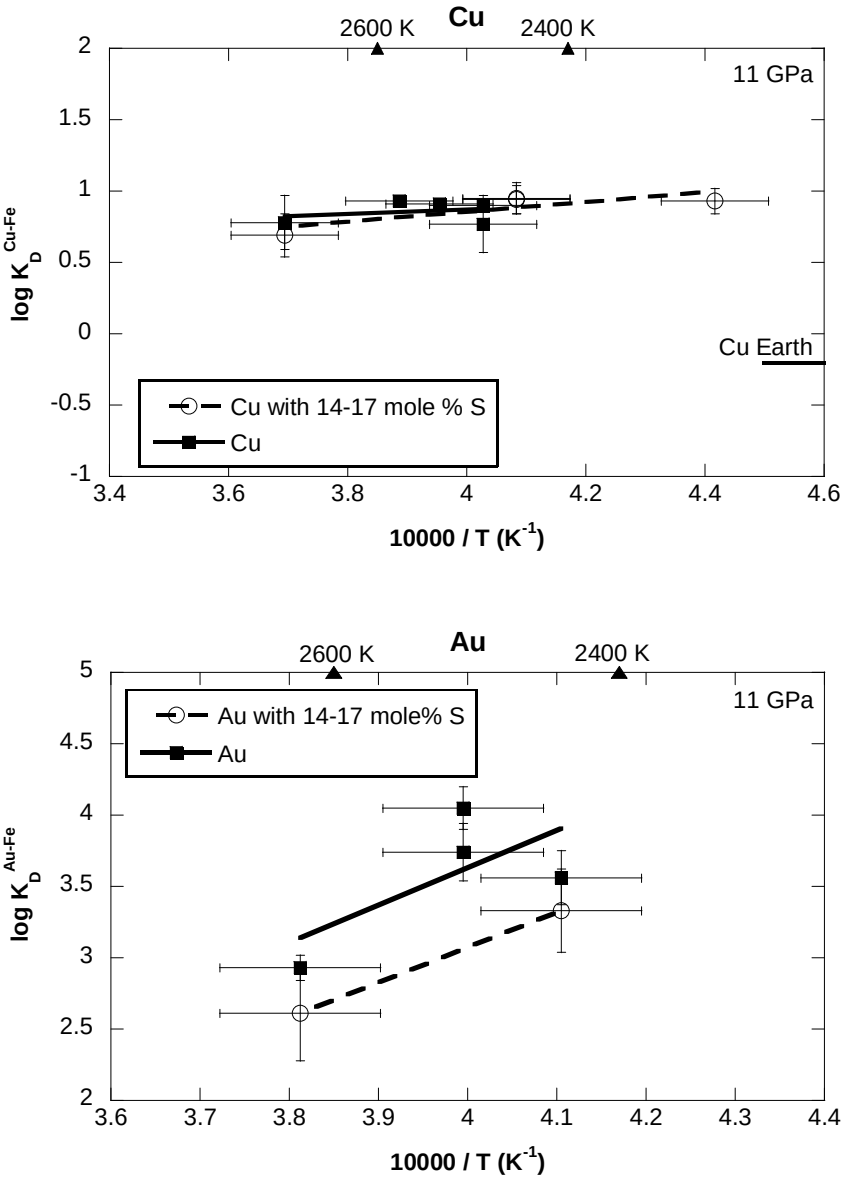

Fig. 4.2-4: The logarithmic exchange coefficients (K_D) of Cu and Au are plotted against inverse temperature (in K^{-1}). Unfilled symbols show S bearing experiments.

c. *The effects of light elements on siderophile element partitioning between liquid metal and silicate melt (Y. Nakajima, D.J. Frost and D.C. Rubie)*

The most important constraints on processes and conditions of core formation in the early history of the Earth are provided by the chemistry of the Earth's mantle combined with experimental data on the partitioning of a wide range of elements between metal and silicate. Of particular interest are the so-called siderophile (metal-loving) elements, such as Ni, Co, and W, that partition

strongly into metal. As a consequence of this partitioning behaviour, the Earth's mantle was depleted in siderophile elements during core formation whereas lithophile elements were retained in the mantle. In recent years element partitioning has been intensely studied at a variety of experimental pressure, temperature and oxygen fugacity conditions. In addition to these physical parameters, light elements such as Si, O and S, which are believed to be dissolved to some extent in Earth's core, are also expected to have an influence on element partitioning behaviour during core formation. In this study, we have investigated the effects of Si, O and S on the partitioning of Ni, Co, W, V, and Cr during core formation.

Partitioning experiments were performed at 15-25 GPa and 2700-3000 K using a Kawai-type multianvil apparatus. Staring materials were powdered mixtures of metal and olivine. The metal sample consists of Fe added with a minor amount of Ni, Co, V, Cr, and W (5 wt.% for Ni and 2 wt.% for the others). Using different compositions of $(Mg_{1-x},Fe_x)_2SiO_4$ olivine (x = 0.05-0.3) or replacing Fe metal by FeSi, the oxygen fugacity in the sample was varied. For S-bearing experiments, FeS powder was added to the metallic powder. The sample was heated by a $LaCrO_3$ heater and temperature was measured using a W3%Re-W25%Re thermocouple. The samples were loaded into MgO capsules. After experiments, chemical analyses were performed by an electron microprobe.

The distribution coefficients K_D of elements between coexisting liquid metal and silicate melt were obtained from chemical analyses of recovered samples. The distribution coefficient is defined as $K_D = (X_M^{met} / X_{MO_{n/2}}^{sil}) / (X_{Fe}^{met} / X_{FeO}^{sil})^{n/2}$, where X is the mole fraction of element M in liquid metal or $MO_{n/2}$ in silicate melt and n is the valence state of the element in silicate melt. With this definition, the K_D is independent of oxygen fugacity. Under the present reducing conditions (1-3 order magnitude lower than the iron-wüstite buffer), Fe, Ni, Co, and Cr in silicate melts are in the divalent oxidation state (2+) and V is in the trivalent state (3+). Although there is some uncertainty in the valence state of W in silicate melt it is assumed here to be 6+. In Figure 4.2-5, the K_D values for each element obtained at 15 and 25 GPa are plotted as a function of Si content of liquid metal. The concentrations of Si and O in metal are also shown. The S contents of metal are almost constant (~ 3 wt.%) in the S-bearing experiments.

The compositions of liquid metal, except for Si, O, and S, are similar through the present experiments. The chemistry of silicate melts are also constant at each pressure and in a narrow temperature range (c.a. 2720-2800 K at 15 GPa and 2850-2950 K at 25 GPa). Therefore the variations of the K_D values obtained at 15 and 25 GPa should be due to the changes of activity of elements in liquid metal by the interactions with Si, O or S. We evaluate the effects on the activity coefficients of Ni, Co, V, Cr, and W an activity composition model taken from the metallurgical literature (Ma, Metallur. Materials Trans. B, 32, 87, 2001). The distribution coefficients $K_M^{Si,O,S-bearing}(P,T)$ obtained at pressure (P) and temperature (T) in the Si, O, and S bearing system were fitted with a simple equation as:

$$\log K_M^{Si,O,S-bearing}(P,T) = \log K_M^{Si,O,S-free}(P,T) + \varepsilon_M^{Si} \log(1-x_{Si}) + \varepsilon_M^{O} \log(1-x_O) + \varepsilon_M^{S} \log(1-x_S)$$

where ε_M^i and x_i are the interaction parameter of element *i* on *M* and the mole fraction of element *i* in the metal sample. The $K_M^{Si,O,S-free}(P,T)$ is the distribution coefficient for element M in the light element free system. The fitting results for data obtained at 25 GPa are shown in Fig. 4.2-5. The tendency of the Si effect on the K_D is similar at both 15 and 25 GPa. Si reduces the distribution coefficients for Ni and Co by the same degree, whereas O has negligible influence for both elements at the present experimental conditions. The effect of S on Co partitioning is much larger than that on Ni. The Si content has less effect on the V partitioning and is negligible on Cr partitioning. In contrast, both S and O can make V and Cr more siderophile although the interaction parameters of O obtained in this study have a large uncertainty. The influence of Si is significantly emphasized in the W partitioning. The K_D for W decreases by 2 order magnitude with the addition of 8 wt.% Si.

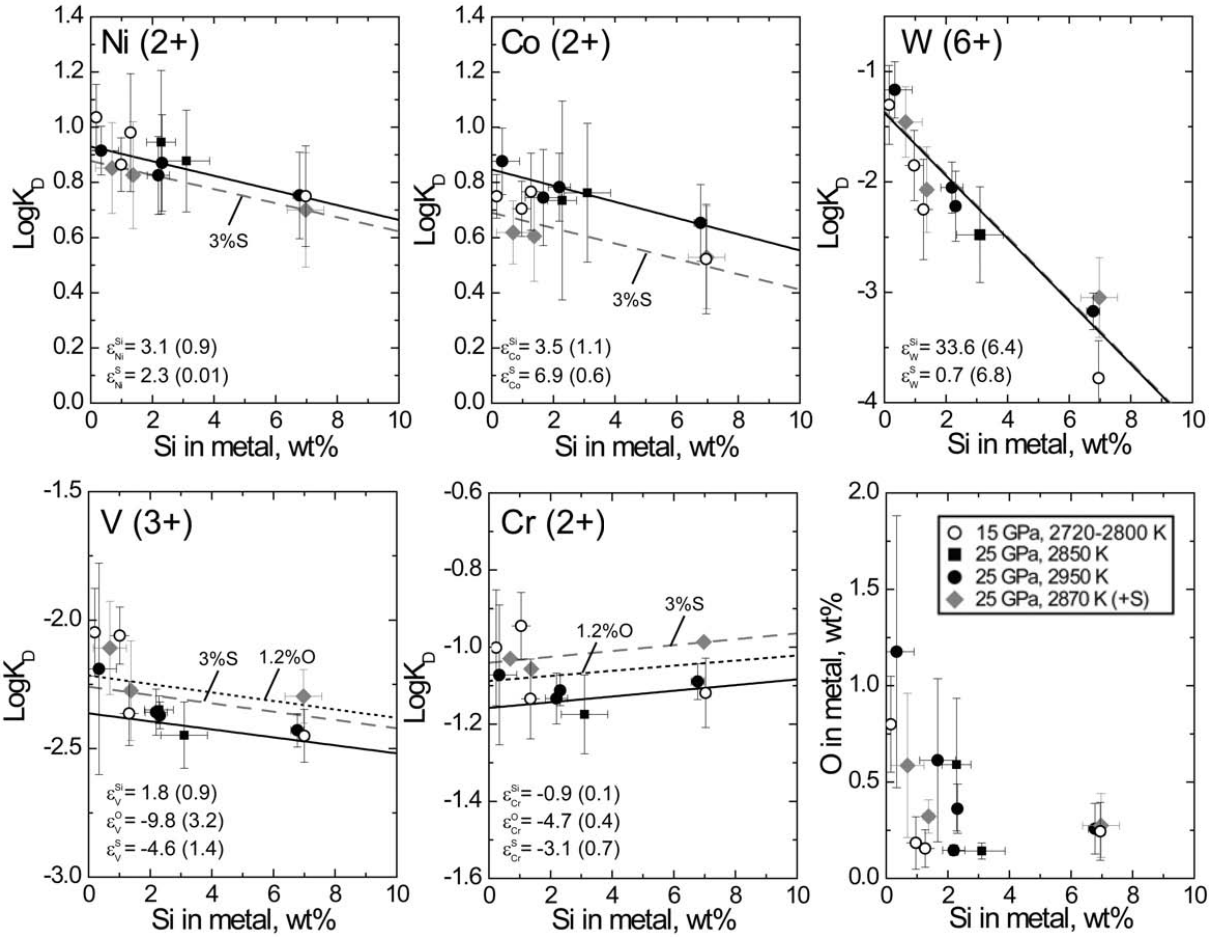

Fig. 4.2-5: The distribution coefficient K_D for Ni, Co, W, V, and Cr between liquid metal and silicate melt. The logarithmic K_D obtained in this study are plotted as a function of Si contents of metal. The O contents of metal are also plotted. The solid, broken and dotted lines are for only Si, Si and 3 wt.% S, and Si and 1.2 wt.% O, respectively, calculated by fitting epsilon values from the activity model. The epsilon parameters obtained for each element are shown with uncertainties in brackets. The legend in the last figure is the same for each diagram.

The recently prevailing view of core formation is that the core forming metal segregated continuously from a silicate magma ocean throughout the Earth's accretional history. N-body simulations of planetary formation predict that the Earth accreted heterogeneously. In these simulations, the material accreting to the proto-Earth changed with time from highly-reducing to oxidizing. In addition, the accreting material in the final stages are expected to be rich in volatile elements such as S. Because Si dissolves strongly into metal under reducing conditions and O does under oxidizing conditions, the dominant light elements in core forming metal coexisting with a silicate magma ocean are expected to vary through such a heterogeneous accretional history. As shown in this study, these elements have some influence on the element partitioning. The change of dominant light elements in core forming metals, as well as pressure, temperature, and oxygen fugacity, could affect the element distributions in relevant phases during core formation. Therefore the effects of light elements should be included in modelling the core formation process.

d. *Liquidus phase relations in the system MgO-SiO_2 (O. Savchuk, R.G. Trønnes/Oslo and D.J. Frost)*

Multianvil studies of melting phase relations on compositions in the systems MgO-SiO_2 and MgO-SiO_2-Al_2O_3 have largely been confined to pressures above 10 GPa. In order to bridge the gap between the early melting experiments in the piston cylinder pressure range and some of the more recent multianvil melting experiments, melting relations in the system MgO-SiO_2 have been investigated at 6 GPa. Such data are important, because the derivation of more complete thermodynamic melting models for mantle relevant compositions requires accurate liquidus phase relations for simple systems over wide pressure ranges.

The experiments were performed in 18-11 mm assemblies using $LaCrO_3$ heaters, axially inserted WRe-thermocouples and multichamber Re-capsules where approximately five different compositions were run simultaneously (Fig. 4.2-6). The starting compositions within the Mg_2SiO_4–$MgSiO_3$ range were prepared by mixing powders of enstatite glass and crystalline forsterite. Outside this range, we used mixtures of either enstatite glass and tridymite or forsterite and periclase.

The phase diagram in Fig. 4.2-7 shows the phase assemblages encountered for different bulk starting compositions. Liquidus curves are also constrained using the results of direct microprobe analyses. The results support congruent melting behaviour of both forsterite and enstatite, and that the MgO-rich eutectic is extremely close to forsterite in composition. The quenched liquids in equilibrium with periclase at 2125-2225 °C are very close to forsterite in composition, demonstrating the steepness of the liquidus curve from the eutectic towards the melting point of periclase (about 3450 °C).

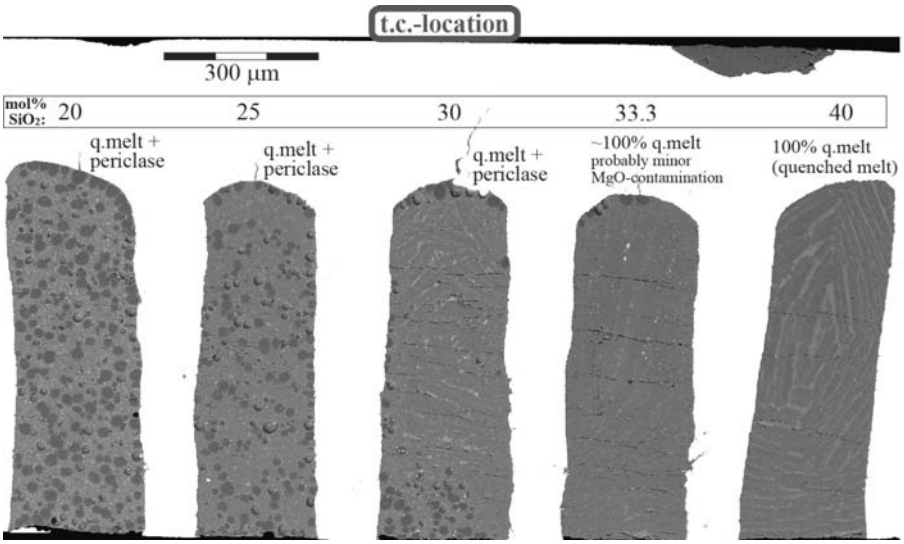

Fig. 4.2-6: Back-scattered electron image of a sectioned surface through the central part of a Re-capsule, 2.0 mm in diameter. The five sample chambers are spark-eroded along a diametric plane in the capsule. An axial section through all of the chambers is made by grinding and polishing. The distances from the thermocouple junction (t.c.) to the nearest sample chamber end and the central hotspot were about 330 and 530 µm, respectively. The small rounded dark grey grains in the left hand samples are periclase. The interstitial liquid compositions in the sample chambers with 20-30 mol.% SiO_2 are all very similar to that of forsterite.

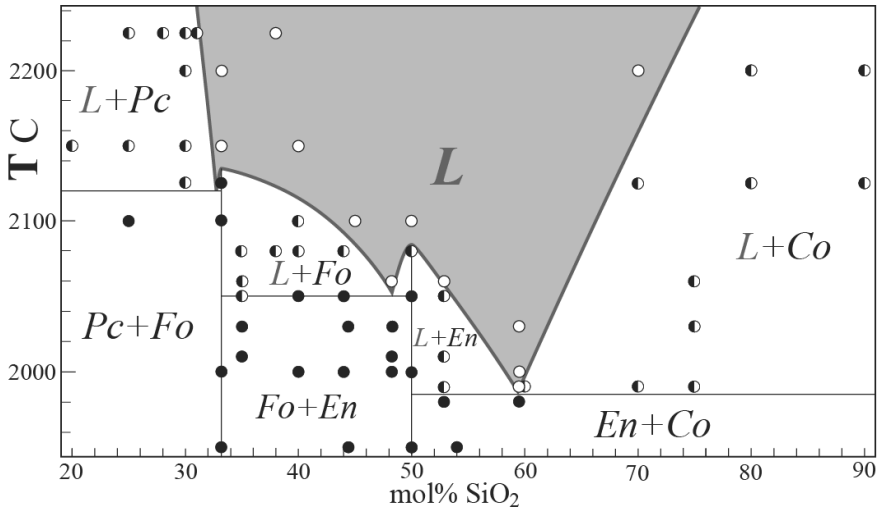

Fig. 4.2-7: Experimental results at 6 GPa in the system MgO-SiO_2. Symbols indicate the phase assemblages observed plotted at the specific starting bulk composition. The liquidus curves can also be further constrained from microprobe analyses of the liquid compositions.

In comparison to the 1 bar phase diagram the low-pressure peritectic melting of enstatite is replaced by congruent melting at 6 GPa. From 1 bar to 6 GPa the liquidus temperatures

increase by about 650° and 860° for the MgO (periclase) and SiO_2 (cristobalite and coesite) components, respectively. For the intermediate compositional range the liquidus increase is about 230° for forsterite and 450-500° for the eutectics and peritectics near enstatite. Between 1 bar and 6 GPa the silica-rich eutectic moves from 55 to 60 mol.% SiO_2. The isobaric invariant point involving forsterite, enstatite and melt becomes more magnesium rich with pressure, while the eutectic involving periclase becomes more silica rich. These observations place important constraints on the thermodynamic properties of the silicate liquid at high pressure. These constraints can be hopefully used to develop a model based on plausible melt species that can reproduce these observations.

e. *Phase relations in the MgO-$MgSiO_3$-H_2O system atop the transition zone (D. Novella and D.J. Frost)*

Magnesium rich olivine (forsterite) and pyroxene (enstatite) are two of the most relevant minerals in the Earth's mantle. In fact, along with clinopyroxene and aluminium bearing phases plagioclase, spinel or garnet, depending on pressure conditions, they build the Earth's upper mantle. Knowledge of the melting processes, and phase relations, of such minerals are fundamental for understanding processes like the differentiation of the mantle and the accretion and evolution of the Earth's interior.

While dry melting in the Earth's interior mostly takes place at shallow depths, when temperatures are above the dry solidus of upper mantle peridotite, hydrous melting can occur at much higher depths for an adiabatically decompressing peridotite. Also, it has been suggested that upwelling mantle material, in the presence of water, can produce hydrous melt when crossing the upper mantle - transition zone boundary, due to the difference in water storage capacity of the dominant mineral phases. Therefore, to fully understand igneous processes in the Earth's mantle, the effect of H_2O on lowering melting solidus and enhancing the production of melt at high depths needs to be addressed.

In the present study, we have performed experiments in the simple system MgO-SiO_2-H_2O. The effect of water on melting upper mantle minerals can be easily quantified in simplified systems, while in complex systems complications arise due to incongruent melting and other chemical shifts that can additionally influence the melting temperature.

High-pressure (HP) and high-temperature (HT) experiments have been conducted with a 5000 ton multianvil apparatus at 13 GPa, and temperatures ranging between 1300 and 1900 °C. These experiments were aimed at determining the phase relations in the systems Mg_2SiO_4-H_2O and $MgSiO_3$-H_2O, as a function of H_2O contentent, at the bottom of the upper mantle. Starting compositions have been prepared from oxides MgO and SiO_2, and $Mg(OH)_2$ brucite. Pure forsterite was synthesized by firing the desired amount of MgO and SiO_2 at 1500 °C for 2 hours and then grinding 1 hour under ethanol. This procedure was repeated 4 times to

provide homogeneity of the mixture. A hydrous forsterite, with 20 wt.% H_2O, was prepared by grinding the desired proportions of brucite and SiO_2 for 1 hour under ethanol, and dried. Mixtures of forsterite with different amounts of water were obtained by mixing the dry and wet end members. The same approach was adopted for the enstatite-H_2O system, where enstatite plus 15 wt.% H_2O was mixed with dry enstatite to obtain starting mixtures with different amounts of water. Platinum discs of 1 mm thickness were used as capsules. Up to six chambers of 250 μm diameter and ~ 700 μm depth were spark eroded on one surface of the disc. The chambers were loaded with different starting compositions and were held closed at HP-HT by placing a 0.25 mm thickness Pt disc at the top. To limit H_2O losses at HP-HT, the experiments were heated for maximum 30 minutes at 1300 and 1500 °C. At higher temperatures, the duration of the experiments was limited between 3 to 20 minutes. Experiments bearing the same starting mixtures were conducted for different durations to confirm that substantial water losses from the capsules at HP-HT did not occur. Melting phase relations were determined for both systems Mg_2SiO_4-H_2O and $MgSiO_3$-H_2O at 13 GPa (Fig. 4.2-8).

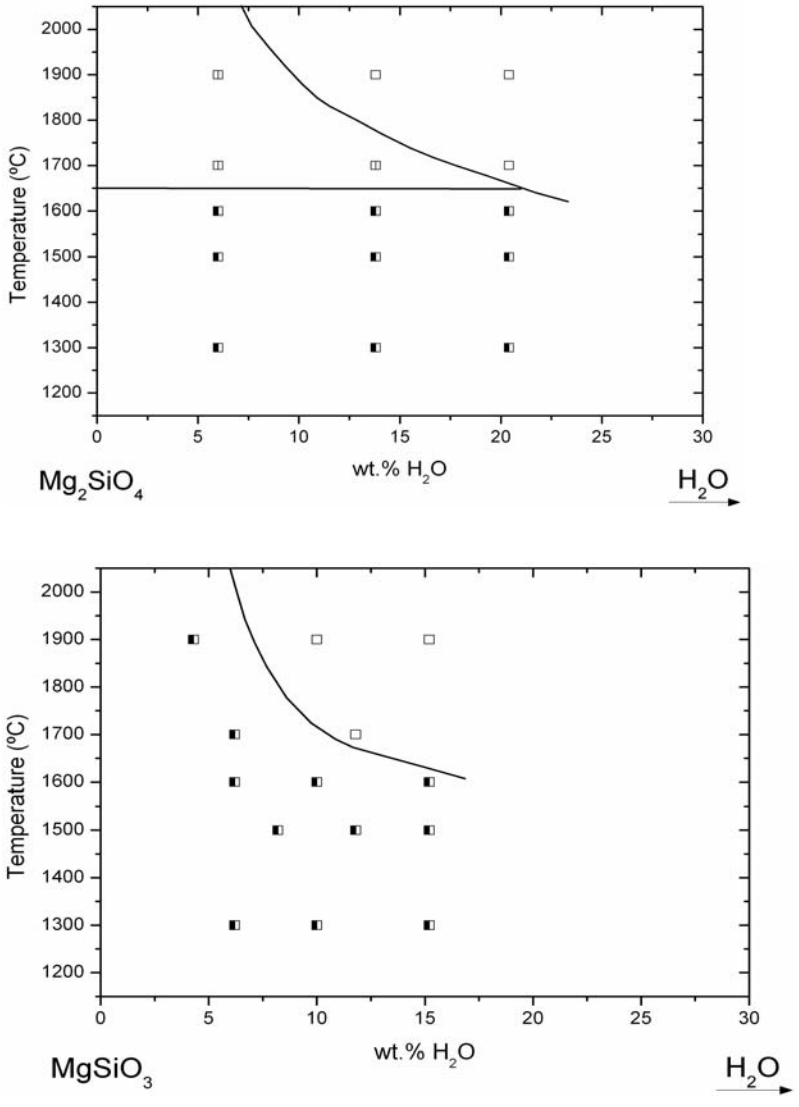

Fig. 4.2-8: Phase relations in the systems Mg_2SiO_4-H_2O (top) and $MgSiO_3$-H_2O (bottom) at 13 GPa. Top: half-filled squares are experiments where crystalline phases forsterite and enstatite were found in equilibrium with melt; empty squares with a vertical line show experiments where only forsterite was in equilibrium with melt; empty squares are experiments where only melt was produced. Bottom: half-filled squares show experiments that produced enstatite and melt, empty squares delimit the region where only melt is produced. Dark solid lines show the liquidi curves constrained by the experiments performed in this study. The estimated temperature uncertainty in the experiments is < 50 °C.

Forsterite was found to melt incongruently below 1600 °C, while enstatite melted congruently at temperatures investigated in this study, in agreement with literature data. Liquidi were determined for both systems between 1700 and 1900 °C (Fig. 4.2-8). At lower temperatures it was not possible to bracket the liquidus curves due to the limitation of the bulk water content in the prepared starting mixture. In the forsterite-H_2O system, melt at 1700 °C has approximately 17.5 wt.% H_2O and at 1900 °C it has 10 wt.%. In the enstatite-H_2O system, the hydrous melt has ~ 9 wt.% H_2O at 1700 °C, and the melt water content decreases to approximately 6 wt.% H_2O at 1900 °C. H_2O contents of the melts at 13 GPa are much higher compared to lower pressure data in the forsterite-H_2O system. At 1700 °C, for example, H_2O concentration of the melt is 3 times higher than at 6 GPa. At the same temperature but in the enstatite-H_2O system, substantial differences are not observed in the water contents of the melt, when comparing values at 13 GPa and 6 GPa.

f. *The chemistry of low degree hydrous melts at 180 km depth (D. Novella and D.J. Frost)*

Melting processes are crucial in terms of the chemical evolution of the Earth and its physical properties. Melts also contribute to the transport of heat from the inner part of the planet to the surface. Fractional melting processes and the formation of melts at different pressure and temperature conditions, give rise to different kinds of igneous rocks that can be observed at the surface.

Water, recycled from the crust into the mantle by subducting slabs, directly influences the melting processes that take place at depth in the Earth. In fact, H_2O has the potential to lower the melting temperature of an upper mantle peridotite, allowing melting to occur at greater depths than compared to H_2O-free conditions, along a mantle adiabat. Low degree melting will likely occur in the presence of water and at pressures much greater than where the main phase of silicate melting occurs beneath mid ocean ridges. These melts will be most likely enriched in incompatible elements, and will cause significant fractionation of these elements compared to shallow depths where most of the basaltic melts are produced. Therefore, in order to better understand the chemical evolution, and dynamics of the Earth's mantle, the composition of incipient melts that could form at greater depths due to the presence of water need to be addressed.

We have performed high-pressure (HP) and high-temperature (HT) experiments in order to investigate the chemical composition of a low degree hydrous melt forming in the upper mantle. Multianvil experiments were conducted at 6 GPa (corresponding to 180 km depth) and 1400 °C, the adiabatic temperature at this depth, in a natural chemical system. Sandwich experiments were performed in order to determine the composition of a low degree melt in a multi component system. The first step in this experimental approach is to equilibrate a dry peridotite at the pressure and temperature of interest, and analyze the chemical composition of the crystallized phases. Following this step, an initial guess hydrous melt composition is

equilibrated with the peridotite at HP-HT. After quenching the experiment, the minerals and the melt that are formed are analyzed. The chemical composition of the melt produced in the experiment is then remixed in the laboratory and equilibrated with the peridotite assemblage in a subsequent experiment. The procedure is followed until a melt is found in equilibrium with minerals having the same chemical composition as in the subsolidus (melt free) experiment. In doing so, the resulting melt will resemble a low degree melt since it does not affect the chemistry of the major chemical components of the peridotitic mineral phases.

Analyses of the mineral phases were performed by electron microprobe, while those on the melts were performed by laser ablation. Melts produced in this study quenched to produce large crystals, which create local chemical heterogeneity. One of the main advantages of the sandwich experiments is that pools of melts, which segregate from the crystalline matrix, are produced. Heterogeneity problems can therefore be avoided by analyzing large spots (~ 70 m diameter) of the quenched melt, which averages out heterogeneity caused by quenching. The laser ablation analyses, providing high accuracy, enabled reliable estimates of the H_2O content of the melt, through mass balance calculations.

In our experiments, particular attention was placed in order to limit loss of H_2O and Fe during the HP-HT experiments. To limit the loss of H_2O, the duration time of the experiments was limited to 30 minutes and a double capsule was employed. An inner Au/Pd capsule, bearing peridotite and melt mixtures, was enclosed in an outer Pt/Rh capsule bearing only the melt composition. To reduce Fe loss, the Au/Pd capsules were treated with Fe before running the experiment. The capsules were loaded with a Fe-bearing silicate mixture and equilibrated in a gas-mixing furnace for 1 day at ~ 1000 °C and an fO_2 2 log units below the FMQ buffer. The capsules were then cleaned with hydrofluoric acid and used in the experiments. Mass balance calculations provided losses of < 10 wt.% relative FeO.

The low degree hydrous melts produced in the experiments were found in equilibrium with crystals of olivine, clinopyroxene, orthopyroxene and garnet. Equilibrating different melt compositions with the peridotite allowed us to constrain the chemistry of the incipient hydrous melt forming at 6 GPa. The incipient melts, in equilibrium with the subsolidus phases are silica undersaturated nepheline normative melts that from mass balance calculations, contain between 11-15 wt.% H_2O. Figure 4.2-9 shows the extent to which water lowers the peridotite melting temperature at these conditions, compared to literature estimates from lower pressure.

The chemistry of the incipient melts produced in the experiments are very similar to those displayed by natural Kimberlites group II rocks. Kimberlites group II rocks, also known as orangeites, are volatiles rich kimberlites, where H_2O is believed to be the most abundant volatile component. Therefore, based on the results gathered in this study, we suggest that orangeites can be produced by adiabatic decompression of mantle peridotite in the presence of water, at approximately 180 km depth.

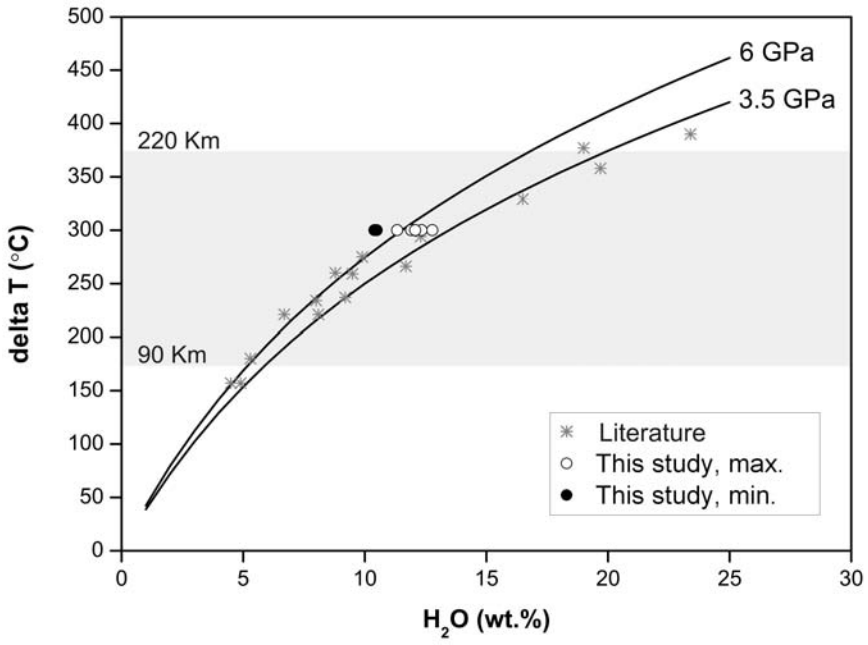

Fig. 4.2-9: The depression of melting temperature (T dry solidus – T) plotted against the melt water content. Grey asterisks are experimental data at 3.5 GPa from the literature. Black circles are data determined at 6 GPa in this study: filled circles indicate H_2O concentration of the melt in the starting mixtures while empty circles are the water contents of the melts given by the mass balance calculations. The actual melt water content should be bracketed by these values. Black lines indicate the parameterization obtained by fitting a cryoscopic equation to literature data and the data presented here. The grey area delimits the range of delta T proposed for the mantle low velocity zone.

g. *An oxy-thermobarometer for eclogitic rocks (D.J. Frost, V. Stagno/Washington D.C. and C.A. McCammon)*

Kimberlitic diamonds are often associated with eclogitic xenoliths and some mineral inclusions in diamonds are also considered to have been derived from eclogite lithologies. In order to understand the conditions of formation of eclogitic diamonds it would be useful to be able to estimate the redox conditions recorded by such rock assemblages. In addition, it is clear that some eclogite xenoliths originated as subducted oceanic crust. During subduction the effect of increasing pressure on ferric/ferrous equilbria, within eclogite assemblages may have influenced the oxidation state and consequently the mobility of carbon-bearing compounds. In order to characterize potential carbon reactions, it is important to be able to describe the oxygen fugacity of eclogitic assemblages as a function of mineral ferric/ferrous ratios at high pressures and temperatures.

In this study a series of experiments on carbonated eclogite compositions have been performed where the fO_2 was measured using a sliding redox sensor. In each experiment the oxygen fugacity should have been buffered by the coexistence of graphite and carbonate melt.

At high temperatures this melt becomes more silica-rich. 5 wt.% of iridium metal was added to the starting charge as a redox sensor and the following equilibrium was employed to then independently measure fO_2,

$Fe_3Al_2Si_3O_{12} = Al_2SiO_5 + 2SiO_2 + 3Fe + 1.5O_2$
garnet kyanite coesite alloy

where the oxygen fugacity is calculated by,

$$\log f_{O_2} = \frac{-\Delta G^o}{1.5RT\ln(10)} - 2\log a_{Fe}^{metal} + \frac{2}{3}\log a_{Fe_3Al_2Si_3O_{12}}^{Garnet} .$$

This required that eclogite starting glasses also contained excess silica and kyanite. In each experiment in addition to an eclogite assemblage a monomineralic layer of either garnet or clinopyroxene was also placed in the centre of the assemblage, in order that Mössbauer spectroscopy measurements of mineral $Fe^{3+}/\Sigma Fe$ ratios could be obtained.

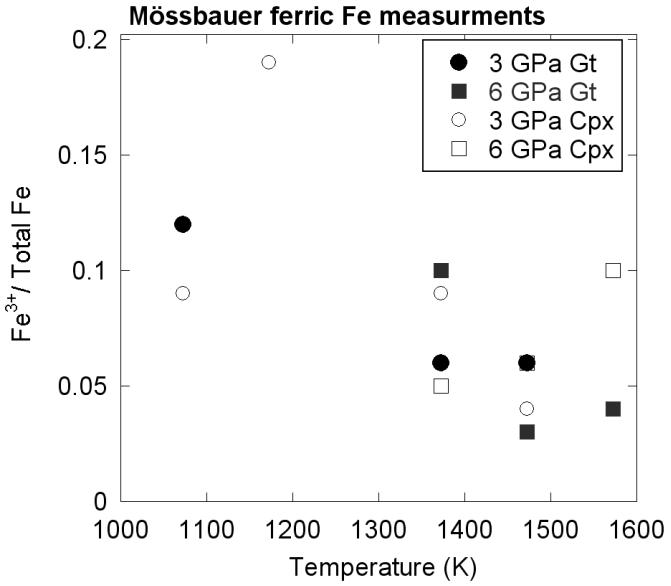

Fig. 4.2-10: Mössbauer measurements of $Fe^{3+}/\sum Fe$ ratios in garnet and clinopyroxene monomineralic layers in experiments performed at 3 and 6 GPa. Oxygen fugacities were nominally buffered by the coexistence of graphite and carbonate-rich melts. Ferric iron contents in garnet decrease strongly with temperature but this is likely due to a lack of effective redox buffering at lower temperatures.

Figure 4.2-10 shows ferric iron contents determined for the garnet and clinopyroxene layers. There is an apparent decrease in mineral ferric/ferrous ratio with temperature. The trend likely arises from an approach to equilibrium, as mineral ferric Fe contents are similar to the starting

materials at low temperature. The small degree carbonate melts that are produced below 1300 K likely do not buffer the oxygen fugacity of the monomineralic layer effectively.

Using measured garnet ferric iron contents combined with estimates of experimental oxygen fugacities it is possible to test plausible oxy-thermobarometry equilibria for determining the fO_2 of eclogite rocks. For this purpose only ferric iron measurements from samples where significant carbonate melting occurred were employed where fO_2 and ferric iron contents are more effectively buffered. We propose an equilibrium where sufficient thermodynamic data exists for all components *i.e.*,

$$\underset{\text{cpx}}{5CaFeSi_2O_6} + \underset{\text{garnet}}{1/3Ca_3Al_2Si_3O_{12}} + O_2 = \underset{\text{garnet}}{2Ca_3Fe_2Si_3O_{12}} + \underset{\text{garnet}}{1/3Fe_3Al_2Si_3O_{12}} + \underset{\text{coesite}}{4SiO_2}$$

where the fO_2 is calculated from

$$\log fo_2 = \frac{\Delta G^o}{\ln(10)RT} + 2\log a^{Gt}_{Ca_3Fe_2Si_3O_{12}} + \tfrac{1}{3}\log a^{Gt}_{Fe_3Al_2Si_3O_{12}} - 5\log a^{Cpx}_{CaFeSiO_6} - \tfrac{1}{3}\log a^{Gt}_{Ca_3Al_2Si_3O_{12}}$$

where ΔG^o is the standard state Gibbs free energy change and $a^{Gt}_{Ca_3Fe_2Si_3O_{12}}$ is, for example, the activity of the andradite garnet component. Activity composition relations for the garnet solid solution are taken from the literature. Clinopyroxenes in eclogite rocks are dominated by diopside and jadeite components with relatively small tschermaks contents but larger Ca-eskola contents that increase with temperature and pressure. A strong increase in Al between 3 and 6 GPa results from increasing jadeite and Ca-eskola contents and causes a decrease in Fe and Ca. For oxygen fugacities calculated with the above equation to match those determined independently from the Ir-Fe alloy sensor, activity composition relations are required to account for the effect of increasing jadeite or Al, or decreasing Ca or Fe on the $CaFeSi_2O_6$ activity. We use a simple ternary mixing model for the M1 site of cpx and by refining a single mixing parameter for Fe-Al interaction it is possible to bring the calculated and observed oxygen fugacities into good agreement.

Using this oxy-thermobarometer, oxygen fugacities from natural samples can be estimated for which garnet ferric Fe contents have been accurately measured. Currently only a few such data exist. Figure 4.2-11 shows oxygen fugacities calculated from measurements made on eclogitic samples from the Udachnaya kimberlite and for eclogites from Kaapvaal craton kimberlites. Temperatures of equilibration for these samples were determined to be in the range 1220-1300 K but pressures were roughly assumed to be 4.5 GPa. In Figure 4.2-11 the fO_2 recorded by these samples is compared with the experimental measurements of the oxygen fugacity where carbonate melts in eclogites are reduced to graphite or diamond. These oxygen fugacities are labeled in terms of temperature and also the range in melt SiO_2 contents is indicated. As can be seen these natural eclogite samples display a range of oxygen fugacities of a similar spread to those observed for peridotite xenoliths. Samples from

Udachnaya appear to be more oxidized with the most oxidized sample being higher in fO_2 than expected for a carbonate liquid in equilibrium with diamond. These high oxygen fugacities may be related to metasomatism. The more oxidized sample from the Kaapvaal craton has an fO_2 and estimated temperature that would be compatible with equilibrium between a carbonate-silicate melt phase and diamond. The most reduced sample would not be in equilibrium with carbonate or silicate-carbonate melt but only with a volatile phase extremely poor in CO_2 but CH_4 bearing.

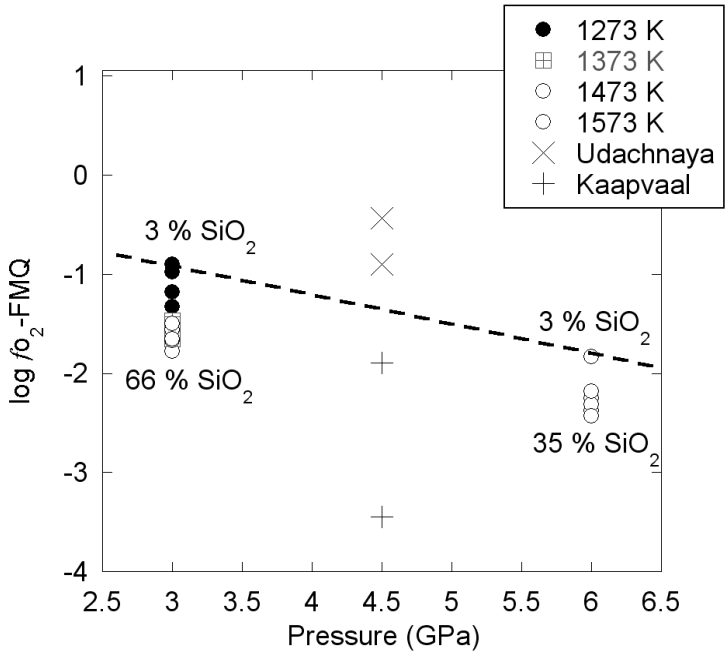

Fig. 4.2-11: Oxygen fugacities for eclogitic xenoliths from the Udachnaya and Kaapvaal craton kimberlites are compared with the experimental determinations of the oxygen fugacity at which eclogitic carbonate melts reduce to diamond or graphite (open and solid symbols). This fO_2 decreases with the melt silica content which increases with temperature. These data are labeled at the top with the SiO_2 content of melt with the highest fO_2, and at the bottom with the melt silica content of the lowest fO_2 data point. Pure carbonate melts are therefore only stable at oxygen fugacities above the dashed line.

h. *The influence of oxygen fugacity on partial melting of eclogite (D.O. Ojwang' and C.A. McCammon)*

Eclogite can be generated from a layer of more or less altered mid-ocean ridge basalt (MORBs) which undergos successive metamorphic changes during subduction. On the basis of thermal modeling calculations, the MORB layer is generally assumed to dehydrate during subduction but remain below its solidus. Its depth of melting in the mantle is controlled by the bulk composition of the mafic rocks. At higher temperature, melting progressively consumes residual minerals and the liquid will migrate into the surrounding lherzolitic mantle. Bimineralic eclogites (garnet and clinopyroxene) that are common in worldwide xenolith

suites are likely a consequence of the extraction of small degree partial melts or hydrous fluids (water) from subducted oceanic crust.

There is limited quantitative information about the influence of oxygen fugacity on the oxidation state of melt and residue in partially melted eclogite. This information can be obtained through experiments conducted under controlled conditions (P, T, x, fO_2) where run products are analysed for both major element composition and oxidation state, providing insight into the behaviour of subducted oceanic crust with respect to changes in oxygen fugacity.

All experimental runs were carried out in a piston-cylinder press using the hot piston-in technique at 3 GPa and 1320 °C over a period of 24 hours. Starting materials consisted of melt and residue, which were either oxidised or reduced using a CO_2-CO gas mixing furnace and loaded in either Fe-Pt or Re-Pt double capsules. Melt was sandwiched between two layers of residue. A typical run product is shown in Fig. 4.2-12. A five-spectrometer JEOL JXA 8200 electron microprobe was employed for quantitative chemical analyses, while Mössbauer spectroscopy was used to determine $Fe^{3+}/\Sigma Fe$ in the starting glass powders and run products.

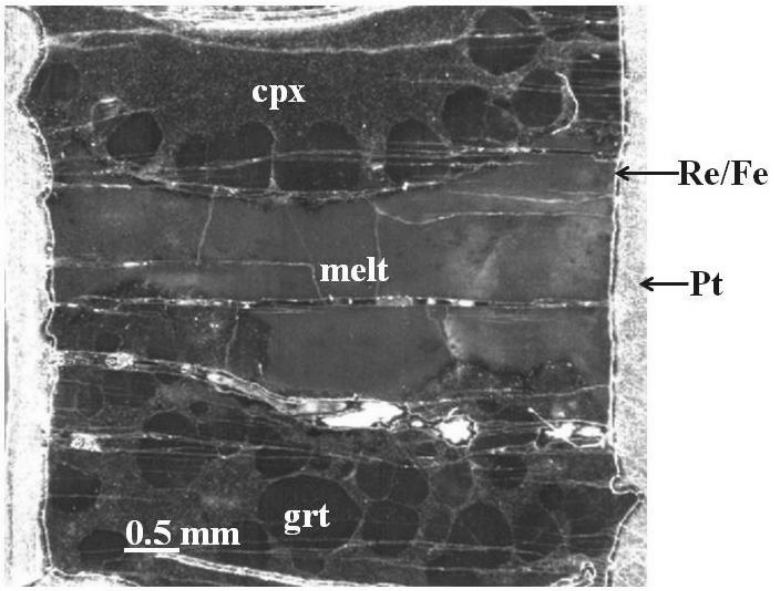

Fig. 4.2-12: An example of a cross-section of an experimental run product examined under an optical microscope showing how a melt layer is sandwiched between layers of coexisting garnet (grt) and clinopyroxene (cpx)

Runs made with reduced starting materials show an increase in melt Fe^{3+} with increasing oxygen fugacity, coupled with a decrease in residue Fe^{3+} (Fig. 4.2-13a). However runs made with oxidised starting materials show a decrease in both melt and residue Fe^{3+} with increasing oxygen fugacity, where the decrease in residue Fe^{3+} is greater (Fig. 4.2-13b). For all

experiments, Fe^{3+} is partitioned more strongly into the residue at reducing conditions and more strongly into the melt at oxidising conditions.

Our experiments suggest that under nominally anhydrous conditions, the oxidation state of melt and residue in partially melted eclogite occurring as a consequence of subduction of basaltic oceanic crust will be influenced by oxygen fugacity. However, to fully understand how oxygen fugacity influences partially melted eclogite, reversal experiments and additional data points need to be determined.

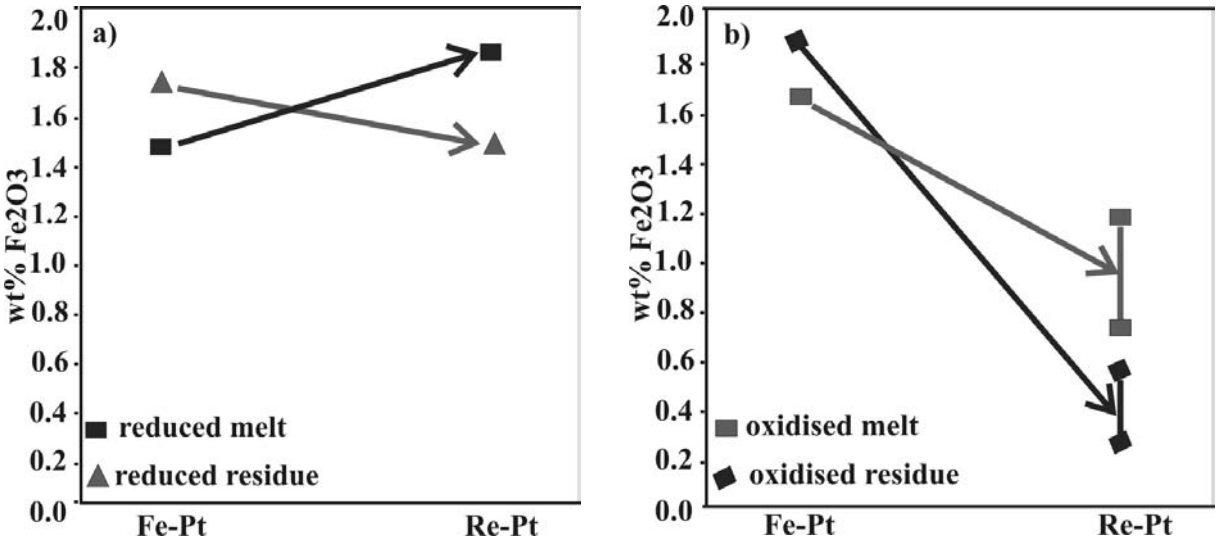

Fig. 4.2-13: (a) Influence of oxygen fugacity (Fe or Re capsule) on wt.% Fe_2O_3 for reduced starting material (b) influence of oxygen fugacity (Fe or Re capsule) on wt.% Fe_2O_3 for oxidised starting material.

i. *Experimental calibration of a geobarometer for eclogites based on Al substitution in clinopyroxene (C. Beyer and D.J. Frost)*

In the past years several geobarometers have been published to determine the depth of origin of eclogite rocks. Most of these models are not based on thermodynamic data but instead rely on empirical formulations applicable to a rather narrow range of pressure, temperature, and composition, and involve various phase assemblages that are not always present in every eclogite. In addition, the large jadeite component in omphacitic clinopyroxene has been frequently neglected. There are several promising approaches using the Ca-Tschermak component in clinopyroxene as a geobarometer in the literature. In this study we have examined the equilibrium:

$$2/3\ Ca_3Al_2Si_3O_{12} + 1/3\ Mg_3Al_2Si_3O_{12} = CaMgSi_2O_6 + CaAlAlSiO_6 \quad (1)$$

Grossular Pyrope Diopside CaTs

We expand the model by taking into account the sodium bearing jadeite component using thermodynamic interaction terms and perform calibration experiments using a natural bulk composition. The derived model is then tested against a large set of existing experimental data over a wide P-T-X range.

A set of high-pressure experiments were conducted in the multianvil apparatus and piston cylinder apparatus between pressures of 3 to 7 GPa and temperatures of 1380 to 1510 °C to address various mineral-mineral partition coefficients. The glass starting material was synthesized according to an average "wet" N-MORB composition containing 2 wt.% H_2O and simplified in terms of minor compounds such as K and Cr. The approach to chemical equilibrium was aided by the presence of large portions of hydrous melt in each experiment. The absence of chemical zoning was taken as strong evidence for near-equilibrium condition. For garnet a ternary asymmetric Margules mixing model was applied with random mixing between the dodecahedral and octahedral sites. For the clinopyroxene solid solution we have used a ternary/quaternary symmetric solution model assuming complete disorder between the M1 site and M2 site. Based on these assumptions, we determine pressure from equilibrium (1) using:

$$P(bar) = -[\Delta G_T + RT\ln K]/\Delta V \qquad (2)$$

where R is the gas constant and ΔV and ΔG_T are the molar volume and standard state Gibbs free energy change of reaction (1) at room pressure. These terms are constrained by fitting the experimental data but the constrained values are very similar to those that can be determined from existing thermodynamic data bases. K is the equilibrium constant of reaction (1).

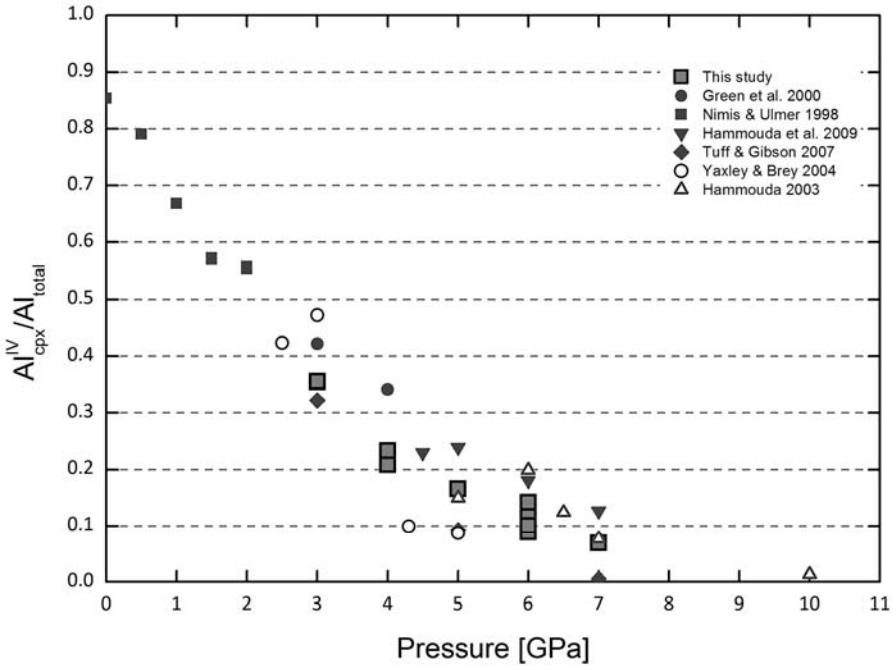

Fig. 4.2-14: Comparison of the Al^{IV}/Al^{total} ratio of different experimental studies. Note that for all studies Al^{IV} was recalculated to obtain a consistent data set.

The substitution of Al in clinopyroxene on the tetrahedral position is highly pressure dependent and suitable to calculate the pressure of eclogitic rocks (Fig. 4.2-14). This geobarometer should be applicable to most eclogitic rocks and we tested the geobarometer with the results of many other experimental studies covering a wide range of compositions and experimental conditions. Our barometer agrees well with the majority of experiments (Fig. 4.2-15). The uncertainty of the current model is in the range of a few kbars. To further improve the model the change of the partial molar volumes with pressure and temperature of the phases involved has to be determined with high precision. In addition, a more advanced formulation for the effect of fO_2 (mainly affecting Fe^{3+}) and temperature will be considered.

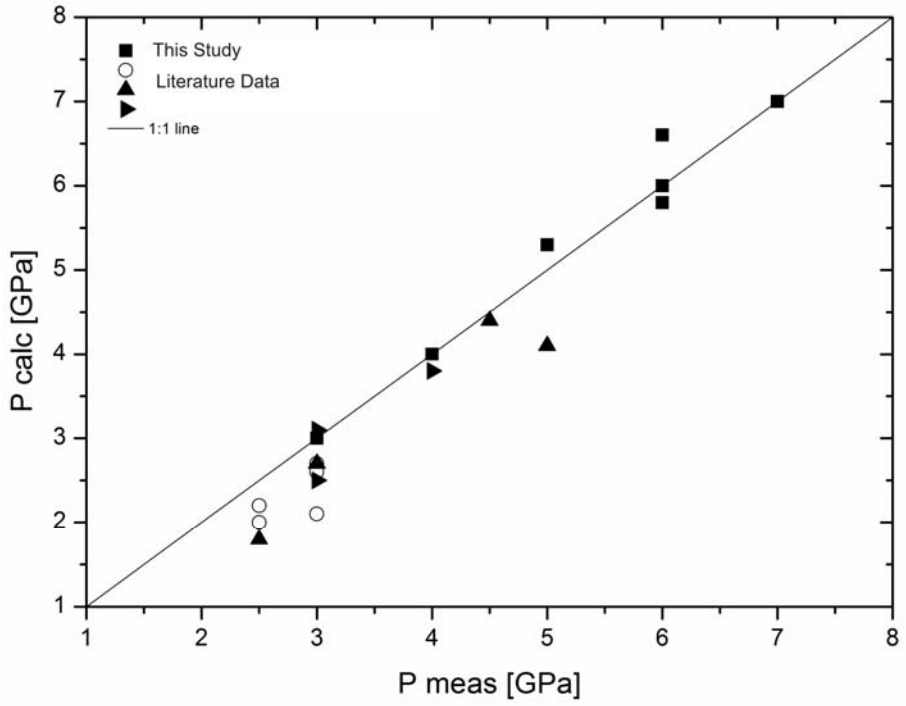

Fig. 4.2-15: Comparison between calculated and measured pressure of various experimental studies. The 1:1 line reflects perfect match between the calculated and measured pressure.

j. *Noble gas solubility in $MgSiO_3$ perovskite and the terrestrial noble gas signature (S. Shcheka and H. Keppler)*

The atmospheres of Earth and Mars are strongly depleted in xenon relative to argon and krypton if compared to a "chondritic" noble gas pattern. This depletion cannot result from hydrodynamic escape alone, which would affect argon and krypton more than the heavier xenon. Despite a number of attempts to find the "missing" xenon somewhere in the Earth, the cause for the observed depletion is poorly understood. Numerous studies on noble gas solubility and noble gas partitioning involving upper mantle minerals have demonstrated that

noble gases are extremely incompatible. However, at higher pressure the behaviour of noble gases could be different. We have therefore considered $MgSiO_3$ perovskite, the main constituent of the lower mantle as a potential reservoir of noble gases and studied the solubility of Ar, Kr and Xe in perovskite.

In order to synthesize Ar, Kr and Xe-saturated $MgSiO_3$-perovskites, glasses with variable Si/Mg ratios and Al contents were loaded together with 40-80 bars of noble gases into platinum capsules and were converted first to denser crystalline phases (enstatite or ringwoodite + stishovite) in a 1200t multianvil press at 1200 °C and 10-18 GPa. Recovered capsules were re-run without opening in a 5000t multianvil press at 1600-1800 °C and 23-24 GPa for 1h. Numerous empty cavities indicating saturation of the samples with Ar, Kr or Xe were observed in the respective run products. The Ar content of the perovskite was measured by electron microprobe. No Ar was found (detection limit: 120-150 wt.ppm) in all stoichiometric perovskites (Si/Mg=1) or in other high-pressure minerals (*e.g.*, ringwoodite, akimotoite, stishovite, periclase, majorite). Electron microprobe analyses of recovered non-stoichiometric perovskites (Si/Mg<1) show that 0.1-1.1 wt.% of Ar is dissolved in perovskite. Kr and Xe contents of perovskites were measured by LA-ICP-MS (limit of detection: 17-43 wt.ppm for Kr and 3-5 wt.ppm for Xe). Up to 0.3 wt.% of Kr was found in perovskite. Xenon solubility in perovskite, however, is an order of magnitude lower (300 wt.ppm Xe) than that of Ar and Kr.

SEM and TEM observations on perovskite crystals did not reveal any impurities or foreign phases, such as gas bubbles, that may account for the observed noble gas contents. We therefore conclude that argon and krypton enter the crystal lattice of the perovskite. In some samples, high argon contents appear to correlate with low Si/Mg ratios. Therefore, noble gas atoms probably occupy oxygen vacancy sites in the structure, which are necessary for reasons of charge balance and which are well documented for magnesium silicate perovskite. The difference in the solubilities of Ar, Kr and Xe is likely due to the size mismatch between noble gas atoms and the oxygen vacancies. While Ar and Kr atomic radii are relatively close to the size of an oxygen vacancy (1.26-1.4Å), xenon with an atomic radius of 1.96 Å is likely too large to fit into this site. Accordingly, the dependence of noble gas solubility on the size of the noble gas atom can be well described by a lattice strain model, which predicts that helium and particularly neon should also be highly soluble in perovskite (Fig. 4.2-16).

Ar, Kr and Xe abundances in the modern atmosphere are roughly proportional to their solubilities in $MgSiO_3$ perovskite. Crystallization of $MgSiO_3$ perovskite from the early magma ocean may have concentrated argon and krypton in the lower mantle, whereas most of the xenon may have been lost together with the primordial atmosphere very early in Earth's history. Accordingly, the noble gas signature of the modern atmosphere may be the result of mixing between a small residue of a mass-fractionated primary atmosphere and an Ar- and Kr- rich component supplied by degassing of the lower mantle. Most of the Ar and Kr present today seems to have originated from the lower mantle and has nearly primordial isotopic

composition, while xenon contains a large mass-fractionated component that is responsible for the observed enrichment in heavier isotopes.

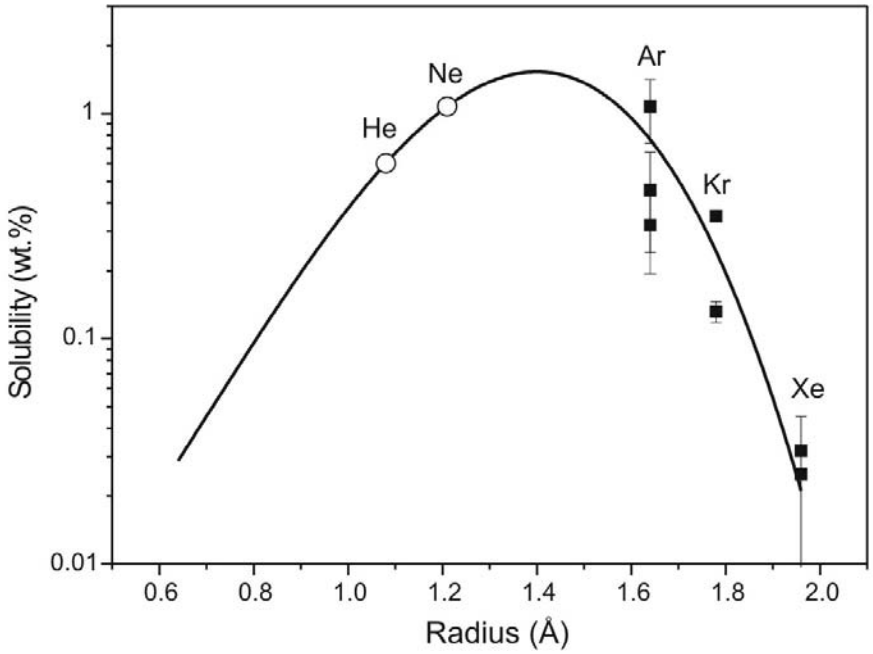

Fig. 4.2-16: A lattice strain model of noble gas solubility in $MgSiO_3$ perovskite. The solid line represents a fit of the Brice equation to Ar, Kr and Xe solubility data at 25 GPa, 1600-1800 °C. Expected values for the solubilities of He and Ne are also shown. Fitting parameters are: E_m = effective Youngs modulus = 35 GPa; r_i = radius of the oxygen site = 1.4 Å, and c_0 = strain-free solubility = 1.53 wt.%. Error bars are one sigma standard deviation.

k. *Nitrogen solubility in upper mantle minerals (Y. Li, M. Wiedenbeck/Potsdam, S. Shcheka and H. Keppler)*

Nitrogen is a volatile element that may help to constrain the evolution and interaction of Earth's different reservoirs. Nitrogen geochemistry is closely linked to atmospheric evolution and may have had a strong effect on the climate of the early Earth and on the formation of the first biomolecules. N_2, the main component in the Earth's present atmosphere, is generally thought to have been derived from degassing of the Earth's interior. If one assumes a chondritic composition of the bulk Earth, most of the N might still be stored in Earth's mantle or core. However, little is known about how much nitrogen could be retained in mantle minerals during the solidification of the magma ocean in the Earth's early history or in the residual mantle minerals after partial melting. Consequently, it is not known how efficiently nitrogen could have degassed into the Earth's atmosphere, and the nitrogen abundance in the bulk silicate Earth is poorly constrained. Therefore, we conducted a systematic study of nitrogen solubility in upper mantle minerals including forsterite, diopside, enstatite, and

pyrope. The experiments were conducted in a piston cylinder apparatus. The temperatures and pressures ranged from 1000 to 1300 °C and from 15 to 35 kbar, to simulate conditions typical of the upper mantle. The minerals were synthesized from well-mixed high purity oxides and hydroxides. About 5 wt.% ^{15}N-labeled $^{15}NH_4{}^{15}NO_3$ was added to the starting mixture as a N source. A modified double capsule technique was used to control oxygen fugacity by three different buffers (Fe-FeO, Co-CoO, Ni-NiO).

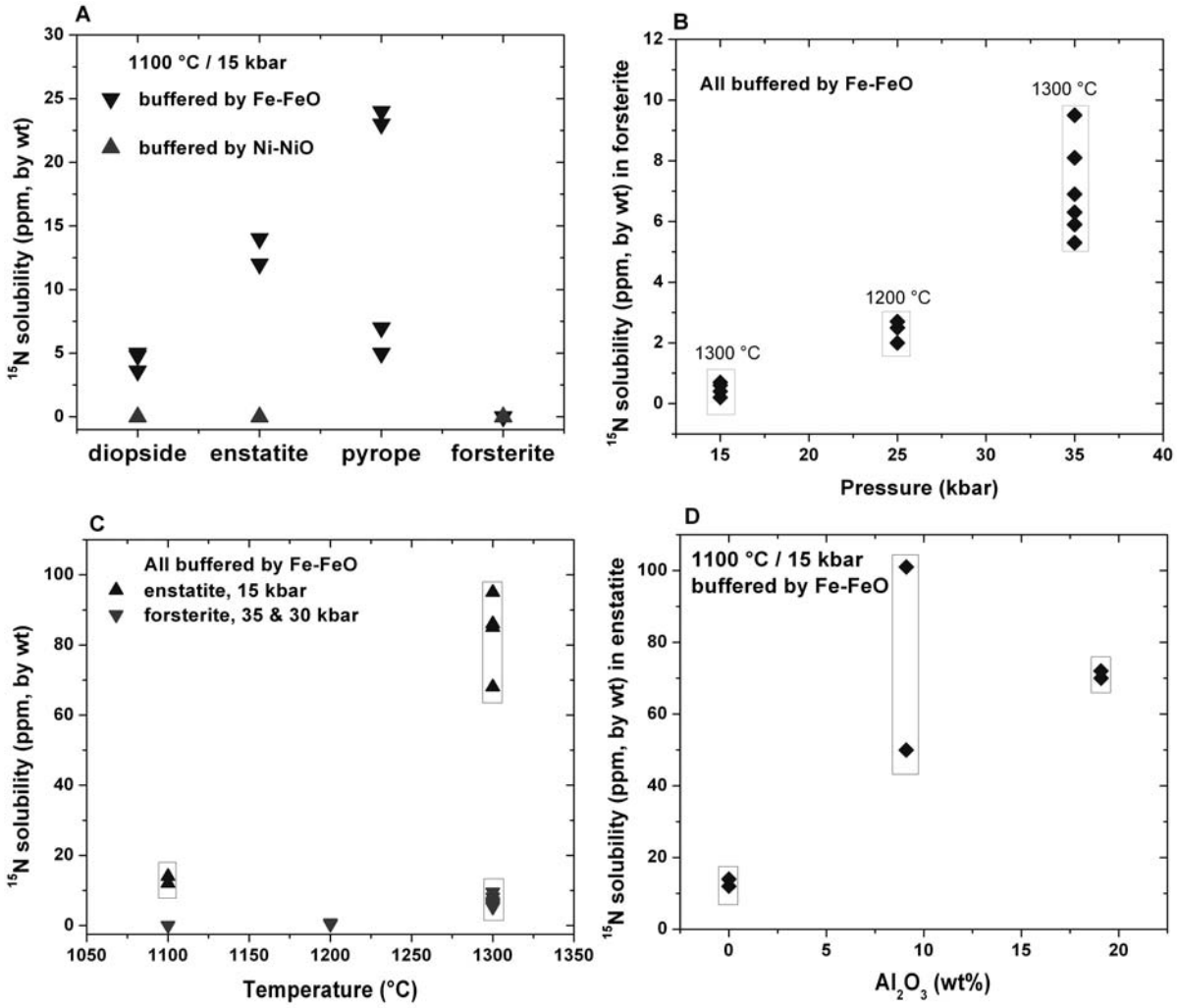

Fig. 4.2-17: Nitrogen (^{15}N) solubility in upper mantle minerals as a function of oxygen fugacity (A), pressure (B), temperature (C), and mineral composition (D).

Nitrogen solubility in synthetic minerals was measured by secondary ion mass spectrometer (SIMS; Cameca, ims 6*f*). The results show that the nitrogen solubility in minerals is significantly affected by temperature, pressure, mineral composition, and oxygen fugacity (see Fig. 4.2-17). In experiments buffered by Ni-NiO or Co-CoO, nitrogen solubility is below detection or reaches a maximum of only a few ppmw (parts per million, by weight) in all minerals investigated. In contrast, 5-24 ppmw nitrogen is determined in diopside, enstatite,

and pyrope buffered by Fe-FeO at 1100 °C / 15 kbar (Fig. 4.2-17A). Even higher nitrogen solubilities of up to 100 ppm are observed at the Fe-FeO buffer in normal enstatite at high temperature, and in Al-bearing enstatite and diopside at lower temperature (Fig. 4.2-17C, D). The nitrogen solubility in forsterite at the Fe-FeO buffer clearly also increases with temperature and pressure (Fig. 4.2-17 B, C); a maximum solubility of 10 ppmw is obtained at 1300 °C / 35 kbar.

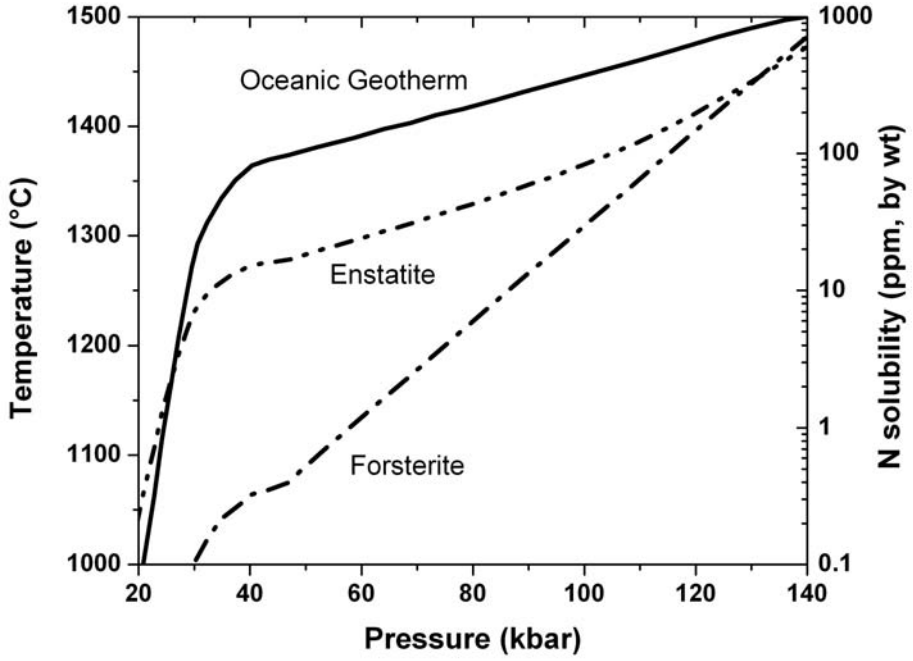

Fig. 4.2-18: Predicted N solubility in forsterite and enstatite in the upper mantle for an oceanic geothermal gradient. The equation used for this prediction is based on fitting experimental data as a function of temperature, pressure, and oxygen fugacity. The high N solubility in both enstatite and forsterite at high pressures illustrates that the deep reduced part of the upper mantle is potentially a large reservoir for N.

The results demonstrate that at oxidizing conditions nitrogen solubility in minerals is generally low, whereas at reducing conditions NH_4^+ can substitute for K^+, and N^{3-} for O^{2-}, resulting in increased nitrogen solubility. This suggests that the reduced lower part of the upper mantle has a large nitrogen storage capacity (Fig. 4.2-18). Using the recently published oxygen fugacity gradient in the upper mantle, application of our nitrogen solubility data to a mantle pyrolite composition yields a nitrogen storage capacity of the entire upper mantle in the order of 10^{20} kg, ~ 20 times as much as the nitrogen in the present atmosphere. Based on N/Ar ratios in mid-ocean ridge basalt, a value of 1-3 ppmw nitrogen has previously been estimated for the bulk silicate Earth. If the nitrogen abundance in chondrites (~ 1100 ppmw) is taken as reference, this would imply that more than 95 % of the nitrogen is 'missing'. The present study indicates that the 'missing' nitrogen is possibly still retained in the Earth's deep, reduced mantle; thus the nitrogen abundance of the bulk silicate Earth may be much higher

than previously thought. The high nitrogen solubility in upper mantle minerals at reducing conditions also indicates that solidification of the magma ocean on the early Earth should have retained significant amounts of nitrogen. However, Ar and C have much lower solubility in upper mantle minerals; as a consequence, preferential degassing of Ar and C should have resulted in much lower N/Ar and N/C ratios in the very early atmosphere than those ratios in the very early upper mantle.

l. *An experimental study on the solubility of chlorine and fluorine in wadsleyite and ringwoodite (M. Roberge, H. Bureau and G. Fiquet/Paris, in collaboration with D.J. Frost, N. Bolfan-Casanova/Clermont-Ferrand, C. Raepsaet/Saclay and S. Surble/Saclay)*

The deep cycling of many volatile elements in the Earth's mantle is still relatively poorly constrained. In particular, very little is understood concerning the cycling and storage of halogens in the Earth. Among volatile species, water is the most well studied in terms of its deep mantle behaviour. A number of studies have examined the recycling of hydrous materials during subduction and it has been variously proposed that subducting slabs may transport water into the deep Earth where minerals in the transition zone (TZ: 410-660 km) may store this water. The major minerals in the TZ, wadsleyite (Wd) and ringwoodite (Rw), have the capability to contain several wt.% of water as hydroxyl groups inside their crystal structures. The study of rocks and magmas from the mantle shows that halogen element concentrations are generally coupled to water contents, particularly in subduction-related rocks. For example, the deepest witnesses to the presence of halogens at depths are aqueous inclusions trapped in natural fibrous diamonds (max depth 200 km). This suggests that halogens are recycled together with water during subduction. Given the ability of Wd and Rw to incorporate hydroxyl groups it is quite plausible that they might also host light halogen elements such as F and Cl, through the substitution of hydroxyl.

The present study is devoted to determining the solubility of F and Cl in wadsleyite and ringwoodite by performing experiments at high pressure and temperature in the multianvil press. Powders of San Carlos Olivine (Fo_{90}) and SiO_2, were mixed either with NaF or NaCl under both hydrous and anhydrous conditions. Experiments were conducted between 14 to 20 GPa and from 1100 to 1450 °C, for several hours. Crystals of Wd and Rw were synthesized, but the very small size of the crystals creates a challenge for the quantification process. In the case of hydrous samples, however, large crystals have been obtained (Fig. 4.2-19).

Fluorine and chlorine concentrations have been measured using ion beam analysis, by employing proton-induced X-ray emission (µPIXE) for chlorine, and proton-induced gamma ray emission (µPIGE) for fluorine, at the nuclear microprobe of the SIS2M/LEEL, CEA Saclay. Preliminary results of the data processing suggest that F and Cl contents in Rw and Wd are higher than in olivine by at least one order of magnitude. The halogen concentrations also show a coupled dependence with the hydroxyl concentrations of the minerals.

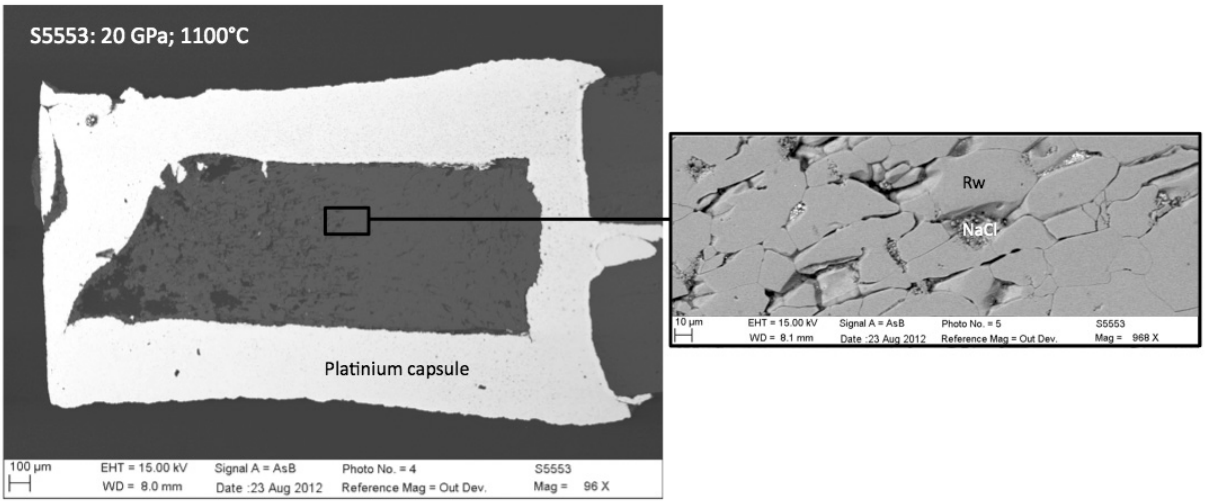

Fig. 4.2-19: Backscattered electron images of MAP thin section of sample #S5553, synthesized at 20 GPa, 1100 °C, in the presence of 2 wt.% of water and excess NaCl. The left image shows the whole capsule; the right image shows the large crystals of Cl-bearing ringwoodite together with smaller NaCl crystals.

m. *Chemical stability of sodium carbonate at high pressures and temperatures (N.A. Solopova, L. Dubrovinsky and N. Dubrovinskaia, in collaboration with Yu.A. Litvin and A.V. Spivak/Chernogolovka)*

Available data on the mineralogy of syngenetic inclusions in superdeep diamonds from the Juina area (Brazil) provided important information on the general chemical composition of the parental medium for the host diamonds and included minerals. Carbonate micro- and nano-inclusions of nyerereite $Na_2Ca(CO_3)_2$, and nahcolite $NaHCO_3$ were identified among the heterogeneous suite of primary inclusions. Chemical and pressure-temperature (*PT*) conditions of formation of the superdeep diamonds and mineral inclusions therein can be investigated using high-pressure experiments focused on the chemical stability and melting behaviour of carbonate components involved in the diamond-forming processes. We have studied experimentally the high-*PT* behaviour of sodium carbonate at pressures up to 46 GPa and temperatures over 2800 K.

Sodium carbonate samples with either ^{13}C or ^{12}C were dried at 600 ºC and used as a starting material. Experiments were performed over a wide pressure range (10-46 GPa) and included two series: multianvil runs at 10-20 GPa and 1000-2400 K, and runs in a laser-heated diamond anvil cell at 20-46 GPa and 1600-3000 K. After quenching, the samples were studied by Raman spectroscopy using a Dilor XY Raman spectrometer and a Ar^+ ion laser source (514.5 nm, Coherent Innova 300). The use of ^{13}C-carbonate in the DAC experiments allows unambiguous distinction between carbon phase(s) produced during the experiments and contamination from ^{12}C-diamond anvils. Recovered samples were also characterized using scanning electron microscopy (SEM).

The results of experiments are shown on a *PT* phase diagram of sodium carbonate (Fig. 4.2-20). According to the multianvil experiments, the melting curve of Na_2CO_3 is almost independent of pressure between 10 and 20 GPa (Fig. 4.2-20). In contrast, the decomposition boundary of sodium carbonate displays a negative slope, extending from 2000 K at 46 GPa to 2550 K at 10 GPa. Its position was constrained by the observation of diamond and graphite at ambient conditions after laser heating in the DAC. These carbon phases contain carbon from both the sodium carbonate $Na_2{}^{13}CO_3$ melt and from the ^{12}C diamond anvils. As a consequence, they have a mixed $^{12+13}C$ isotopic composition, as indicated by shifts in the main diamond and graphite band positions in the Raman spectrum (Fig. 4.2-21). For example, the main Raman band for ^{12}C diamond occurs at 1332 cm^{-1}, but for ^{13}C diamond - it occurs at 1284 cm^{-1}. Therefore, the band position of diamond with mixed $^{12+13}C$ isotopic composition will occur in the range of 1284 - 1332 cm^{-1}. The formation of a solid carbon phase with ^{13}C or $^{12+13}C$ demonstrates that carbonate melt decomposes at high pressures and temperatures. The obtained results are important for determining the conditions of diamond crystallization in carbonate melts in the transition zone and the lower mantle, as well as for reconstructing the geochemical evolution of Na in the deep Earth .

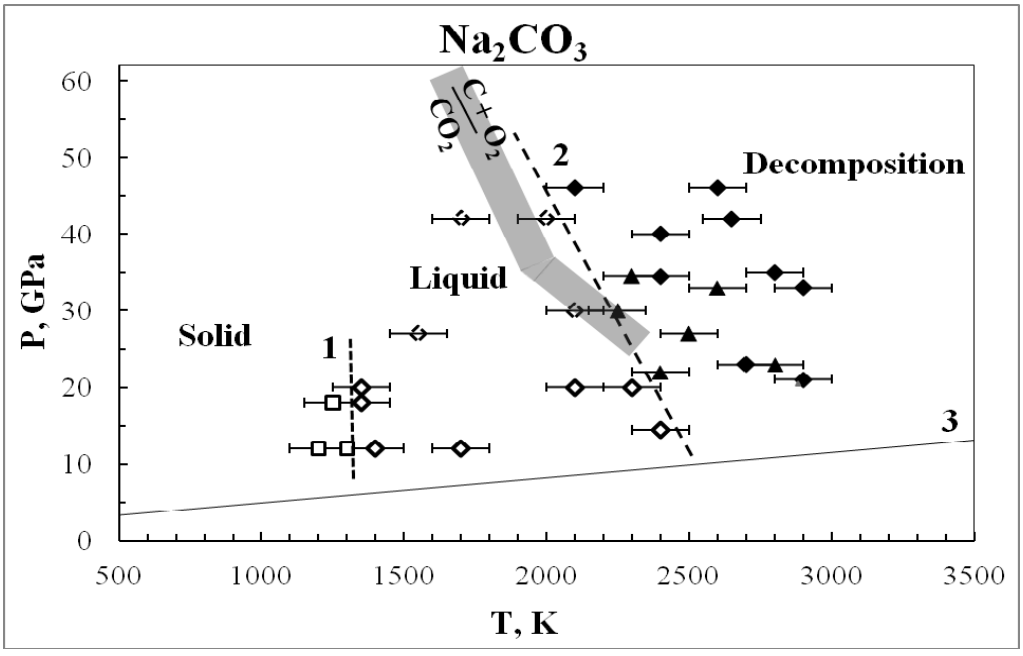

Fig. 4.2-20: *PT* phase diagram of Na_2CO_3. Experimental points at > 20 GPa are from DAC runs; points at ≤20 GPa are from multianvil runs. Empty squares indicate experiments where there is no melting of sodium carbonate; empty octahedrons indicate runs with melting of Na_2CO_3; filled octahedrons and triangles indicate formation of diamond and graphite, respectively. Line 1 represents the melting curve of Na_2CO_3; line 2 represents the decomposition boundary of Na_2CO_3; line 3 is the graphite – diamond equilibrium curve. The grey field shows the decomposition boundary of CO_2 to C and O_2 (taken from the literature).

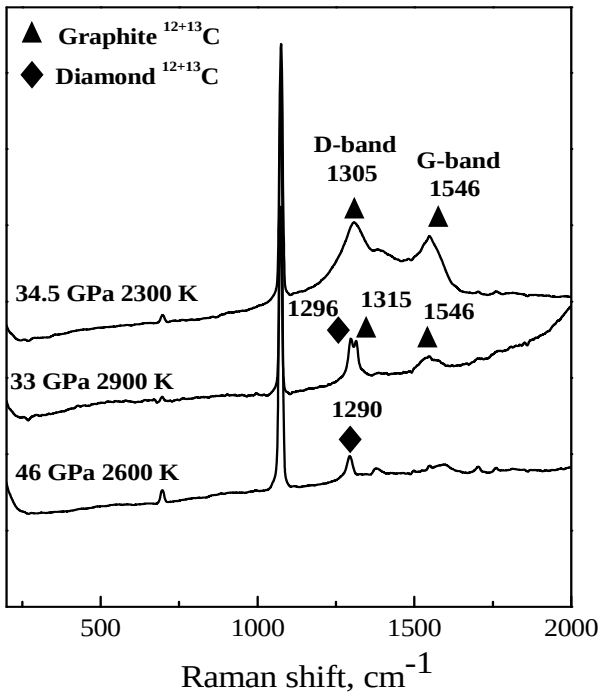

Fig. 4.2-21: Raman spectra of recovered samples after laser heating of Na_2CO_3 in the DAC at three different PT-conditions.

n. *The partitioning of copper between mantle minerals and silicate melts (X. Liu, X. Xiong/Guangzhou, A. Audétat, H. Keppler and Y. Li)*

Copper (Cu) is an important ore-forming element and indicator of magmatic evolution. The primitive upper mantle has an estimated Cu concentration of between 20 and 30 ppm. Mantle-derived primitive basaltic magmas such as mid-ocean ridge basalts (MORB), island arc basalts (IAB) and ocean island basalts (OIB) have Cu concentrations ranging in general from 60 to 80, 60 to 100 and 100 to 130 ppm, respectively. This suggests that Cu is incompatible during mantle melting. The upper mantle consists mostly of olivine, orthopyroxene, clinopyroxene and an Al-phase mineral (*i.e.*, garnet, spinel or plagioclase), and minor sulphides (*i.e.*, monosulphide solid solution and sulphide liquid). Knowledge of the partition coefficients of Cu between such minerals and mantle-derived magmas is required for quantitative modeling of the behaviour of Cu during mantle melting.

Cu is a typical chalcophile (*i.e.*, sulphide loving) element. It has very high sulphide-silicate melt partition coefficients ($D_{Cu}^{sulphide/silicate\ melt}$) ranging from several hundreds to over a thousand. The incompatible behaviour of Cu during mantle melting suggests that the role of residual sulphide, if present, is limited in catching hold of Cu (*i.e.*, there is insufficient sulphide in the residual solid to hold back the increase of Cu concentration in the mantle-derived melts). Therefore, Cu behaviour during mantle melting is largely dependent on its partitioning between silicate minerals and melts. In particular, Cu behaviour is entirely controlled by silicate mineral-melts partitioning during the early fractional crystallization of a mantle-derived magma that is later emplaced at a shallow depth in the crust, since a sulphide-saturated magma from great depth would become sulphide-unsaturated due to the increase of sulphur solubility in the melt with decreasing pressure. Therefore, precise partition

coefficients between silicate minerals and melts are necessary for a quantitative understanding of the behaviour of Cu during partial melting and magmatic differentiation.

Most published experimentally determined mineral-melt Cu partitioning data are problematic due to the use of Cu-free noble metal capsules, since Cu, like Fe, also easily forms alloys with the noble metal capsules during high P-T experiments, especially under reducing conditions such as the graphite buffer. The Cu loss during experiments not only leads to a very low concentration of Cu in the experimental products and big analytical uncertainty, but also disturbs the Cu partitioning equilibrium between minerals and melts. To avoid these problems, we have used $Pt_{95}Cu_{05}$ (95%Pt5%Cu) alloy capsules as the source of Cu to determine the partition coefficients of Cu between olivine, orthopyroxene, clinopyroxene, spinel, garnet and hydrous silicate melts. Three synthetic compositions a komatiite, a MORB and a Di-An eutectic melt were used as experimental starting materials. The experiments were conducted using piston cylinder equipment at 1.0-3.5 GPa and 1100-1300 °C with oxygen fugacity varying from approximate ΔNNO-2 (2 log units below the nickel-nickel oxide buffer) to ΔNNO+5. Minerals and quenched glasses (melts) in the run products were analyzed using both EMP and LA-ICP-MS to obtain Cu partition coefficients. The results indicate that Cu is incompatible in all the silicate minerals investigated with $D_{Cu}^{mineral/melt}$ = 0.04-0.11 for olivine (9 mineral-melt pairs), 0.04-0.08 for orthopyroxene (3 mineral-melt pairs), 0.02-0.20 for clinopyroxene (13 mineral-melt pairs), 0.03-0.04 for garnet (2 mineral-melt pairs) and 0.19-0.82 for spinel (9 mineral-melt pairs). Temperature, pressure and oxygen fugacity appear to have no significant effects on the Cu partitioning for these minerals, but compositions of clinopyroxene and spinel have significant influence on the partitioning. $D_{Cu}^{mineral/melt}$ for clinopyroxene increases with increasing jadeite content (Fig. 4.2-22) and $D_{Cu}^{mineral/melt}$ for spinel increases with increasing total FeO content (Fig. 4.2-23). These results can be applied, in conjunction with published sulphide-silicate Cu partitioning data, to explain the Cu fractionation trend during mantle melting and fractional crystallization of mafic magmas.

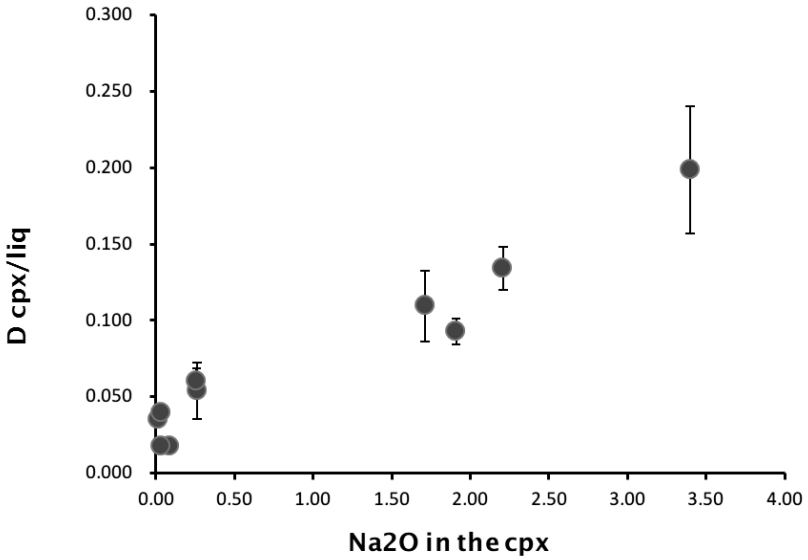

Fig. 4.2-22: Cu partitioning between clinopynoxene and silicate melts, showing that $D_{Cu}^{mineral/melt}$ increases with increasing Na_2O content in clinopyroxene.

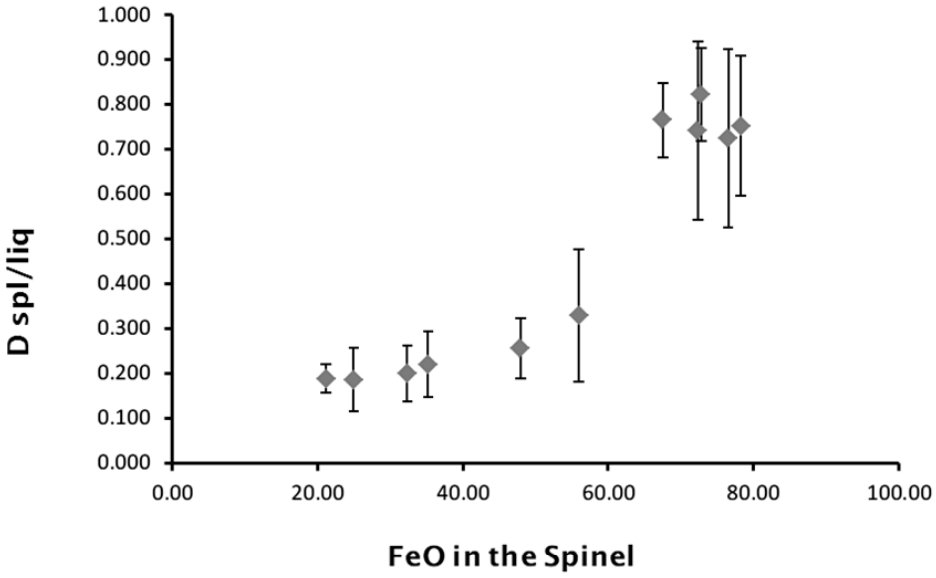

Fig. 4.2-23: Cu partitioning between spinel and silicate melts, showing that $D_{Cu}^{mineral/melt}$ increases with increasing total FeO content in spinel.

o. *Oxidation state of the continental crust from the Hadean to the present (X. Yang/Nanjing, and C. McCammon)*

The presence of a chemically evolved continental crust makes the Earth distinguishably different from other rocky planets in our solar system, and provides some of the prerequisites that led to the evolution of life and the final appearance of Homo sapiens. The emergence of evolved continental crust on the Earth's surface might be tracked back to ~ 4.4 billion years (Ga) ago. The continental crust covers ~ 40 % of the Earth's surface area, and being the interface between the underlying mantle and overlying atmosphere, it plays a critical role in buffering the exchanges and interactions between the Earth's interior and exterior. Moreover, the continental crust, although volumetrically insignificant (~ 0.35 % of the Earth's mass), is a dominant reservoir for several of the most incompatible elements during melting and crystallization and is a substantial sink for CO_2 through weathering and erosion. Therefore, any significant temporal change in the composition, structure and other physicochemical properties of the continental crust would have crucial implications for understanding the evolution of the whole Earth.

Oxidation state, as reflected by its prevailing oxygen fugacity (fO_2), is an important parameter in controlling many chemical and physical properties and geological processes of the Earth, and a critical role of Earth Sciences is to evaluate the oxidation state of Earth's different reservoirs and their secular changes over time. Available reports have well established that the oxidation state of the present upper mantle is within ±2 log units of the quartz-fayalite-magnetite (QFM) buffer, and has remained nearly constant since at least ~ 3.9 Ga ago based on trace element studies of mantle-derived komatiites, kimberlites, basalts and volcanics. In

contrast, the oxidation state of the continental crust and its secular evolution has only rarely been addressed.

Zircon is a common accessory mineral in nature, occurring in a wide variety of igneous, sedimentary and metamorphic rocks. Typically, zircon crystallizes from high silica melts and at moderate to high grades of metamorphism, and is almost ubiquitous in upper crustal rocks, although mantle zircons have also been found as megacrysts in kimberlites and as tiny grains in ocean-crust gabbros and mid-ocean ridge basalts (MORB). The physical and chemical durability of zircon makes it widely used in many geochemical studies in terms of trace elements, isotopes, ages and melt/mineral inclusions. In particular, zircon is persistent under most crustal conditions and can survive many secondary processes including metamorphism, weathering and erosion. As a result, zircon in felsic granites has the potential to record chemical and isotopic information about the deep crust that is otherwise inaccessible. Due to the absence of suitable rock records (particularly older than ~ 4.0 Ga), studies on the temporal evolution of the composition, formation and other properties of the continental crust, and especially the Hadean crust, have relied largely on inherited/detrital zircons.

Natural igneous zircon usually contains rare earth elements and other trace elements such as Ti, Hf, Th, U, Y and P in its structure at concentrations controlled by the temperature, pressure, fO_2 and composition of the crystallization environment. Thus, the contents of REE and other trace elements of igneous zircons can be used to predict their growth conditions and the nature of their source materials. The concentration of Ce relative to other REE in igneous zircons is largely determined by the fO_2 during their growth, and the chondrite-normalized Ce anomalies of igneous zircons has been quantitatively described in a recent study reported in the literature:

$$\ln(Ce/Ce^{*})_{CHUR} = (0.1156 \pm 0.0050) \times \ln(fO_2) + \frac{13860 \pm 708}{T} - (6.125 \pm 0.484) \qquad (1)$$

where $(Ce/Ce^{*})_{CHUR}$ is the chondrite-normalized Ce anomaly, and T is the temperature of crystallization (K). We have applied this formulation to data compiled from the literature for igneous zircons of crustal origin and with different formation ages to offer some insight into the oxidation state of the continental crust and its secular change over time.

The results are summarized in Fig. 4.2-21. In general, the fO_2 of modern continental crust is QFM-2 to QFM+10 (mostly QFM-2 to QFM+8), *e.g.*, between the present upper mantle and atmosphere, and probably obtained its present oxidation state ~ 3.6 Ga ago. In contrast, the fO_2 of Hadean zircons shows more reduced values, mostly ranging from QFM-10 to QFM+4, and the zircons prior to 4.0 Ga ago record even more reduced conditions, down to as low as QFM-10. We suggest that the continental crust was more reduced in the Hadean than in the post-Hadean time, and has undergone a transitional period between ~ 4.0 and 3.6 Ga ago in which the magmatic environments of zircon crystallization, and thus the processes of crustal

reworking and recycling, changed profoundly. In the present day, fO_2 decreases with increasing depth below the Earth's surface, where the continental crust is oxidized relative to the upper mantle. If the continental crust prior to ~ 4.0 Ga ago was also more oxidized than the underlying mantle, this would imply a more reduced Hadean upper mantle compared to the present day, which could have important implications for the evolution of the Earth's atmosphere.

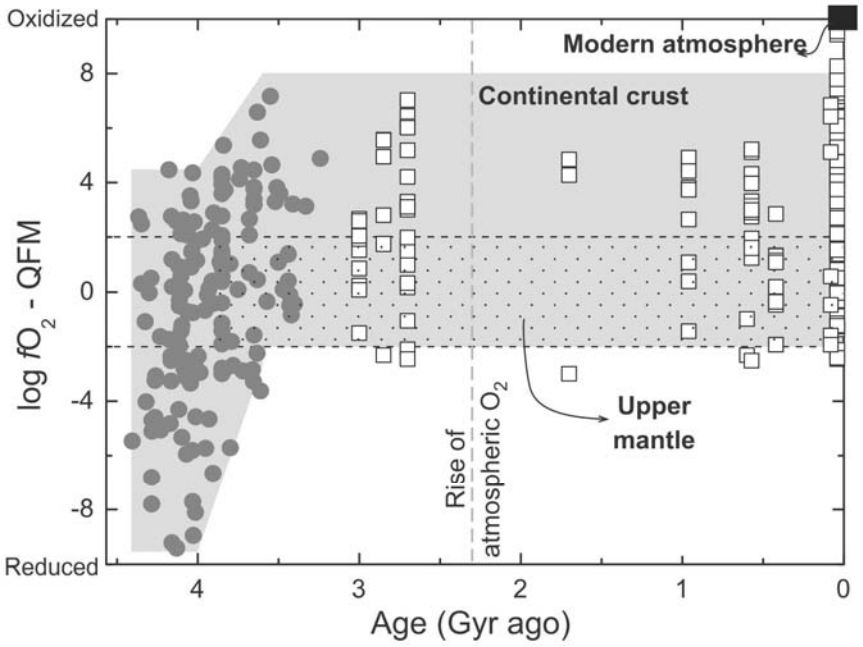

Fig. 4.2-21: Oxidation state of the continental crust from the Hadean to the present based on the application of Eq. 1 to literature data. Temperature was calculated from the Ti-in-zircon thermometer, or assumed to be 700 °C in the absence of Ti data. Open squares are post-Hadean zircons from various crustal igneous and metamorphic rocks, while solid circles are detrital zircons from the Jack Hills and Wyoming Province. Uncertainty of the calculated fO_2 is ~ 2 log units (1 s.d.).

p. *Solubility of rutile in hydrous rhyolite melts at 750-900 °C and 2 kbar (K. Kularatne and A. Audétat)*

The Ti-in-quartz (TitaniQ) thermobarometer is a promising tool to constrain the crystallization conditions of volcanic and intrusive rocks because quartz is an abundant, weathering- and reequilibration-resistant mineral in a large number of silicic magmas. In order to apply TitaniQ to natural samples (which usually were not saturated in rutile) one has to know the TiO_2 activity in the silicate melt. However, currently available methods to calculate TiO_2 activities in silicate melts return highly inconsistent results that commonly vary by more than a factor of three. The aim of the present study is to develop a new TiO_2 solubility model that is particularly suitable for shallow rhyolite magmas, which are a common target for TitaniQ applications.

At the conditions relevant for shallow rhyolite magmas (700-900 °C, 1-2 kbar) Ti diffusion in silicate melts is extremely slow. It was thus necessary to develop a new experimental approach to determine TiO_2 solubility (Fig. 4.2-22). In a first step, crystal-free glass with a smooth TiO_2 gradient over several mm length was prepared in a high-temperature furnace at 1 atm. One piece of this glass was loaded together with enough H_2O to reach fluid saturation into a Au capsule and equilibrated for several days at the desired run conditions of *e.g.*, 850 °C, 2 kbar in a rapid-quench cold-seal pressure vessel ("crystallization experiment" in Fig. 4.2-22). This treatment caused rutile to crystallize in the TiO_2-rich parts of the sample, whereas the TiO_2-poor parts of the sample remained rutile-free (Fig. 4.2-23). The run was terminated by *in situ* rapid quenching, which resulted in cooling below the glass transition temperature within a few seconds. The TiO_2 content of the glass at the contact between rutile-bearing and rutile-free glass was then measured by laser-ablation ICP-MS. In principle, this value should correspond to the saturation value.

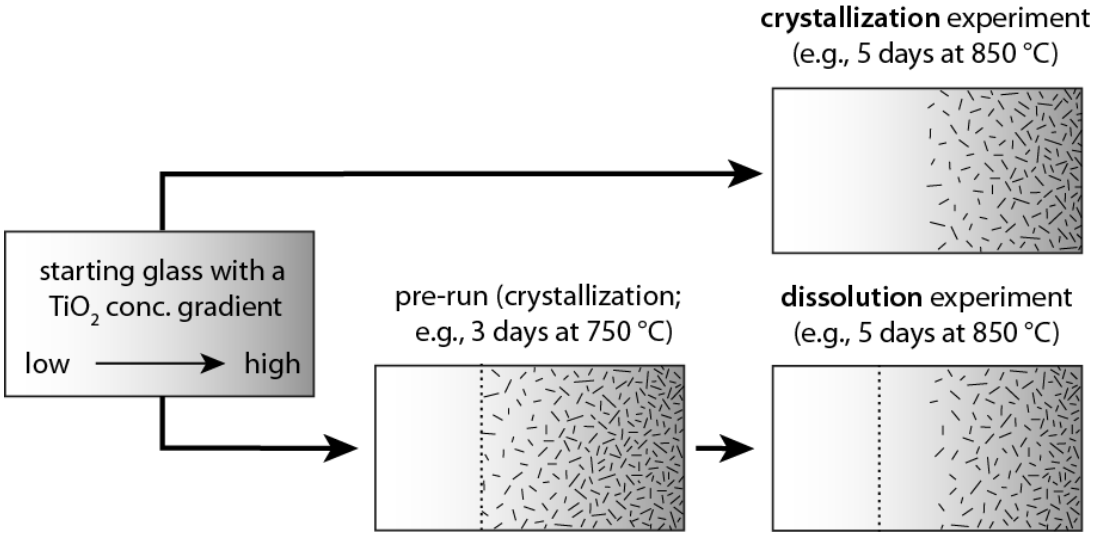

Fig. 4.2-22: Principle of how TiO_2 solubility was determined by forward and reverse experiments in the present study. In both set of experiments, TiO_2 solubility was constrained by laser-ablation ICP-MS analysis of the recovered glass at the contact between rutile-free and rutile-bearing parts of the sample.

However, because crystal nucleation typically requires some degree of supersaturation it is feasible that this approach results in a slight overestimation of the true rutile solubility. Equilibrium was thus approached from the other side in a second type of experiments. For this purpose we first conducted a run similar to the one described above but at 50-150 °C lower temperature (*e.g.*, 750 °C, 2 kbar) , and then equilibrated the recovered glass piece in a new run at the final run condition (*e.g.*, 850 °C, 2 kbar). In this way, some of the rutile that formed during the first step became re-dissolved during the second step ("dissolution experiment" in Fig. 4.2-22).

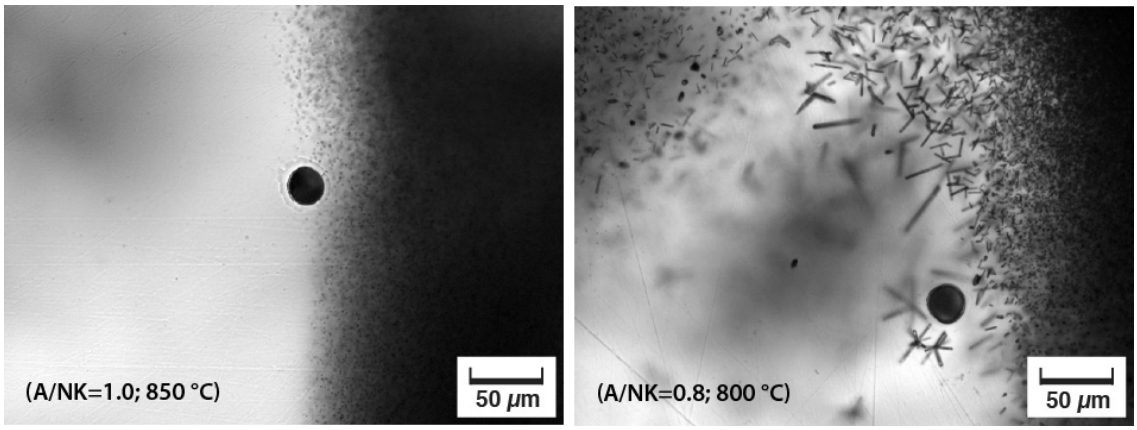

Fig. 4.2-23: Photomicrographs of two experimental run products, showing rutile-free glass in the (lower) left parts of the images, and rutile-bearing glass in the right parts of the images. Also shown are laser-ablation ICP-MS craters where TiO_2 solubility was measured at the contact between rutile-bearing and rutile-free glass.

In most cases, both forward and reverse runs were performed in a single experiment, *i.e.*, untreated glass pieces and pre-conditioned ones were loaded into the same capsules. All experiments were conducted at 750-900 °C, 2 kbar using water-saturated, haplogranitic melts with molar $Al_2O_3/(Na_2O+K_2O)$ ratios (A/NK) ranging from 0.8 to 1.2. One additional experiment was conducted with a natural rhyolite melt. TiO_2 solubilities measured in crystallization runs and dissolution runs generally agree well with each other and show a systematic dependence on temperature and the A/NK ratio (Fig. 4.2-24).

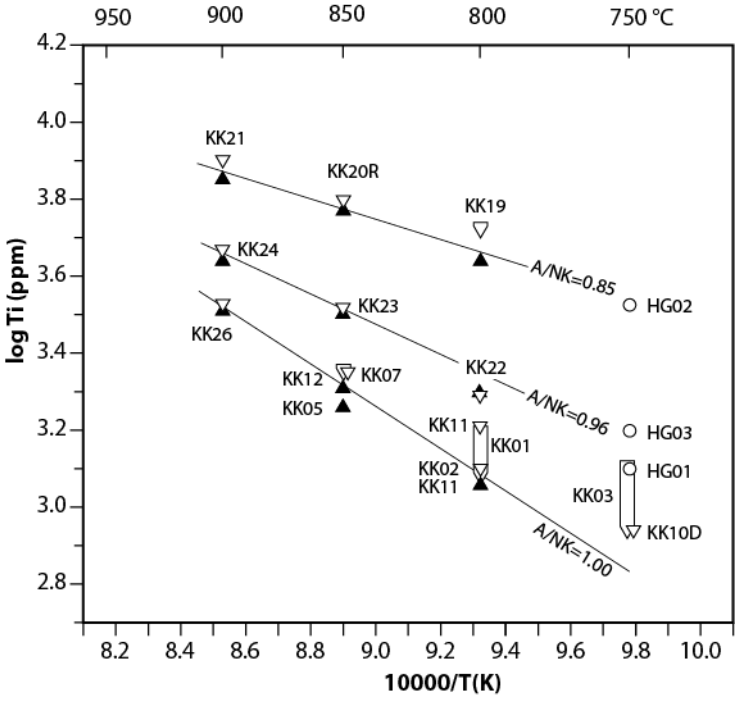

Fig. 4.2-24: Summary of TiO_2 solubilities (in µg/g) obtained in subalkaline to peralkaline melt compositions. Black triangles represent dissolution experiments; white triangles represent crystallization experiments; open circles represent TiO_2 solubilities measured after the pre-conditioning step in the dissolution experiments. Solid lines denote fits obtained by equations (1) and (2).

Unfortunately it was not possible to obtain a satisfying fit through all data by a single equation. For this reason the data from peralkaline melts (eq. 1) and those from peraluminous melts (eq. 2) were fitted separately:

$$\log Ti(\mu g/g) = EXP(20.5189-19.712082/ANK)+6-10000/T*(1/(45.415205 - 42.157358*ANK^2))^{0.5} \quad (1)$$

$$\log Ti(\mu g/g) = 1/(-25.0476+25.4936*ANK^3)+6+10000/T*(1/(-290.8903+287.102/ANK^2)-0.29) \quad (2)$$

In these equations, ANK refers to the molar A/NK ratio as defined above, and T is given in Kelvin. Although our melts did not contain any Ca, Fe or Mg, this TiO_2 solubility model successfully reproduces TiO_2 solubilities measured in previous studies in natural melts of trondhjemitic to leucogranitic composition, plus those obtained from using our natural rhyolite melt composition. Application of our TiO_2 solubility model to natural samples formed at known P-T formation conditions results in pressure estimates that agree well with independent pressure constraints (Fig. 4.2-25), thus validating the titanium-in-quartz model that was presented in the 2011 BGI yearbook and was published in GCA 84:75-89, 2012.

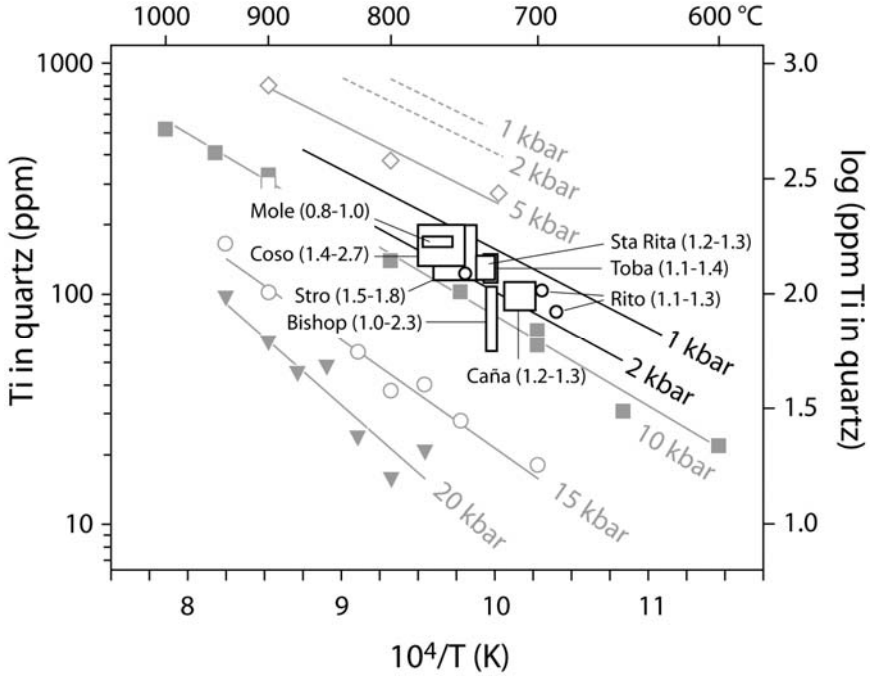

Fig. 4.2-25: Titanium concentrations of natural igneous quartz that crystallized at known pressures and temperatures, recalculated to a TiO_2 activity of unity based on Ti concentrations in melt inclusions and our new TiO_2 solubility model. Independent pressure estimates (in kbar) are shown in parentheses next to the sample names. Black lines represent isobars calculated by the titanium-in-quartz model presented in the BGI yearbook 2011, whereas light grey data points and isobars are from Thomas *et al.* (CMP 160:743-759, 2010).

q. *The origin of metals in the Guocheng gold deposit, China (J. Tan and J.H. Wei/Wuhan; A. Audétat and T. Pettke/Bern)*

The Guocheng gold deposit is one of several hundred Mesozoic gold deposits occurring in the Jiaodong Peninsula at the eastern rim of the North China Craton, which represents the largest gold district in China. The gold occurs in sulphide-rich veins and disseminations hosted by NE-trending fractures, some of which also host dikes of mafic alkaline composition. Rb-Sr dating of fluid inclusions in vein quartz constrains mineralization to 119±10 Ma, an age that is only slightly older than the U-Pb ages of 114±2 to 116±1 Ma obtained for the dikes. The present study aims at investigating a genetic relationship between mafic alkaline magmatism and gold ore formation by presenting extensive petrographic, geochemical, microanalytical and isotopic data from both dike rocks and ore samples.

More than 90 % of the dikes in the vicinity of the gold deposit are of doleritic composition and crosscut the ore bodies. However, some of them also predate mineralization and share the same structural features as the ore, suggesting that dike formation and ore formation was broadly simultaneous. Fresh samples contain 5-20 vol.% phenocrysts of hornblende, plagioclase, biotite, and minor clinopyroxene. Hornblende and clinopyroxene phenocrysts commonly show reverse zoning with Fe-rich cores overgrown by Mg- and Cr-rich rims, indicating that mafic magma intruded into already existing, more evolved magma chambers. At the contact between Fe-rich cores and Mg-rich rims numerous inclusions of anhydrite and sulphide occur (Fig. 4.2-26). This feature, together with biotite compositions and temperature estimates obtained from amphibole-plagioclase thermometry suggests that the hybrid magma was sulfur-rich and crystallized at 911-924 °C and log fO_2 = NiNiO+1 to NiNiO+1.6. The sulphide inclusions are composed mainly of pyrrhotite plus small amounts (< 5 %) of chalcopyrite, and most likely represent a trapped sulphide liquid.

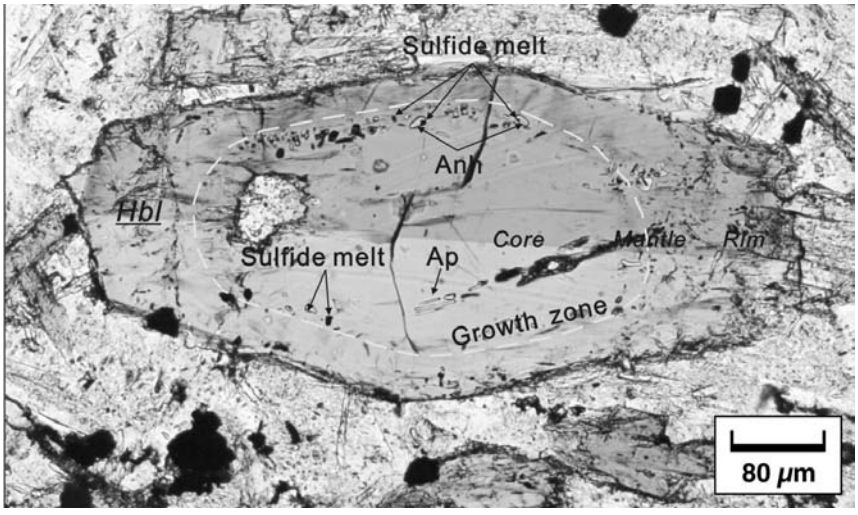

Fig. 4.2-26: Photomicrograph of a hornblende phenocryst showing a Fe-rich core and a Mg-rich rim, plus the presence of numerous inclusions of sulphide melt and anhydrite at the core-rim boundary.

Laser-ablation ICP-MS analysis of individual sulphide melt inclusions in hornblende phenocrysts revealed that their minor to trace element signature is similar to that of the bulk ore in the gold deposit, with most element ratios agreeing within ±0.6 orders of magnitude (Fig. 4.2-27). Exceptions are Au, As and Ni, which in the case of Au and As can be explained by selective metal precipitation from the mineralizing fluids to produce of Au-rich, arsenian pyrite, and in the case of Ni by its preferred incorporation into chlorite-group minerals.

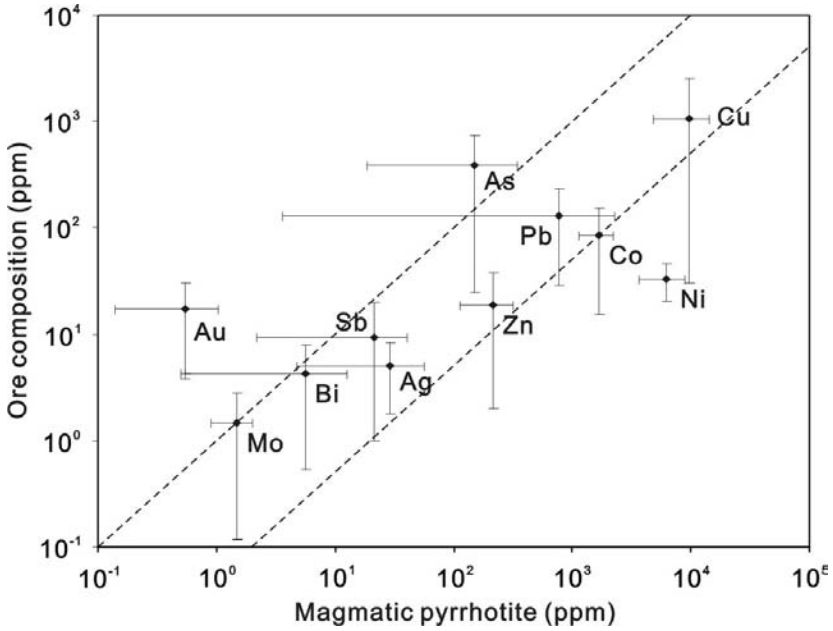

Fig. 4.2-27: Comparison between the trace metal signature of magmatic sulphide inclusions in hornblende phenocrysts of the dolerite dikes and that of bulk ores associated with gold mineralization.

The most convincing evidence for a genetic link between dolerite magmatism and gold mineralization, however, stems from lead isotopic data. Both dolerite whole-rocks and pyrite / pyrrhotite fractions from the gold ore show virtually identical lead isotopic compositions that are unusually non-radiogenic and lie to the left of the Geochron and above the MORB-source mantle Pb isotopic evolution line (Fig. 4.2-28).

In summary, this study provides strong evidence that the metals in the Guocheng Au deposit and in other gold deposits of the Jiaodong peninsula were provided by magmatic-hydrothermal fluids derived from sulfur-rich, mafic alkaline magmas that were produced by partial melting of lithospheric mantle that was metasomatized during the Paleoproterozoic by subduction-related fluids. This model has been substantiated by Li *et al.* (2012, EPSL 349-350: 26-37) who demonstrate a similar genesis for Au mineralization at the southern margin of the North China Carton, and it shares many similarities with recent models of porphyry-type ore formation.

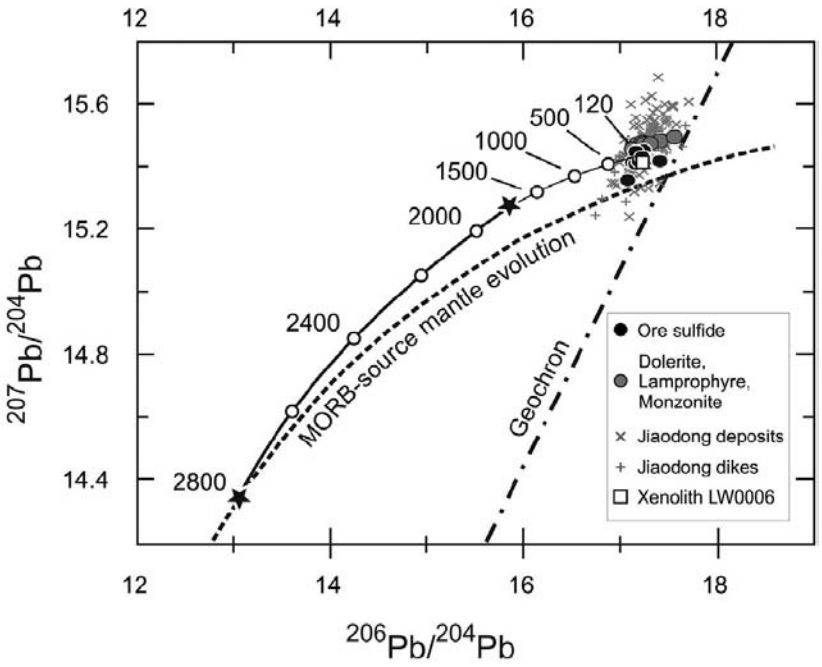

Fig. 4.2-28: $^{207}Pb/^{204}Pb$ vs. $^{206}Pb/^{204}Pb$ diagram showing the isotopic composition of ore sulphides (black dots) and mafic alkaline dikes (grey dots) at Guocheng, plus that of dikes and sulphides associated with other Au deposits in the Jiaodong peninsula (vertical and diagonal crosses, respectively). Also shown are the Geochron, the MORB-source mantle evolution line, and a three-stage evolution model involving the formation of juvenile crust at ca. 2.8 Ga, subduction of this crust and associated fluid metasomatism of the overlying lithospheric mantle by a fluid with drastically reduced U/Pb at ca. 1.85 Ga, and partial melting of this lithospheric mantle at ca. 120 Ma.

r. *The origin and enrichment of molybdenum in porphyry Mo deposits (L. Lerchbaumer and A. Audétat)*

To better understand the factors leading to porphyry Mo mineralization we have studied melt and fluid inclusions in two sub-economically Mo-mineralized granites in well-known Mo provinces: the Treasure Mountain Dome in the Colorado Mineral Belt (USA), and the Drammen granite in the Oslo Rift (Norway). Melt and fluid inclusions were investigated in samples ranging from coarsely crystallized whole rocks to euhedral quartz crystals within miarolitic cavities. The major and trace element chemistry of individual inclusions was determined by laser-ablation ICP-MS. Melt inclusions are rhyolitic in composition and record a clear trend of increasing Mo concentration with increasing degree of melt differentiation which was monitored by Cs, extending from ~ 5-10 ppm Mo at 5 ppm Cs to ~ 17-40 ppm Mo at 100 ppm Cs. Coexisting magmatic fluids were single-phase, had a salinity of 4-6 wt.% $NaCl_{equiv}$, a density of 0.6-0.7 g/cm^3 and contained ~ 0.5 wt.% S and up to 6 mol.% CO_2. Molybdenum concentrations in these fluids ranged from ~ 20 ppm to ~ 200 ppm Mo, except for some fluids that exsolved from highly fractionated melts, which had lower Mo contents due to precipitation of molybdenite.

Comparison of our data with published fluid and melt inclusion data from other porphyry Mo deposits and barren intrusions reveals that there are no systematic differences in the metal content of fluids and melts from barren versus productive intrusions (Figs. 4.2-29, 4.2-30). This suggests that the mineralization potential is not simply a function of the amount of Mo dissolved in melts and fluids, but rather is controlled by other factors such as the size of the magma chambers and the extraction efficiency of fractionated melts and fluids from the magma and their focusing into small apophyses. Based on our data it can be calculated that magma volumes of at least several tens of km^3 are required to form intermediate-sized Mo deposits, and at least several hundred km^3 to form giant (≥1Mt Mo) deposits.

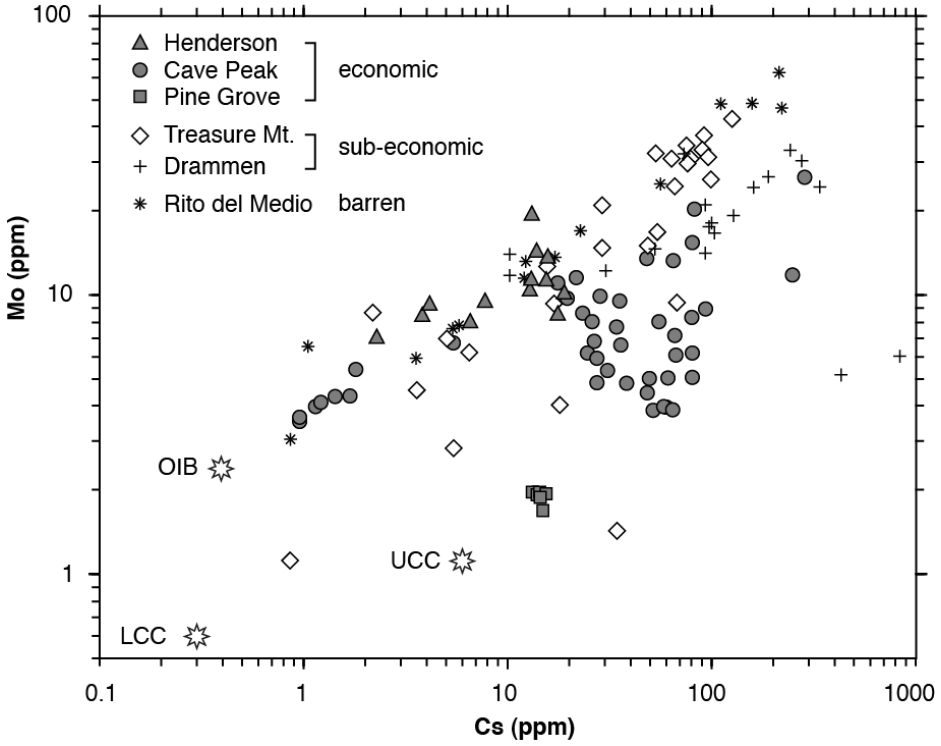

Fig. 4.2-29: Concentrations of Mo and Cs in melt inclusions analyzed from Mo-mineralized and barren intrusions. There is no correlation between the Mo contents and extent of mineralization. Notice also that most data points lie on trends that project towards the composition of ocean island basalts (OIB) rather than towards that of average upper (UCC) or lower (LCC) continental crust, which suggests that Mo may have been derived from the mantle.

Although the two granites investigated in this study would have been large enough to produce at least intermediate-sized Mo deposits they are only sub-economically mineralized. Their low productivity appears to be the result of poor fluid focusing. Factors that promote fluid focusing include: (i) accumulation of major volumes of fractionated, crystal-poor melts at the top of the magma chamber, (ii) formation of apophyses, and (iii) the development of convection cells allowing efficient circulation of fractionated melts (+ fluids exsolving

thereof) through these apophyses. None of these mechanisms have operated to significant extents in the Treasure Mountain Dome and the Drammen Granite.

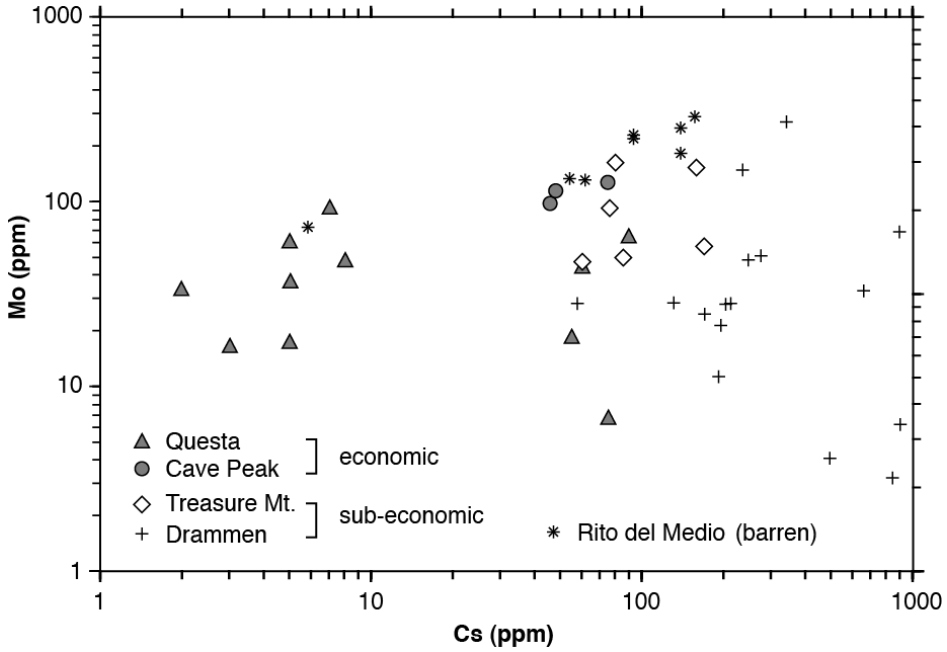

Fig. 4.2-30: Concentrations of Mo and Cs in intermediate-density fluid inclusions analyzed from Mo-mineralized and barren intrusions. Again, there is no obvious correlation between Mo content and extent of mineralization, with some fluids analyzed from the barren Rito del Medio Pluton containing similar to even higher Mo concentrations than those analyzed from economically mineralized intrusions.

4.3 Mineralogy, Crystal Chemistry and Phase Transitions

The behaviour of crystal and melt structure can change with pressure and temperature, but it can also be influenced by oxygen fugacity and chemical composition. Research continues to improve our understanding of the processes that control the dynamics of the Earth's interior and the physical properties of materials. This chapter focuses on recent efforts to elucidate the behaviour of different materials, classified into four topics: *crystal structure, electronic structure, compression behaviour,* and *phase stability*.

The first eight contributions focus on *crystal structure* and its relation to chemical and physical properties. Single-crystal X-ray diffraction studies of lower mantle silicate perovskite using a diamond anvil cell (DAC) coupled with a portable double-sided laser-heating system at synchrotron facilities show no iron spin crossover arising from chemical exchange reactions between the A- and the B-sites. A similar methodological approach using $CaIrO_3$ as an analogue for $MgSiO_3$ post-perovskite reveals puzzling features during compression that may be relevant for elucidating its compression mechanism. Raman spectroscopy coupled to a DAC is also a powerful method to detect structural changes with pressure, and has been applied to study carbonates from the $MgCO_3$ and $FeCO_3$ solid solution in order to understand their likely fate in the lower mantle. A similar study on the majorite-knorringite solid solution reports an important breakthrough in elucidating its crystallochemical characteristics. The next four contributions focus on analytical electron microscopy studies of ringwoodite, hibonite, meteoritic diamond and large $MgSiO_3$ perovskite single crystals. The distribution of iron in ringwoodite in the Mg_2SiO_4-Fe_2SiO_4 system studied using the TEM-ALCHEMI technique reveals site distributions, and the determination of valence state and the site occupancy of titanium in hibonite provide useful constraints on the oxygen fugacity during solar nebula condensation. The origin of diamond in ureilites is likely due to a chemical vapour deposition process, and a low density of dislocations in single crystals of $MgSiO_3$ perovskite determined using weak-beam dark-field TEM imaging techniques reveals that the crystals are ideal for deformation studies.

The physical properties of melts in the Earth's mantle and outer core can fundamentally influence the chemical and thermal evolution of the Earth. Some of these properties are assessed through *electronic structure*, where experimental and theoretical approaches address the iron spin state in silicate glass and electronic transport properties of liquid aluminium under extreme conditions. The spin state of iron can be affected by densification of silicate melt with pressure, but no evidence of spin crossover from high spin to low spin was found in iron-bearing silicate glass up to 84 GPa. In a second contribution, liquid aluminium is adequately described as a free electron metal under extreme conditions, which means that it can be used for case studies of electronic transport properties.

Pressure is an important variable not only for geosciences, but also in applied material sciences. In the topic *compression behaviour*, two studies examine the remarkable effect of

pressure on materials including a simple SiO_2 glass and a complex zeolite-like mineral using *in situ* X-ray diffraction and ultrasonic interferometry techniques. The behaviour of the hydroxyl species in mantle minerals is investigated in a study on OH-bearing $MgSiO_3$ akimotoite that shows a significant change in physical properties with hydration, and in a study on wadsleyite and ringwoodite at high pressure and high temperature using *in situ* infrared spectroscopy focused on water speciation under mantle conditions.

Phase transformation is one of most drastic responses of a crystal structure to pressure, and almost all materials are affected in some critical range of pressure and temperature. In the final topic *phase stability*, two contributions report the phase relations of a new iron oxide phase, Fe_4O_5, at high pressure and high temperature based on electron microscopy and in-house and synchrotron X-ray diffraction techniques. Finally, Raman spectroscopy of a pressure-induced transition in coesite provides constraints on complex silica polymorphism and amorphisation processes.

a. *Single crystal X-ray diffraction of Fe,Al-rich magnesium silicate perovskite in a double-sided laser heated DAC (I. Kupenko and L.S. Dubrovinsky; N.A. Dubrovinskaia/Bayreuth; K. Glazyrin, E. Bykova, T. Boffa Ballaran and R. Sinmyo; M. Hanfland and W.A. Crichton/ Grenoble; M. Merlini/Milan)*

Iron- and aluminium-bearing magnesium silicate perovskite $(Mg,Fe,Si,Al)O_3$ is likely the main component of the Earth's lower mantle. Iron and aluminium may significantly affect the properties of magnesium silicate perovskite, especially due to electronic transitions in Fe^{2+} and Fe^{3+}. Recent single crystal diffraction studies reveal that ferrous and ferric magnesium silicate perovskites do not demonstrate any sign of irregular changes in the behaviour of the molar volume, lattice parameters, and mean bond distances of the $(Si,Al)O_6$ octahedra and $(Mg,Fe)O_8$-polyhedra which could be related to the high-spin – low-spin (HS-LS) crossover. A recent study suggested that spin crossover could be favoured at high temperatures and pressures above ~ 40 GPa by the reaction $Fe^{3+(HS)}{}_A+Al^{3+}{}_B \rightarrow Fe^{3+(LS)}{}_B+Al^{3+}{}_A$ (where subscripts "A" and "B" denote the corresponding positions in the perovskite structure). However a subsequent study by our group (BGI Annual Report 2011) did not find evidence of such a process for Fe^{3+}- and Al^{3+}-rich compositions ($Fe^{3+}/\Sigma Fe>0.9$, $Al^{3+}\sim0.4$). In order to check if such a site exchange would take place in magnesium silicate perovskite with moderate aluminium and ferric iron content, we employed a portable double-sided laser heating system (Fig. 4.3-1) at beamline ID09a at the ESRF.

Single crystals of $(Mg_{0.87}Fe^{3+}{}_{0.09}Fe^{2+}{}_{0.04})(Si_{0.89}Al_{0.11})O_3$ perovskite (the crystal chemical formula is based on results of electron microprobe analysis and Mössbauer spectroscopy) were synthesized in a multianvil apparatus. A crystal with dimensions of ~ 0.015 × 0.010 × 0.010 mm^3 was loaded along with Ne as a pressure-transmitting medium into a pressure chamber made from a Re gasket (with an initial diameter of 100 μm and a height of about 30

μm) and compressed using a symmetric piston-cylinder type DAC equipped with ALMAX-type diamonds (80° opening and 250 μm culets). Diffraction data were collected with radiation of wavelength 0.4149 Å, beam size 10 × 10 μm^2, and a crystal-to-detector distance of about 399 mm using a MAR555 Flatpanel detector. A total of 96 frames in the omega scanning range of -28 - +20 degrees were collected (0.5° scanning step size) with an exposure time of 1 s. At each pressure-temperature point, data were collected at two different positions of the DAC that varied by 90° along the compression direction, and the datasets were merged. The data were processed using Crysalis software (Oxford Diffraction 2006 Crysalis RED, version 1.171.31.8. Oxford Diffraction Ltd., Abingdon, Oxfordshire). Crystal structure refinements of integrated intensities were carried out with the SHELXL-97 WinGX version.

We collected diffraction data at pressures between 65 and 78 GPa (where pressure was determined from the Ne thermal equation of state) in several sets, namely before, during and after laser heating at 1750(50) K. For each *P*, *T* data point we obtained between 105 and 125 unique reflections. In addition to the atomic coordinates and isotropic thermal parameters, we refined the occupancy of the B-site by Si and Fe (Si and Al are not distinguishable), and that of the A-site by Mg and Fe. Structural refinements on the integrated intensities converged with values of the R-factor below 5 %. We found that (a) the refined amount of iron in the A-site coincides, within uncertainty, with the value determined by microprobe data, (b) laser heating does not affect the chemical composition of the magnesium silicate perovskite in our experiments, and (c) high temperature does not promote any chemical exchange reactions between the A- and B-sites (*i.e.*, there is no evidence that Fe enters the B-site during heating). It should be mentioned that homogeneous heating is a critical parameter suppressing undesirable diffusion and formation of chemical inhomogeneities. Our results are in full agreement with our previous results obtained from magnesium silicate perovskite of another composition.

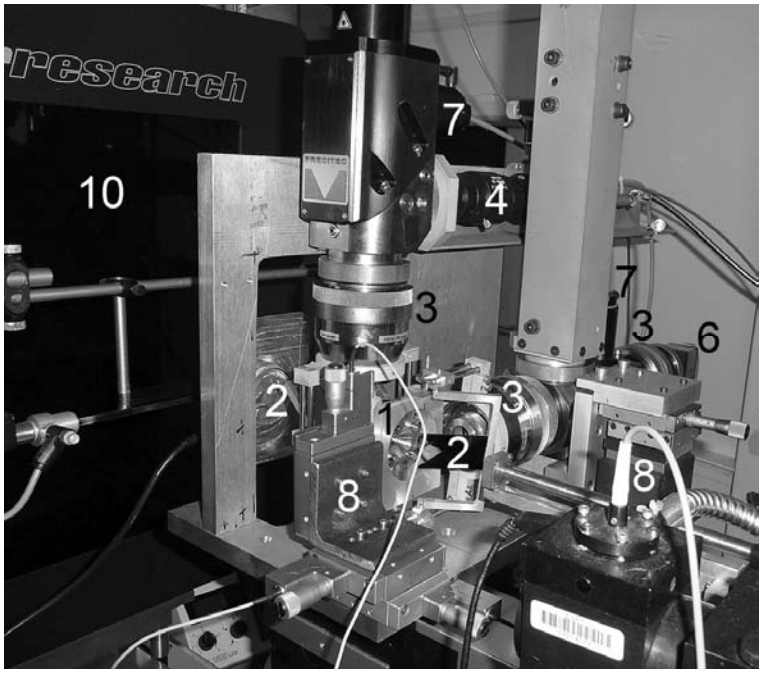

Fig. 4.3-1: Photograph of the double-sided portable laser-heating system mounted for experiments at ESRF beamline ID09a. 1: holder with DAC; 2: carbon mirrors; 3: focusing optics; 4: π-shaper; 5: beam-splitter cube; 6: CCD camera; 7: LED; 8: 3-axis translation stages; 9: adjustable screws for spectrometer focusing; 10: MAR555 CCD detector.

b. *High-pressure structural behaviour of $CaIrO_3$ perovskite (T. Boffa Ballaran and K. Kularatne, in collaboration with R.G. Trønnes/Oslo)*

The two known polymorphs of $CaIrO_3$ are isostructural analogues for $MgSiO_3$ perovskite and post-perovskite which are likely the dominant phases of the Earth's lower mantle and deep lower mantle, respectively. For this reason $CaIrO_3$ compounds have been the focus of many studies in the last decade. The structure of the $CaIrO_3$ phase stable at ambient conditions has been known since the late 1960s and it was renamed subsequently as the post-perovskite structure, at least in the geoscience community. This compound transforms at pressures above 2 GPa and temperatures above 1350 °C to an orthorhombic perovskite structure whose atomic positions are still unknown. However without a correct knowledge of the atomic structure and its response to changes in pressure and temperature it is difficult to assess to what degree $CaIrO_3$ compounds can be used as analogues of lower mantle phases. The aim of this study is therefore to obtain single-crystal structural data of $CaIrO_3$ both at ambient conditions and at high pressure and to compare them with high-pressure structural data of $MgSiO_3$ perovskite.

Single crystals of $CaIrO_3$ perovskite were selected from the same run product obtained using a piston cylinder apparatus at 1525 °C and 2.5 GPa with a starting material of a mixture of high-purity $CaCO_3$ and IrO_2 decarbonated and sintered at 900-950 °C. A single-crystal of 0.06 x 0.08 x 0.09 mm was measured using an Xcalibur diffractometer (Oxford Diffraction) operating with MoKα radiation at 50 kV and 40 mA and a CCD detector. The crystal to detector distance was 45 mm. Combined *omega* and *phi* scans were chosen to obtain a coverage of a full reciprocal sphere up to $2\theta_{max} = 73°$ with high redundancy in order to better constrain the absorption from the crystal. The exposure time was 12 s per frame. Structural refinements were performed using the program SHELX97 and converged to a discrepancy factor of 3.9 % for all 568 reflections observed.

The orthorhombic distortion of perovskite derives from the cubic aristotype by tilting of the octahedra around the pseudocubic axes resulting in out-of phase tilting and in-phase tilting angles. The tilting of $CaIrO_3$ perovskite is only slightly larger than that reported for $MgSiO_3$ perovskite, however the octahedral site is much more distorted since all Ir-O bond distances are very different and the O-Ir-O angles deviate significantly from 90°.

A puzzling feature of the $CaIrO_3$ perovskite structure is that the octahedra are shortened along the *c*-axis, therefore one would expect this axis to be the least compressible. However, this is not the case since it has been reported that $\beta_a > \beta_c > \beta_b$. Moreover the behaviour of $CaIrO_3$ perovskite clearly deviates from the relationship between bulk moduli and molar volume reported in the literature for Ca-oxide perovskites (Fig. 4.3-2). Its larger incompressibility may be a result of the octahedral tilting approaching some limiting value, given that the tilting angles are already quite large at ambient conditions. Since it is generally accepted that the dominant compression mechanism of orthorhombic perovskites is volume reduction via tilting of relative rigid octahedra, a high-pressure structural study is obviously necessary to clarify this peculiar incompressibility.

The same single crystal used for structural analysis was polished down to 20 μm thickness, resulting in a smaller crystal of dimensions 0.05 x 0.05 x 0.02 mm preserving the original good quality. This smaller crystal was introduced into a diamond anvil cell together with a ruby for pressure determination and Ne as pressure transmitting medium. Intensity data collection are planned at different pressures up to 15-20 GPa and structural data are expected to shed light on the compression mechanism of $CaIrO_3$ perovskite.

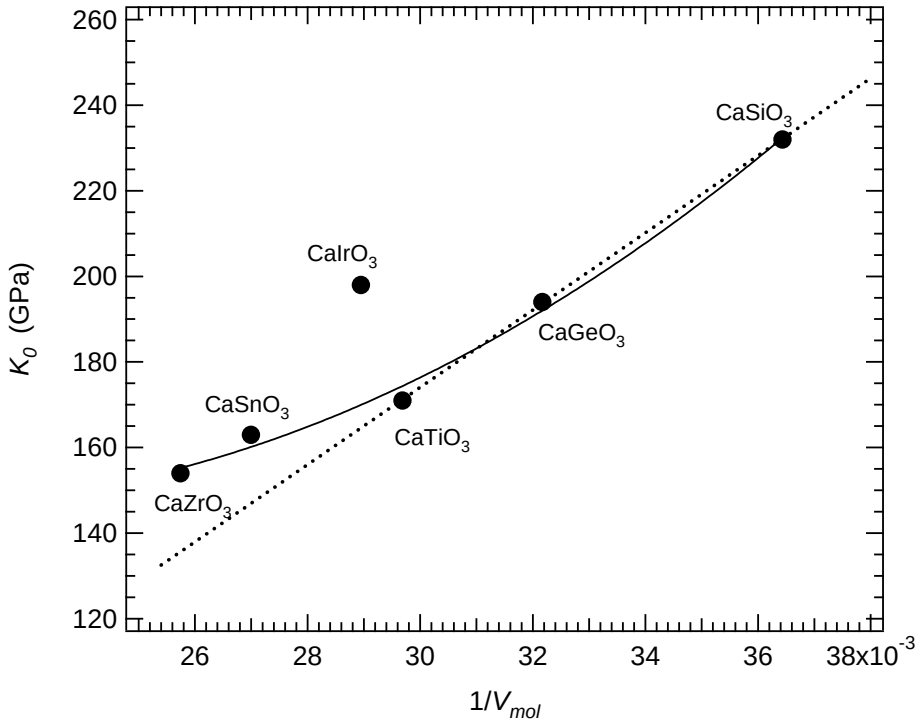

Fig. 4.3-2: Variation of the isothermal bulk moduli of Ca-oxide perovskites reported in the literature with inverse molar volume. Symbols are larger than the uncertainties.

c. *High-pressure Raman study of carbonates from the $MgCO_3$ and $FeCO_3$ solid solution (A.V. Spivak, E.S. Zakharchenko and Yu.A. Litvin/Chernogolovka; N.A. Solopova, E. Bykova and L.S. Dubrovinsky)*

There is growing mineralogical and experimental evidence that carbonates may be stable at conditions of the Earth's lower mantle. Information on carbonate transformations at the pressure-temperature conditions of the transition zone and lower mantle is therefore important for understanding their behaviour in the Earth's deep interior. Fe^{2+} and Mg^{2+} substitution is common in mineral systems, and Fe^{2+} and Mg^{2+} form a complete solid solution in the $FeCO_3$-$MgCO_3$ system. In this work we characterized the behaviour of different members of the Mg-Fe carbonate solid solution by means of Raman spectroscopy at high pressure and ambient temperature.

Samples of $Mg_{1-x}Fe_xCO_3$ with different composition (x=0.05, 0.09, 0.2, 0.5) were synthesized using a multianvil apparatus at 18 GPa and 2000 °C. High-pressure spectroscopic experiments were carried out in a diamond anvil cell. The LabRam system (Horiba Sceintific Inc.) with a He-Nd-laser (excitation wavelength 632 nm) was used for collection of the Raman spectra.

Magnesite-stuctured carbonates with rhombohedral symmetry have six characteristic vibrational modes in Raman spectra – four modes represent internal vibrations within the $(CO_3)^{2-}$ unit and two modes represent external vibrations of the crystal lattice. We determined positions of the Raman bands and pressure-induced shifts of external modes T (188/213 cm^{-1} for end members siderite/magnesite and 197-210 cm^{-1} for solid solutions with composition $Mg_{0.5}Fe_{0.5}CO_3$-$Mg_{0.95}Fe_{0.05}CO_3$) and L (284/330 cm^{-1} and 301-328 cm^{-1}) and internal modes ν_4 (729/737 cm^{-1} and 730-737 cm^{-1}), ν_1 (1087/1092 cm^{-1} and 1086-1092 cm^{-1}), ν_3 (1425/1442 cm^{-1} and 1427-1442 cm^{-1}), $2\nu_2$ (1724/1759 cm^{-1} and 1733-1758 cm^{-1}) (Fig. 4.3-3). Raman shifts calibrated as a function of Mg or Fe number may be used in turn to evaluate the chemical composition of natural carbonate samples. Apart from Raman bands characteristic for magnesite-type structured materials, we observed an additional Raman peak in the range 868-874 cm^{-1} for solid solutions of composition $Mg_{0.5}Fe_{0.5}CO_3$-$Mg_{0.95}Fe_{0.05}CO_3$. A similar peak was observed at 870 cm^{-1} for siderite and described in the literature as an additional peak that was not predicted by factor group analyses. This peak was explained in the literature to arise from an infrared mode becoming Raman active due to a local loss of inversion symmetry as a result of Fe ordering.

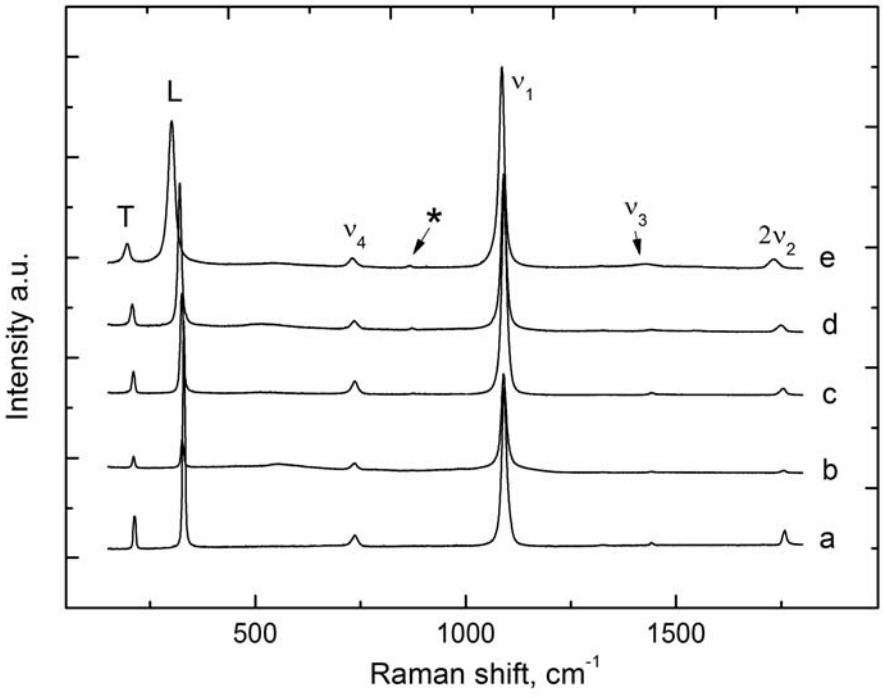

Fig. 4.3-3: Raman spectra of carbonates: (a) magnesite; (b) $Mg_{0.95}Fe_{0.05}CO_3$; (c) $Mg_{0.91}Fe_{0.09}CO_3$; (d) $Mg_{0.8}Fe_{0.2}CO_3$; (e) $Mg_{0.5}Fe_{0.5}CO_3$. Peaks are assigned to external vibrations (L, T), internal vibrations (ν_1-ν_4), and an additional band (*).

At high pressure in our Raman study we observed and followed the behaviour of four modes of carbonates with the following compositions: $Mg_{0.5}Fe_{0.5}CO_3$, $Mg_{0.8}Fe_{0.2}CO_3$, $Mg_{0.91}Fe_{0.09}CO_3$ and $Mg_{0.95}Fe_{0.05}CO_3$. Our high pressure Raman spectra show that the frequency of the ν_1 mode of all studied carbonates increases monotonically up to 40-42 GPa, where an additional peak appeared at 1220 cm^{-1}. The position of the internal mode ν_4 increases monotonically in all cases. The frequency of external modes T and L of $Mg_{0.91}Fe_{0.9}CO_3$ increase linearly up to 46 GPa, with a change in slope above this pressure. For all carbonates with intermediate compositions we observed additional peaks in the range 868-874 cm^{-1} at 0 GPa (Fig. 4.3-4). This peak was not detectable in diamond anvil cell experiments at low pressures, but become visible above 30 GPa and then its frequency increased monotonically with increasing pressure.

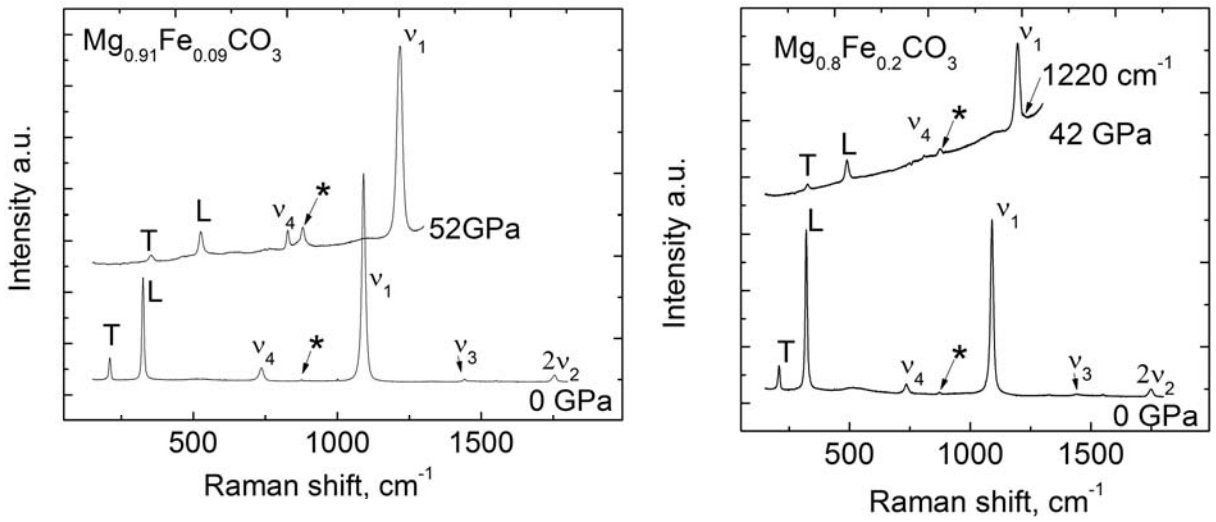

Fig. 4.3-4: Raman spectra of $Mg_{0.91}Fe_{0.09}CO_3$ and $Mg_{0.8}Fe_{0.2}CO_3$ at ambient conditions and high pressure. Peaks are labelled as in Fig. 4.3-3.

d. *Synthesis of knorringite $Mg_3Cr_2Si_3O_{12}$, single-crystal X-ray diffraction, and Raman spectroscopy (A.V. Bobrov and E.A. Sirotkina/Moscow; E. Bykova, L.S. Dubrovinsky and S.V. Ovsyannikov; Yu.A. Litvin/Chernogolovka)*

Garnets are widely abundant as inclusions in diamonds and those of the ultrabasic paragenesis are characterised by significant chromium admixture in the knorringite ($Mg_3Cr_2Si_3O_{12}$, *Knr*) end-member. It was established that incorporation of knorringite in garnet occurred from 3 GPa (beyond the diamond depth facies), and the concentration of chromium reached significant values (5-10 wt.% Cr_2O_3 and more) in the range of stability of most natural diamonds (4-7 GPa), which is an indicative feature of diamondiferous dunite-harzburgite paragenesis of the lithospheric mantle. Incorporation of a majoritic component ($Mg_4Si_4O_{12}$, *Maj*) is another important peculiarity of mantle garnets.

Garnets of majorite-knorringite composition were synthesised in multianvil experiments performed at 12-16 GPa and 1400-1600 °C. The starting compositions $Knr_{100}Maj_0$ and $Knr_{50}Maj_{50}$ (mol.%) were studied in the system MgO-SiO_2-Cr_2O_3 at 16 GPa and 1600 °C. The main phases obtained in multianvil experiments are garnet of majorite–knorringite composition and eskolaite (Fig. 4.3-5). The synthesized garnets contain from 15 to 25 mol.% majoritic component. It is typical that even for the starting composition of pure knorringite $Mg_3Cr_2Si_3O_{12}$, we obtained a garnet solid solution containing 15 mol.% $Mg_4Si_4O_{12}$, which reflects the more significant influence of pressure on the formation of majorite compared to knorringite.

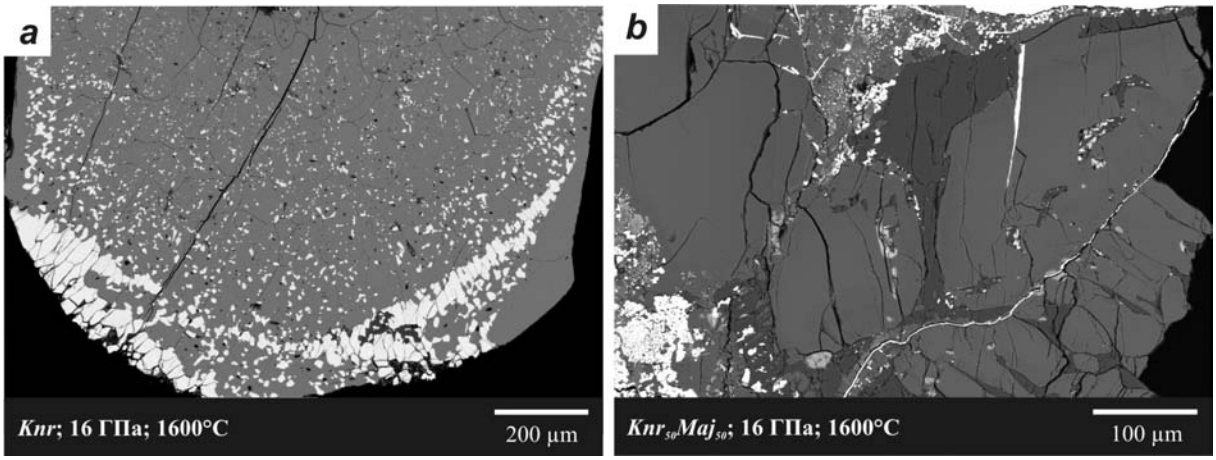

Fig. 4.3-5: Back-scattered images of textural features of experimental samples obtained from multianvil experiments in the system MgO–SiO_2–Cr_2O_3 at 16 GPa and 1600 °C for the starting composition $Mg_3Cr_2Si_3O_{12}$ (H3420, *a*) and $Knr_{50}Maj_{50}$ (H3421, *b*). We observe large knorringite grains (gray) and small grains of eskolaite (white) in the groundmass.

It should be noted that garnet monocrystals with such a high proportion of knorringite component have not been previously synthesised in experiments, which has not allowed reliable crystallochemical characteristics of knorringite to be obtained. In our study the synthesised knorringite-rich garnet crystal was investigated by single-crystal X-ray diffraction for the first time. We established its cubic symmetry with space group *Ia*-3*d* and cell parameters a = 11.5718(1) Å, V= 1549.54(2) $Å^3$.

Fig. 4.3-6 illustrates the Raman spectra of synthesized garnets compared to data for pure pyrope and majorite. Since the data for Raman spectra are not available for pure knorringite, the morphology of spectra of garnets obtained from the starting compositions $Knr_{50}Maj_{50}$ (H3421) and $Knr_{100}Maj_0$ (H3420) may be analysed by their mutual comparison, as well as by comparison with the spectra of pyrope and majorite. As garnet from sample H3421 contains a higher portion of majoritic component (25 mol.%) compared to garnet from sample H3420

(15 mol.%), we suggest that the peaks at 625 cm^{-1} for H3421 and 624 cm^{-1} for H3420 correspond to the spectrum of majorite. The same is evident for the peaks in the range 937-943 cm^{-1}. Garnets (H3420 and H3421) synthesised at 12-16 GPa are represented by the majorite–knorringite solid solution and consequently all other peaks correspond to knorringite.

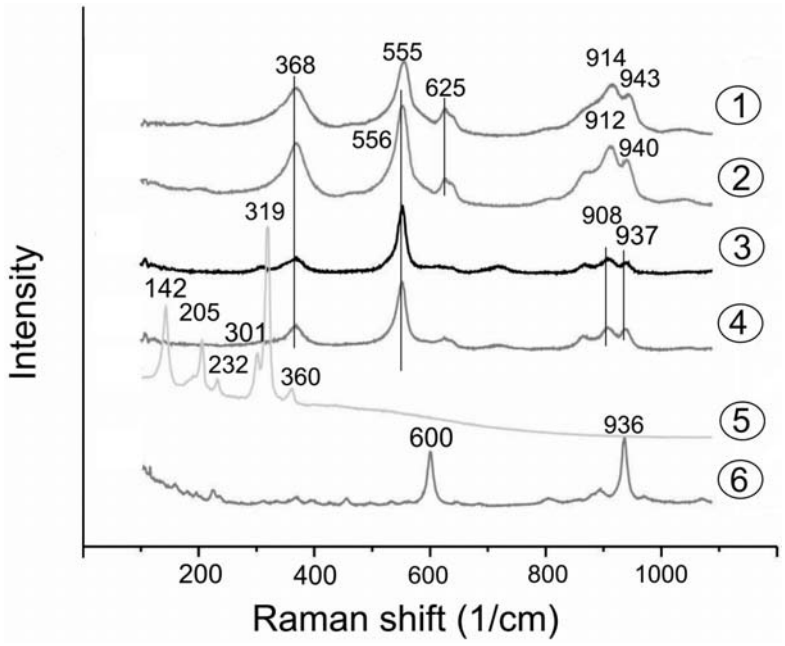

Fig. 4.3-6: Raman spectra of garnets with majorite–knorringite composition synthesised in runs H3421 (1, 2) and H3420 (3, 4) at 16 GPa compared to the spectra of pyrope (5) and majorite (6).

e. *Site-specific energy dispersive X-ray analysis of ringwoodite in the Mg_2SiO_4-Fe_2SiO_4 system. The TEM-ALCHEMI determination of site-occupancies of Fe (K. Kularatne and N. Miyajima)*

X-ray diffraction and neutron diffraction techniques are the most widely used methods for determination of site occupancy of atoms in crystals. However, with these methods it is difficult to analyse elements present in small concentrations, or when atoms have similar scattering amplitudes. In these conditions, the determination of site occupancy of atoms can be performed more precisely using transmission electron microscopy. The ALCHEMI-Technique (Atom Location by CHaneling Enhances MIcro analysis) is a powerful technique for the determination of site occupancies of atoms in crystal structures. Particularly for high-temperature and high-pressure studies, it can be used to obtain the valance state of multi-valence ions and the site occupancy of such ions in the mineral structure (*e.g.*, magnesium silicate perovskite). The distribution of Fe in ringwoodite, which is a major mantle mineral phase in the Mg_2SiO_4-Fe_2SiO_4 system, can be studied using the TEM-ALCHEMI technique with higher accuracy compared to other methods.

Ringwoodite synthesised at 21 GPa and 1500 °C in a conventional multianvil press using natural enstatite ($MgSiO_3$) crystals with Mg number of 0.87 and from synthetic glass of enstatite-ferrosilite solid solution series with a Mg number of 0.7 ($Mg_{0.7}Fe_{0.3}SiO_3$) displays a strong channelling effect (*i.e.*, variations of the R-ratio described below) under positive and negative excitations with diffraction spot, $\boldsymbol{g}$ = 400. The TEM-EELS results show that Fe in the ringwoodite structure is almost exclusively in the 2+ oxidation state. The s = 0 diffraction condition refers to the Bragg condition of $\boldsymbol{g}$ = 400 and this is obtained by co-excitations of un-diffracted (000) and (400) diffraction spots. Therefore the Kikuchi band will fall along the (000) and (400) diffraction spots. The s > 0 diffraction condition is obtained by irradiating the (000) and (800) diffraction spots, so that the Kikuchi band will lie on the outside of the (400) diffraction spot (Fig. 4.3-7).

The variation between channelling and non-channelling spectra provides direct information about the cation distribution within the particular structure. Figure 4.3-8 shows the differences between the three spectra corresponding to three distinct diffraction conditions: s = 0, s < 0 and s > 0. In ringwoodite (normal spinel structure) Fe can occupy either the Si site or the Mg site. Excitation of octahedral sites (Mg site) is denoted by the s > 0 diffraction condition, while excitation of tetrahedral sites (Si site) refers to the s < 0 condition. Therefore, at the s > 0 diffraction condition the emission of characteristic X-rays from the Mg site is enhanced; hence the Mg peak will dominate. If Fe occupies the Mg site, the Fe peak will also be enhanced. Similarly at the s < 0 diffraction condition the emission of characteristic X-rays from the Si site is enhanced and the Si peak will dominate. This variation is clearly visible in the EDX spectra in Fig. 4.3-8. The heights of the spectra are normalised to the Si peak. The variation of the Fe peak with changing diffraction condition is clearly visible in both spectra. It is well displayed in both spectra that, under the s > 0 diffraction condition, incident electrons are interacting selectively on the octahedral site (*i.e.*, electron channelling): the Fe peak increases simultaneously with the Mg peak. This variation of the Fe peak with the Mg peak indicates that both Mg and Fe occupy the octahedral sites in the ringwoodite structure.

From Table 4.3-1 it can be seen that R(Fe/Si) > R(Fe/Mg) ≈ 1, and R(Fe/Si) is roughly in the range 2 to 3. Following the definition of the R value, the results indicate that Mg has the strongest octahedral preference and Si has the strongest tetrahedral preference. Therefore most or nearly all of the Fe is on the octahedral site. The value of R(Al/Mg) for $MgAl_2O_4$ which is known to be normal spinel, *i.e.*, all Al atoms are on the octahedral site and all Mg atoms are on the tetrahedral site, were also observed in a previous study reported in the literature to be between 2 and 3 under the same excitation condition with $\boldsymbol{g}$ = 400. In conclusion, the distribution of cations in ringwoodite in the Mg_2SiO_4-Fe_2SiO_4 system can be studied with the TEM-ALCHEMI technique with reasonable accuracy, because ringwoodite displays a strong channelling effect (*i.e.*, variation of the R-ratios) under positive and negative excitations with diffraction spot, $\boldsymbol{g}$ = 400, which is consistent with the results for $MgAl_2O_4$ spinel.

Table 4.3-1: R(Fe/X) values for different EDX measurements in ringwoodite.

EDX spectra	R(Fe/Mg)	R(Fe/Si)
90812-5&6	1.06	2.75
80812-4&5	1.16	3.21
220812-2&4	1.12	2.14
270812-7&11	1.15	2.67
290812-1&4	1.06	2.65
290812-2&5	1.24	2.66

Note: Variation in R(Fe/Si) and R(Fe/Mg) values between measurements may be caused by diffuse scattering out of the Bragg reflections which, as reported in the literature, can reduce the intensity modulation over the crystal unit cell with variations in thickness.

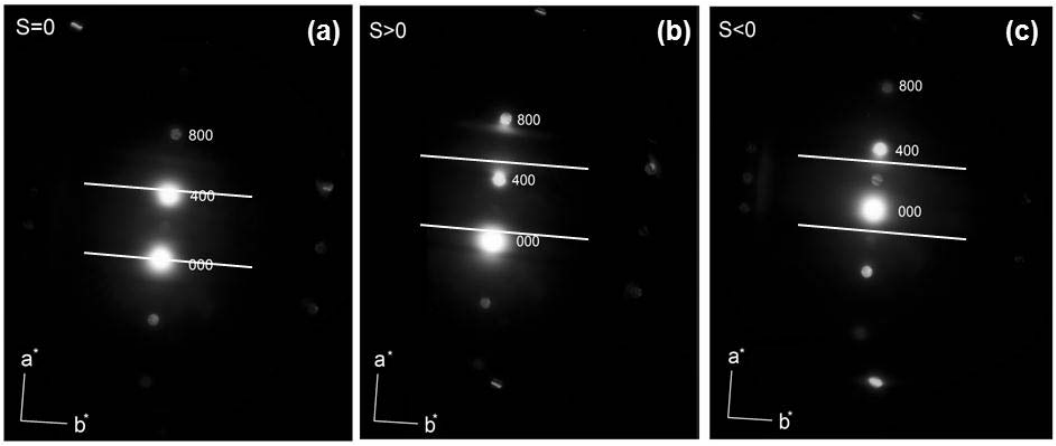

Fig. 4.3-7: Electron diffraction patterns (near the two-beam condition) with (a) s = 0 for the Bragg condition (***g*** = 400) in the systematic diffraction condition along the a_1-axis, (b) positive excitation error s > 0, and (c) negative excitation error s < 0.

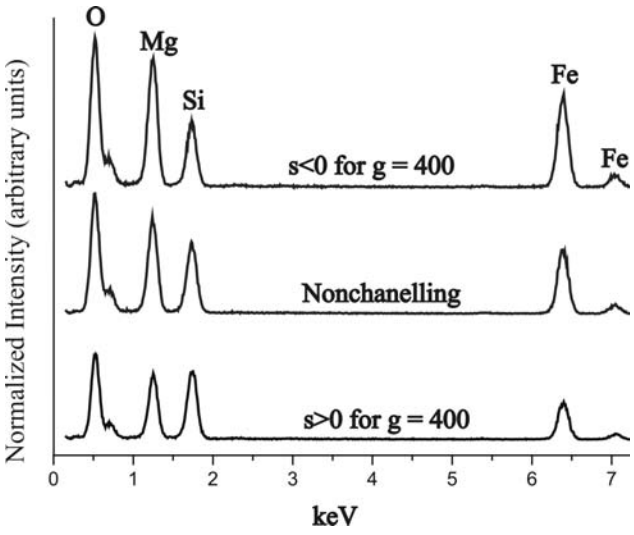

Fig. 4.3-8: EDX spectra of ringwoodite for s < 0 (top), non-channelling (middle), and s > 0 (bottom) conditions.

f. *Synthesis and characterization of Mg,Ti-bearing hibonite (M. Giannini and T. Boffa Ballaran, in collaboration with F. Langenhorst/Jena)*

The oxidation state of titanium in different minerals present in chondritic meteorites, the most primitive matter of our solar system, has attracted considerable attention over the years as the Ti oxidation state could be used to constrain the oxygen fugacity ($f\,O_2$) during solar nebula condensation. The earliest condensates from a hot gas of solar composition are known to be the constituents of Calcium-Aluminium-rich Inclusions (CAIs), in which the most refractory minerals are corundum (Al_2O_3) and hibonite ($CaAl_{12}O_{19}$). Our study is focused on the latter mineral since it can contain significant amount of titanium. Hibonite has a hexagonal structure (space group $P6_3/mmc$) where a sequence of cubic and hexagonal closed-packed oxygen layers create a 12-fold coordination site for Ca and different bypiramidal, octahedral and tetragonal sites for Al and its substituting cations. Studying the cation distribution in hibonite is crucial to better understand and interpret data from other measurements, such as Electron Energy Loss (EELS) and optical spectroscopies.

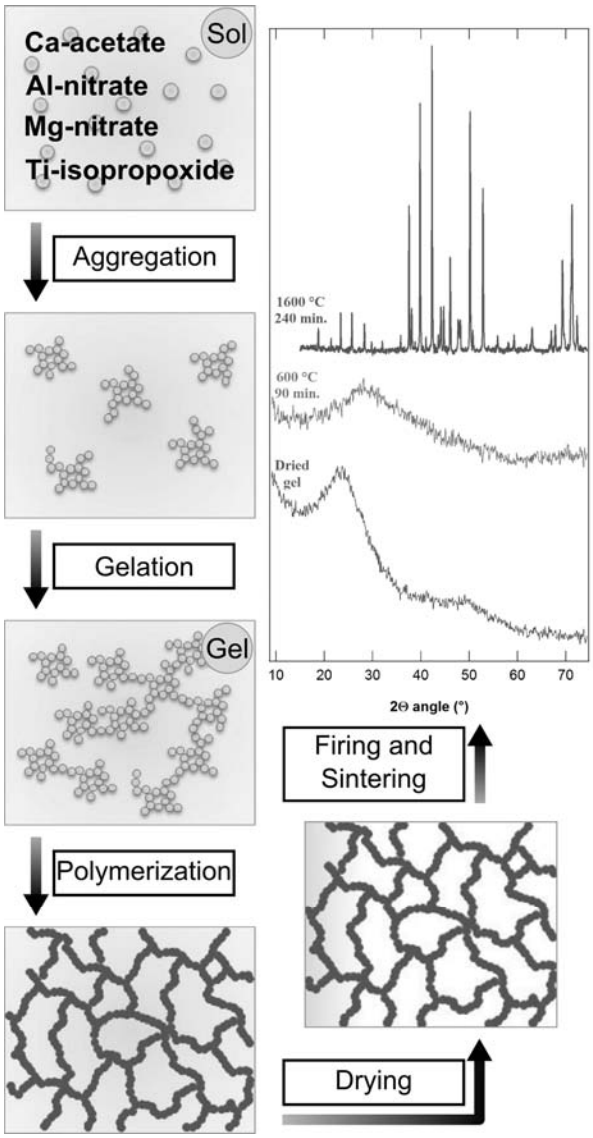

Fig. 4.3-9: Schematic representation of the sol-gel synthesis. X-ray diffraction patterns of different intermediate products are shown.

Synthetic hibonites containing variable amounts of Mg and Ti were prepared at different oxygen fugacities. We have recently adopted a citrate-based sol-gel synthesis which, compared to the ceramic method, yields chemically more homogeneous samples. The initial gel is formed from calcium acetate, aluminium and magnesium nitrates and titanium isopropoxide, dissolved in a solution of citric acid in ethanol and allowed to reflux (~ 80 °C) for 6 h. Subsequent heating at ~ 150 °C promotes polymerisation of the gel to form a resin; further heating up to ~ 600 °C results in removal of all organics giving an amorphous material in which the cations are, ideally, uniformly dispersed on an atomistic scale throughout the sample. Heating this material to temperatures up to 1600 °C both in air and under controlled oxygen fugacities leads to the formation of pure hibonite (Fig. 4.3-9), sometimes even in the form of single crystals up to 80 µm in size. We have characterised these samples by means of Electron Micro Probe Analysis (EMPA), Ti-$L_{3,2}$ EELS and X-ray diffraction.

Structural refinements were carried out on complete diffraction datasets, acquired on an Xcalibur diffractometer equipped with a CCD detector. Fourier maps analysis does not allow a determination of the site distribution of Ti and Mg due to small differences in their scattering factors and low concentrations. However the analysis of M-O bond distances, compared with structural data published in the literature, confirms our previous observation. Titanium appears to be located on two different sites: a trigonally distorted octahedron occurring in face-sharing pairs and a bypiramidal site; magnesium is more likely to sit on a tetrahedral site.

g. *Nature and origin of diamond in Almahata Sitta MS-170 (M. Miyahara and E. Ohtani/Sendai; A. El Goresy; Y.-T. Lin, L. Feng and J.-C. Zhang/Beijing; P. Gillet/Lausanne; T. Nagase, J. Muto and M. Nishijima/Sendai)*

Near Earth Object (NEO) 2008 TC_3 impacted the Earth at north Sudan on October 7th, 2008. Its fragments were recovered immediately according to the predicted impacting site and named Almahata Sitta as a meteorite. Almahata Sitta is the first meteorite to be observed and have its trajectory determined before its fall. Almahata Sitta 2008 TC_3 is a polymict asteroid, and consists mainly of coarse-grained and fine-grained ureilite with less abundant chondritic fragments. Ureilite is a clan of achondrites. The ureilitic fragments contain carbonaceous materials such as graphite and diamond. There are three major models for the diamond formation mechanism; *i.e.*, 1) formation from a fluid or melt in the deep interior of an ureilite parent-body, 2) formation through chemical vapour deposition (CVD) and 3) shock-induced transformation of graphite at the moment of planetesimal collision. Currently the shock-induced transformation model is widely accepted although the origin of the diamond in ureilites is a still matter of debate. Most diamond in ureilites is a polycrystalline assemblage, and its polycrystalline grain size ranges up to several micro-meters. However, we found a huge single diamond crystal in the ureilite of Almahata Sitta-170.

The petrological and mineralogical textures of the coarse-grained ureilite were studied with a low-vacuum SEM (Hitachi S-3400N) without carbon coating. Euhedral grains of diamond can be readily recognised in a graphite matrix, and both phases were confirmed with laser micro-Raman spectroscopy. Chemical compositions of the constituent minerals were determined with an EMPA (JEOL JXA-8800M), and some diamond and graphite were observed with a TEM (JEOL JEM-2010). Isotope distribution images were also taken with a NanoSIMS Cameca 50L. Samples for TEM observations and NanoSIMS measurements were prepared by a FIB slicing system (JEOL JEM-9320FIB).

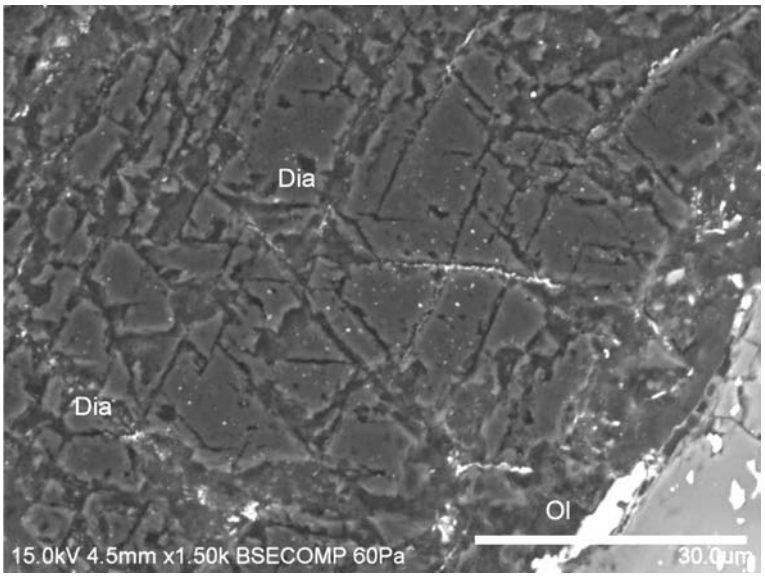

Fig. 4.3-10: BSE image of a huge single diamond (Dia) between olivine (Ol) grains. The original single diamond is divided into several fragments still oriented along fractures at the {001} and/or {111} planes.

The coarse-grained ureilite, Almahata Sitta MS-170 consists mainly of olivine (Fa_{18-21}) and low-Ca pyroxene, with less abundant troilite, kamacite, magnetite, schreibersite (Fe_3P) and diamond-graphite assemblages. Most diamond-graphite assemblages exist in pockets between the olivine grains. The olivine grains adjacent to the diamond-graphite assemblages usually show a reduction texture; *i.e.*, olivine dissociates into enstatite and kamacite. Because of its high hardness, diamond appears above the polished surface, and is easily seen under an optical microscope and with a SEM. The main diamond Raman band stays within a narrow range (1333.7 cm^{-1}, σ = 2.2, n = 15), implying that the diamond is well-crystallised. High-magnification BSE images show that many diamonds have hexahedron- or octahedron-like habits, which correspond to idiomorphic {001} or {111} diamond, respectively, although they are not always idiomorphic. TEM images and EBSD analyses show that most diamonds are single crystals, because several diamond fragments have similar crystallographic orientations. One of the biggest single crystal diamonds that we found is at least ~ 100 μm in dimension (Fig. 4.3-10). We could not find a specific crystallographic orientation between graphite and diamond. The isotope distribution images obtained with a NanoSIMS 50L show

heterogeneous nitrogen abundance and $\delta^{13}C$ among individual diamond grains and even within the same grains. The idiomorphic huge single diamond was not formed from graphite through a martensitic phase transformation mechanism under high-pressure and -temperature conditions induced by a dynamic event. The nitrogen sector zoning texture implies that the diamond grew very slowly. It is likely that the diamond was formed by chemical vapour deposition (CVD) process (or formed from a C-H-O fluid in the deep interior of an ureilite parent-body). Nonetheless, some deformation textures were observed by TEM in the diamonds, which is due to a later dynamic event after primary diamond formation.

h. *Transmission electron microscopy of large $MgSiO_3$ perovskite single crystals (N. Miyajima and T. Katsura)*

Current developments in high-pressure and high-temperature techniques enable us to synthesise large single crystals of $MgSiO_3$ perovskite (MgPv). Large single crystals are necessary for the accurate determination of physical properties, such as elasticity, plasticity and transport properties. In particular, it is important to characterise defect structures of the single crystal for further deformation studies at high pressures and high temperatures (*e.g.*, dislocation recovery experiments). However, a number of obstacles have been encountered in the study of silicate perovskites, owing to their intrinsic instability at low-pressure conditions (*e.g.*, ambient conditions). Here we report defect characterisations of large single crystals of MgPv synthesised at 25 GPa and 1500 °C in a Kawai-type multianvil press following a procedure reported in the literature. We performed optical microscopy and transmission electron microscopy of the recovered single crystal of MgPv.

In TEM sample preparation, a conventional Ar-milling technique was used with and without a liquid-nitrogen cooling stage in a Gatan Dual Ion Mill and a Gatan Precision Ion Polishing System (PIPS), respectively. Conventional TEM observations by bright-field, dark-field and weak-beam dark-field imaging techniques with a liquid nitrogen-cooling holder were performed in a 200 kV-transmission electron microscope (Philips CM20FEG) at Bayerisches Geoinstitut. The defect microtextures can be compared with those of polycrystalline $MgSiO_3$ perovskite and $CaIrO_3$ perovskite analogue.

Polarised light microscopy of a petrological thin section displays low retardation, {110} twins (Fig. 4.3-11) and some mineral inclusions of MgO and ringwoodite, which were later identified by TEM. The electron-transparent foils of the crystalline silicate perovskite were successfully Ar-thinned by both Ar-milling techniques at low temperature and at ambient temperature. The weak-beam dark-field TEM images display a very low density of dislocations and {110} twins. For example, the density of the [010] dislocations with the second shortest Burgers vector, is less than 2×10^{10} m^{-2} (Fig. 4.3-12a) and no dislocation with the other Burgers vectors, $\boldsymbol{b}$ = [100] and [001] were visible with diffraction vectors, $\boldsymbol{g} = h0l$ (Fig. 4.3-12b). The low density of dislocations in the single crystals is ideal for further deformation studies at high pressures and high temperatures (*e.g.*, dislocation recovery). In conclusion, we have demonstrated that we are able to characterise dislocation microstructures

(*i.e.*, type of dislocations and their densities) of MgPv using weak-beam dark-field TEM imaging techniques.

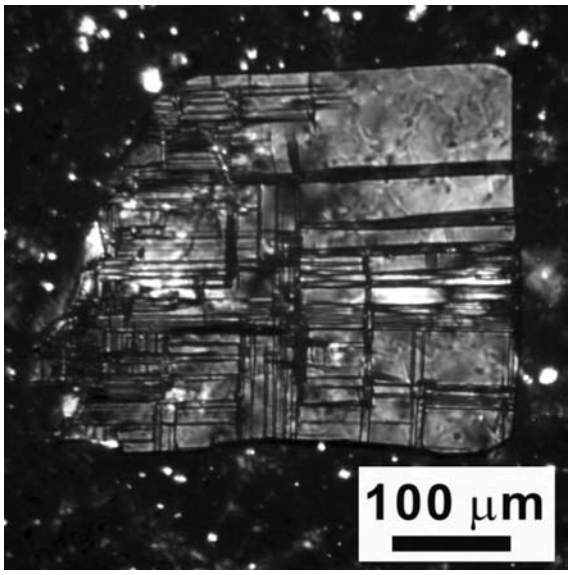

Fig. 4.3-11: Crossed polarised light optical microscopy of single crystals in a petrological thin section with 25 μm thickness. The thin crystal is normal to the [001] direction and displays a low retardation and orthogonal {110} twins.

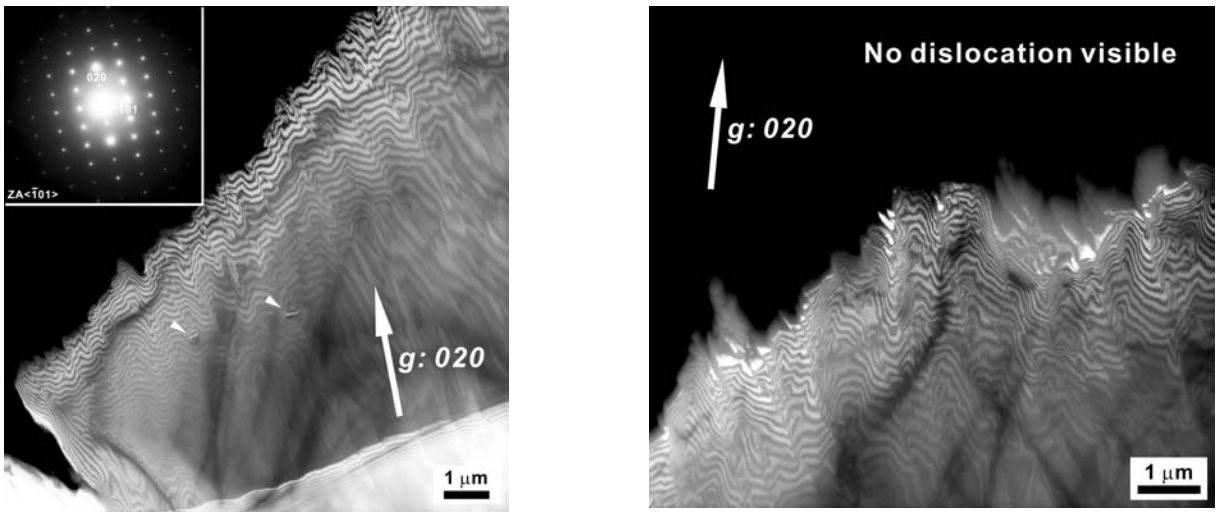

Fig. 4.3-12: Weak-beam dark-field TEM images along the <101> zone axis, indicating that a density of the [010] dislocation (indicated by arrowheads) is further less than 2×10^{10} m^{-2} (*e.g.*, two dislocations within a square area of 10 μm × 10 μm).

i. *Iron spin state in silicate glass at high pressure: Implications for melts in the Earth's lower mantle (C. Prescher, C. Weigel/Montpellier, C. McCammon, O. Narygina/Almelo, V. Potapkin/Grenoble, I. Kupenko, R. Sinmyo, A.I. Chumakov/Grenoble and L.S. Dubrovinsky)*

The physical properties of melts in the Earth's mantle have a fundamental influence on the chemical and thermal evolution of the Earth. Especially the density contrast between solid and

melt is a major factor affecting chemical stratification during an early magma ocean after the moon-forming impact.

In principle there are two mechanisms for melts becoming denser than solids. The first mechanism is by faster densification of the melt network with pressure, *e.g.*, coordination changes occurring in a melt at lower pressure than in the solid, while the second mechanism is by preferential partitioning of heavier elements into the melt. A recent study proposed the second mechanism to occur in the mid part of the lower mantle based on experiments in an olivine composition $(Mg_{0.89}Fe_{0.11})_2SiO_4$. They observed a sharp discontinuity in the pressure dependence of the Fe/Mg solid/melt partition coefficient at 76 GPa, resulting in a strong enrichment of Fe in the melt, which would produce a denser negatively buoyant melt. The sharp discontinuity was explained by an iron spin crossover seen in their X-ray emission spectroscopy (XES) data collected on $(Mg_{0.95}Fe_{0.05})SiO_3$ glass during room temperature compression. However, another recent study reported a much lower degree of iron enrichment in silicate melt based on partitioning experiments at liquidus temperatures on a (Ca,Mg,Al,Si,Fe) oxide glass with chondritic composition, resulting in a melt that would be lighter than the surrounding mantle and hence would segregate upwards.

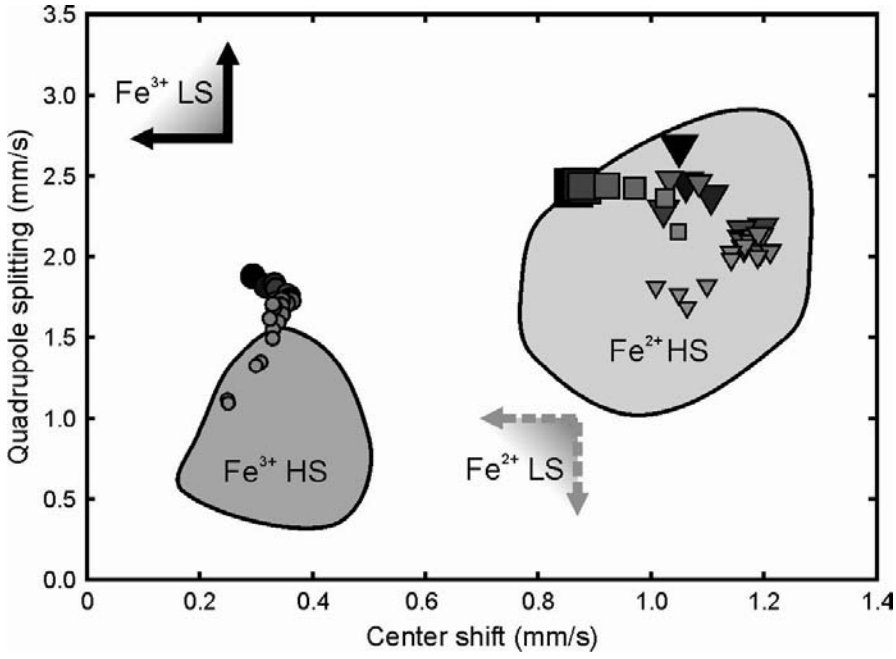

Fig. 4.3-13: Variation of centre shift (CS) and quadrupole splitting (QS) for Fe^{2+} and Fe^{3+} in glasses. Symbols indicate results from this study, where symbol size increases with increasing pressure. The shaded regions indicate values derived from Mössbauer spectra at ambient conditions of HS Fe^{2+} and HS Fe^{3+} in inorganic glasses taken from the literature. Values of ΔCS and ΔQS during HS to LS transitions were taken from the literature for Fe^{2+} and Fe^{3+} in order to estimate the corners of the regions where LS hyperfine parameters would be predicted to fall for the glasses in the current study (indicated in dashed gray and solid black for LS Fe^{2+} and LS Fe^{3+}, respectively).

In order to reconcile the difference between the two studies, we conducted a Mössbauer spectroscopic study of a Fe^{2+}-rich aluminous silicate glass and a Fe^{3+}-rich sodium silicate glass measured in a diamond anvil cell up to 84 GPa to obtain a more direct indication of the iron spin state in silicate melts in the Earth's lower mantle. The variations in centre shift (CS) and quadrupole splitting (QS) vary smoothly with pressure and are consistent with a gradual increase in coordination number of Fe with pressure. Both, Fe^{2+} and Fe^{3+}, remain in the high spin state and show no evidence of spin crossover over the measured pressure range (Fig. 4.3-13).

Although our measurements of the Fe^{2+} and Fe^{3+} spin state in silicate glasses do not fully cover the pressure range of the Earth's lower mantle, our results suggest that no sharp spin crossover would be expected at P,T conditions down to the base of the lower mantle. Even if a spin crossover were to occur at the base of the lower mantle, there would be strong thermal broadening due to Boltzmann statistics of the crossover region. Our results therefore support the second study, which excludes the possibility of negatively buoyant melts in a chondritic Earth's lower mantle solely due to strong preferential partitioning of iron into the melt phase.

j. *Free electron nature of liquid Al at high pressures and temperatures from* ab initio *calculations (V. Vlček, N. de Koker and G. Steinle-Neumann)*

The electronic structure of elemental aluminium at ambient conditions, with three valence electrons ([Ne] $3s^2$ $3p^1$), shows near "free-electron" nature, *i.e.*, the ionic external potential can be considered as a weak perturbation of free electron eigenstates. As a result, Al is a very good conductor and due to its simplicity it is widely used for case studies of electronic transport properties. Previous computations for warm dense aluminium showed that this picture remains valid at high temperatures, though this notion was challenged by calculations for solid Al close to its melting temperature. The behaviour of liquid aluminium at extreme conditions, namely high pressures and temperatures, remains an open question. This additional insight would be helpful for experimental measurements of electrical conductivity, which are indirect and based on assumptions of near free-electron nature.

Using first principles calculations within the framework of density functional theory (DFT), we calculated the frequency dependent electrical conductivity $\sigma(\omega)$ of liquid Al within the linear response regime using the Kubo-Greenwood equation. Our calculations rest on the assumptions that: 1) the Kohn-Sham approach with conventional PBE exchange-correlation functional and norm-conserving pseudopotential remains valid for energies up to 6 eV above the Fermi energy; 2) the Born-Oppenheimer approximation holds and allows us to simulate the liquid using classical molecular dynamics (MD) approach with supercells containing 160 atoms. We performed simulations of Al liquid at temperatures ranging between 2000 and 8000 K and pressures from 0 to 110 GPa. From MD trajectories, representing a P-T point of simulations, we have selected 10 uncorrelated configurations, for which we computed $\sigma(\omega)$ at discrete angular frequencies ω. The electrical conductivity as a function of ω is given by the Drude formula

$$\mathrm{Re}[\sigma(\omega)] = \frac{\sigma_0}{1+(\omega\tau)^2}, \tag{4.3-1}$$

with relaxation time τ and the zero frequency limit σ_0 given by

$$\sigma_0 = \frac{Ne^2\tau}{m}. \tag{4.3-2}$$

Here, N is the number of carriers of charge e and mass m.

Analogously to experiments we use a single relaxation time for all the electronic eigenstates. By fitting Eq. 4.3-1 to the first principles results we obtain τ and σ_0 (Fig. 4.3-14), which are subsequently used for an estimate of the effective number of electrons N through Eq. 4.3-2. The results for all conditions investigated yield N = 2.8 ± 0.2, which implies that pressure causes only negligible localisation of the electrons. This validates the previous experimental results for Al plasmas and shows that electronic transitions among eigenstates diminish for $\omega \rightarrow 0$.

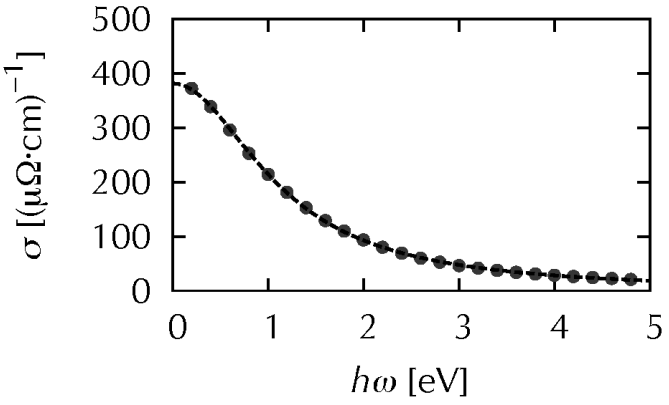

Fig. 4.3-14: Frequency dependent electrical conductivity obtained as an average from 10 uncorrelated atomic configurations (the error bars are smaller than the symbol size) fitted by the Drude formula (Eq. 4.3-1; black dashed line) at 90 GPa and 4000 K. A deviation from free-electron behaviour is not observed.

k. *Crystal structure, equation of state, and Raman spectra of OH-bearing $MgSiO_3$ akimotoite (Y. Ye, J.R. Smyth and D.A. Brown/Boulder; T. Katsura; S.D. Jacobsen, Y.-Y. Chang and J.P. Townsend/Evanston; P. Dera and S. Tkachev/Argonne; C. Goujon/Grenoble)*

Ilmentite-type $MgSiO_3$ (akimotoite) is stabilised relative to majorite-garnet under lower temperature geotherms within steeply subducting slabs. Two compositions of Mg-akimotoite have been synthesized under similar conditions: one sample (Z674) contains about 550 ppm wt. H_2O and was synthesised at 22 GPa and 1500 ºC, and the other (H3413) was synthesised at 22 GPa and 1250 ºC and is nearly anhydrous. Crystal structures of the two samples have been refined from single-crystal X-ray diffraction intensity data to give nearly identical results

within error, but both differ significantly from previously studies to give slightly smaller Si sites and slightly larger Mg sites. This result suggests that there may have been some Mg-Si disorder in samples in previous studies.

Thermal expansivity at ambient pressure of sample Z674 was measured by single crystal X-ray diffraction to give bulk thermal expansion coefficients (153 K-839 K) of $a_1 = 20(3) \times 10^{-9}$ K^{-2} and $a_0 = 17(2) \times 10^{-6}$ K^{-1}, with an average of $\alpha_0 = 27.1(6) \times 10^{-6}$ K^{-1} (Fig. 4.3-15). Compression at ambient temperature of sample Z674 was measured up to 34.6 GPa by single crystal X-ray diffraction at Sector 13 (GSECARS) at the Advanced Photon Source, Argonne National Laboratory, USA. A second-order Birch-Murnaghan equation of state (BM2 EoS) fitting yields: V_0 = 263.7(2) $Å^3$, K_{T0} = 217(3) GPa (K' fixed at 4) (Fig. 4.3-16). The anisotropies of axial thermal expansivities and compressibilities are similar for this sample: α_a = 8.2(3) and α_c = 10.68(9) (10^{-6} K^{-1}); β_a = 11.4(3) and β_c = 15.9(3) (10^{-4} GPa).

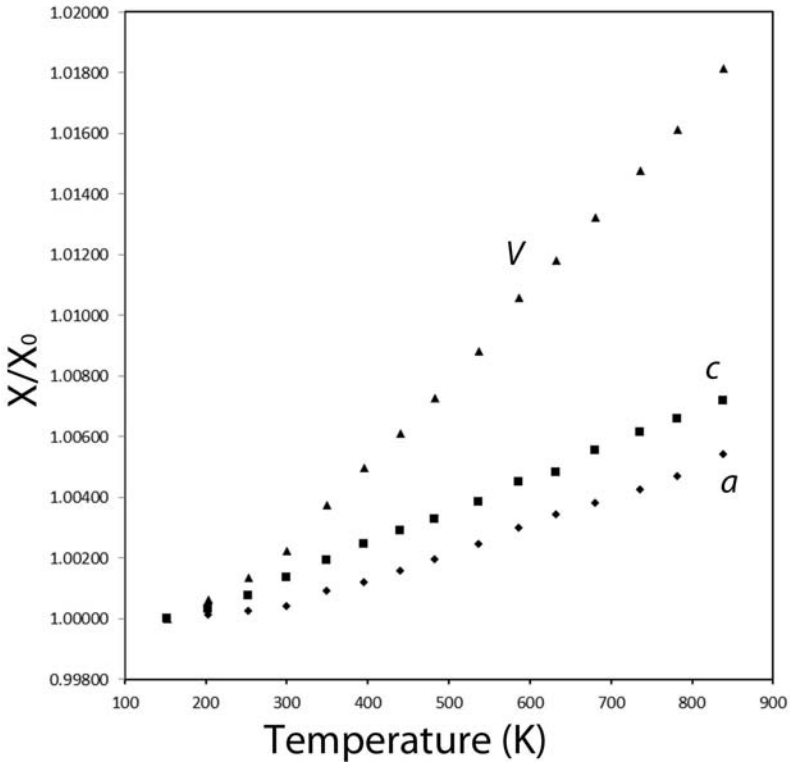

Fig. 4.3-15: Thermal expansivity at ambient pressure of hydrous akimotoite (sample Z674) as measured by single crystal X-ray diffraction.

Akimotoite is thus stiffer in the *a* direction than the *c* direction, and the *c*/*a* ratio increases with increased temperature and decreases with increased pressure. Contrasting the hydrous sample Z674 (~ 550 ppm wt. H_2O) with the anhydrous ones from this and previous studies, hydration may slightly, but significantly, increase both the bulk thermal expansivity and compressibility, and decrease the anisotropies of both axial thermal expansivity and compressibility.

Raman spectra of both samples in the lattice mode region show peaks at 290, 350, 400,410, 480, 500, 620, and 680 cm^{-1}, plus a large peak at 800 cm^{-1}. The H-bearing sample (Z674) also shows OH features at 3295, 3320, 3350 cm^{-1}. These results indicate that pure $MgSiO_3$ akimotoite can incorporate small, but significant, amounts of H.

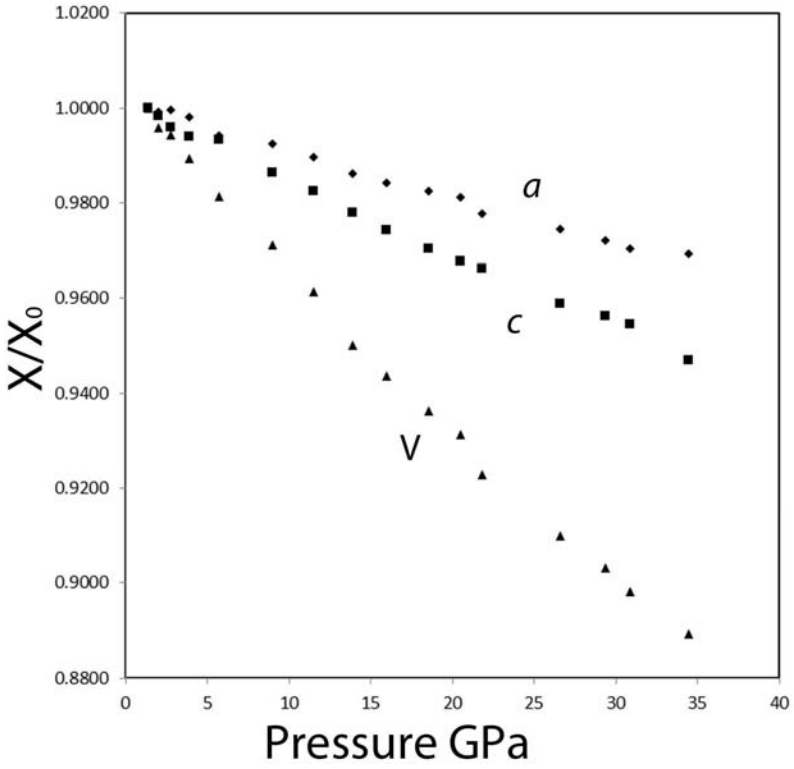

Fig. 4.3-16: Compression at ambient temperature of hydrous akimotoite (sample Z674) measured up to 34.6 GPa by single crystal X-ray diffraction.

l. *High-pressure densification of SiO_2 glass up to 14 GPa (J. Chantel and W.A. Crichton/Grenoble; D.J. Frost)*

The investigation of the densification of SiO_2 glass at high pressure is driven by both an interest in causing permanent changes in the optical properties of glasses, and from a geoscience interest in the behaviour of silicate liquids at high pressures. Here we have measured acoustic wave velocities within a sample of silica glass at high pressure, employing ultrasonic interferometry techniques. In addition, *in situ* powder diffraction of calibrant materials has been used to determine the pressure during the multianvil experiments.

Both V_P and V_S as functions of pressure were obtained to 14 GPa during three single compression experiments. Measurements were performed in a 2000-ton uniaxial DIA multianvil apparatus (LPO 2000-ton, ID06, ESRF). The cell assembly for the high-pressure ultrasonic experiments was based on the 10/4 configuration (10mm: length of the octahedron edge, 4mm: length of the anvil truncation). In order to provide a pseudo-hydrostatic pressure

environment and avoid cracking of the sample, the specimen was backed by a disk of NaCl on the bottom and surrounded by a sleeve of MgO. Two thin Au foils were placed at the rear and far ends of the sample to measure precisely its length using X-ray radiography.

The pressure of each experiment was calibrated using a combination of the equations of state of NaCl and Au, using X-ray diffraction patterns collected from those materials at each pressure while the ultrasonic measurements where performed. The round trip travel times of the acoustic compressional and shear waves were measured by ultrasonic phase comparison interferometry. The average round trip travel time of the acoustic *P* and *S* waves through each sample was calculated from the 40 - 55 MHz and 10 - 25 MHz regions, respectively. Velocities were calculated from the high-pressure travel times with consideration of the specimen length changes under compression using the images collected with a CCD camera.

The V_P and V_S values for the SiO_2 glass, obtained from high-pressure ultrasonic interferometry measurements, are reported in Fig. 4.3-17. The velocities are consistent within the three runs. Since the samples were sufficiently long (1 mm), the bond corrections in the travel times for both the P and S waves, taking into account the gold foil at each interface, are generally less than 0.5 ns, resulting in uncertainty of 0.1 % for V_P and V_S. An increase in both V_P and V_S from 11 to 13 GPa has already been documented and results from a densification of the SiO_2 glass at high pressure. However, in the present study we observe a sharp jump in V_P at 8 GPa, with no concurrent increase in V_S being apparent.

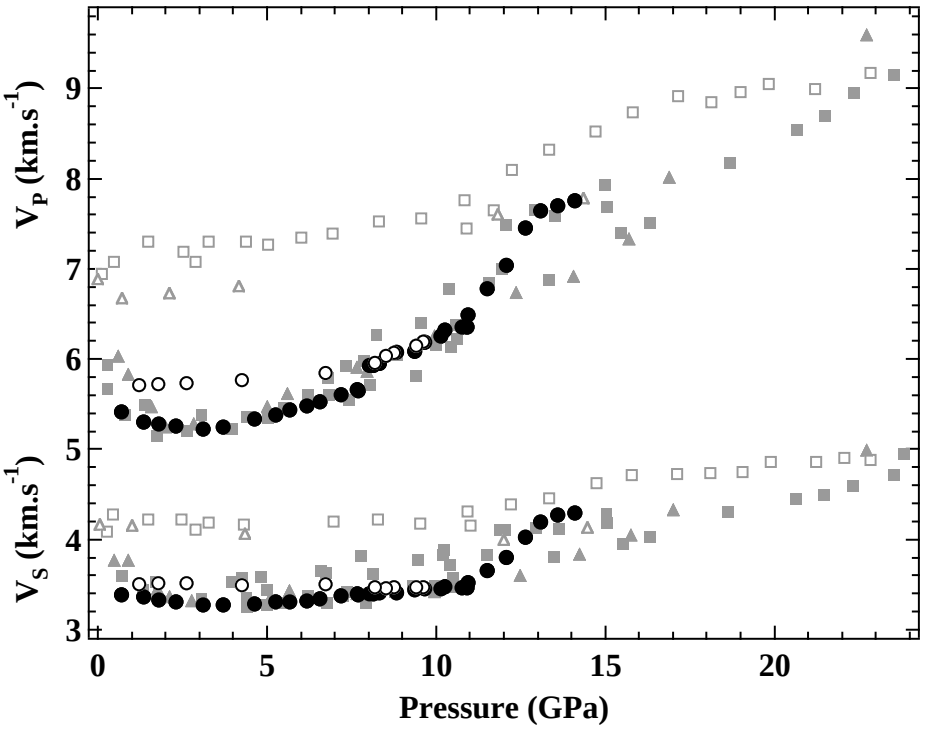

Fig. 4.3-17: V_P and V_S for the SiO_2 glass from this study during compression (solid black dots) and decompression (open circles). Literature data are shown as solid grey squares, open squares, solid grey triangles and open triangles.

We calculated the density of the SiO_2 glass samples up to 14 GPa, using the acquired V_P and V_S in our runs, the density at ambient conditions ρ_0 = 2.18 g.cm^{-3} and the bulk modulus K_0 = 31.7 GPa from the literature (Fig. 4.3-18). The densities do not follow the trend, meaning that there are two stages of densification of the SiO_2 glass when the jumps in V_P are taken into account. Densification resulting in a drastic increase in V_P implies a change in the density at ambient conditions, ρ_0, and the bulk modulus, K_0, of each of those denser phases. The refined values for the densified phase stable from 8 to 11 GPa, termed the β glass, are ρ_0 = 2.24 g.cm^{-3} and K_0 = 35 GPa, while the values for the so-called γ glass phase present at pressures higher than 11 GPa are ρ_0 = 2.67 g.cm^{-3} and K_0 = 60.2 GPa (Fig. 4.3-18).

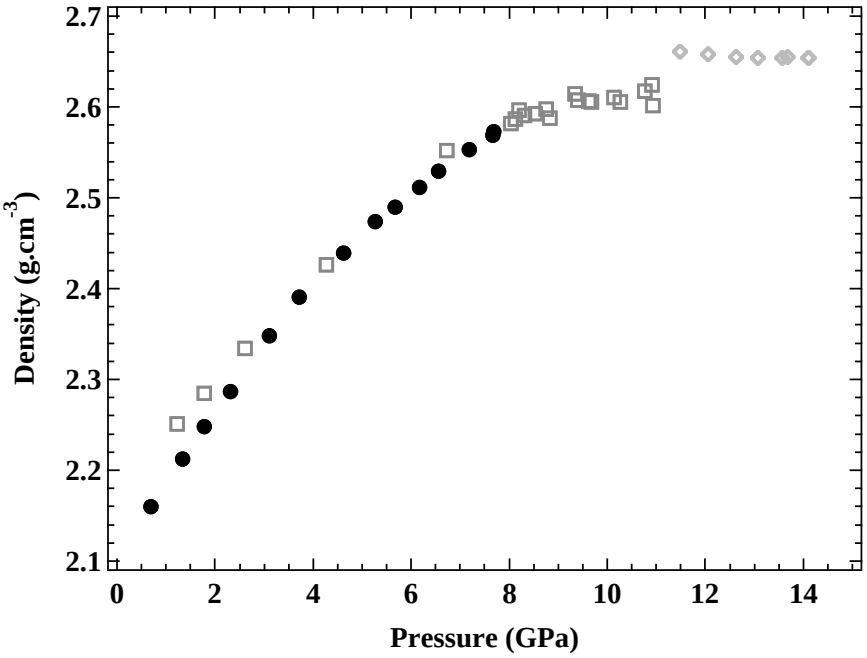

Fig. 4.3-18: Densities of the SiO_2 glass as a function of pressure. Densities calculated with fixed room pressure values of density, ρ_0, and bulk modulus, K_0, are shown as solid circles. Densities calculated by independently refining ρ_0 and K_0 for each densified phase are reported for the glass structure formed between 8-11 GPa by open squares (glass β) and that formed above 11 GPa by open diamonds (glass γ).

m. *High-pressure structure behaviour of labuntsovite-Fe (S.M. Aksenov, R.K. Rastsvetaeva, N.V. Chukanov and I.P. Makarova/Moscow; E.A. Bykova, A. Kurnosov; N.A. Dubrovinskaia/ Bayreuth and L.S. Dubrovinsky)*

Specific "zeolitic" properties of microporous framework heterosilicates depend on the configuration of the channels. Ion-exchange properties of microporous titanosilicates are of great interest taking into account their capability to accumulate various radioactive species. However, there are no investigations of these materials under high pressure.

Labuntsovite-group (LG) minerals with the generalised formula (Z=1) $A_4B_4C_{4-x}[D_x(H_2O)_{2x}][M_8(O,OH)_8[Si_4O_{12}]_4 \cdot 8H_2O$ (A = Na, Ca; B = K, Na, H_3O; C = K, Ca, Sr, H_3O, H_2O, OH; D = Fe^{2+}, Mn, Zn, Mg; M = Ti, Nb, Fe^{3+}, Fe^{2+} and x = 0 – 2) are characterised by a framework consisting of chains of (Ti,Nb)O_6-octahedra with shared trans-vertices. The chains are linked by tetrahedral four-member rings [Si_4O_{12}], forming a three-dimensional framework that contains cavities in the form of channels and cages which are usually occupied by H_2O molecules and extra-framework large alkali and alkali-earth metal cations (Fig. 4.3-19). These characteristic features of labuntsovite and related minerals make them similar to zeolite-type minerals. High-pressure structural investigation of these minerals provides significant insight into the nature of ion-exchange properties of microporous heterosilicates.

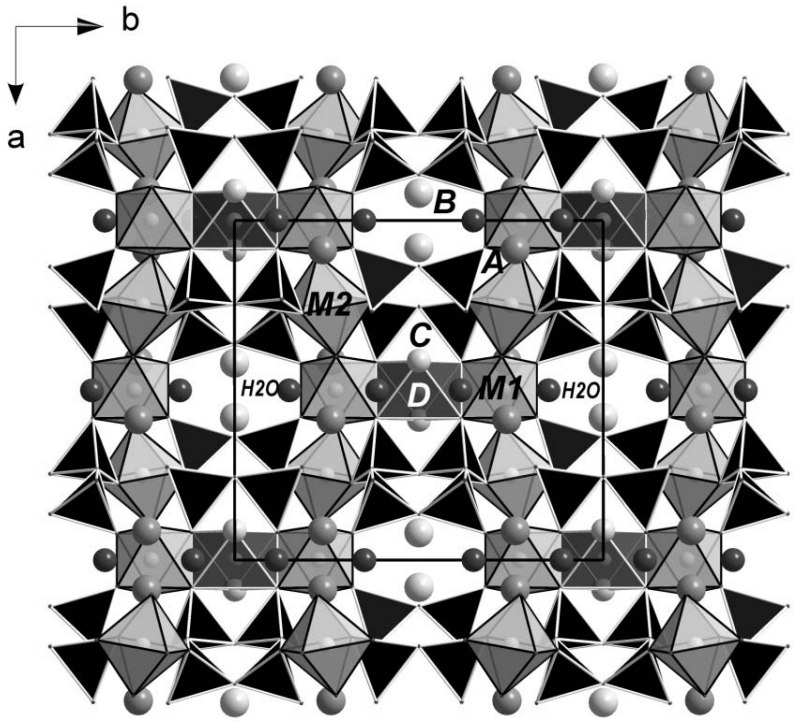

Fig. 4.3-19: The crystal structure of the labuntsovite-group minerals.

The crystal structure of the natural labuntsovite-Fe with the idealised formula $Na_2K_2Ba_{0.7}Fe_{0.5}Ti_4(Si_4O_{12})_2(OH,O)_4 \cdot 5H_2O$ (space group $C2/m$, Z=2) was refined previously at ambient conditions. The unit cell parameters were found to be a=14.234(2) Å, b=13.7742(7) Å, c=7.7741(8) Å, β=116.787(17)°; R=3.89 % for 758 independent reflections with $|F_{obs}| > 3\sigma$.

Now we present the *in situ* single crystal X-ray diffraction study of the labuntsovite-Fe conducted in a diamond anvil cell. Measurements were carried out at the ID09 beam line at ESRF. Ne was used as a pressure transmitting medium and the pressure was determined by

the ruby fluorescence method. The data were collected on compression up to 22.5 GPa with a step of ~ 2.5 GPa. Data treatment was performed with the CrysAlis RED software.

Figure 4.3-20 (upper) shows the pressure dependence of the unit cell volume of labuntsovite-Fe. The fit of experimental data with a 3rd order Birch-Murnaghan equation of state resulted in the bulk modulus K = 72(2) GPa and K'= 3.7(2) with V_0= 1363(2) Å^3. The linear compressibility is represented in the relative change of the unit cell parameters. It is clearly seen in Fig. 4.3-20 (lower) that the compressibility of the material along the *c* direction is considerably larger than that along the *a* and *b* directions.

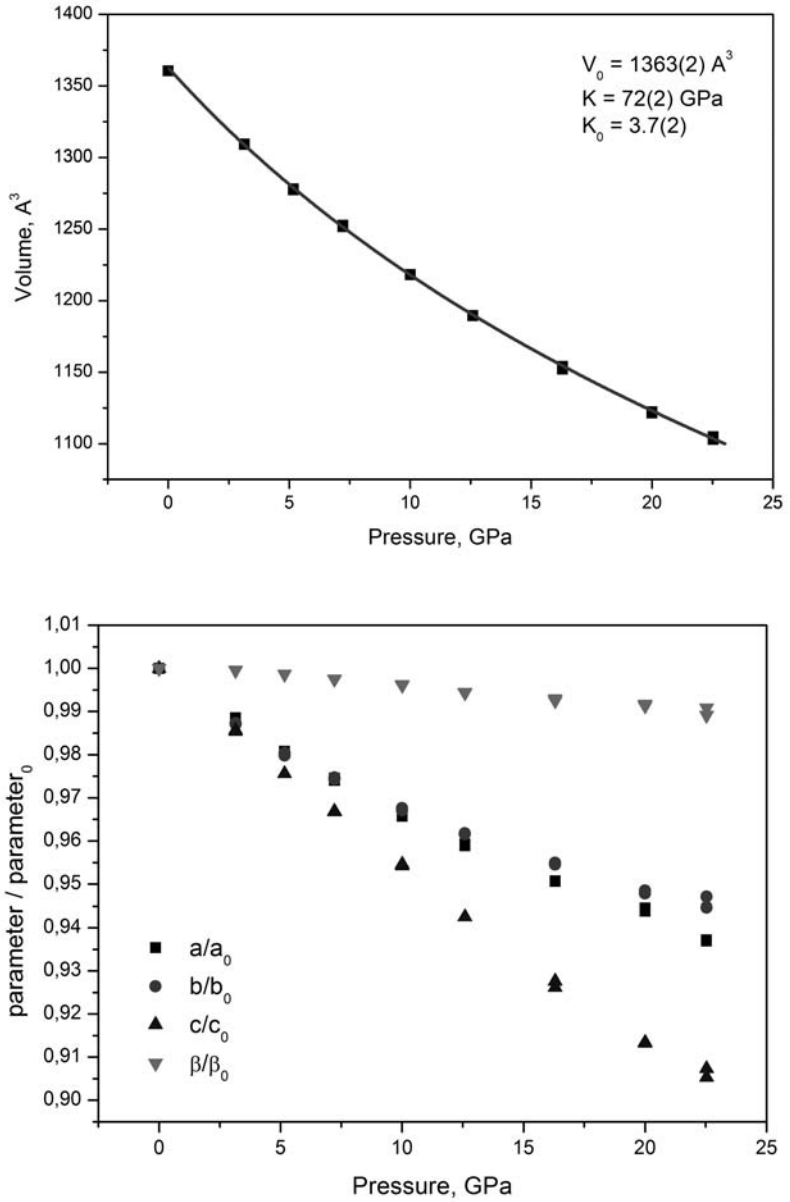

Fig. 4.3-20: The volume and linear compressibility of labuntsovite-Fe: (upper) unit cell volume as a function of pressure; (lower) relative unit cell parameters as a function of pressure.

n. In situ *infrared spectra of hydroxyl in wadsleyite and ringwoodite at high pressure and high temperature (X. Yang/Nanjing, H. Keppler, L.S. Dubrovinsky and A. Kurnosov)*

Wadsleyite and ringwoodite (β- and γ-Mg_2SiO_4), the high-pressure polymorphs of olivine, are generally believed to be the most abundant minerals in the transition zone of Earth's mantle, between 410- and 660-km depth, and accordingly, they should control the chemical and physical properties of the transition zone and may affect the dynamics of the whole mantle. Wadsleyite and ringwoodite are able to accommodate significant amounts of water, up to more than ~ 2 % (by weight), in the form of hydroxyl groups in their structure, and they likely are major water reservoirs in Earth's interior. The presence of H in wadsleyite and ringwoodite could affect electrical conductivity, melting temperatures, bulk modulus, creep strength and phase stability. Structural models of H incorporation into wadsleyite and ringwoodite are indispensable for understanding water storage and predicting the effect of water on physical and chemical properties. Infrared spectroscopy provides a unique approach in revealing the speciation and structural information of H in materials; up to now, however, the speciation of H in wadsleyite and ringwoodite has been nearly exclusively measured at room temperature. Therefore, it is uncertain whether the models of hydrogen dissolution in wadsleyite and ringwoodite, derived from spectra measured at ambient conditions, correctly describe the mechanisms of water dissolution deep in the mantle. Given the high mobility of H, it is possible that its location in a mineral structure may change upon modifying pressure and especially temperature. Therefore, it is necessary to carry out *in situ* studies of H-species in wadsleyite and ringwoodite at simultaneous high-pressure and high-temperature conditions.

Hydrous wadsleyite and ringwoodite were synthesised from commercially available high-quality synthetic single crystals of forsterite. A mixture of talc plus brucite powder with a weight ratio of 1.4:1 was used as a water source, and the syntheses were conducted at 18 GPa and 1400 °C for wadsleyite and 22 GPa and 1400 °C for ringwoodite, with durations of 200 min in a 1200-tonne multianvil apparatus using a 10/5 and 10/4 octahedral multianvil assembly for wadsleyite and ringwoodite, respectively. The recovered wadsleyite and ringwoodite crystals are of high quality, free of any visible impurities or inclusions and up to ~ 300 µm in size. High-pressure, high-temperature and hydrostatic conditions for *in situ* infrared analyses were generated in a symmetric piston-cylinder diamond anvil cell (DAC) with diamonds of 300 µm culet size with an externally resistive heater and neon gas as the pressure transmitting medium (Re gasket). Temperature was monitored by an S-type thermocouple, and pressure was measured by ruby fluorescence. *In situ* infrared spectra were collected up to ~ 19 GPa at room temperature and up to 650 °C at 14.5 ± 0.2 GPa for wadsleyite and up to ~ 21.5 GPa at room temperature and up to 900 °C at 18.4 ± 0.2 GPa for ringwoodite.

Raman analyses of the sample crystals before and after the runs exclude phase changes during the measurements. The results show that the synthetic samples reproduce nearly all of the important OH bands observed at ambient conditions. For wadsleyite, with increasing pressure

to ~ 19 GPa at room temperature, the frequencies of the bands at ~ 3600 cm^{-1} remain almost unchanged, while the bands at 3200-3400 cm^{-1} shift to lower frequencies, accompanied by band broadening (Fig. 4.3-21a). Upon heating to 650 °C at 14.2 GPa, the position of the bands at ~ 3600 cm^{-1} hardly changes, but the bands at 3200-3400 cm^{-1} gradually shift to lower frequencies and the band at ~ 3250 cm^{-1} (at 14.2 GPa), initially at ~ 3360 cm^{-1} at ambient conditions, disappears by heating to ~ 300 °C (Fig. 4.3-21b). For ringwoodite, with increasing pressure to ~ 21.5 GPa at room temperature, the frequencies of the bands at ~ 3600-3700 cm^{-1} remain almost unchanged, while the bands at 3000-3200 cm^{-1} progressively shift to lower frequencies (Fig. 4.3-22a). Upon heating to 900 °C at 18.4 GPa, no frequency shift was observed for the bands at ~ 3600-3700 cm^{-1}, but the bands initially at 3000-3200 cm^{-1} shift very slowly to higher frequencies, which should yield almost the same band positions at ~ 1300-1400 °C as those measured at ambient conditions (Fig. 4.3-22b). Our data suggest that water speciation in hydrous wadsleyite at ambient conditions may not reflect completely that in the mantle transition zone, but that water speciation in hydrous ringwoodite at ambient conditions should be comparable to that under mantle conditions, except perhaps for subtle changes in hydrogen bonding.

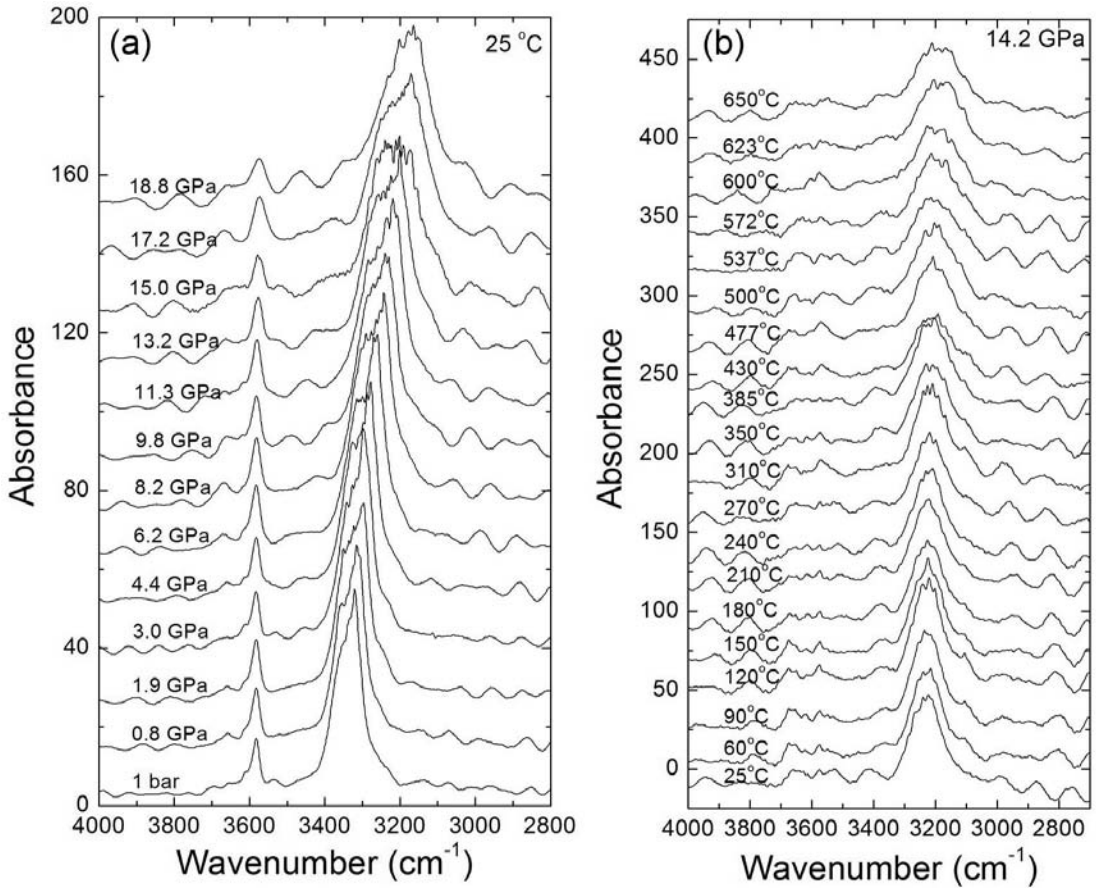

Fig. 4.3-21: *In situ* infrared spectra of wadsleyite (a) to ~ 19 GPa at room temperature, and (b) to 650 °C at 14.2 GPa. Variation of pressure before and after each measurement was usually less than 0.1 GPa for (a) and less than 0.2 GPa for (b). The spectra were normalized to 1 mm thickness and vertically offset.

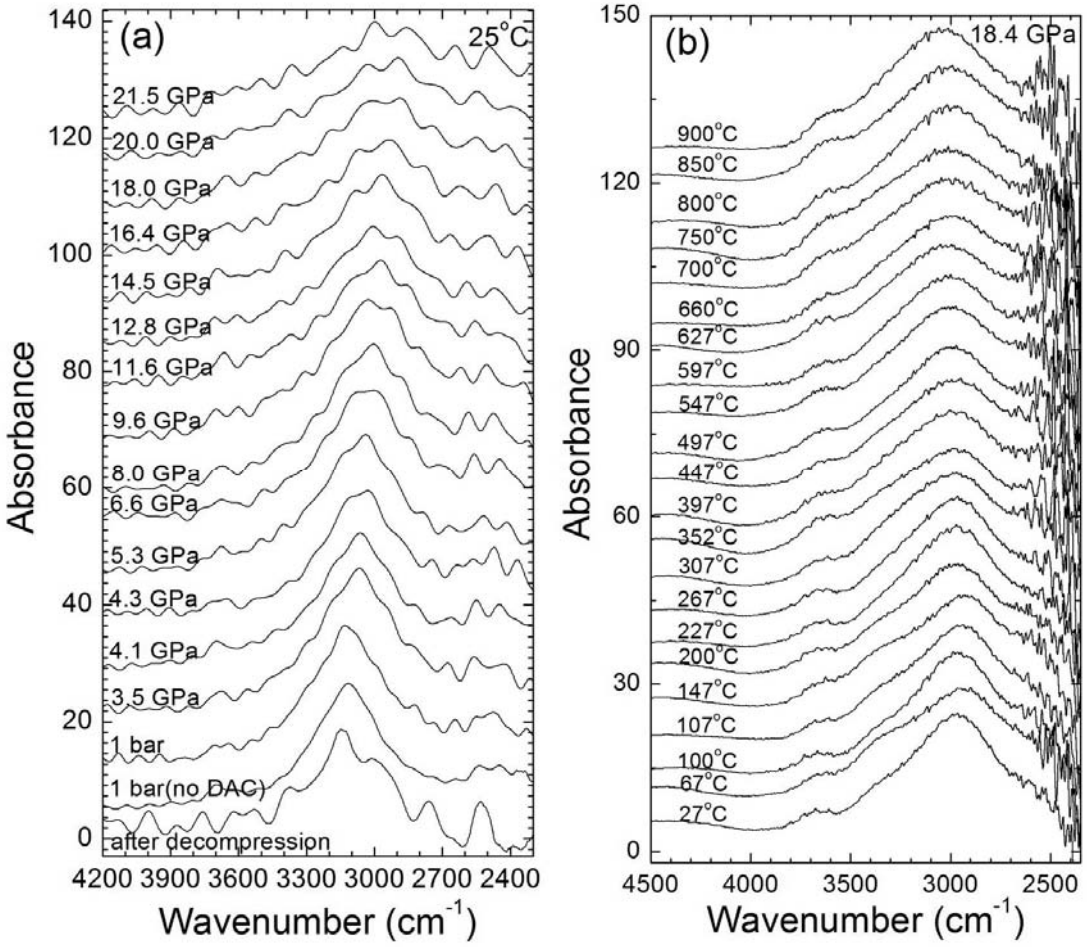

Fig. 4.3-22: *In situ* infrared spectra of ringwoodite (a) to 21.5 GPa at room temperature, and (b) to 900 °C at 18.4 GPa. Variation of pressure before and after each measurement was usually less than 0.1 GPa for (a) and less than 0.2 GPa for (b). The spectra were normalised to 1 mm thickness and vertically offset. The bottom spectrum in (a) was measured from the recovered sample after final decompression (note that the crystal cracked upon rapid decompression to room pressure). The spectra labelled as 200 and 100 °C in (b) were measured upon cooling to room temperature.

o. *The stability field of Fe_4O_5 (D.O. Ojwang', T. Boffa Ballaran and D.J. Frost)*

Iron oxides are composed of two of the most abundant elements on Earth, *i.e.*, oxygen and iron, and they can exhibit strong magnetic properties. Their ability to host extensive numbers of defects helps to explain their variable stoichiometry. The stability and composition of iron oxides in the Earth's mantle depends on pressure, temperature, oxygen fugacity and bulk composition as a function of depth. Until recently only four compounds had been extensively investigated, *i.e.*, wüstite (FeO), hematite (Fe_2O_3), magnetite (Fe_3O_4) and the unquenchable high-pressure polymorph of magnetite (h-Fe_3O_4). Recently a new iron oxide phase with the formula Fe_4O_5 has been observed as a breakdown product of siderite. This new compound is stable at pressures above ~ 10 GPa and is quenchable to ambient conditions. It was referred to

as a “mystery” phase by earlier studies in the Fe_3O_4-Fe_2SiO_4-Mg_2SiO_4 system and it appears to be stable also in the Fe_3O_4 - Cr_3O_4 system. Its phase stability is therefore fundamental to understanding the chemically simple Fe-O system which forms the basis for more complex chemical systems.

In order to constrain the stability field of Fe_4O_5 we have synthesised and analysed several samples obtained from experiments performed in the pressure range between 8 and 24 GPa and temperatures between 1000 and 1400 °C using the multianvil apparatus. The starting material consisted of a mixture of magnetite, Fe_3O_4, produced by reducing Fe_2O_3 in a 1 atm CO_2-CO gas-mixing furnace, and Fe metal. Re capsules were used for all high-pressure experiments. All of the run products were analysed by SEM, electron backscattering diffraction (EBSD), X-ray powder and X-ray single crystal diffraction techniques.

Run products recovered from syntheses performed between ~ 8 and ~ 24 GPa contain the Fe_4O_5 phase (Fig. 4.3-23). However, most of the samples do not consist of a single phase, since Fe_3O_4 and Fe_2O_3 phases were also present. The presence of multi-phase mixtures at the conditions where only Fe_4O_5 should be stable may be due either to oxidation of the sample during the experiments (*e.g.*, due to uncontrolled oxygen fugacity) or an inhomogeneous starting material (*e.g.*, due to incompletely mixed Fe powder and magnetite). Also we cannot exclude that some Fe_4O_5 back-transformed to magnetite during sample polishing as Fe_4O_5 is temperature sensitive.

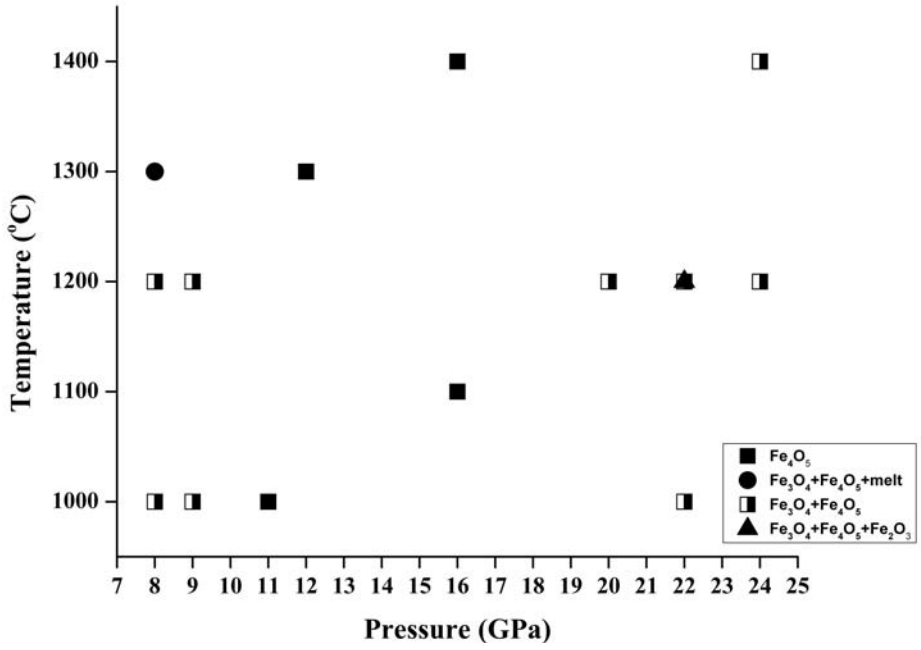

Fig. 4.3-23: Phases synthesised in the Fe-O system in P/T space constructed from SEM, EBSD and X-ray diffraction analyses. Closed circles indicate a mixture of melt, Fe_3O_4 and Fe_4O_5; solid squares indicate Fe_4O_5; half-filled squares indicate the coexistence of Fe_3O_4 and Fe_4O_5 , while the triangle indicates a mixture of Fe_4O_5, Fe_3O_4 and Fe_2O_3.

The complex nature of the run products can be more effectively seen using EBSD analysis. EBSD images (Fig. 4.3-24) of samples V743 and S5570 illustrate how a structural analysis can distinguish between magnetite and Fe_4O_5 phases. In both samples we observe crystals with smooth surfaces together with crystals with lamellae, suggesting that they belong to two different phases. However in the case of sample V743 only Fe_3O_4 was found; whereas only Fe_4O_5 was present in sample S5570 despite the similarity in their textural appearance and surface contrast. The presence of lamellae may be due to a back-reaction during quenching or sample preparation. In order to understand the complex microstructure of this compound and the origin of such lamellae, we are currently undertaking a further study of the samples using TEM.

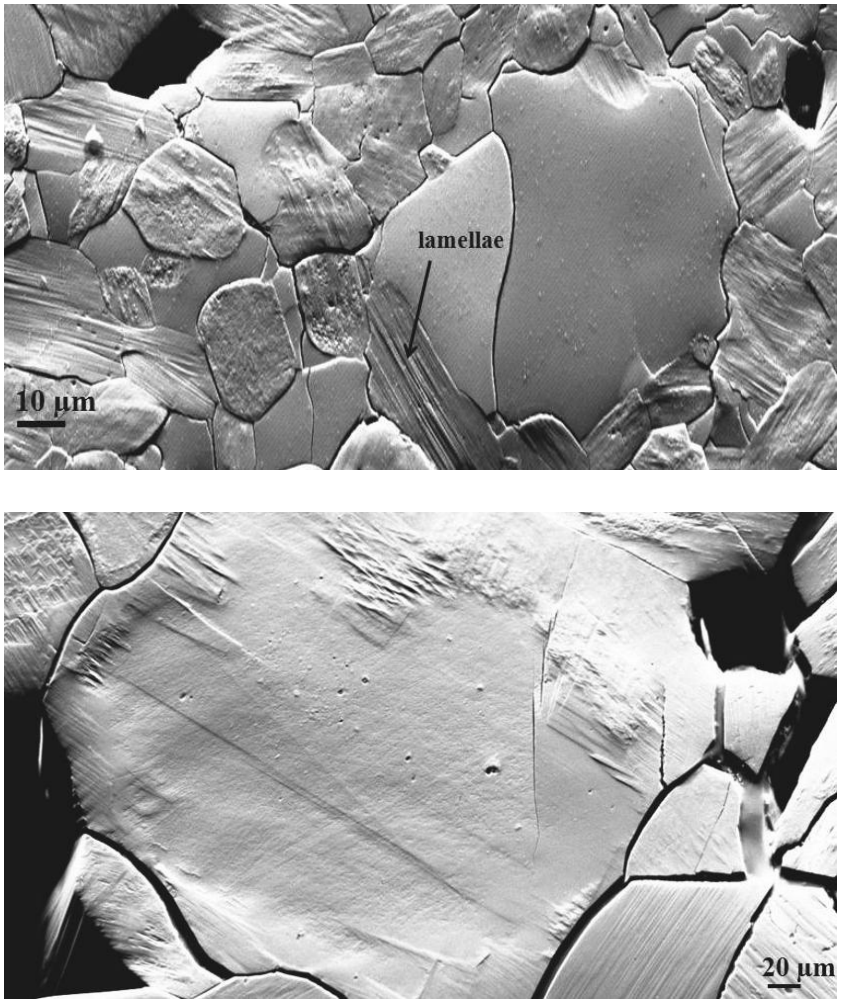

Fig. 4.3-24: EBSD photograph of V743 (upper) and S5570 (lower) recovered run products where smooth crystals and crystals with lamellae can be observed.

p. *The thermal breakdown of Fe_4O_5 at ambient pressure (D.M. Trots, A. Kurnosov and D.J. Frost, in collaboration with A.B. Woodland/Frankfurt)*

Fe_4O_5 is a recently discovered Fe-oxide that is stable at pressures of ~ 10 GPa, where under such conditions magnetite is now known to break down to an assemblage of Fe_4O_5 + Fe_2O_3. It is thus important to determine the properties of Fe_4O_5 as it apparently plays an important role

in the simple Fe-O system at high pressures and temperatures. To this end we measured accurate molar volumes of Fe_4O_5 as a function of temperature at ambient pressure conditions to measure its thermal expansion. Our study was complicated by the low thermal stability of the phase at 1 bar, which revealed a series of different transformations.

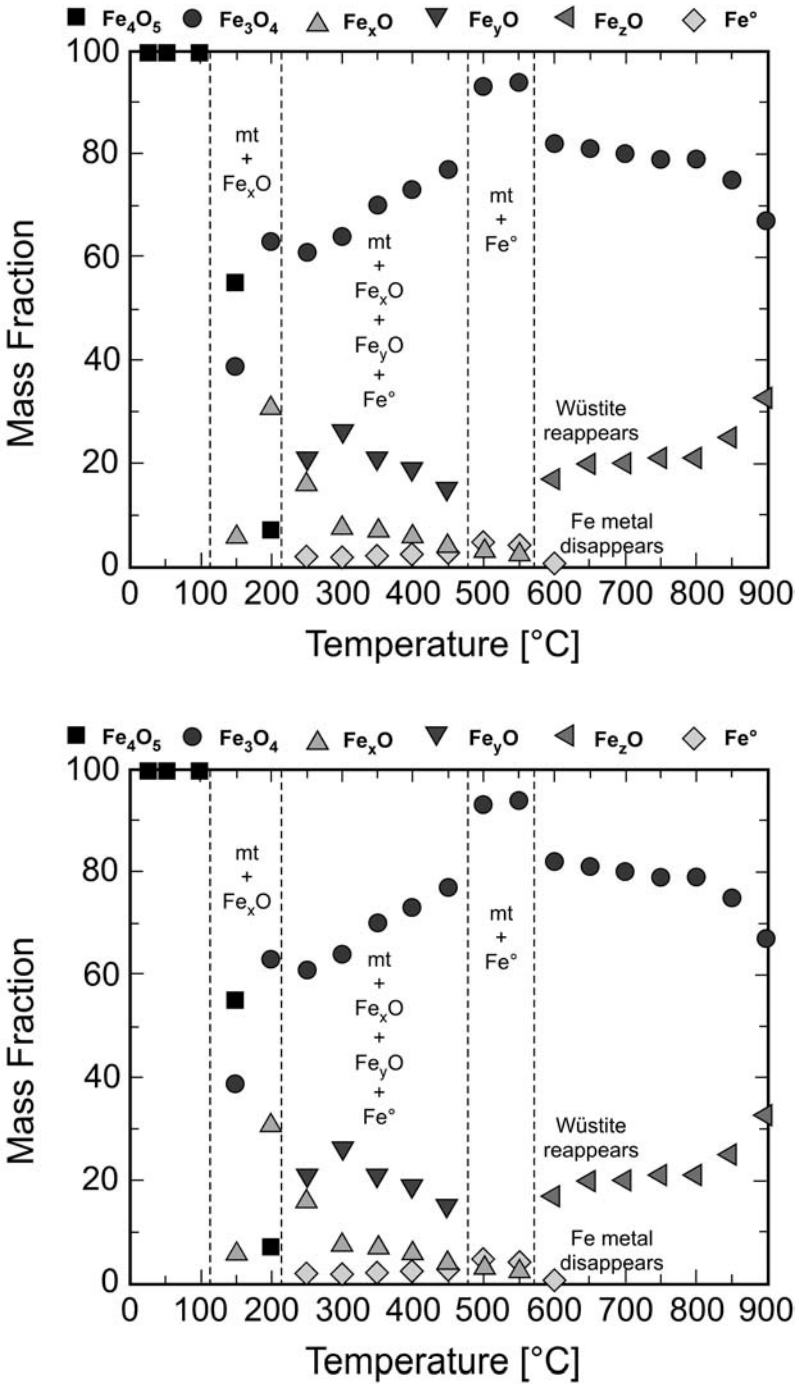

Fig. 4.3-25: Proportions of iron-bearing phases determined from powder X-ray diffraction produced during the breakdown of Fe_4O_5 upon heating at room pressure. The wüstite stoichiometry was determined to be x ~ 0.8, y ~ 0.96 and z ~ 0.93.

Fe_4O_5 was synthesised from a mixture of magnetite and Fe at 11 GPa and 1000 °C in a multianvil press. The lattice parameters at ambient P and T are a = 2.89339(6) Å, b = 9.8067(3) Å, c = 12.5834(3) Å with a volume of 357.05(2) $Å^3$. Subsequently we sealed the powder in a quartz-glass capillary along with iron powder and collected data at the high-resolution beamline B2 at HASYLAB/DESY. X-ray powder diffraction measurements were performed as a function of temperature up to 900 °C.

At 150 °C new diffraction peaks appeared, indicating the decomposition of Fe_4O_5 to a mixture of Fe_3O_4 and Fe_xO. The unit cell of Fe_xO corresponded to a composition of x ~ 0.8. By 200 °C diffraction peaks from Fe_4O_5 virtually disappeared. Between 200 and 250 °C, metallic Fe and an additional Fe_yO phase appeared that had a unit cell closer to stoichiometric FeO (y ~ 0.96), indicating a further reaction where Fe^{3+}-rich Fe_xO broke down to a mixture of Fe_3O_4 + Fe^{3+}-poor Fe_yO + metallic Fe. With increasing T, both Fe_xO and Fe_yO progressively underwent a disproportionation reaction producing metallic Fe and Fe_3O_4. Above 450 °C, Fe_yO disappeared, producing a stable assemblage of metallic Fe + Fe_3O_4. At T > 570 °C, the true wüstite stability field was reached and metallic Fe reacted with magnetite to produce Fe_zO, where z = 0.93(1). No further changes were observed up to 900 °C. The calculated phase proportions at 900 °C were 0.37 Fe_zO and 0.63 Fe_3O_4, which correspond very closely to the initial Fe_4O_5 composition, indicating that the series of reactions was not driven by oxidation or reduction, but occurred at nearly constant oxygen content. The metastable appearance of Fe_xO at low T is likely related to the fact that the Fe_4O_5 crystal structure contains wüstite-like octahedral layers that alternate with Ca-ferrite slabs. The initial breakdown favours the formation of Fe^{3+}-rich Fe_xO, which may be an indicator of the cation distribution in the original Fe_4O_5 phase.

q. *Pressure-induced transformation in coesite at 25 GPa (A. Cernok, L.S. Dubrovinsky and N. Miyajima)*

Silica exhibits a rich polymorphism with more than thirty stable or metastable phases, most of which occur at ambient to moderate pressures (< 9 GPa) and consist of SiO_4 tetrahedra. Because of the relatively strong Si-O binding in silica, there are high kinetic barriers associated with the transitions to stable high-pressure phases (> 9 GPa) consisting of SiO_6 octahedra. This results in highly complicated metastable phenomena at high pressure and ambient temperatures such as persistence of low-pressure phases far out of their stability fields and transitions to metastable crystalline and amorphous phases. Coesite is a polymorph of silica thermodynamically stable above ~ 2.5 GPa. It is the densest known silica polymorph with tetrahedrally coordinated Si atoms, and it crystallises in the C 2/c space group. Terrestrial occurrence of coesite was reported from deeply (> 100 km) subducted crustal rocks, which have been exhumed under conditions that prevent retrograde transition to quartz. Coesite can be also found in rocks related to meteorite impact sites, where it is formed from

quartz in a high-pressure and high-temperature regime and quenched rapidly to prevent reversion to quartz.

Earlier experimental and computational studies on the high-pressure behaviour of coesite at ambient temperatures reported a phase transition in the 22-25 GPa range, followed by pressure-induced amorphisation. To our knowledge, this phase transition in coesite has not been further investigated and no exact structural analysis of the higher pressure phase exists. We have therefore undertaken a high-pressure study of coesite single crystals by means of Raman spectroscopy, XRD, and TEM on recovered materials.

Coesite single crystals were synthesized in Pt capsules using a standard piston cylinder assembly. SiO_2 glass was pressurised to 3.5 GPa and slowly heated to 1250 °C, where it remained overnight. Slow cooling to 1100 °C over 5 hours resulted in the growth of relatively large (above 100 µm in linear dimension) single crystals. The high-pressure behaviour of coesite was investigated at ambient temperatures and (quasi)hydrostatic conditions using a diamond anvil cell (DAC) with 250 µm culet size diamonds loaded with Ne as a pressure transmitting medium. Crystals with a typical size of 15 × 30 × 50 μm^3 were placed in a cylindrical pressure chamber of 30-40 µm height and ~ 125 µm diameter drilled in a Re gasket. Ruby chips were used as pressure markers.

High-pressure Raman spectroscopy of coesite confirmed the phase transition at ~ 22-25 GPa, mainly marked by splitting of the most intense band (521 cm^{-1} at ambient conditions). This band has been assigned to the ν_s(Si-O-Si) stretching mode and it is centred around 600 cm^{-1} at pressures of 22-35 GPa. However, further compression has not indicated transformation to an amorphous form as previously reported. We found that the doublet band persists towards much higher pressures (to ~ 45 GPa), showing a positive pressure shift and continuous weakening in spectra above 30 GPa (Fig. 4.3-26a). On decompression from 45 GPa we observed the reverse phase transition at about 24 GPa and found the pressure-quenched material to be coesite (Fig. 4.3-26b). Synchrotron single crystal X-ray diffraction confirmed the phase transition to occur at ~ 24 GPa.

One of the samples that was bridged during compression in an unsuccessful DAC experiment was additionally studied by TEM. After decompression, several residual grains were recovered from the bridged crystal. Like most of the recovered material from this experiment, the thick central part of the grain is an amorphous material. In contrast, the thin edge of the sample that was not bridged shows an electron diffraction pattern that can be assigned to coesite. This observation supports our other observations on sufficiently thin single crystals, that upon decompression from the highest pressures so far reached (45 GPa), the structure returns to that of coesite.

In summary, our recent studies have shown that coesite undergoes phase transition at ~ 25 GPa to a crystalline metastable phase which is not quenchable to ambient conditions.

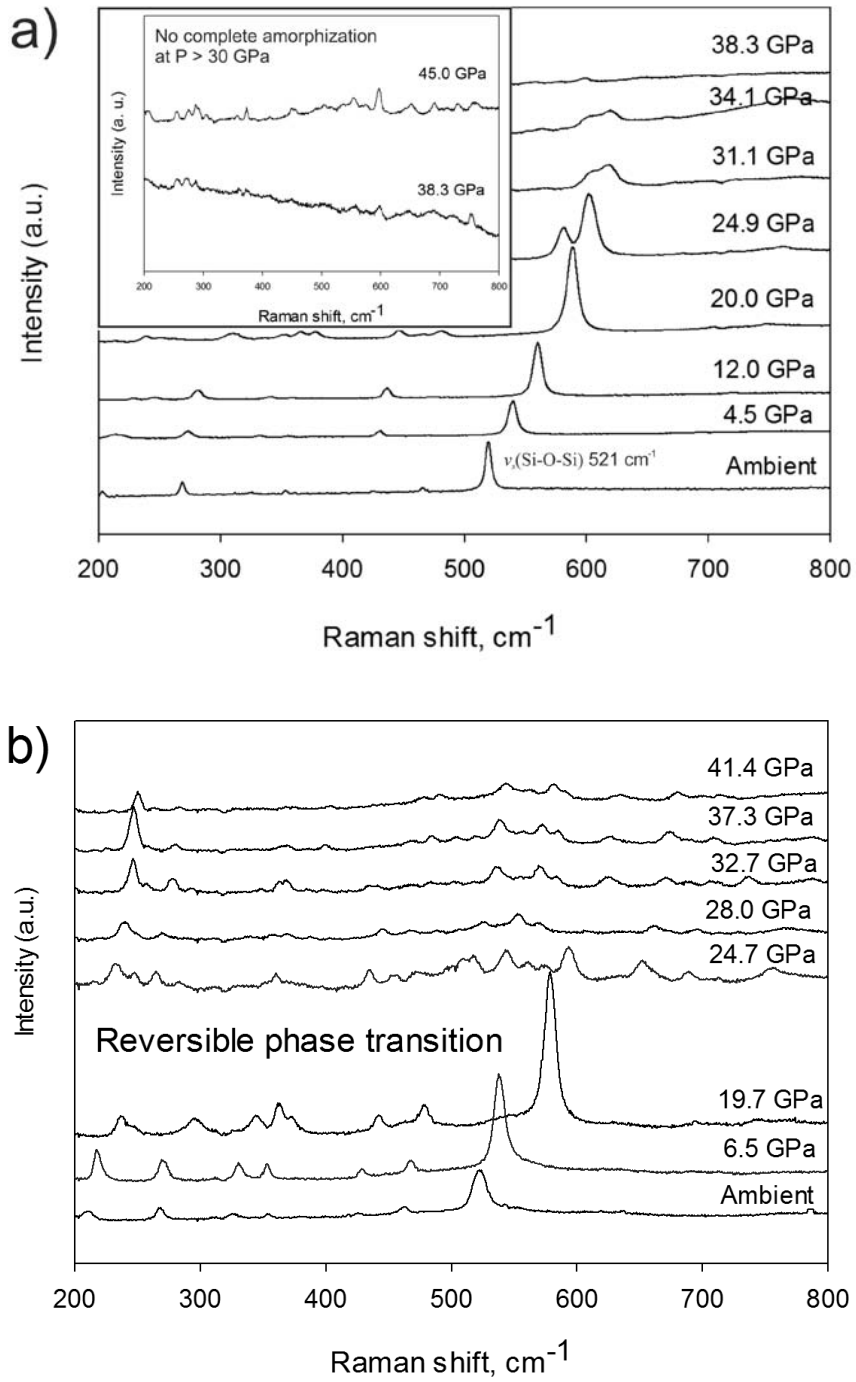

Fig. 4.3-26: a) Raman spectra collected during compression of coesite to 45 GPa at ambient temperature. Spectra in the main diagram display two main features: 1) a phase transition at ~ 25 GPa marked by peak-splitting of the main vibration mode at 521 cm^{-1}; and 2) persistence of this mode to pressures greater than 30 GPa. The inset diagram shows magnified Raman spectra at 38 and 45 GPa demonstrating that material is not amorphous. b) Raman spectra collected during coesite decompression from 42 GPa at ambient temperature indicating a reversible phase transition at ~ 25 GPa.

4.4 Physical Properties of Minerals

Geophysical and geochemical studies provide us with indirect observations of the Earth's interior whose interpretation relies heavily on direct experimental measurements of physical and chemical properties conducted at the relevant pressure and temperature conditions.

The first step for constraining geophysical models is the understanding of seismic profiles throughout the Earth which requires knowledge of the elastic properties of mantle minerals. It is not surprising, therefore, that major efforts also during last year have been undertaken at BGI to determine both compressibility and acoustic wave velocities of different materials as described in the first six contributions of this chapter. Compressibility studies on garnet crystals with complex compositions and of the new Al-rich phases (NAL) are aimed to give insights on the properties of mid-ocean ridge basalt subducting down to the lower mantle.

The possible chemical nature of seismic velocities anomalies at the base of the lower mantle have been addressed by measuring the variation of wave velocities with pressure of polycrystalline $MgSiO_3$ perovskites containing both Fe^{3+} and Al using combined X-ray diffraction and ultrasonic measurements coupled with a synchrotron source. At the same time, the full elastic tensor of Fe^{2+}-bearing $MgSiO_3$ perovskite single crystals has been determined at different pressures using the Brillouin/high brilliance X-ray system installed at the BGI. Recently, nuclear inelastic scattering (NIS) has been used to measure wave velocities of (Mg,Fe)O producing, however, controversial values. A careful experiment performed at ESRF using samples synthesised and characterised at the BGI has been able to show that such discrepancy is likely due to the local nature of the NIS measurements.

A still open question is whether experiments performed in the laboratory at either quite high frequency or at zero frequency (as in the case of computational or static studies) can be used to interpret seismic wave velocities or whether dispersive effects need to be taken into account. A compilation of bulk and shear moduli values reported in the literature for MgO and obtained with different techniques reveals no clear trend as a function of frequency, though. Therefore the elastic moduli can be used for the interpretation of seismologic results at least for MgO.

Elastic properties are of course not the only physical properties which we can use to constrain the structure of the Earth's interior. Laboratory electrical conductivity data for example provide critical data on how the chemical and thermal state of the material influences its conductivity and can be used to interpret electromagnetic induction data which are more sensitive to temperature and iron content than seismic data. The electrical conductivity data collected for a Fe- and Al-rich $MgSiO_3$ perovskite presented in the seventh contribution show that the $Fe^{3+}/\Sigma Fe$ ratio and not just the total iron content will affect the conductivity significantly at mid-mantle depths.

Since the pioneering work of Ringwood, the use of analogue phases has been a powerful tool for understanding the properties of materials whose pressure and temperature stabilities are

difficultly accessible. The use of post-perovskite (Ppv) structured fluorides for example may provide better analogues for $MgSiO_3$ Ppv than $CaIrO_3$ or $CaPtO_3$ materials. In the last contribution neutron powder diffraction has been used to determine the structure and magnetic transition of $NaCoF_3$.

a. *Compressibility of an eclogitic garnet solid solution up to 16 GPa (C. Beyer, T. Boffa Ballaran and D.J. Frost)*

The knowledge of elastic properties of garnet solid solutions is crucial for understanding seismic profiles of subducting slabs and slab processes in general. The bulk moduli of the different garnet end-members vary significantly among each other. Moreover, the contribution of each end-member in more complex solid solutions and their excess volume terms are scarcely known. We have, therefore, undertaken a compressibility study of a synthetic garnet having a quite complex chemistry in order to assess the effect of cation substitutions on its *P*-*V* equation of state.

A garnet sample (46 mol.% pyrope, 19 mol.% almandine, 31 mol.% grossular, andradite and spessartine < 3 mol.%) was synthesized in a multianvil apparatus at 5.4 GPa and 1350 °C from a synthetic hydrous N-MORB starting material. The recovered garnet crystals show an idiomorphic shape and are free of chemical zonations. One crystal (70 x 60 x 35 μm^3) with sharp reflection profiles was selected and loaded into a Boehler-Almax diamond anvil cell (DAC) using anvil diamonds with culets of 500 µm and a rhenium gasket pre-indented to 78 µm with a 250 µm hole. Neon gas was loaded as hydrostatic pressure transmitting medium with a gas loading apparatus. A small ruby sphere loaded together with the garnet, was used as pressure sensor. Pressure was increased in ~ 1 GPa steps, with a relaxation time between each increment of at least 24h hours.

The unit cell parameters were measured up to 16 GPa using a 4 - circle Huber diffractometer equipped with a MoKα emitting X-ray tube. The unit cell volume, normalized with respect to its room pressure value, V/V_0, of the analysed garnet is plotted versus pressure in Fig. 4.4-1. Also shown are the data of three aluminous garnet end-members for comparison.

We fitted a 3rd order Birch-Murnaghan EOS through the collected 17 data points obtaining the following parameters: V_0 = 1469.4(4) $Å^3$, K_0 = 168(3) GPa, and K' = 4.4(4). The analysed garnet has a similar bulk modulus to grossular (K_0 = 168-175 GPa) and pyrope (K_0 = 171), whereas the effect of 20 mol.% almandine, which is relatively stiff (K_0 = 185 GPa) is negligible in spite of the suggested ideal mixing behaviour between pyrope and almandine. It is not yet clear why pyrope is significantly more compressible than almandine; a possible explanation may reside in the size of Mg^{2+} which is too small for the garnet dodecahedral site, allowing therefore a larger compression of this site in pyrope with respect to that in almandine. What is clear from these preliminary results is that the mechanism of compression

in garnets solid solutions cannot simply be derived from the behaviour of the end-members. In order to shed light on the compression mechanism of mixed garnets, we will perform a high-pressure structural study on the same garnet composition so far compressed to 16 GPa.

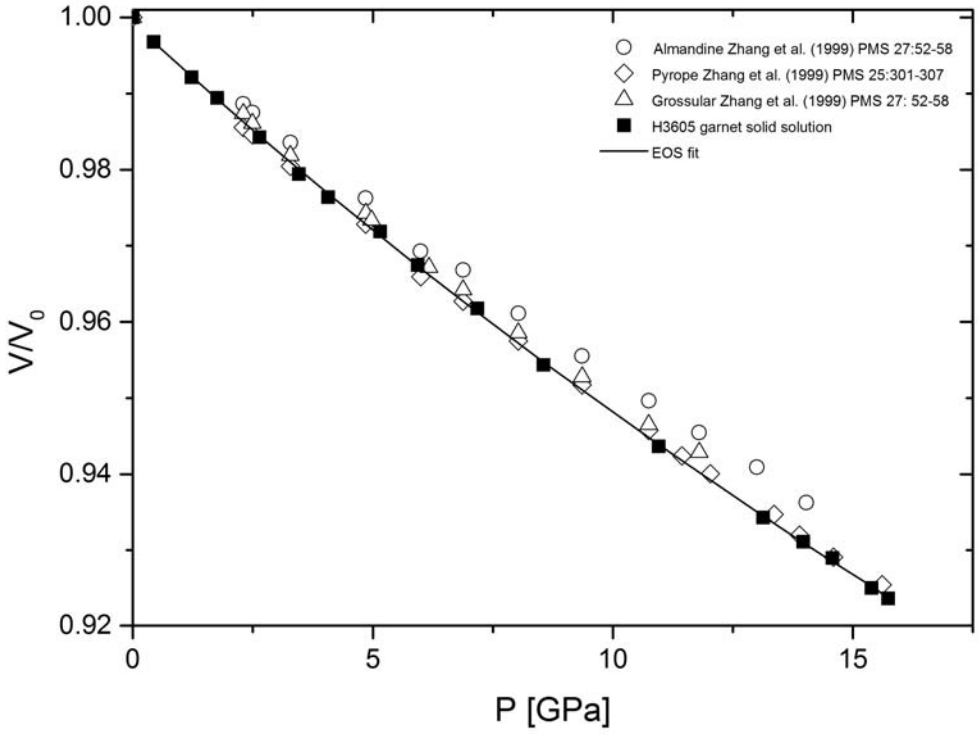

Fig. 4.4-1: Normalised unit-cell volume plotted as a function of pressure for almandine, pyrope and grossular end-member and for the analysed garnet sample.

b. *Elasticity of $Na_{1.18}Mg_{1.59}Al_{4.78}Si_{1.33}O_{12}$ NAL phase (M.G. Pamato, T. Boffa Bollaran, A. Kurnosov, D.J. Frost and D.M. Trots)*

At lower mantle conditions, subducting mid-ocean ridge basalt (MORB) can contain more than 20 % of an aluminium rich phase, which is referred to as NAL (short for new Al-rich) phase. NAL crystallising in MORB compositions exhibits complex solid solutions and has the general chemical formula $XY_2Z_6O_{12}$ with X being a large monovalent or divalent cation (Ca^{2+}, K^{+}, Na^{+}); Y a middle-sized cation (Mg^{2+}, Fe^{2+} or Fe^{3+}); and Z a small sized cation (Al^{3+} and Si^{4+}). NAL phases are potential hosts for alkali elements and, together with calcium ferrite (CF)-type phases, are considered to be a major mantle component of MORB at lower mantle conditions. The knowledge of its elastic properties and how they change with composition is therefore of crucial importance for understanding the bulk elastic properties of the lower mantle and thus the fate of subducted MORB. To date several studies have been conducted on the compression of NAL phases both in complex and simplified systems. However, large discrepancies in the equations of state can be observed among these studies, most likely due to uncertainties in the pressure determination. Moreover only in one study, a

single-crystal structural analysis has been reported. Every other study has dealt with powdered samples.

The aim of this study is hence to determine an accurate *P-V-T* EoS using NAL single-crystals. Pressures will be determined using the *P-V-T* EoS of a crystal of Sm-YAG which has been calibrated against an absolute pressure scale determination, performed by combining X-ray diffraction and Brillouin spectroscopy (see Trots *et al.* 2011, BGI Yearbook), whereas temperatures will be measured using a thermocouple placed close to the sample.

A first step of this project has been to develop a methodology for synthesising large single-crystals of NAL at conditions of the Earth's lower mantle. In fact, the growth of high quality single crystals of mantle minerals of more than 50-70 µm is extremely challenging and has been one of the major barriers to the study of single crystal elastic properties in the past. For this, a flux is required to promote melting for crystal growth. In particular, a fine balance between temperature, pressure and flux proportion has to be found. For the synthesis of the NAL single crystals it was necessary to perform experiments slightly above the dry melting solidus at temperatures in excess of 2300 °C and pressures of 20 GPa. This is due to a remarkable change in the melting behaviour of Na-rich compositions at high pressure. As a result, large single-crystals (up to 120 µm) of $Na_{1.18}Mg_{1.59}Al_{4.78}Si_{1.33}O_{12}$ were obtained. A suitable crystal of NAL optically free of defects was selected from the capsule and mounted on a glass fiber for single crystal X ray diffraction using an Xcalibur diffractometer (operated at 50 kV and 40 mA and equipped with a CCD detector) using Mo*K*α radiation (graphite monochromator).

A single-crystal structural refinement for the NAL phase has been performed. The crystal structure of the NAL phase synthesized in this study could be refined using the structural model reported in the literature, and is reported in Fig. 4.4-2. It consists of a double chain of $M1O_6$ octahedra with disordered occupancy of Al^{3+} and Si^{4+} that are connected by shared edges. Mg^{2+} occupies the M2 site (six fold coordinated triangular tunnel-like spaces along the **c**-axis and surrounded by three double chains of $M1O_6$ octahedra) whereas Na^{+} occupies the M3 site (tunnel-like cavity surrounded by six double chains of $M1O_6$ octahedra and coordinated by nine O atoms). Note that in the structural model reported in the literature, Na occupies a fixed position at the coordinate x = 0 y = 0 and z = 1/4, whereas the single crystal refinements in this study result in a very large displacement factor for Na, which could be explained with a large degree of disorder of the Na atoms along the tunnel.

The crystal (70 x 70 µm) has been doubled side polished to a thickness of approximately 15 µm and loaded in a piston cylinder diamond anvil cell, together with ruby and Sm-doped YAG as pressure standard, for the X-ray and Brillouin measurements. A neon gas, as hydrostatic pressure medium, was loaded into the sample chamber and a specially designed internal resistive heater was prepared and placed for high-temperature measurements. Brillouin spectra and density of NAL will be measured at high pressures and high temperatures up to pressures of 20 GPa and temperatures of 900 K.

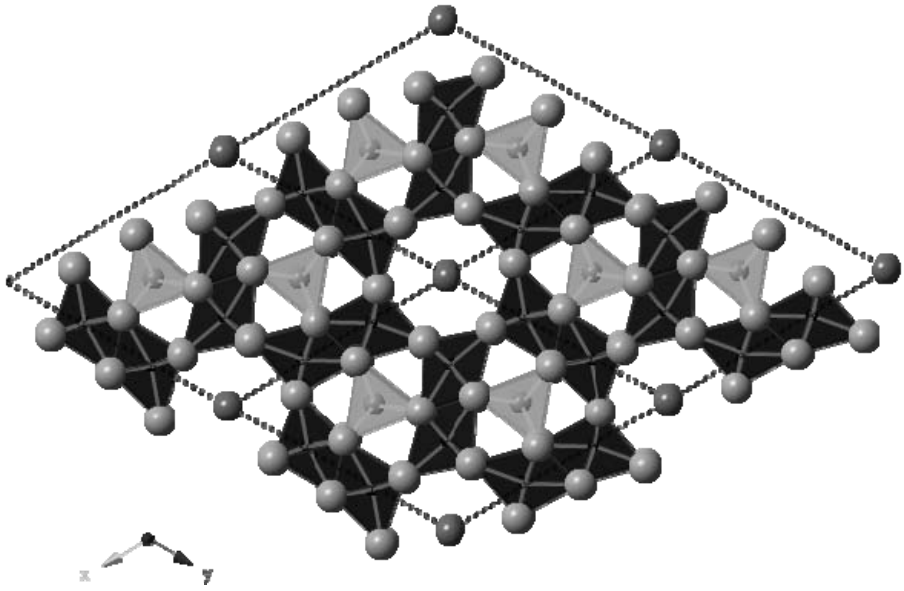

Fig. 4.4-2: Crystal structure of NAL phase projected along the *c* axis.

c. *The effects of Fe and Al substitution on ultrasonic wave velocities of magnesium silicate perovskite (J. Chantel/Grenoble, D.J. Frost, D. Novella, M.A.G.M. Manthilake and C.A. McCammon, in collaboration with Z. Jing and Y. Wang/Chicago)*

Magnesium-silicate perovskite is the most abundant mineral in the Earth's lower mantle. The composition of perovskite in the mantle is dominated by the $MgSiO_3$ component but it will also contain significant amounts of Al and Fe. In addition, possible chemical heterogeneities in the lower mantle, arising either from subduction of oceanic crust or the presence of primordial material, may also contain regions with perovskite enriched in Al and Fe. In order to interpret one dimensional seismic velocity profiles for the lower mantle, it is therefore crucial not only to determine velocities for the major mineral phases but also to assess how variations in major chemical substitutions may influence their elasticity.

Combined *in situ* X-ray and ultrasonic measurements were conducted up to 25 GPa and 1300 K at the 13-ID-D beam line of GSECARS, APS, on monomineralic hot-pressed powdered perovskite samples with compositions $(Mg_{0.962}Fe_{0.04})(Al_{0.025}Si_{0.98})O_3$ (2 % Fe-Al) and $(Mg_{0.932}Fe_{0.075})(Al_{0.049}Si_{0.943})O_3$ (5 % Fe-Al) presynthesized and fully characterized at the BGI. Ultrasonic measurements were conducted for both *P*- and *S*-waves using the pulse–echo method. The overall uncertainties of the present velocity measurements are within 0.5 % in both V_P and V_S. X-ray diffraction from the sample and the pressure markers was observed using an energy-dispersive system, and the sample length was measured with a high-resolution (1 pixel ~ 2 μm) charge-coupled device (CCD) camera (Fig. 4.4-3). Measurements were performed up to 26 GPa and approximately 1200 K. These results were fitted to a thermo-physical model in order to extrapolate the data to the temperature conditions at the top of the lower mantle.

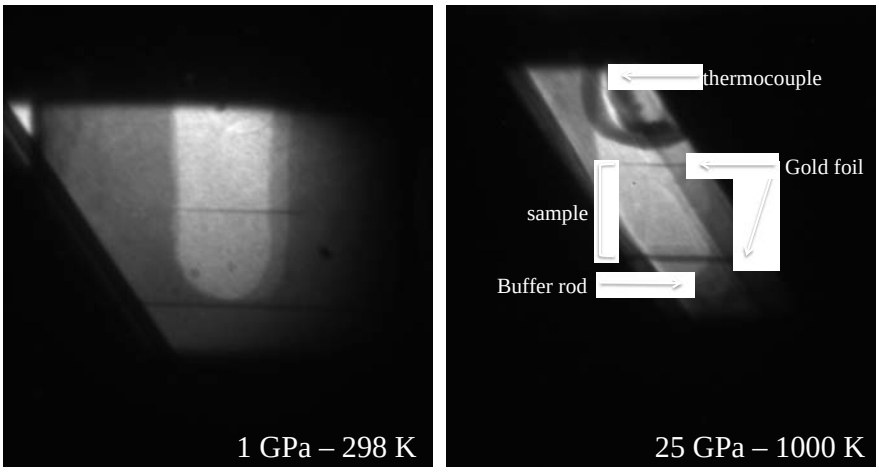

Fig. 4.4-3: X-ray radiography of the cell assembly under low and elevated pressure and temperature conditions. The diagonal window is framed by the tungsten carbide anvils.

The velocities measured for 2 % Fe-Al are about 3 % lower than for the $MgSiO_3$ end-member perovskite, for both compressional and shear waves. For the 5 % Fe-Al sample, the velocities are approximately 5.5 % lower than for $MgSiO_3$ perovskite. The results when compared with previous studies on pure and Fe-bearing perovskite, indicate that the bulk modulus of perovskite decreases with increasing Fe content, whereas the shear modulus decreases with increasing Al content. Moreover, the reduction in P-wave velocity with increasing temperature is greater for Fe and Al bearing perovskites.

The transformation of ringwoodite and garnet to magnesium silicate perovskite is considered to cause a discontinuity in seismic velocity at approximately 660 km. An absence of observed underside P wave reflections from the 660 km has puzzled seismologists for many years. While underside S reflections can be observed globally, strong corresponding P reflections are absent. This has motivated seismologists to propose that the magnitude in the change in bulk modulus across the discontinuity may be small. The results from this study are totally consistent with this observation. A calculation of the velocity change across the 660 km discontinuity for a bulk silicate earth composition along an average mantle adiabat, made using the results from this study is shown in Fig. 4.4-4. These estimates are compared with two one dimensional seismic reference models. The absolute seismic velocities in the region of the discontinuity may not be precisely depicted by the reference models, due to pay offs between the size and structure of the discontinuity and the velocity gradient over these depths. Although estimates for V_S at 660 km are slightly below the seismic models, a sharp discontinuity in *Vs* is predicted. However, the low bulk modulus estimated for perovskite containing plausible Fe and Al contents at 660 km, means that a jump in P velocity is absent across the transformation. These models are in excellent agreement with the reflection seismology observations for the 660 km discontinuity. The determined P velocities are significantly lower than those expected for the bulk of the lower mantle, however. The most plausible explanation for this is that the temperature dependence of the P wave velocity determined in this study at conditions compatible with the top of the lower mantle, may not extrapolate well into the bulk of the lower mantle.

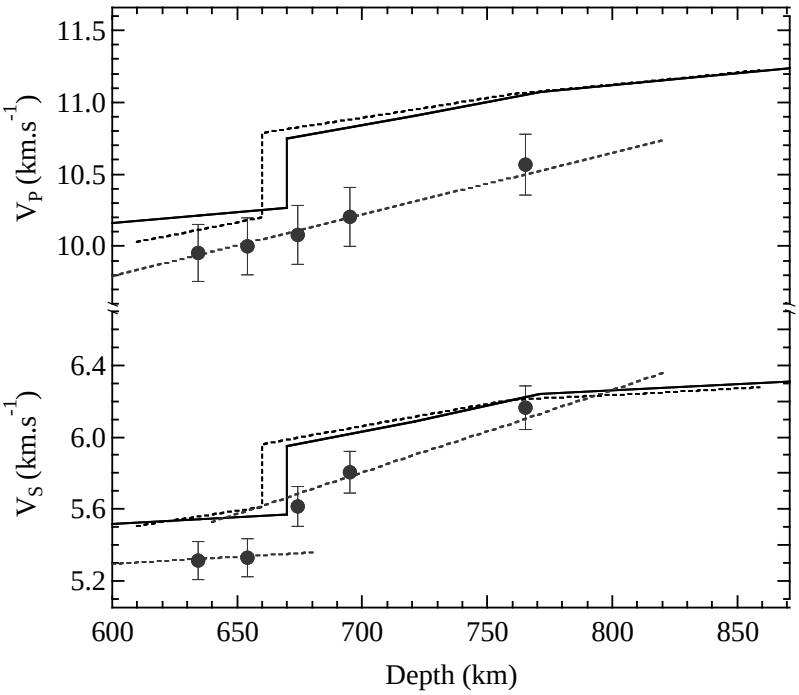

Fig. 4.4-4: Estimates for Vs and Vp of a bulk silicate Earth composition around the 660km discontinuity. Modelled compositions are shown as the filled circles calculated at the pressures and temperatures corresponding to 600-850 km depth. Data for (Mg,Fe)(Al,Si)O_3 perovskites and garnets are taken from the equation of state model determined in this study. Models for the other phases are taken from the literature. The continuous and dashed black curves show respectively PREM and AK135 seismic reference models for this region.

d. *Elastic properties of (Fe,Mg)SiO_3 perovskite single crystal at high pressures (A. Kurnosov, T. Boffa Ballaran, D.M. Trots and D.J. Frost)*

$MgSiO_3$ perovskite (with some Al and Fe) is considered to be the dominant mineral in the Earth's lower mantel and as such it dominates the seismic signature of the deep Earth. We can therefore expect that the seismic velocity anomalies observed at the base of the lower mantle, which are thought to have a chemical origin, are due to $MgSiO_3$ perovskite with a composition distinct from that of the surrounding mantle. The lack of appropriate laboratory data collected at the relevant pressures and temperatures, however, prevents a direct comparison with the observed seismic velocities and hence makes it difficult to constrain the chemical composition and structure of the Earth's interior. A major challenge for obtaining the required experimental data is that single-crystal measurements are necessary for constraining the full elastic tensor of this material, requiring the synthesis and recovering of high-quality single-crystals as well as accurate double-side polishing of relatively small samples.

Here we report the first high-pressure single-crystal study of $MgSiO_3$ perovskite containing 4 % of Fe^{2+} aimed to obtain the effect of Fe on the elastic behaviour of perovskite. To this end a

combined single-crystal X-ray diffraction and Brillouin scattering study has been performed in order to measure both velocities and density simultaneously. High quality crystals were selected from a run-product synthesized at 25 GPa and 1300 °C using a multianvil press. The crystals were mechanically polished from both sides to a thickness of 10 µm and loaded in diamond anvil cells with an optical opening angle of 80º together with He as pressure transmitting medium.

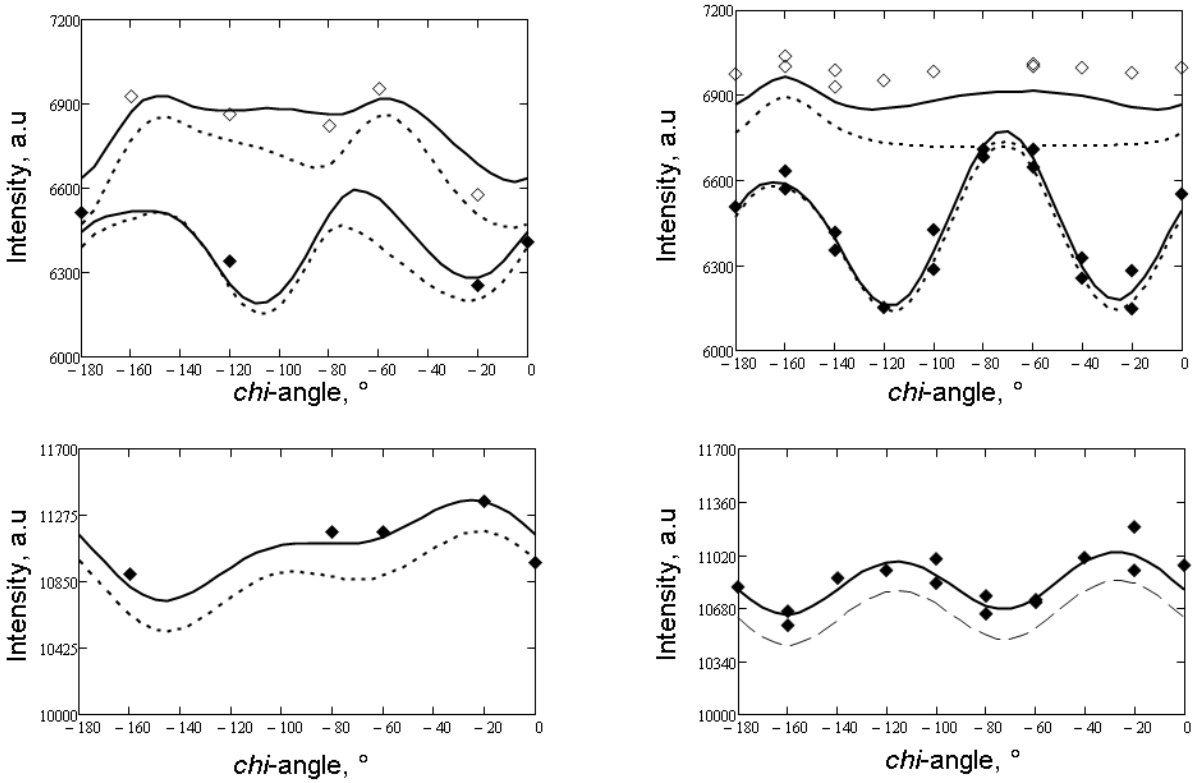

Fig. 4.4-5: Dispersion curves of two differently oriented crystals of Fe-$MgSiO_3$ perovskite at 3.1 GPa. The symbols represent the sound velocities measured experimentally. The solid lines are the fit of Christofel's equation to both sets of data simultanously, whereas the dotted lines represent the sound velocity values calculated for an iron-free $MgSiO_3$ perovskite having the same crystallographic orientation as our crystals using the room pressure elastic constants reported in the literature.

The elastic tensor of $MgSiO_3$ perovskite is characterised by 9 independent C_{ij} constants which can be extracted by fitting the dispersion curves of the two shear and one compression velocities collected at different crystallographic orientations for each pressure, once density is known. Because of significant correlations between the constants we need to measure at least two differently oriented samples at any pressure. C_{ij} have been obtained so far at 3.1 and 6.9 GPa. We have not collected Brilluoin spectra at room pressure because even using a laser power of only 100 mW causes major damage to the sample surface. The dispersion curves obtained at 3.1 GPa for both crystals as well as fitting of the full elastic tensor are reported in Fig. 4.4-5. The bulk modulus values obtained from the C_{ij} at both pressures using the Voigt

approximation for the orthorhombic system are in excellent agreement with the values calculated at the same pressure using the equation of state parameters of the same sample reported in a recent study. The final goal of this project is to obtain the variation of Cij with pressure up to at least 45-50 GPa to understand whether an elastic softening is associated with a decrease of the shear strain component of this sample with respect to pure $MgSiO_3$ perovskite observed above 40 GPa (see Boffa Ballaran *et al.* Yearbook 2011).

e. *Effect of iron composition on the elastic wave velocities of (Mg,Fe)O (R. Sinmyo, C. McCammon, K. Glazyrin, L. Dubrovinsky and I. Kupenko, in collaboration with V. Potapkin, A.I. Chumakov, R. Rüffer and A. Kantor/Grenoble)*

The Earth's lower mantle constitutes about half of the Earth in volume and therefore plays a major role in determining the Earth's bulk chemistry, structure and dynamics. The chemical composition of the lower mantle can be estimated from a comparison between observed seismic wave velocities and laboratory-measured elastic wave velocities of minerals under high pressure. The elastic wave velocity is commonly determined by Brillouin spectroscopy, ultrasonic measurement, etc. Recently, nuclear inelastic scattering (NIS) measurements have been applied to determine elastic wave velocities of lower mantle minerals. However, the reported sound velocities of (Mg,Fe)O ferropericlase by NIS were considerably lower than the velocities obtained from other methods, such as Brillouin spectroscopy or ultrasonic measurements. One possible explanation for this discrepancy may be the existence of a short-range structure of iron in the (Mg,Fe)O crystals, given the local scale of the measurements. In fact, a solid solution involving iron exchange on one of the crystallographic sites can contain a mixture of "phases", each with a different next-neighbor configuration of iron and hence effectively a different iron composition.

In order to test this hypothesis, we measured elastic wave velocities of $(Mg_{1-x}Fe_x)O$ ferropericlase by using NIS measurements. Fine grained MgO and Fe_2O_3 (95 % enriched in ^{57}Fe) were grounded together for 1 hour. Mixtures were then heated at 1273 K for 1 day in CO-CO_2 gas-mixing furnace, in which oxygen fugacity was controlled to the value of log fO_2 = -21. A Kawai-type multianvil press was used for high-pressure and -temperature generation. The sample was loaded into a Re capsule and then packed into a MgO container. $LaCrO_3$ was used as a heater. A total of six compositions ranging between x = 0.07 and x = 0.77 were synthesised at 14 GPa and 1673 K. NIS measurements were carried out at ESRF under ambient conditions. The fitting of the resulting good quality spectra allowed us to determine the partial phonon density of states with good accuracy (Fig. 4.4-6). However, the Debye sound velocity value calculated for each sample was smaller than that obtained from other methods. Recalculating the Debye velocity on the basis of a mixture of different iron next-neighbour configurations with different compositions resulted in a better agreement with the results obtained from other methods (Fig. 4.4-7). This recalculating method can also be applied to high-pressure data by using a combination of established EOS data of MgO and FeO.

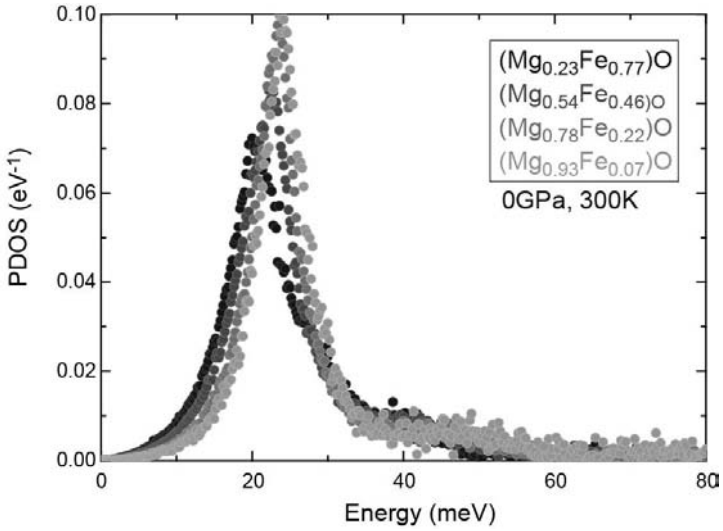

Fig. 4.4-6: Partial density of phonon states for four compositions of (Mg,Fe)O derived from NIS measurements at ambient conditions.

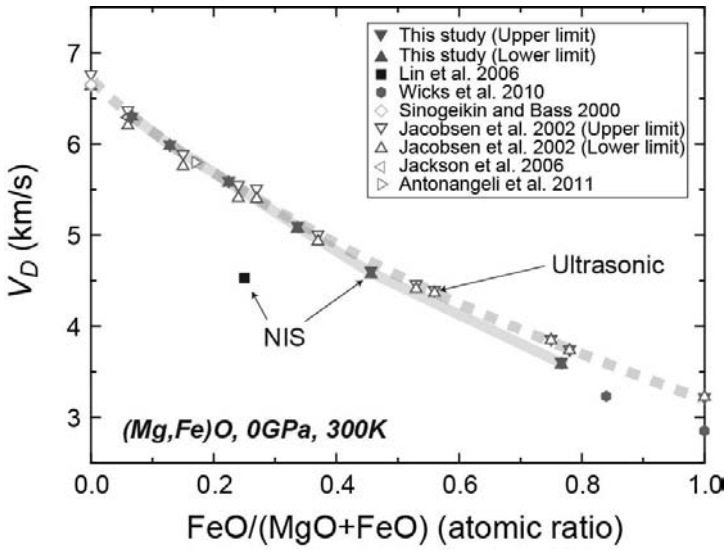

Fig. 4.4-7: Variation of the Debye sound velocity (V_D) after recalculation as a function of iron composition for our NIS data (filled triangle) compared with values from the literature. Filled symbols: NIS data; open symbols: data collected with other methods (Brillouin spectroscopy, ultrasonic measurements and inelastic X-ray scattering measurements). Lines represent velocities determined in this study (bold line) and from ultrasonic measurements (dashed line).

f. *Dispersion of elastic constants in MgO (G. Steinle-Neumann and H. Mohseni)*

Models of Earth structure are based on measurements of the propagation of acoustic waves excited by earthquakes through the interior of our planet, and provide us with a picture of the shear and compressional wave velocity with depth. Combined with density models obtained

from free oscillations the shear and bulk modulus of the Earth's interior can be determined. Natural seismic waves range in frequency (ν) between 0.1 mHz (free oscillations) and 10 Hz (body waves), but their interpretation is based on laboratory experiments and computational work in mineral physics which operate at very different frequencies: on the one hand, experiments are typically performed at much higher ν (typically MHz – THz); on the other hand, static compression experiments and computations yield zero frequency results. The question whether values obtained in the laboratory or computer are applicable to seismic frequencies or whether elastic parameters are dispersive, *i.e.*, frequency dependent, remain largely unexplored in the literature. We have compiled a large database of elastic moduli on MgO at ambient conditions, high temperature, and high pressure from the literature to see whether elastic parameters do or do not depend on frequency.

We have chosen MgO for this study for several reasons: (i) it is the second most abundant mineral in the Earth's lower mantle, and hence of geophysical interest; (ii) MgO is considered a prototype oxide due to its structural simplicity (B1 cubic); (iii) MgO is stable in the B1 structure over a wide range in temperature and pressure; (iv) with only three independent elastic constants (C_{11}, C_{12} and C_{44}) the elastic constant tensor is simple; (v) MgO is widely studied in geo- and material sciences, and a large number of experiments on its elastic moduli with various techniques have been published. Generally speaking three groups of experimental approaches exist: (i) ultrasonic resonant methods can only be applied to relatively large unconfined samples at ambient pressure and use frequencies of 1-3 MHz. In the other hand, ultrasonic wave speed measurements cover a wide ν spectrum from 10 MHz to 2 GHz, depending on the sample size. At ambient pressure and in the multianvil press transducers with frequencies in the 10-60 MHz are used, in the diamond anvil cell the frequencies are in the GHz range. (ii) Optical methods include sideband fluorescence and Brillouin spectroscopy in the 500 THz range, and can be applied to transparent samples in optically accessible high-pressure devices. The sideband method allows access to acoustic phonons by the introduction of a fluorescing ion and in Brillouin spectroscopy the incident photons couple to the phonons of the lattice. (iii) Inelastic X-ray scattering provides access to the phonon frequencies through energy transfer from the high brilliance X-rays to the phonons (ν ~ 600 PHz), and hence the acoustic phonons.

Figure 4.4-8 shows the aggregate moduli (the adiabatic bulk modulus K_S and the shear modulus G) at ambient conditions as a function of log ν. With the exception of the GHz ultrasonic data (log ν = 9) all adiabatic zero pressure bulk moduli fall in the range 161-164 GPa, and no frequency dependence can be detected. This value is also consistent with the zero frequency limit as established by lattice dynamics computations (162.4 GPa at 300 K) and static compression experiments where the bulk modulus (162.5-163.5 GPa) is obtained from a *P-V* equation of state fit. The spread of data for the shear modulus is slightly larger, with the value of G in the range 128-134 GPa. Again, no dependence on the frequency is apparent, and the lattice dynamics simulations for G (127.6 GPa) yield a result that is consistent with the experiments. For the individual elastic constants the situation is similar: Within the

experimental uncertainty no frequency dependence can be observed and the spread of moduli is limited, with 5 GPa for the longitudinal constant C_{11} being the largest (3 GPa for C_{44} and 2 GPa for C_{12}). With a smaller number of experiments at high pressure or high temperature, no trend can be established.

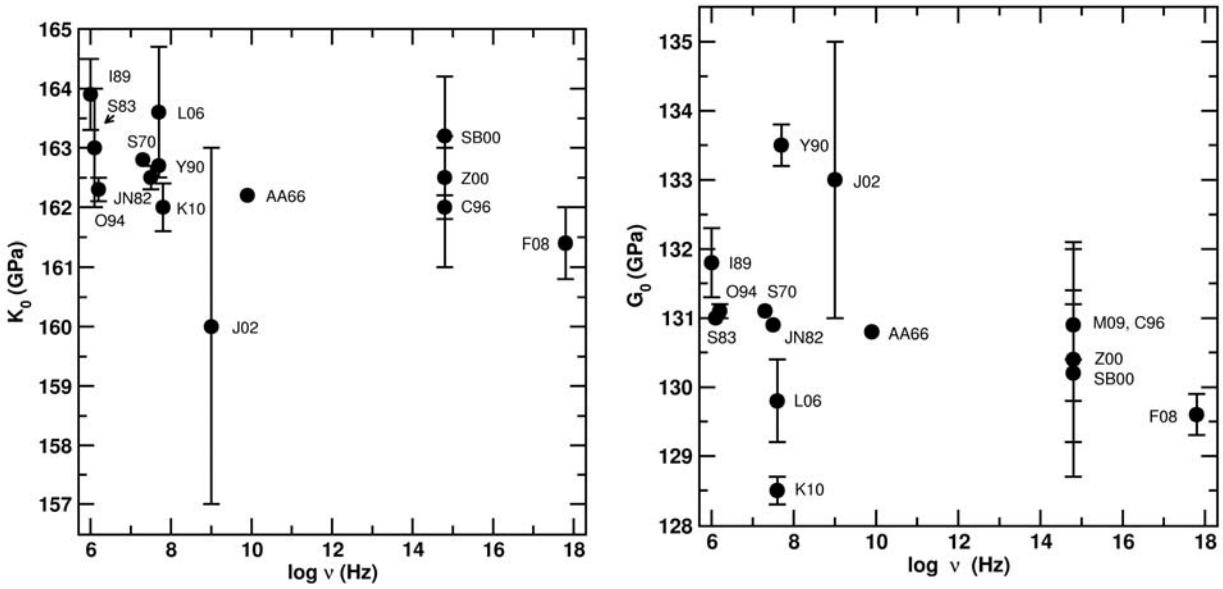

Fig. 4.4-8: Adiabatic bulk (left) and shear modulus (right) of MgO at ambient conditions for different excitation frequencies. The data points are from Anderson and Andratch, *J. Am. Ceramic Soc.* 8, 404, 1966 (AA66), Chopelas, *Phys. Chem. Minerals* 23, 25, 1996 (C96), Fukui *et al.*, *J. Synchr. Rad.* 15, 618, 2008 (F08), Isaak *et al.*, *Phys. Chem. Minerals* 16, 704, 1989 (I89), Jackson and Niesler, in *High Pressure Research in Geophysics*, pg. 93, 1982 (JN82), Jacobsen *et al.*, *J. Geophys. Res.* 107, B22037, 2002 (J02), Kono *et al.*, *Phys. Earth Planet Inter.* 183, 196, 2010 (K10), Li *et al.*, *J. Geophys. Res.* 111, B11206, 2006 (L06), Murakami *et al.*, *Earth Planet Sci. Lett.* 277, 123, 2009 (M09), Oda *et al.*, *J. Geophys. Res.* 99, 15517, 1994 (O94), Sinogeikin and Bass, *Phys. Earth Planet. Inter.* 120, 43, 2000 (SB00), Spetzler, *J. Geophys. Res.* 75, 2073, 1970 (S70), Sumino *et al.*, *Phys. Chem. Minerals* 9, 38, 1983 (S83), Yoneda, *J. Phys. Earth* 38, 19, 1990 (Y90) and Zha *et al.*, *Proc. Natl. Acad. Sci. USA* 97, 13494, 2000 (Z00).

Based on our compilation it appears that, aside from possible anelastic effects, the elastic moduli obtained in the laboratory for a relatively stiff material like MgO can be used for the interpretation of seismologic results. This can be further understood if one considers the phonon dispersion curves for MgO from neutron inelastic scattering: the individual acoustic phonon branches show almost linear behaviour up to ~ 4 THz frequencies and 0.4 wave vectors between the center and the high symmetry points on the edge of the Brillouin zone. For other minerals, such as SiO_2 quartz the situation is different: the phonon dispersion curves show a deviation from linear behaviour at much lower frequency and wave vector, and the bulk modulus is considerably lower than in MgO. However, quartz has not been studied as extensively in elasticity experiments.

g. *Effect of iron oxidation state on the electrical conductivity of the Earth's lower mantle (C. McCammon, L. Dubrovinsky, V. Potapkin/Grenoble, K. Glazyrin, C. Prescher, I. Kupenko and R. Sinmyo; A.I. Chumakov, R. Rüffer and A. Kantor/Grenoble; G.V. Smirnov/Moscow)*

Electromagnetic induction data offer an important complement to seismic data with respect to lower mantle modelling, since the former are more sensitive to temperature and iron content, while the latter better constrain the mineralogy. Laboratory electrical conductivity data of the relevant minerals are an important component of the approach, since they provide critical data on how the chemical and thermal state of the material influences the conductivity. Laboratory measurements of single-phase $(Mg,Fe)(Si,Al)O_3$ perovskite show a decrease in conductivity above 50 GPa (Fig. 4.4-9), comparable to the electrical conductivity decrease reported in the literature caused by spin crossover of Fe^{2+} in (Mg,Fe)O. The drop in $(Mg,Fe)(Si,Al)O_3$ perovskite conductivity has been attributed in the literature to a high-spin (HS) to low-spin (LS) transition of Fe^{3+}; however this explanation is ruled out by our recent results that show no Fe^{3+} spin crossover in $(Mg,Fe)(Si,Al)O_3$ perovskite at lower mantle conditions (BGI Annual Report 2011).

To investigate the relative contributions of Fe^{2+} and Fe^{3+} to the electrical conductivity, we measured the electrical conductivity of $Mg_{0.6}Fe_{0.4}Si_{0.63}Al_{0.37}O_3$ perovskite (93 % $Fe^{3+}/\Sigma Fe$) at high pressure and high temperature using a split gasket configuration with a laser heated diamond anvil cell. In contrast to the large drop seen in samples dominated by Fe^{2+}, there is a continuous increase in electrical conductivity with pressure (Fig. 4.4-9). Such behaviour strongly suggests that the conductivity drop in samples dominated by Fe^{2+} is due to the HS to intermediate-spin (IS) transition in Fe^{2+} (BGI Annual Report 2007) where electron mobility is reduced due to the spin transition, analogous to the behaviour of (Mg,Fe)O. The greater drop at high temperature (grey circles in Fig. 4.4-9) is consistent with the increasing stability of the IS state with temperature. Previously temperature and total iron content have been considered to have the greatest influence on lower mantle electrical conductivity profiles, but our data show that $Fe^{3+}/\Sigma Fe$ will also affect conductivity significantly at mid-mantle depths (1200-1900 km).

A complementary structural study on single crystal $(Mg,Fe)(Si,Al)O_3$ perovskite has shown that $Fe^{3+}/\Sigma Fe$ will also affect bulk sound velocity in the lower mantle (BGI Annual Report 2011); hence joint inversion of electromagnetic and seismic data based on these new data will likely yield different results. For example the superadiabatic temperature gradient inferred in the literature for the lower mantle from such a joint inversion may not be required due to the reduced electrical conductivity of silicate perovskite resulting from the HS-IS transition. Three-dimensional inversions of electromagnetic data are now possible, and literature reports show variations of more than one order of magnitude, many of which are correlated with fast and slow regions of seismic tomography models. Our new data indicate that for silicate perovskite with lower mantle composition, a lower $Fe^{3+}/\Sigma Fe$ ratio will cause lower conductivity (reduction of conductivity due to the Fe^{2+} HS-IS transition) and a higher bulk sound velocity. Indeed many regions were found in literature studies to show such a correlation, which could be indicative of bulk mantle properties away from areas associated

with subduction. Our results provide improved constraints for forward modelling of electromagnetic data as well as for joint inversion of electromagnetic and seismic data, providing a new probe of heterogeneity in the lower mantle.

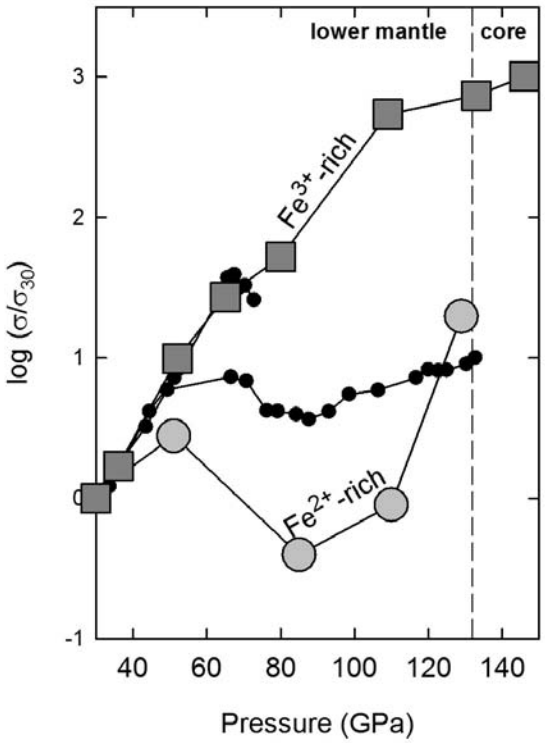

Fig. 4.4-9: Effect of pressure on the relative electrical conductivity of $(Mg,Fe)(Si,Al)O_3$ perovskite. Grey squares indicate new data for $Mg_{0.6}Fe_{0.4}Si_{0.63}Al_{0.37}O_3$ perovskite ($Fe^{3+}/\Sigma Fe$ ~ 93 %) collected at 1800 K. Also shown are two sets of literature data for $Mg_{0.9}Fe_{0.1}SiO_3$ perovskite ($Fe^{3+}/\Sigma Fe$ ~ 12 %) at room temperature (small black circles) [Ohta *et al.*, Phys. Earth Planet. Int. 180: 154, 2010] and a pyrolite assemblage ($Fe_{pv}^{3+}/\Sigma Fe_{pv}$ ~ 30 %) at 1800 K (grey circles) [Ohta *et al.*, Earth Planet. Sci. Lett. 289: 497, 2010]. Data are plotted relative to the conductivity values at 30 GPa (σ_{30}).

h. *The crystal structure and magnetism of $NaCoF_3$ post-perovskite by neutron diffraction (D.P. Dobson, A. Lindsay-Scott, I.G. Wood and A. Wills/London; N. Walte; R.I. Smith/Didcot)*

The post-perovskite (Ppv) structured fluorides are thought to provide better analogues to $MgSiO_3$ Ppv than the $CaIrO_3$ and $CaPtO_3$ analogues which have been used in the past. The main disadvantage of the fluoride Ppv's is that they are only stable above ~ 15 GPa meaning that multianvil syntheses are necessary, resulting in small sample volumes which may preclude the use of certain techniques. Neutron diffraction is one of such techniques, but it is distinct from X-ray diffraction in the fact that it can be readily used to investigate magnetic structures, the position of protons and selective element scattering in amorphous materials. POLARIS is a medium-resolution powder diffraction instrument at the ISIS pulsed neutron

source and, with the improved flux provided by a recent upgrade, it should be capable of collecting high-quality structural datasets from multianvil samples in reasonable counting times.

In order to test the upgraded POLARIS instrument we have used the 5000 tonne press at the BGI to produce a ~ 10 mm^3 sample of $NaCoF_3$ Ppv for powder diffraction studies. The neutron diffraction pattern is presented in Fig. 4.4-10 left. High-quality crystal structure refinements were possible with data collections as short as 4h. $NaCoF_3$ Ppv undergoes a magnetic transition to a canted antiferromagnetic structure at ~ 25 K (Fig. 4.4-10 right) and we intend to determine the magnetic structure at 10 K using POLARIS: this would require two synthesis runs on the 5000 tonne press to provide sufficient sample scattering compared to the background from the cryostat.

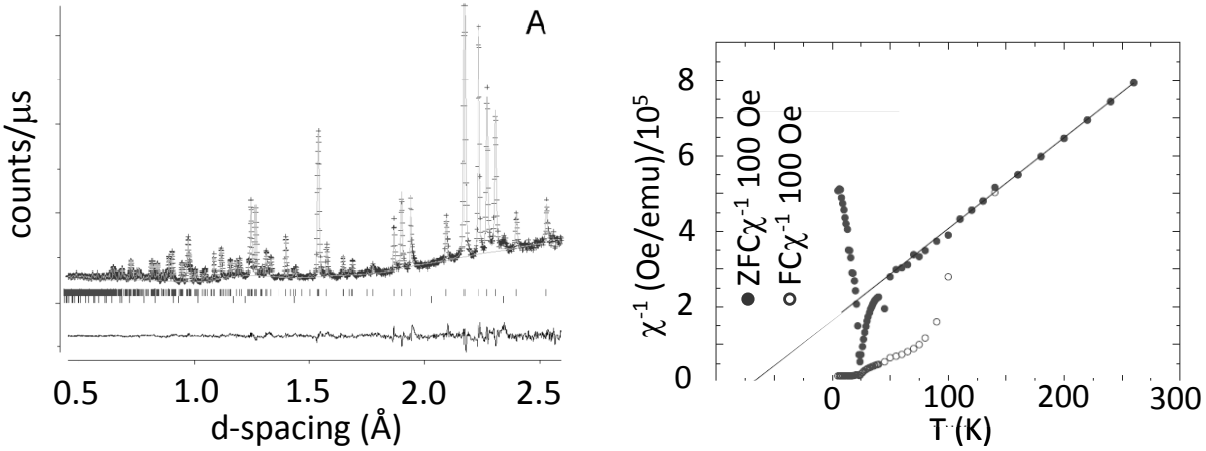

Fig. 4.4-10: Left: Neutron diffraction pattern of $NaCoF_3$ PPv collected on POLARIS at 298 K. Dots are data points and the solid line is the Riedvelt refinement of the structure. Ticks indicate positions of reflections from $NaCoF_3$ (top) and Au (bottom). The difference between the refinement and observations is plotted at the bottom. Right: Magnetic susceptibility measured as a function of temperature showing the antiferromagnetic transition at around 12 K.

4.5 Fluids, Melts and their Interaction with Minerals

The Earths atmosphere is ultimately the product of the degassing of the mantle by volcanic activity. At the same time, the exsolution of volatiles from the magma is the driving force behind all explosive volcanic activity. An essential step in volatile release is the formation and growth of gas bubbles, which may also lead to the disruption of the magma. So far, these processes have only been studied by classical quench experiments, where only the texture of a sample after the experiment may be studied, but not the evolution of texture during the run. The first contribution in this section of the annual report describes experiments in which the nucleation and growth of bubbles in magmas has for the first time been observed *in situ* at high temperature. The experiments show, among other things, that direct coalescence – and not Ostwald ripening, as often assumed – is the main mechanism for the coarsening of the bubbles.

Two contributions in this section look at the release of volatiles, *i.e.*, of sulfur and nitrogen during volcanic eruptions. In oxidized felsic magmas, most of the sulfur may be locked away as anhydrite $CaSO_4$, so that it cannot be easily transferred into a gas phase on the short timescales of a typical Plinian eruption. It is shown that anhydrite stability is well described by the solubility product of CaO and SO_3 in the melt and that this solubility product strongly increases with temperature. The data on nitrogen partitioning between hydrous fluids and granitic or basaltic melts are the first ever reported at pressures relevant for volcanic systems. A special protocol for electron microprobe measurements had to be developed to quantify nitrogen at very low concentration in quenched glasses.

The last two contributions in this section investigate the behaviour of water in the upper mantle. The partition coefficients of water between mantle minerals and silicate melts have been measured at 6 GPa, yielding a bulk partition coefficient of water between peridotite and melt of 0.018. Together with further experimental data, this suggests that hydrous melts are not stable at a depth of 180 km in the upper mantle. Finally, the critical curve in the system H_2O-H_2 has been mapped out throughout the upper mantle. The data show that immiscibility between water and hydrogen may occur along a present-day mantle geotherm, but even along a much hotter Archean geotherm. Outgassing of nearly pure hydrogen from a reduced mantle may have been an important factor in stabilizing an early reducing atmosphere on Earth.

a. In situ *observation of bubble evolution in silicate melts: implications for volatile release in explosive volcanic systems (M. Masotta, H. Ni and H. Keppler)*

Explosive volcanic eruptions are powered by volatiles exsolving from magmas during their ascent toward Earth's surface. The solubility of volatile species (mostly H_2O and CO_2) is related to magmatic pressure and melt composition. The combination of these two parameters determines the depth at which volatiles may exsolve from the melt, generating a fluid phase,

the expansion of which controls the effusive or explosive behaviour of magmas during volcanic eruptions. The eruptive style is thus determined by the mechanisms through which bubbles grow, coalesce and form networks, leading then to magmatic degassing and fragmentation. Information on these mechanisms can be obtained through bubble distribution analysis of volcanic rocks or of experimentally produced samples. However, both natural samples and experimental run products record only a single final frame of the entire exsolution process. For this reason, truthful modelling of the exsolution process is possible only through the direct observation of the process at magmatic conditions. In this study, we use the moissanite cell assembly to perform controlled exsolution experiments. We use the direct in-situ observation under the microscope to constrain the mechanisms of bubble nucleation and growth.

Preliminary experiments performed at 1 atm indicate that bubble nucleation starts already at very low values of volatile super-saturation (H_2O and CO_2 contents in the melt less than 0.1 wt.%) and that the exsolution of the gas phase causes a major volumetric expansion of the sample upon heating (Fig. 4.5-1). This expansion is likely to be even larger under conditions of higher volatile super-saturation and therefore increases the explosive potential of volatile-saturated magmas.

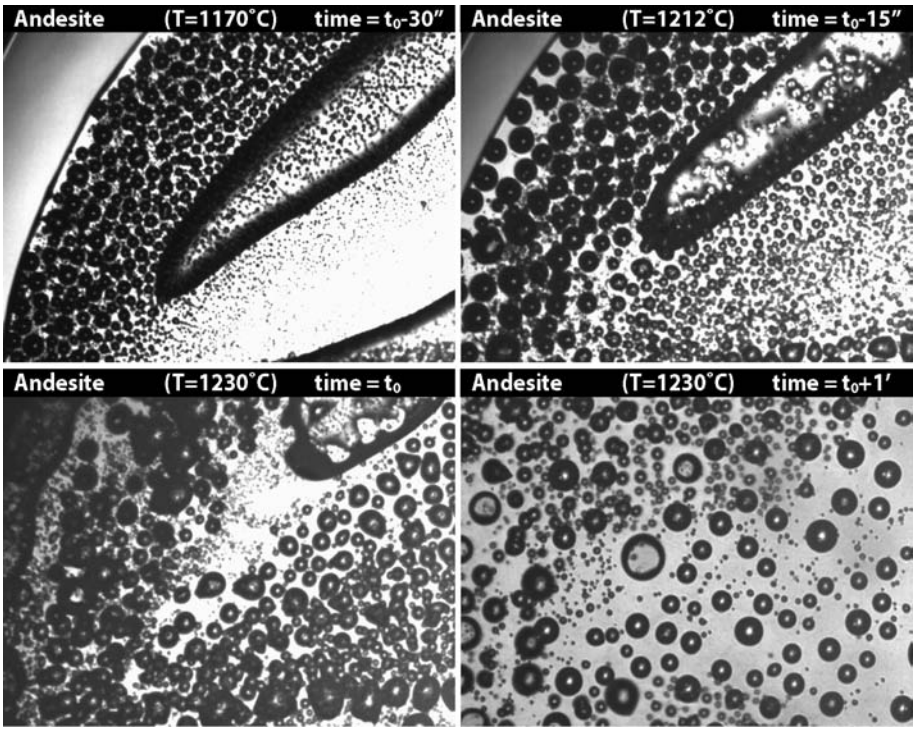

Fig. 4.5-1: Heating experiment using an andesitic glass in the moissanite cell. Heating rate is ca. 167 °C/min; the 1230 °C setpoint is reached at t_0. Note the expansion of the melt due to the exsolution of volatiles in the 30 min before t_0 is reached and the coarsening of bubbles toward the edge of the sample.

Bubble nucleation always occurs as a single event and is then followed by bubble accretion. The initial bubble number density (N_B) ranges between $8*10^7$ and $2*10^8$ cm^{-3} for the different melt compositions and decreases exponentially with time (Fig. 4.5-2). The composition of the melt primarily controls the initial N_B and the bubble growth rate. Bubble coalescence seems to be the preferential accretion mechanism during the early stage of the experiment, whereas Ostwald ripening takes place only at lower values of bubble number density ($N_B<5*10^7$) when bimodal bubble size distributions are eventually achieved.

The nucleation of larger bubbles in the basaltic-andesitic melts indicates a lower surface tension for the less viscous melts as compared to the rhyodacitic melt. As a result, basaltic and andesitic melts could be more susceptible to failure immediately upon vesiculation than at later times, when the increasing permeability decreases the explosive potential. On the other hand, the higher strength of the rhyodacitic melt may make its fragmentation more energetic.

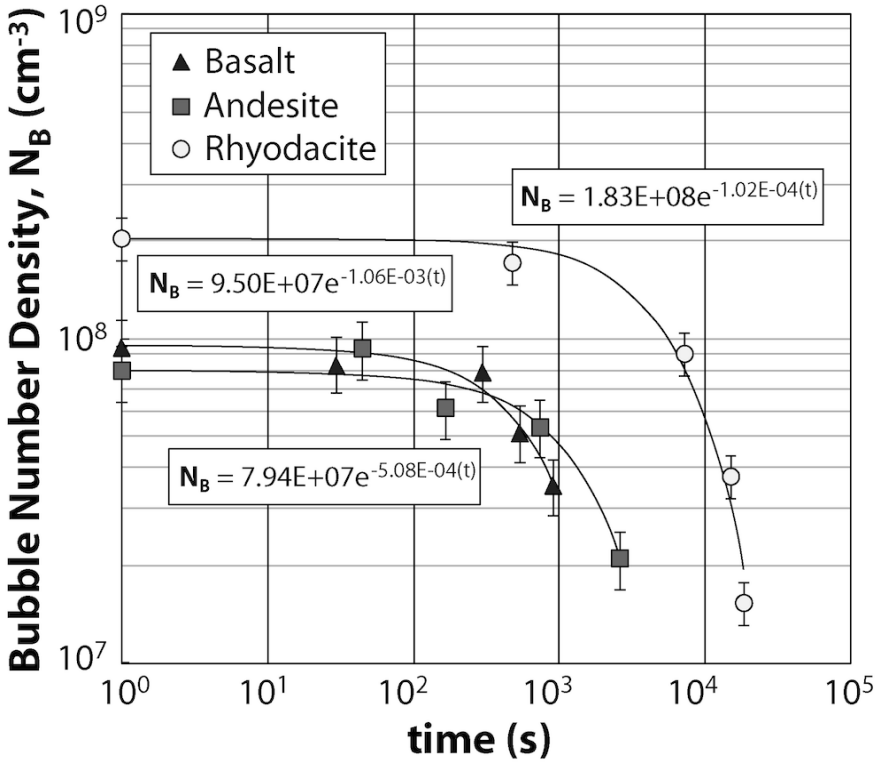

Fig. 4.5-2: Variation of bubble number density (N_B) with time for different melt compositions (basalt 1240 °C; andesite 1230 °C; rhyodacite 1100 °C). The N_B decreases exponentially with increasing time. Time refers to the time elapsed after reaching the setpoint temperature (t_0).

b. *Solubility of anhydrite $CaSO_4$ in felsic melts (R. Huang and H. Keppler)*

The effect of volcanic eruptions on climate is mostly due to the release of sulfur compounds. The amount of sulfur that may be potentially extracted into a fluid phase depends, among

other things, on the stability of minerals that may lock up sulfur and make it unavailable for transfer into the gas phase. Under reducing conditions, pyrrhotite FeS is stable in many basaltic magmas and therefore very much limits the amount of sulfur that may be released upon eruption. While pyrrhotite solubility is quite well studied, the stability of anhydrite $CaSO_4$ is not well known. Anhydrite is often found as accessory phase in felsic magmas at high oxygen fugacity. We therefore carried out a systematic study on the stability of anhydrite in granitic melts in the simplified system Na_2O-K_2O-CaO-Al_2O_3-SiO_2-S-H_2O, under water-saturated conditions. Experiments were carried out at 2 kbars in rapid-quench cold seal vessels at 750-950 °C, either at the intrinsic oxygen fugacity imposed by the autoclave (0.5 to 1 log unit above the Ni-NiO buffer) or with a Re-ReO_2 buffer. Run products usually contained anhydrite crystals in a matrix of quenched hydrous glass.

Figure 4.5-3 shows for a constant temperature of 850 °C the relationship between the sulfur content and the CaO content of granitic melts coexisting with anhydrite. There is clearly an inverse relationship between CaO and SO_3, which is expected to be the main sulfur component in the melt at these oxidizing conditions. This suggests that upon dissolution, anhydrite dissociates in the melt according to

$$CaSO_4 \text{ (anhydrite)} = CaO \text{ (melt)} + SO_3 \text{ (melt)}$$

so that the solubility product of the concentration of CaO and SO_3 is constant.

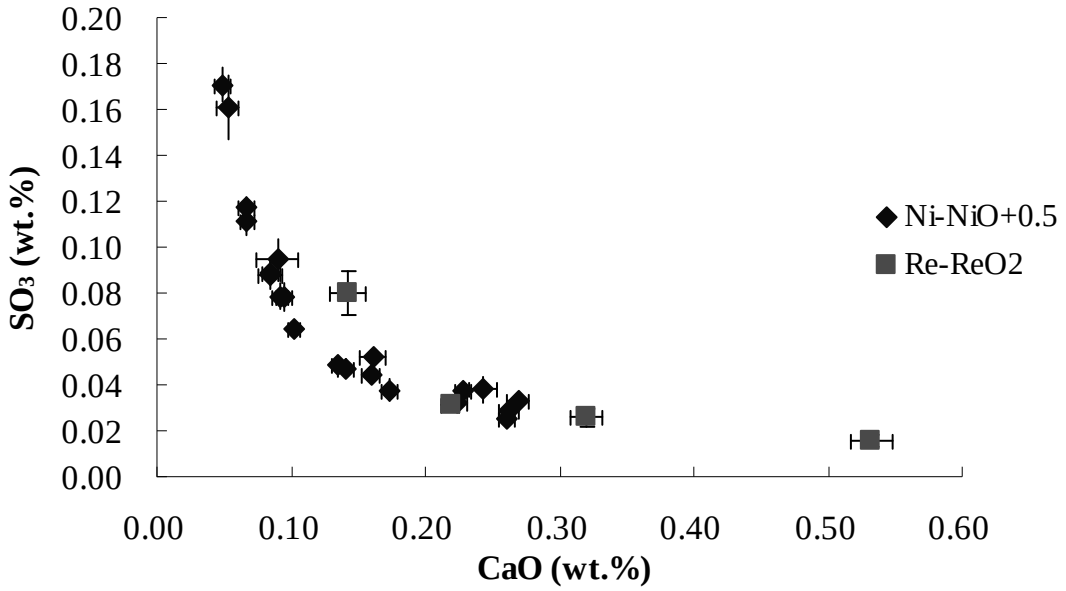

Fig. 4.5-3: CaO and SO_3 contents of hydrous granitic melts in equilibrium with anhydrite at 850 °C and 2 kbar. The inverse relationship between CaO and SO_3 suggests that the solubility product [CaO][SO_3] is constant. Data are from microprobe analyses of quenched glasses.

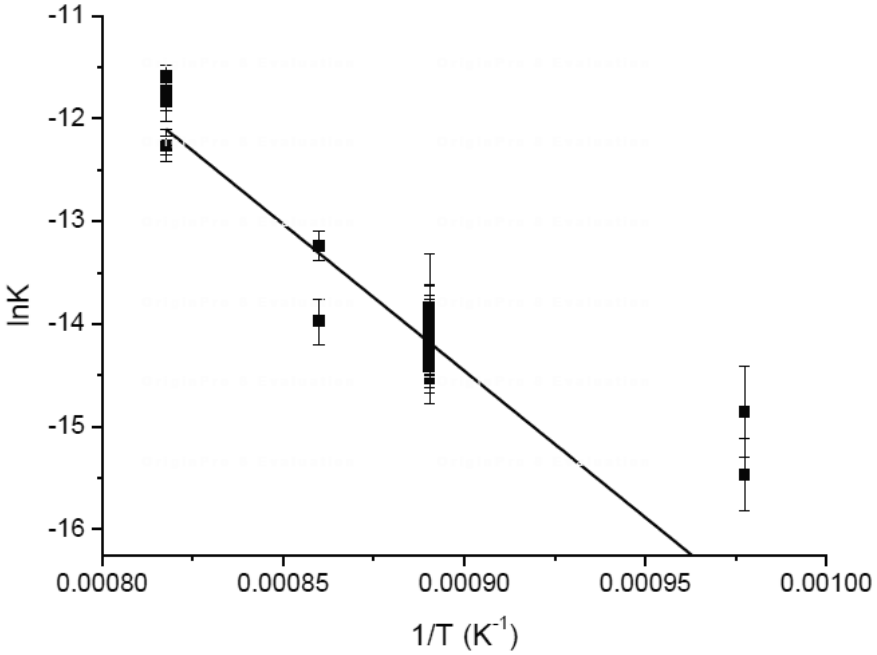

Fig. 4.5-4: Temperature dependence of the solubility product K of anhydrite in granitic melts at 2 kbar. K is the product of the molar fractions of CaO and SO_3 in the melt.

In a further series of experiments, we studied the temperature dependence of the solubility product of anhydrite. Anhydrite solubility very strongly increases with temperature (Fig. 4.5-4).

Our results imply that the CaO content of a felsic melt is a very important factor in controlling the potential environmental impact of an eruption. At high CaO content and oxidizing conditions, most of the sulfur will be locked away as anhydrite and will therefore not be available for release during an eruption. Moreover, anhydrite solubility could be a potential sensor for sulfur oxidation state in a melt. This is because only hexavalent sulfur (SO_3) will enter in the solubility product. If the amount of SO_3 in equilibrium with anhydrite is calibrated as a function of P and T, any "excess" sulfur in the melt must occur in a different oxidation state.

c. *Nitrogen partitioning between silicate melts and hydrous fluids (Y. Li, R. Huang and H. Keppler)*

Earth's atmosphere is a product of mantle degassing. Nitrogen is the main constituent of our present atmosphere, but the degassing of nitrogen as well as nitrogen recycling in subduction zones is hardly understood. As part of a major program on nitrogen geochemistry, we have studied the partitioning of nitrogen between hydrous fluids and haplogranitic or basaltic

melts. Experiments were carried out at 1-2 kbar between 800 and 1100 °C in rapid-quench cold-seal vessels at oxygen fugacities ranging from the iron wüstite buffer to several log units above the Ni-NiO buffer. Nitrogen was added to the capsules usually as dilute ammonia solutions. In some experiments, silver azide AgN_3 was used as a source of nitrogen, in order to demonstrate attainment of redox equilibrium with the external buffer. Nitrogen in quenched glasses was measured by electron microprobe. Here, a special analytical procedure had to be developed because of the very low signal and the curved background. A nitrogen-free black sample was always measured under identical conditions and the count rates of the blank were subtracted from the sample counts before converting them into nitrogen concentration. Experimental results are shown in Figure 4.5-5. Nitrogen always strongly partitions into the fluid phase, with fluid/melt partition coefficients ranging from 74 under reducing conditions to about 200 under oxidizing conditions. The even higher partition coefficients measured in experiments with AgN_3 as nitrogen source may reflect incomplete equilibrium, because the reaction of N_2 (produced by decomposition of AgN_3) to NH_3 is very sluggish.

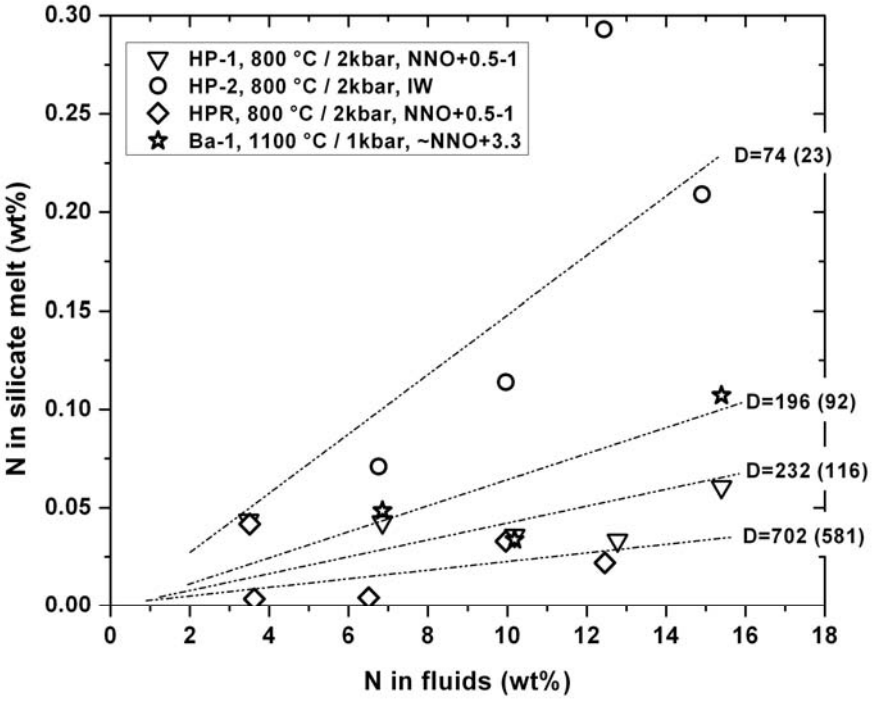

Fig. 4.5-5: Nitrogen partitioning between haplogranitic (HP-1, HP-2, HPR) or basaltic (Ba-1) melt and hydrous fluid. Note the strong effect of oxygen fugacity. Nitrogen was originally loaded into the sample capsules as ammonia solution, except in the HPR experiments, where it was loaded as AgN_3. D is the fluid/melt partition coefficient.

Our experiments are consistent with other data recently obtained in our laboratory, which suggest that redox condition have a strong effect on the behavior of nitrogen and that the formation of a nitrogen-rich atmosphere likely occurred already very early in Earth's history, likely at the same time as the uppermost mantle became oxidized.

d. *Water distribution between nominally anhydrous minerals and incipient, hydrous melts in the upper mantle (D. Novella and D.J. Frost, in collaboration with E.H. Hauri/Washington D.C.; M. Roberge, H. Bureau and C. Raespeat/Paris)*

Volatile free melting of the mantle is predicted to occur only at relatively shallow depths (<50 km). However, as a result of the presence of H_2O in the mantle, small degree melts are likely produced at greater depths and may therefore influence the extraction of volatile and incompatible elements from the mantle. The dominant upper mantle minerals olivine, clinopyroxene, orthopyroxene and garnet can all incorporate H_2O as hydroxyl defects in their structure at high pressure conditions. The onset of hydrous melting at depth will consequently depend on the H_2O contents of these minerals and the partition coefficient $D_{H2O}^{min/melt}$ of H_2O between peridotite minerals and melts, defined as the H_2O content of the mineral divided by that of the melt.

In this project, the H_2O contents of low degree hydrous melts forming at 180 km depth, which corresponds to a pressure of 6 GPa and an adiabatic temperature of 1400°C, have been constrained in a series of experiments. Crystallization experiments were performed in a natural system using a multianvil apparatus. The H_2O contents of low degree melts forming in equilibrium with a peridotite assemblage at conditions equivalent to 180 km were constrained to be approximately 11 wt.% H_2O.

In the present study, we have measured the H_2O contents of the peridotitic mineral phases coexisting with these low degree melts. The melts have been produced in equilibrium with the minerals olivine + clinopyroxene ± orthopyroxene + garnet. The H_2O contents of the crystals have been analyzed by secondary ion mass spectrometry (SIMS) and elastic recoil detection analyses (ERDA). Measuring mineral H_2O contents in phases synthesized from high pressure and high temperature experiments is challenging, as crystals need to be inclusion and crack-free, unzoned, and for ERDA measurements >50 μm across. In many of the melting experiments, large crystals (>100 μm across) were synthesized, suitable for such measurements. In order to facilitate the growth of crystals, the melting experiments were initially heated to 50 °C higher than the target temperature and kept at these conditions for 5 minutes. After this step, the experiment was slowly cooled down to target temperature of 1400 °C. A series of widely studied and well-calibrated mineral and melt equilibria were used to test whether the resulting assemblages were in chemical equilibrium. A number of experiments that failed these tests were discarded. In some of the experimental charges, however, olivine, clinopyroxene or garnet failed to grow into sufficiently large crystals, attaining dimensions of <20 μm across. On such small-size crystals only SIMS analyses could be performed to determine the water content.

Analyses have been conducted on minerals from 9 different melting experiments. Between 5 and 10 analyses on each phase were conducted on every charge. In all the experiments, no large variation among the analyses on a particular phase was observed. In the experiments investigated here, the H_2O content of olivine ranges between 380-480 ppm by weight, clinopyroxene 1080-1450 ppm, orthopyroxene 670-830 ppm and garnet 150-400 ppm. With

the known melt H_2O contents, these values are used to calculate H_2O partition coefficients for each mineral phase as shown in Figure 4.5-6. Using the individual mineral melt partition coefficients, the bulk partition coefficient for peridotite and low degree melt ($D_{H2O}^{pdt/melt}$) can be calculated. In order to do so, the relative abundance of each mineral phase in the peridotite needs to be determined. A subsolidus experiment, containing a dry peridotite mixture, was performed at 6 GPa and 1400 °C, that crystallized 54 % olivine, 32 % clinopyroxene and 14% garnet, with orthopyroxene being absent from the phase assemblage. With this information we determine $D_{H2O}^{pdt/melt}$ to be 0.018 at 180 km. As normal mantle H_2O concentrations are estimated to be in the range 50-300 ppm, typical mantle, therefore, contains insufficient water to instigate melting at 180 km.

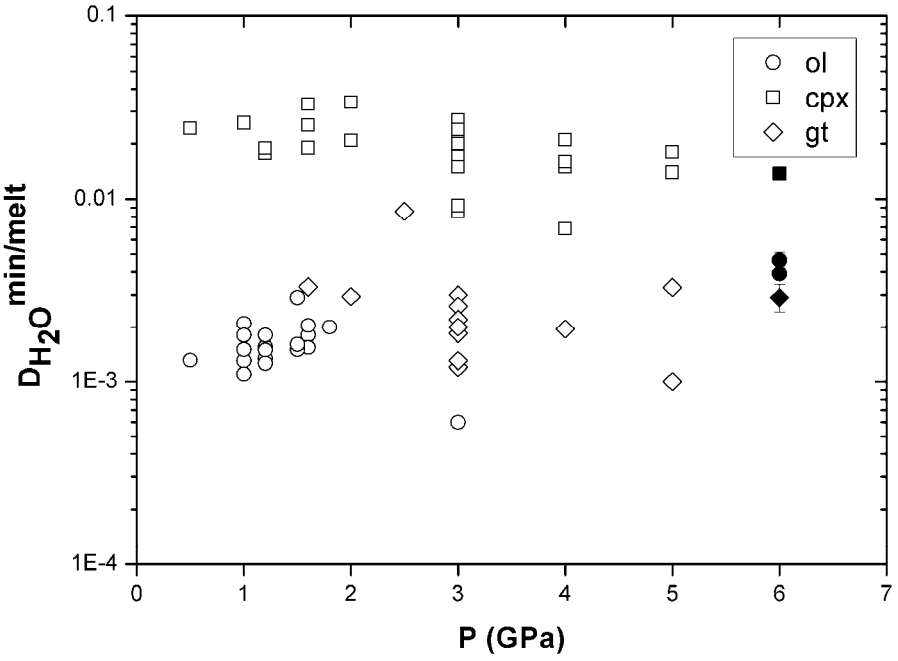

Fig. 4.5-6: Partitioning coefficients of water between nominally anhydrous minerals and melt as a function of pressure. Black, empty circles are data from the literature (up to 5 GPa) while black, filled symbols are data points determined in this study (at 6 GPa).

e. *Water-hydrogen immiscibility in the Earth's mantle (E. Bali, A. Audétat and H. Keppler)*

After the discovery of immiscibility between H_2 and H_2O at upper mantle conditions, as reported in the previous annual report, we have systematically mapped out the critical curve in the H_2-H_2O system. Aqueous fluids were trapped as synthetic fluid inclusions in quartz or olivine at oxygen fugacities of the iron-wüstite buffer in a pressure and temperature range corresponding to approximately 50-80 km depth in the Earth. After the run, fluid inclusions were studied by optical microscopy and Raman spectroscopy. Optical microscopy revealed two types of fluid inclusions below certain temperatures at all pressures studied. One type of inclusion has a weak optical contrast towards the host mineral and while the other type has a strong optical contrast (Fig. 4.5-7). Raman spectroscopy confirmed that the inclusions with a

weak contrast contain almost pure water, whereas the dark inclusions are almost pure hydrogen. The coexistence of these two types of inclusions demonstrates that at the given conditions hydrogen-rich and water-rich fluid forms two immiscible phases. Above a certain temperature, however, we always observed only one type of fluid inclusions that contained after quenching to room temperature a water-rich liquid phase and a hydrogen-rich bubble (Fig. 4.5-7). In these experiments, hydrogen and water were completely miscible at run conditions.

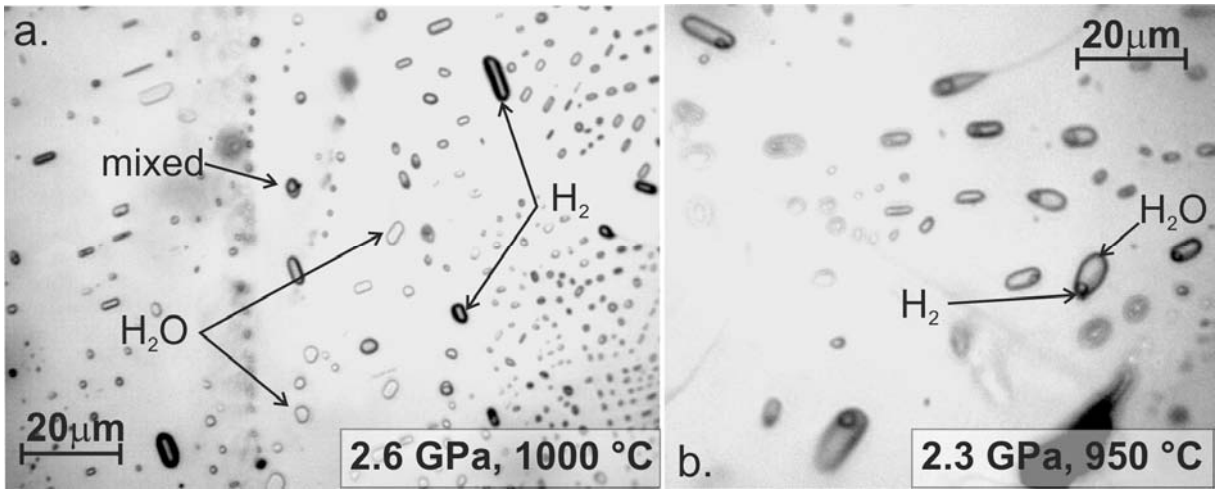

Fig. 4.5-7: Synthetic fluid inclusions trapped in olivine in equilibrium with Fe-FeO buffer. (a) Three different types of fluid inclusions are visible in the photomicrograph. The dark inclusions with strong optical contrast to the olivine contain high-density hydrogen, while the light colored inclusions contain liquid water. Few mixed inclusions with accidentally trapped hydrogen and water are also seen. These textural features indicate that hydrogen and water formed two immiscible fluid phases in these conditions. (b) Only one type of fluid inclusion is visible, with a bubble of high-density hydrogen inside liquid water. These textural features indicate that in these conditions the fluid was homogeneous.

Conducting a series of experiments we could locate the approximate critical curve of the water-hydrogen system (Fig. 4.5-8). Comparing the location of the critical curve to modern and ancient geotherms shows that immiscibility between hydrogen and water occurs in reducing, hydrous fluids in Earth's mantle and it likely also occurred during the Earth's early evolution.

Due to its very low density and low viscosity, the hydrogen-rich fluid may separate and rapidly migrate upwards, locally producing ultra-reducing domains in the mantle that contain moissanite (SiC) and other phases indicative for extremely reducing conditions. The origin of these phases was enigmatic so far. Moreover, the immiscibility between water and hydrogen may provide a mechanism for the rapid oxidation of Earth's upper mantle immediately following core formation without affecting significantly its bulk or trace element

composition. Hydrogen outgassing during the early evolution of the Earth might have also stabilized a reducing atmosphere for a limited period of time.

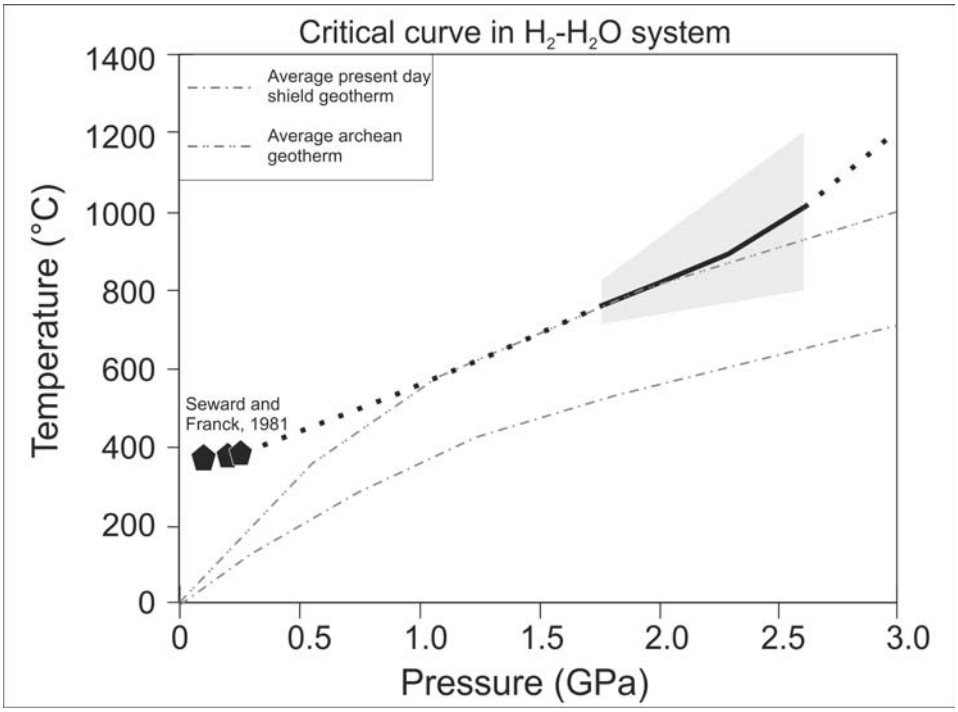

Fig. 4.5-8: Critical curve in the H_2-H_2O system. The grey field shows the experimental conditions. The thick black line is the approximate location of the critical curve.

4.6 Rheology and Metamorphism

In geosciences rheology is the investigation of the flow properties of Earth materials at pressure and temperature conditions similar to the Earth's interior. These properties can then be linked to large-scale deformation processes such as global mantle convection. The study of metamorphism investigates the phase transformations that take place in rocks as they experience changing P and T conditions during such flow processes. This year's contributions provide excellent examples of how the experimental investigation of the microscopic properties of small rock samples can result in a better understanding of the large-scale properties of the dynamic Earth.

The first three contributions deal with the question of how strongly the incorporation of traces of water weakens olivine, the major mineral phase in the upper mantle. Based on earlier laboratory studies water weakening was suggested as an explanation for the existence of the asthenosphere, a soft layer in the upper mantle that is crucial for the operation of plate tectonics. By measuring self-diffusion of the rate limiting Si and O as a function of water content the authors show that water has a much smaller weakening effect than previously thought, thereby questioning its role in the asthenosphere. In the third contribution the authors present first results of a study that links the mobility of line dislocations in olivine to the incorporation of water.

Another important aspect of deformation in polycrystalline aggregates is the formation of a crystallographic preferred orientation (CPO) that can result in seismic anisotropy, which is observed in the upper mantle of the Earth and close to the core-mantle boundary. In the fourth contribution the CPO formation is investigated during experimental deformation of lawsonite, a water bearing mineral that forms during high-pressure metamorphism in subducting lithospheric plates. Lawsonite is a possible candidate to explain seismic anomalies at the top parts of subducting slaps. The authors present evidence for a deformation texture; however, complexities of the system require further analysis. Following the path of the subducting slaps deeper in the mantle, phase transitions produce dense hydrous magnesium silicates. In the next contribution a TEM study of the dislocations in "superhydrous B" is presented that form as a response to experimental deformation at high-pressure conditions. Moving even deeper into the lower mantle, in the 6th contribution CPO in samples of deformed $CaIrO_3$ perovskite are presented. $CaIrO_3$ has been used as an analogue for (Mg, Fe)SiO_3 perovskite and post-perovskite, the dominating phases in the lower mantle. In this study it was shown that the samples displayed a strong CPO when indexed in their orthorhombic crystal structure. The authors show that the CPO is compatible with the seismic anisotropy measured in the D" layer at the core-mantle boundary of the Earth.

Many upper mantle rock samples display pyroxene bands that were interpreted as a result of deformation and reaction of olivine with a silicate melt. In the 7th contribution this interplay was investigated in an olivine aggregate with a silica oversaturated melt. The authors were

able to simulate the formation of pyroxene bands for the first time and explain their orientation. In the 8th contribution the deformation behaviour of coexisting metallic and silicate melt in an olivine matrix is investigated to understand the possible mechanism of core-mantle differentiation in planetesimals. The authors show the relative immobility of metallic melt with respect to silicate melt during deformation and thus confirm the necessity of large-scale melting for efficient metal segregation. In the final contribution three distinct episodes in the geological history of two martian meteorites are reconstructed by a detailed investigation of the metamorphic phase assemblages in the samples.

a. *Small effect of water on upper mantle rheology based on silicon self-diffusion coefficients (H. Fei, M. Wiedenbeck/Potsdam, D. Yamazaki/Misasa and T. Katsura)*

Water has been considered to significantly affect mantle dynamics. In particular, previous deformation studies claimed that even several tens μg/g of water enhanced the creep in olivine by orders of magnitude. However, we note that they used polycrystalline samples with saturated water, in which free water would enter the grain boundaries and largely enhanced grain boundary sliding. On the other hand, the Earth's mantle is water under-saturated and free water should not exist. Therefore, the role of water might be overestimated. High-temperature creep of silicate minerals is controlled by silicon self-diffusion. In this study, we measured D_{Si} in forsterite as a function of C_{H2O}, and show that the effect of water on upper mantle rheology is much smaller than considered previously.

Forsterite single crystals were doped with water at 1600 K, 8 GPa using talc + brucite water sources and graphite buffer (or enstatite + Au). The C_{H2O} in the doped samples varied from < 1 up to ~ 800 μg/g determined by FT-IR (Fig. 4.6-1a) well-controlled by the ratio of water sources to graphite (or enstatite + Au). The C_{H2O} in the crystals was homogenous after a sufficiently long annealing duration (50-70 h) (Fig. 4.6-1b). The water doped samples were polished, deposited with 500 nm ^{29}Si and ^{18}O enriched Mg_2SiO_4 films, and subsequently annealed at 8 GPa, 1600 or 1800 K for diffusion. In the diffusion experiments the same proportion of water sources was used as in the initial doping experiments to ensure a constant C_{H2O} (Fig. 4.6-1c). The diffusion profiles were obtained by SIMS. C_{H2O} in the samples were also examined by SIMS (Fig. 4.6-1d).

Our results of D_{Si} vs C_{H2O} (Fig. 4.6-2) yield a relationship: $D_{Si} \alpha \ (C_{H2O})^{0.32\pm0.03} = (C_{H2O})^{1/3}$. This is explained by defect chemistry, where $D_{Si} \alpha \ [V_{Si}''''] \times [V_O^{\bullet\bullet}] \alpha \ (C_{H2O})^{2/3} \times (C_{H2O})^{-1/3} = (C_{H2O})^{1/3}$ under the charge neutrality condition of $[(OH)_O^{\bullet}] = 2[V_{Mg}'']$ because Si ions are surrounded by O in tetrahedrons and therefore both Si and O vacancies are needed for Si ions to diffuse. The C_{H2O} exponent (1/3) determined in this study is strikingly lower than 1.2, which was estimated based on deformation studies (Fig. 4.6-3). The high nominal creep rates in those published deformation studies under wet conditions can be explained by excess grain boundary water promoting grain boundary sliding, which is supported by a large grain-size dependence of their dislocation creep rates.

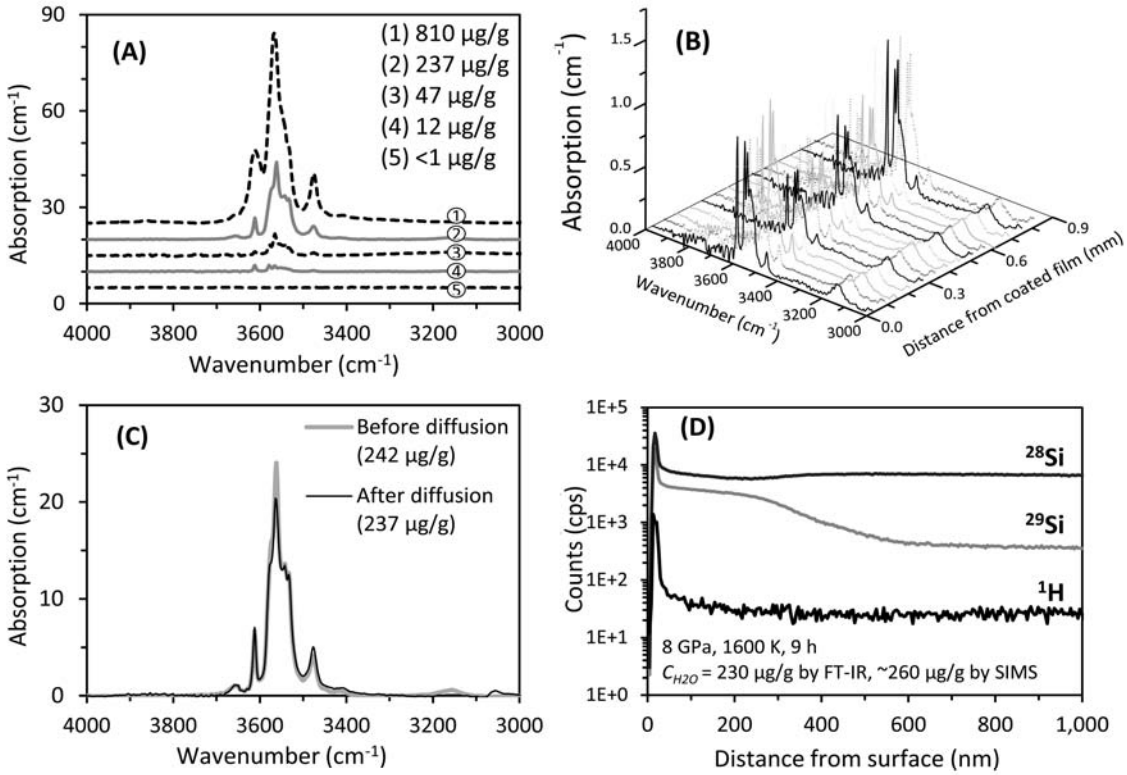

Fig. 4.6-1: C_{H2O} in the samples. (A) Various C_{H2O} from < 1 to ~ 800 µg/g. (B) Homogenous C_{H2O} in the crystal. (C) Constant C_{H2O} before and after diffusion annealing. (D) Constant ^{1}H counts in the region deeper than 100 nm where Si diffusion profiles were obtained. The C_{H2O} estimated from the H/Si ratio by SIMS is slightly higher than, but generally in agreement with that from FT-IR. C_{H2O} from FT-IR spectra were calculated using Bell's calibration after a background baseline correction and thickness normalization to 1 cm.

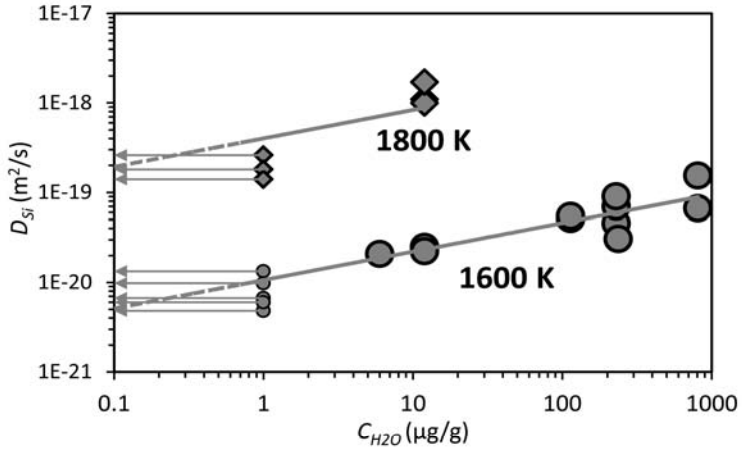

Fig. 4.6-2: D_{Si} versus C_{H2O} at 1600 and 1800 K. The data points shown by small circles with an arrow are taken from Fei *et al.* (2012, *EPSL*, **345-348**, 95) on D_{Si} in dry forsterite at 8 GPa, with C_{H2O} < 1 µg/g, which are below the detection resolution of FT-IR and SIMS.

The small C_{H2O} exponent demonstrates that the effect of water on upper mantle rheology is very small in comparison with other factors such as temperature or shear stress. The softening of oceanic asthenosphere was believed to be caused by mineral hydration. However, since water has a very small effect on D_{Si} as shown in this study, the viscosity of minerals only slightly decreases with increasing C_{H2O}. As a result, the viscosity in the upper mantle calculated from D_{Si} continuously decreases with increasing depth without appearing as a minimum zone, and therefore, the softening of oceanic asthenosphere cannot be caused by mineral hydration. The immobility of hotspots was also explained by C_{H2O} differences between their source and surrounding regions. However, using the water exponent of 1/3, the C_{H2O} differences only cause a viscosity contrast by a factor of ~ 2, which is rather small in comparison with that caused by temperature differences. Therefore, C_{H2O} differences cannot be the major reason that leads to the immobility of hotspots.

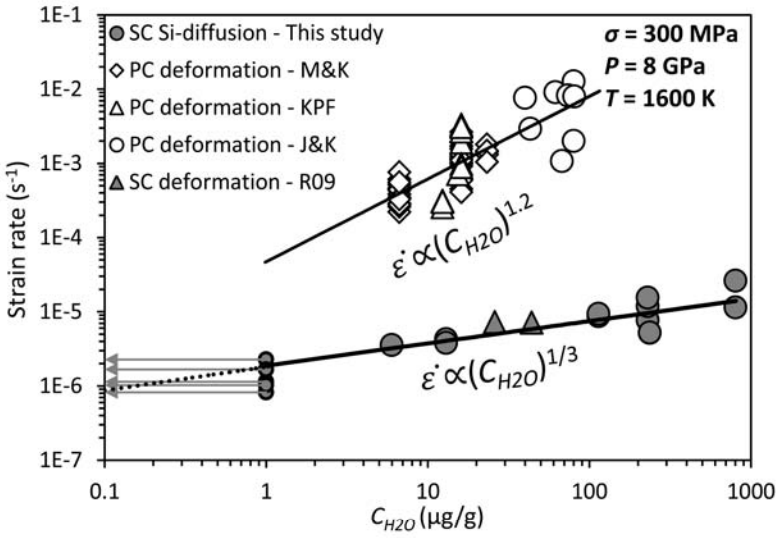

Fig. 4.6-3: Strain rate ($\dot{\varepsilon}$) versus C_{H2O}. D_{Si} from this study is converted to $\dot{\varepsilon}$ using the proportional relationship of D_{Si} and $\dot{\varepsilon}$. All data are normalized to 8 GPa, 1600 K, and a stress of 300 MPa. SC: single crystal. PC: polycrystalline. M&K: Mei and Kohlstedt (2000, *JGR*, **105**, 21471). J&K: Jung and Karato (2001, *Science*, **293**, 1460). KPF: Karato *et al.* (1986, *JGR*, **91**, 8151). R09: Raterron *et al.* (2009, *PEPI*, **172**, 74).

b. *The effect of water on oxygen self-diffusion coefficients in forsterite (H. Fei, M. Wiedenbeck/Potsdam, D. Yamazaki/Misasa and T. Katsura)*

High-temperature creep of olivine is controlled by self-diffusion of silicon, which has the slowest self-diffusion rate. On the other hand, Si ions are surrounded by oxygen in Si-O tetrahedrons in the crystal structure. As a result, the Si diffusion rate is limited by O diffusion. Therefore, measurement of Si and O self-diffusion coefficients (D_{Si} and D_O) in olivine is essential for understanding the upper mantle rheology. Water is believed to affect the rheological properties of mantle minerals. The effect of water on D_{Si} in the Mg end-member

of olivine, namely, forsterite, is described in the previous contribution (section 4.6 **a**). Here we report our experimental results of water content (C_{H2O}) dependence of D_O in forsterite, which were measured simultaneously with D_{Si}.

The results of D_O plotted against C_{H2O} in Fig. 4.6-4. show that D_O is independent of C_{H2O} ($D_O \propto C_{H2O}^{0.06\pm0.14}$). It can be understood on the basis of defect chemistry. The self-diffusion coefficient of O is proportional to the vacancy concentration of O, $[V_O^{\bullet\bullet}]$. Because OH^- has a lower charge than O^{2-}, it will have higher a mobility due to its smaller Coulomb Force, and therefore, oxygen ions diffuse mainly through OH^-. There are three main types of hydroxyl in wet olivine: (1) $(OH)_O^{\bullet}$ associated with V_{Me}'' (metal vacancies). (2) $(OH)_O^{\bullet}$ associated with V_{Si}''''. (3) $(OH)_O^{\bullet}$ without associating with cation vacancies. The third should have much higher mobility because the association of $(OH)_O^{\bullet}$ with V_{Si}'''' or V_{Me}'' should lower the mobility of $(OH)_O^{\bullet}$. Therefore, O diffusion should be dominated by un-associated $(OH)_O^{\bullet}$. Namely,

$$D_O \propto [V_O^{\bullet\bullet}] \times [(OH)_O^{\bullet}]^{\text{un-associated}} \quad (1)$$

Under the charge neutrality condition of $[(OH)_O^{\bullet}] = 2[V_{Me}'']$, we have,

$$D_O \propto [V_O^{\bullet\bullet}] \times [(OH)_O^{\bullet}]^{\text{un-associated}} \propto (C_{H_2O})^{-1/3} \times (C_{H_2O})^{1/3} = (C_{H_2O})^0 \quad (2)$$

which is in good agreement with our experimental results: $D_O \propto C_{H2O}^{0.06\pm0.14} \approx C_{H2O}^0$.

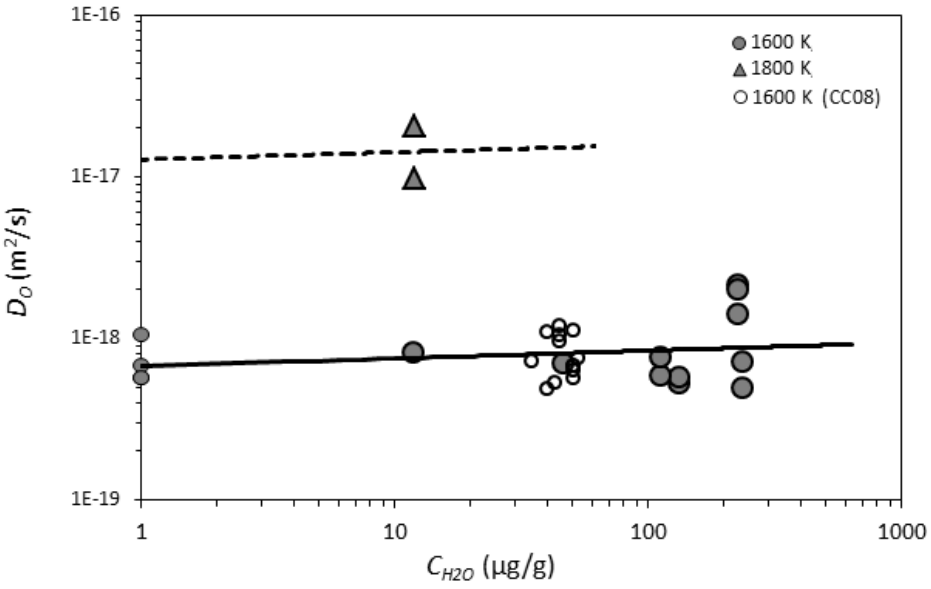

Fig. 4.6-4: D_O vs C_{H2O} at 8 GPa, 1600 K. The C_{H2O} of samples at dry conditions are below the detector limitation of FT-IR (< 1 μg/g). These data points are plotted at C_{H2O} = 1 μg/g with smaller symbols. CC08: Costa and Chakraborty (2008, *PEPI*, **166**, 11).

In Figure 4.6-5 the effects of water on D_{Si}, D_O, as well as D_{Me} in olivine are compared. The C_{H2O} exponents are 0.9, 0, and 1/3 for D_{Me}, D_O, and D_{Si}, respectively. Plastic deformation of olivine in the Earth's upper mantle is controlled by Si diffusion, which has a very small C_{H2O} dependence as discussed in section 4.6 **a**. On the other hand, D_O is nearly independent from C_{H2O}. Therefore, water is not a significant factor that affects the plastic deformation of olivine in moar part of upper mantle.

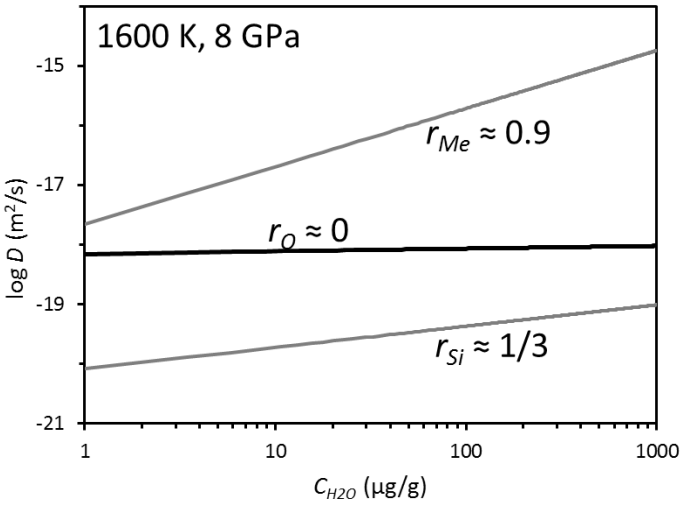

Fig. 4.6-5: D_{Si}, D_O, and D_{Me} vs C_{H2O} at 8 GPa, 1600 K. The r_{Me} data is from Hier-Majumder *et al.* (2005, *JGR*, **110**, B02202) calibrated to the same *T* and *P* conditions.

c. *Annealing of deformed olivine single-crystals (S. Blaha and T. Katsura)*

Knowledge of rheological properties of Earth's materials is essential to understand geological processes. Open questions are the water content and crystallographic orientation dependences of dislocation creep rate, because the dominant slip system changes with increasing water content, which suggest different dislocations have different water content dependence. This project focuses on olivine, which is the most abundant mineral of the upper mantle. It is also considered to be the weakest phase and hence should control the rheology of the upper mantle. Several slip systems were reported for olivine, which are [100](010) (A-type) [001](010) (B-type), [001](100) (C-type) and [100](001) (E-type), each of which appear under different water content and stress conditions. In this study, the water content dependence of mobility of different dislocation is investigated.

Variation in dislocation creep rate according to change in physical conditions can be estimated by dislocation recovery experiments. In this technique, deformed crystals are annealed, in which the dislocation density is expected to decrease due to coalescence of two dislocations. Dislocation densities are measured before and after the annealing. Dislocation mobility, which should be directly proportional to the dislocation creep rate, is estimated based on the change in dislocation density and duration of annealing. This technique has

significant advantages, partly because information of strain rate and deviatoric stress, which are difficult to measure, are unnecessary, and partly because dislocation annealing is conducted under quasi-hydrostatic conditions, which allows wide ranges of P and T conditions.

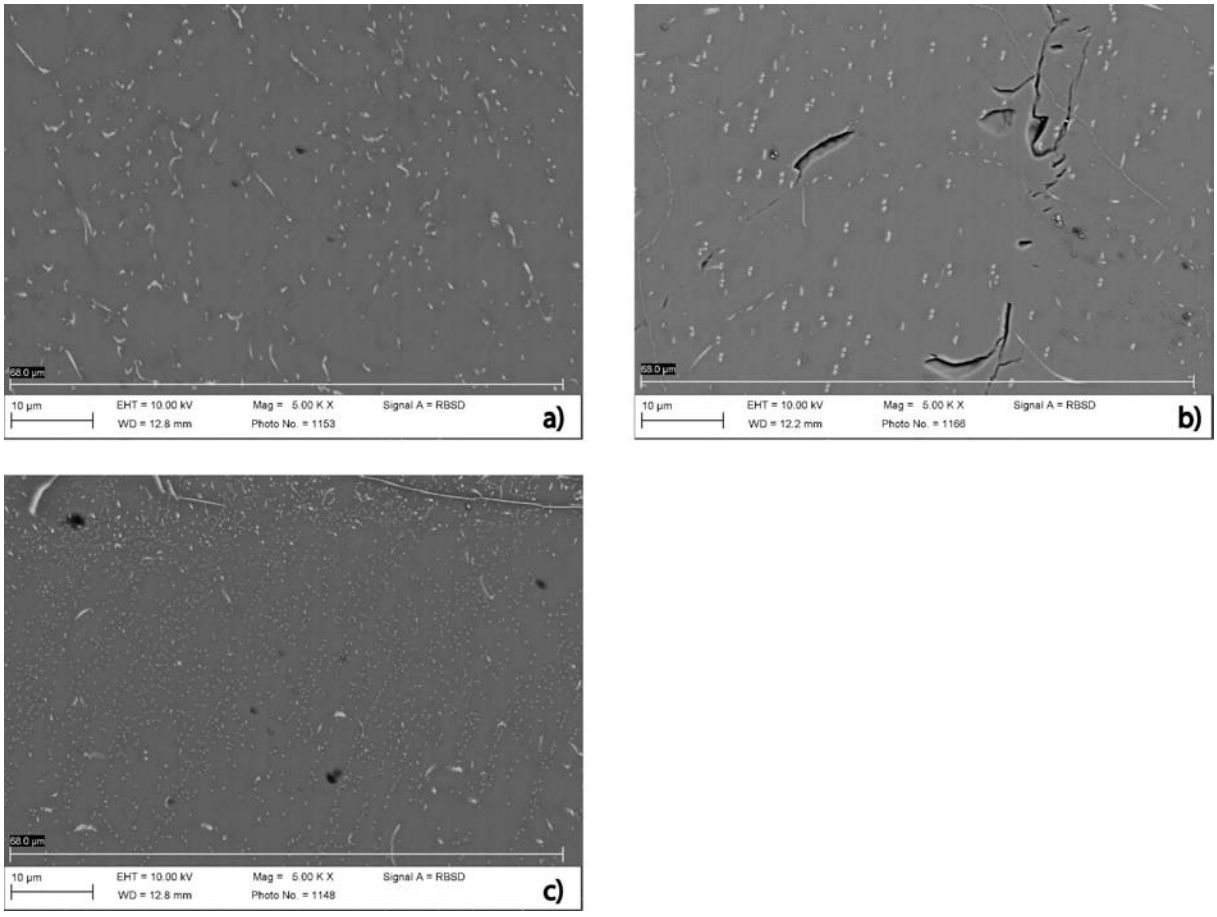

Fig. 4.6-6: Distribution of dislocations on the c-plane in an olivine crystal deformed with [001](010) oriented in the shear plane and direction. a) Close to the center before annealing, b) close to the center after annealing, and c) near the shear piston before annealing.

The first step of the experiments is to deform a single crystal of olivine. For this purpose, we developed an assembly for stress relaxation experiments, which deforms a single crystal in simple-shear geometry and prevents breakage, sub-grain formation and recrystallization of the crystal. The assembly has a edge length 25 mm and therefore makes it possible to deform large samples (1.5 mm in diameter and 1.5 mm in height). Olivine single-crystals were cored from natural olivine crystals. The crystals were oriented using EBSD. They were placed in the high-pressure assembly so that a particular slip system is activated. So far experiments to activate [001](010) (responsible for B-type textures) and [100](001) slip (E-type) were performed. The assemblies were compressed to 3 GPa. During compression the samples were heated to 600 K to avoid fracturing.

The shear deformation was conducted at 1600 K. EBSD measurements indicate that the recovered crystals remain single crystals and sub-grain formation did not occur in most cases. The second step is to anneal the samples under the same P-T conditions as those of the deformation experiments. Annealing experiments were also performed at ambient pressures at 1600 K. Dislocation density was measured by means of the oxidation decoration technique. The samples were firstly polished and then oxidized at 1200 K for 50 min. As is shown in Fig. 4.6-6, the dislocations are preferably oxidized, so that the presence of dislocations can be observed using SEM.

As is shown in Fig. 4.6-6a and 4.6-6b, the dislocation density decreased by annealing. The density decreases by ~ 1/4 in this particular case with an annealing period of 10 h. We recognized that the dislocation density is higher near the shear piston than in the central part (Fig. 4.6-6a and 4.6-6c).

d. *Deformation of lawsonite at high pressure and high temperature: Implication for low velocity layers in subduction zones (R. Iizuka/Tokyo, T. Yagi/Ehime, V. Soustelle, N. Walte and D.J Frost)*

Low-velocity layers (LVLs) are regions of apparently low seismic wave velocity that occur in the top portions of subducting slabs and persist to depths of 100−250 km. One explanation for their existence is that they comprise regions of hydrated mafic rocks containing hydrous minerals, which also may transport water into the deep mantle. The elasticity and rheological properties of such hydrous minerals are important for clarifying the origin of such LVL observations. Rheological properties are of particular importance because deformation may induce crystal preferred orientation (CPO) of such hydrous minerals, which would influence seismic velocities and anisotropy along the slab.

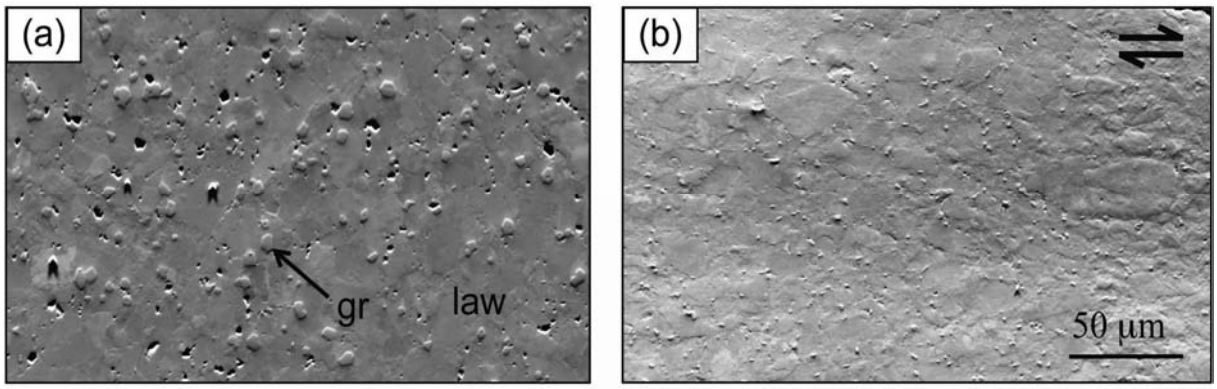

Fig. 4.6-7: SEM images of recovered experimental samples (a) statically compressed at 6 GPa, and annealed at 700 °C and (b) deformed by simple shear at 5 GPa, 700 °C. Arrows indicate shear direction. Gr: grossular, law: lawsonite.

Lawsonite ($CaAl_2(Si_2O_7)(OH)_2\ H_2O$) is one of the candidate hydrous minerals that may be present in LVLs at depths greater than the serpentine stability field. Although there are previous studies of CPO fabrics of natural lawsonite, no deformation experiments on lawsonite exist to characterize the likely CPO under high PT conditions corresponding to > 150 km depth. The present study aims to investigate the deformation behaviour of lawsonite under subduction zone conditions, and to clarify whether or not CPO of this mineral strongly influences LVLs.

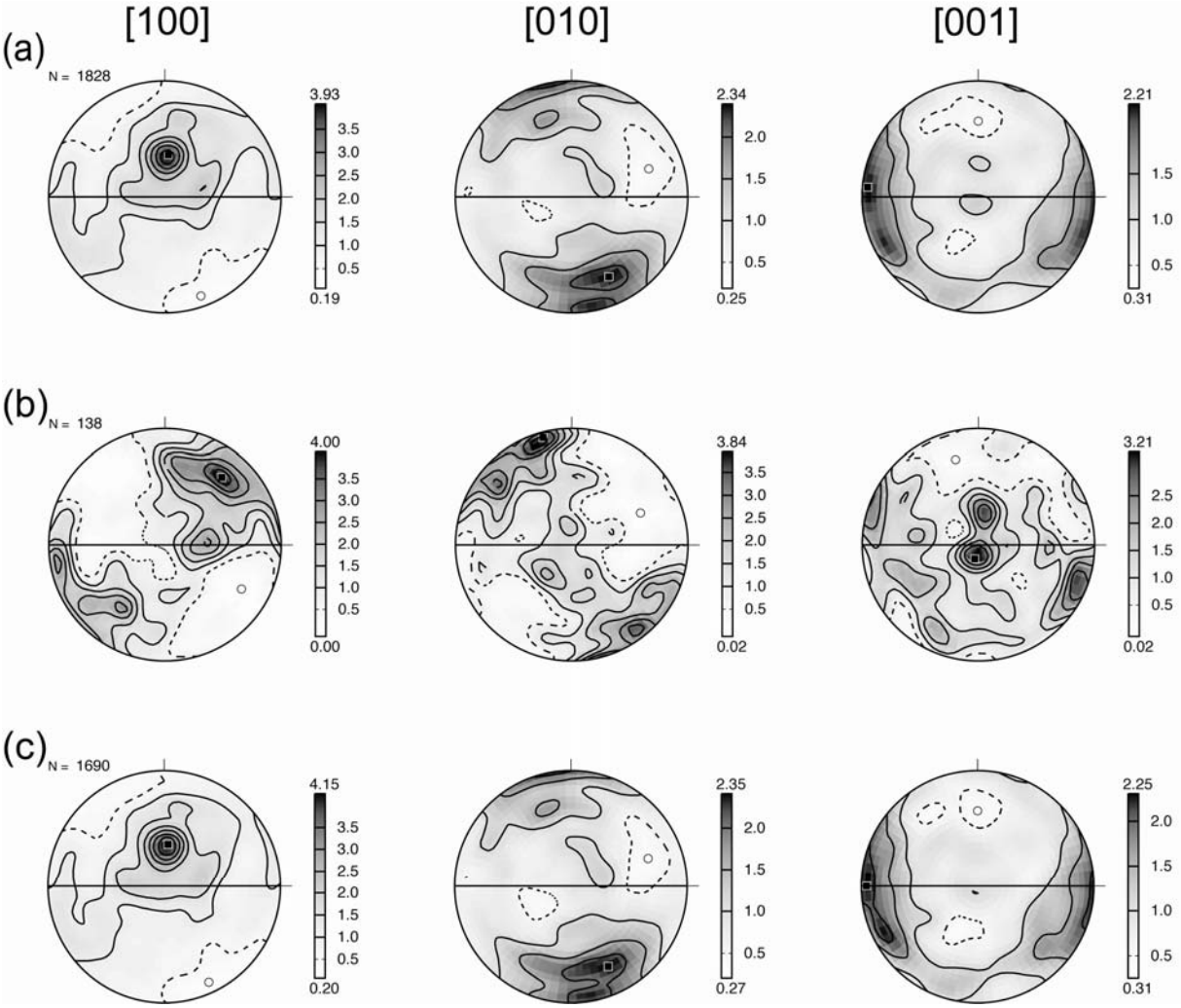

Fig. 4.6-8: Lower-hemisphere pole figures of deformed lawsonite. (a) Entire bulk (whole grains), (b) porphyroclast (coarse grains), and (c) fine-grained matrix analyzed by crystallographic orientation mapping data. The horizontal direction corresponds to shear direction.

The starting material was fine-grained powder of natural lawsonite which contained < 4 % of quartz and calcite with grain size > 3 µm. For pure shear experiments, this powder was loaded into a Pt capsule and deformed for ~ 20 h at 5 GPa and 700 °C using a 6-ram multianvil apparatus. For simple shear, the powder was first hot-pressed at 6 GPa, 700 °C using a

multianvil apparatus, then cored and sliced at an angle of 45°. The slices were placed between pre-cut alumina pistons in Pt capsules. Samples were deformed at strain rates of ca. 10^{-4}–10^{-5} s^{-1} with a finite strain γ from 0.2 to 2.

All recovered samples included a small amount (~ 7 %) of grossular randomly distributed in the aggregate (Fig. 4.6-7), which was formed by the reaction of lawsonite and impurities. The deformed samples have a porphyroclastic texture with coarse grained porphyroclasts of 20-50 µm surrounded by a fine-grained matrix of ~ 2 µm in size. Twinning and subgrain boundaries are frequently observed in the porphyroclasts. These observations of dynamic recrystallization suggest that lawsonite is deformed by dislocation creep. As the statically compressed experiments showed no texture, we assume that the observed textures in deformed samples result from the deformation.

In all deformed samples, lawsonite displays a CPO with a maximum concentration of the [010] axes approximately normal to the shear plane, and a maximum concentration of [001] close to the shear direction (Fig. 4.6-8a). If dislocation creep is the dominant deformation mechanism, these CPOs suggest that the dominant slip system of lawsonite would be [001](010). However, this seems unlikely given that the [001] Burgers vector is the longest and therefore potentially the most difficult slip direction. When the CPO is measured separately for porphyroclasts and the fine-grained matrix, the results are quite different. The porphyroclast CPO displays a [100] slip direction (Fig. 4.6-8b), while the fine-grained matrix (Fig. 4.6-8c) displays a similar CPO to the bulk lawsonite sample (Fig. 4.6-8a). The porphyroclasts display clear evidence for dislocation creep, whereas the deformation mechanism in the matrix is as yet not clear. Hence, these observations suggest that the dominant slip system in lawsonite is likely [100](010), which includes the shortest [100] Burgers vector, while the CPO of the fine-grained lawsonite matrix may be caused by another mechansim. Furthermore, our CPOs are quite different from those of previous studies. In order to constrain the deformation mechanism responsible for the texture in the fine-grained matrix, which dominates the whole sample and may still control the seismic properties, we need further deformation studies under different experimental conditions and TEM measurements.

e. *Transmission electron microscopy characterization of the dislocations and slip systems of superhydrous B (P. Cordier and A. Mussi/Lille; D.J. Frost)*

Water present in hydrous phases (antigorite, talc, etc.), can be deeply buried in the Earth's mantle during subduction. Hydrous phases are destabilized during deep subduction and partly transformed into dense hydrous magnesium silicates (DHMS). In this study, we focus on the deformation of superhydrous B (shy B) since this DHMS has the highest stability domain and since this domain coincides with the conditions in the transition zone. There is no previous study of the plastic properties of shy B. Consequently, we have decided to study the slip systems of this phase under cold slab subduction conditions, using transmission electron microscopy (TEM).

The crystal structure of shy B is orthorhombic with a Pnnm space group at high temperatures (near 1400 °C) and a Pnn2 space group at low temperatures (near 1200 °C).

To synthesize shy B, high-purity oxides (MgO, SiO_2 and brucite) have been mixed, and annealed at 20 GPa, 1100 °C during 3 hours. The resulting sample has been deformed under the same confining pressure at temperatures of 1000-1100 °C for 30 min.

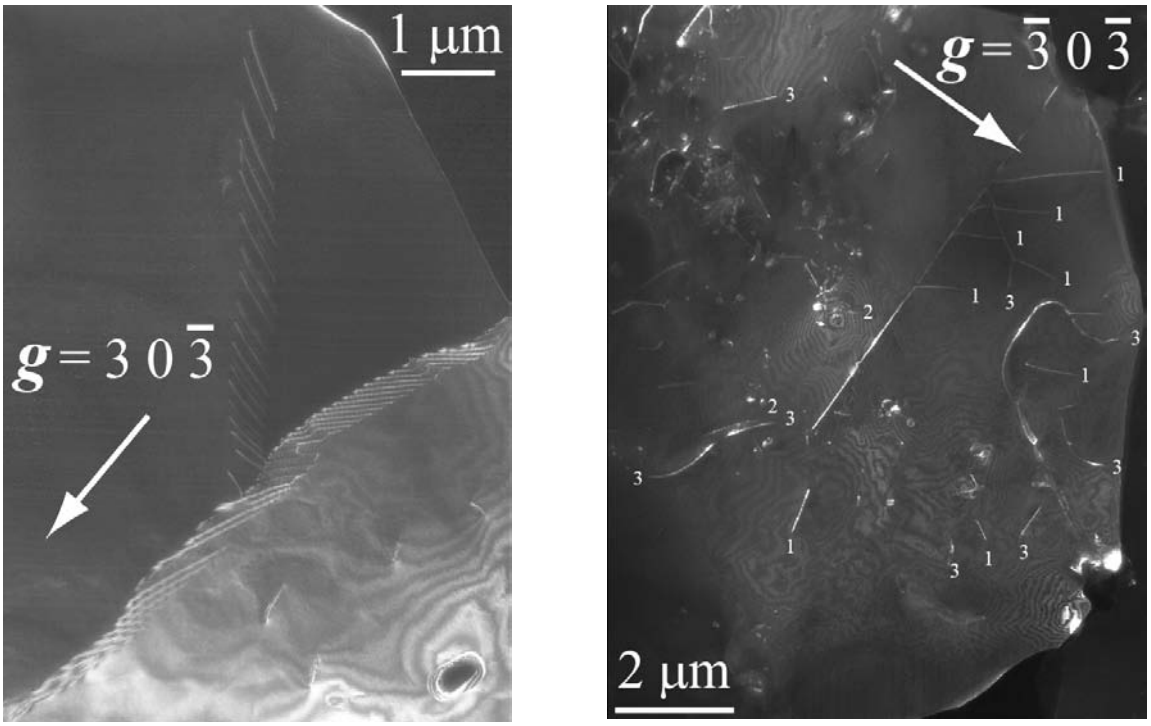

Fig. 4.6-9: TEM micrographs in weak-beam dark-field conditions (g = diffraction vector). On the left; sub-grain boundaries composed of dislocation whose Burgers vectors is [100]. On the right; dislocations 1, 2 and 3 are [100], [001] and [101] respectively.

Two thin foils were extracted from the sample. They were mechanically polished then ion milled at liquid nitrogen temperature in order to avoid ion damage. Dislocations and slip systems have been characterized by TEM, with a Philips® microscope operating at 300 kV (CM30). Analyses were conducted with a Gatan® cold stage in order to reduce electron damage.

The sample microstructure is composed of grain of 30 ± 5 μm, with a dislocation density of approximately $2x10^{12}$ m^{-2}. Several sub-grain boundaries are noted. Cold compression activates glide of <101> dislocations ($|b_{101}| \approx 10.1$ Å) under high stresses on the (010) and the {111} planes. At high temperature, we have observed glide, on the (010) plane, of dislocations with [100] and [001] Burgers vectors (Fig. 4.6-9).

f. *Deformation textures in orthorhombic perovskite – consequences for seismic anisotropy (F. Heidelbach/Berlin and N. Walte)*

Plastic deformation at high temperatures and pressures may generate crystallographic preferred orientations (CPO) which in turn may be detectable in seismic or geoelectrical studies of the deep Earth as physical anisotropies. Silicate perovskite is the main constituent of the lower mantle and likely to develop CPOs during convective flow, especially near the boundary regions. Since lower mantle pressures are difficult to achieve in quantitative deformation experiments and also silicate perovskite is notoriously unstable at ambient conditions, we used the analogue system of $CaIrO_3$ to investigate the potential deformation textures of the perovskite structure. In this system, the perovskite to post-perovskite phase transition occurs at experimentally achievable pressures and temperatures and we have used this to shed light on potential post-perovskite deformation and transformation fabrics (see previous BGI annual reports).

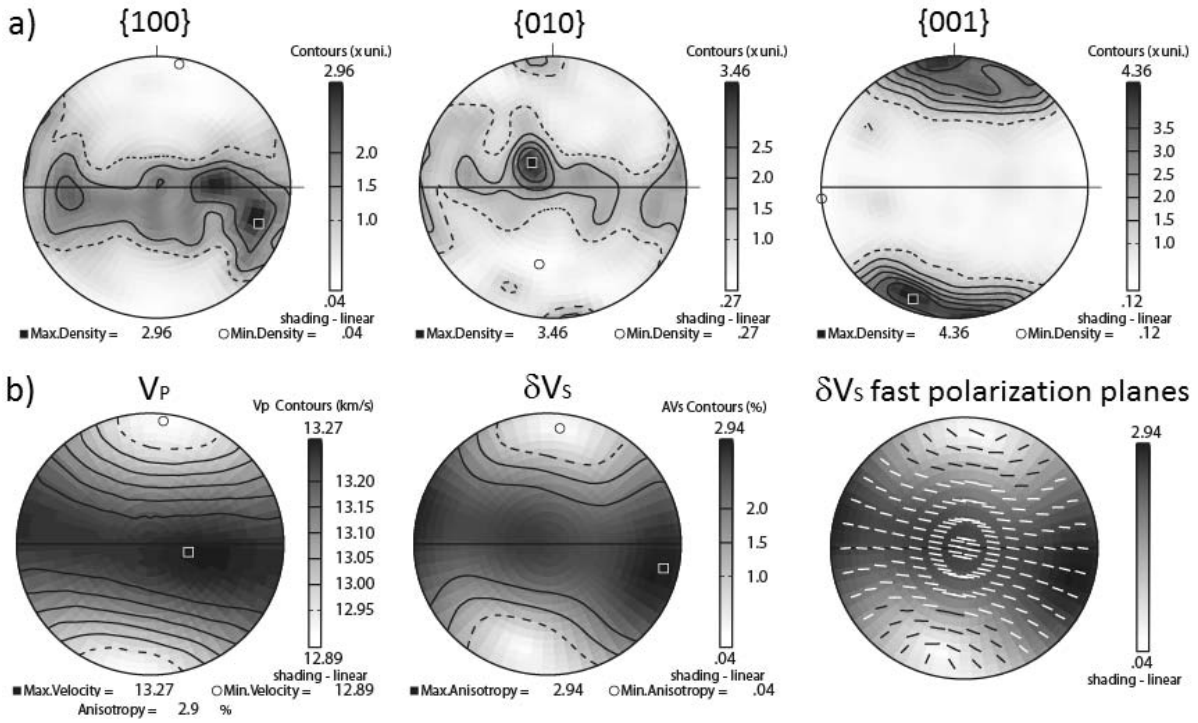

Fig. 4.6-10: a) Pole figures of deformed orthorhombic $CaIrO_3$ perovskite (standard Pnma setting); compression axis is vertical in the plane of the paper; n= 6798; b) seismic anisotropy for the same sample calculated with a theoretically calculated single crystal tensor for 88 GPa and 3500 K; all projections are equal area and lower hemisphere.

With decreasing temperature or increasing temperature perovskite structures undergo a series of symmetry changes; at the P,T conditions of our experiments (1 GPa, 1400 °C) the structure

of $CaIrO_3$ is orthorhombic, but the distortion from the cubic perovskite structure is only about 2 %. Microstructurally this is immediately obvious through the occurrence of twins which follow twin laws that mimick some of the cubic symmetry axes. The unequivocal detection of these twins is a challenge for CPO analysis with the electron backscattering diffraction (EBSD) technique in the scanning electron microscope (SEM) since it is based solely on the angles between reflections in a single diffraction pattern. The difference in angles between the pseudocubic solutions is only about 1-2° (depending on orientation and reflections used) and until now it has been proven to be very difficult to resolve the orthorhombic symmetry reliably with this technique. Nevertheless this is quite important since the elastic behaviour of the orthorhombic structure is very strongly anisotropic. By increasing the detector resolution and exposure time as well as the number of reflections used for the solution of each diffraction pattern we managed to get reliable results in automated EBSD mapping of the orthorhombic perovskite structure. Closer inspection of the results shows that the indexing algorithm finds consistently a better matching angle for the correct solution. However, further testing showed that it is important to calibrate the system not with the perovskite phase but with a phase that is easier to index unequivocally (in our case we used the corundum of the pistons).

For our tests we used samples that had been produced for an earlier study on deformation and transition textures in post-perovskite (see previous annual reports). Here we just show one example of a perovskite sample deformed in its stability field in axial compression to moderate strains which was the starting material for a phase transition experiment. The CPO of orthorhombic perovskite and the seismic anisotropy pattern calculated from that CPO are displayed in Fig. 4.6-10. The CPO is characterized by an alignment of <001> parallel to the compression axis and a girdle of <100> and <010> in the plane of compression, indicating slip on the (001) plane, possibly in the [100] and/or [010] direction. For the calculation of the seismic anisotropy pattern these CPO data were combined with theoretically calculated single crystal elasticity data of silicate perovskite at 88 GPa and 3500 K representing P,T conditions of the deep lower mantle. The resulting anisotropies are almost 3 %, both for p-wave velocities and shear wave splitting. Fast p-waves and maximum values of shear wave splitting are produced in directions parallel to the compression plane with the fast shear wave polarization plane also being parallel to the compression plane. Anisotropy patterns of this type and magnitude have been observed seismologically in the D" layer at the base of the Earth's mantle indicating they may very well be caused by deformation fabrics of orthorhombic perovskite**.**

g. *Interactions between deformation and reactive melt percolation in the upper mantle: Simple-shear deformation experiments at high pressure and temperature (V. Soustelle, M.A.G.M. Manthilake, N. Walte and D.J. Frost)*

Subduction zones and oceanic ridges, which are driving plate tectonics, cause the majority of both volcanic activity and deformation at the Earth's surface. To better constrain their

dynamics, it is necessary to study and understand the interactions between deformation, melt percolation and melt-rock reactions. Most experiments involving partially molten mantle rocks imply the presence of a melt that is in chemical equilibrium with a solid matrix. In contrast, natural samples deformed in the presence of melt often display evidence for petrological reactions between the percolating melt and the surrounding minerals. These reactions occurring during deformation may be responsible for structural and textural differences observed between experimental and natural samples.

This study consists of a series of simple shear deformation experiments using a 6-ram multianvil apparatus at 2 GPa and 1150 °C. The samples comprise a San Carlos olivine aggregate mixed with 10 % of Si-rich hydrous melt in chemical disequilibrium with the solid matrix. The samples were deformed at shear strain rates between $1x10^{-5}$ and $7x10^{-4}$ s^{-1}. The finite strain ranged from a γ of 0.3 to 2. The reaction between the melt and the olivine induces the precipitation of orthopyroxene and minor amounts of clinopyroxene.

The analysis of the melt pockets' topology and orthopyroxene shape preferred orientation displays a clear difference between their directions of elongation (Fig. 4.6-11). The melt pockets are mostly elongated at 45 to 75° counterclockwise from the shear direction, *i.e.*, 0 to 30° to the compression axis. These pockets may be aligned forming melt rich bands at ~ 20° from the shear direction, as shown in previous studies involving partially molten rocks. The orthopyroxene single crystal and aggregate long axis is parallel to the lineation defined by olivine elongation, which is orientated at 0 to 45° clockwise to the shear direction. These new experiments may then reconcile previous experiments and field observations.

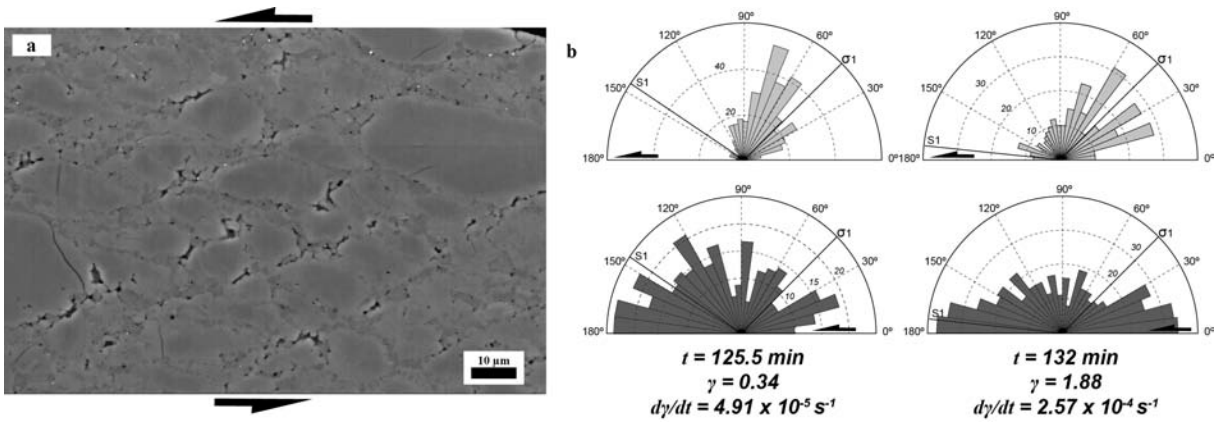

Fig. 4.6-11: (a) Backscattered electron image of the sample M169; light grey: olivine, dark grey: orthopyroxene, black: melt pockets. (b) Distribution of the elongation axes orientation of melt pockets (light grey) and orthopyroxenes (dark grey) in two defomed sample; S1 is the lineation; σ_1 is the compression axis.

The crystallization of pyroxene is roughly positively correlated with the shear strain rate and shows no correlation with the shear strain and the time duration. Different processes may account for that observation: (1) the increase of the reaction surface between melt and olivine due to olivine grain size decrease, and/or grain boundary density increase, resulting from a more efficient dynamic recrystallization at higher strain rate; or (2) considering pyroxene crystallization as a solution-precipitation process, stress concentrations at olivine grain boundaries that are a function of strain rate would directly determine the reaction progress.

Crystal preferred orientation (CPO) measurements on olivine show a maximum concentration of the [010] axes close to the normal of the shear plane. The [100] axes form a girdle close to the shear plane with one or two maxima concentrated normal or normal and parallel to the shear direction, respectively. The [001] axes display a maximum concentration, which becomes closer to the shear direction with increasing strain. Such CPO patterns may be explained by different processes: (1) deformation in high strain rate conditions that change the olivine dominant slip direction from [100] to [001]; (2) a partitioning of the deformation between melt rich band and the olivine matrix. Orthopyroxenes displays stronger CPO than olivines with the maximum concentration of the [001] axes close to the shear direction, and a maximum concentration of the [100] and [010] axes close to the normal to the shear plane. This CPO pattern may result from the deformation of the orthopyroxene under relatively high water and Al contents.

h. *Deformation of a crystalline system with two immiscible liquids: Implications for early core-mantle differentiation (V. Cerantola, N.P. Walte and D.C. Rubie)*

The differentiation of small planetesimals into a metallic core and a silicate mantle is the most important event during their accretion history. It has been suggested that partial core-mantle differentiation might have been initiated by static or deformation-induced segregation of molten Fe-S through a solid peridotite matrix after overstepping the FeS solidus. As a result of further temperature increases in planetary bodies, the silicate solidus is overstepped, which raises the question of the efficiency of the percolation of liquid Fe alloy in a partially molten peridotite. The aim of this study was to investigate whether a low percentage of basaltic silicate melt (dihedral angle < 60°) enhances the interconnection and segregation of FeS melt (dihedral angle > 60°) during deformation at varying strain rates.

The experiments were performed with simplified systems consisting of Fo_{90}-olivine (86 wt.%), iron sulphide (5 wt.%) and a synthetic primitive MORB (9 wt.%). The samples were deformed by means of a deformation-DIA cubic multianvil apparatus and the new MAVO six-ram press at pressures and temperatures of 20 kbar and 1450 °C and strain rates varying from 10^{-3} s^{-1} to 10^{-5} s^{-1}. Samples with an original capsule length of ca. 1500 μm were deformed by axial compression or pure shear to low finite strain (4 % bulk shortening), moderate strain (15 % shortening) or high strain (35 % shortening).

At a strain rate of 10^{-4} s^{-1} and moderate bulk shortening the silicate melt-free experiment shows that the sulphide melt distribution is predominantly controlled by deformation (Fig. 4.6-12a). Elongation and interconnection of sulphide patches are observed that may promote local grain boundary sliding. In contrast, under identical conditions but in the presence of basalt, the FeS melt pockets are hardly affected by deformation and show a more roundish shape probably driven by the minimization of surface energy (Fig. 4.6-12b). In this experiment the role of the grain boundary lubricant may have been taken over by the basalt melt.

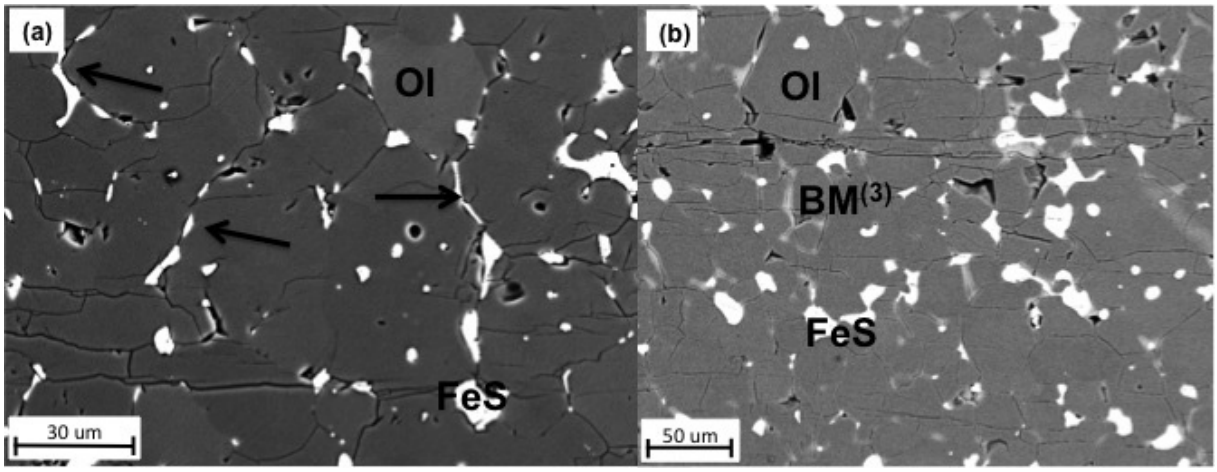

Fig. 4.6-12: Back scattered electron images of two samples shortened at a strain rate of 10^{-4} s^{-1} (vertical shortening) (a) System composed of Fo_{90} (95 wt.%, dark grey) and FeS (5 wt.%, white); FeS melt is strongly elongated by the deformation. (b) Same as (a) with the addition of 9 wt.% basaltic melt (light grey). Melt pockets are roundish and are little effected by deformation.

Similar observations have been made in all experiments. Under given conditions, the metal alloys in the silicate-melt containing samples are less affected by deformation than silicate-melt-free samples. Efficient segregation of high-dihedral angle melt such as FeS requires deformation enhanced interconnectivity as in Fig. 4.6-13a (stress dominated regime). If the FeS melt distribution is dominated by surface energy as in Fig. 4.6-12b (surface tension dominated regime), no segregation can occur. Considering the larger picture, it has been shown that the experimentally determined boundary between stress and surface tension dominated behaviour can be scaled to natural conditions, since systems with a constant product of melt pocket radius r and differential stress $\Delta\sigma$ fall in the same deformation regime (r x $\Delta\sigma$ = const => same regime, Fig. 4.6-13). Within this framework the role of the silicate melt can be understood by its weakening effect on the system rheology, *i.e.*, a given strain rate is coupled with a lower differential stress. Hence, the boundary between surface tension and stress domination is raised with respect to silicate-melt free systems (Fig. 4.6-13b) thereby enlarging the surface tension dominated regime and suppressing liquid percolation.

Further experiments have added additional complications. At higher finite strains a preferential separation of basalt is observed, leaving most of the FeS liquid stranded in the olivine matrix. Thus, deformation of a three-phase system can result in a complex sequence of behaviour: (1) Addition of basaltic melt pushes the system into a surface tension dominated regime. (2) Progressive deformation causes expulsion of basalt. (3) The remaining two-phase system deforms in the stress dominated regime. (4) FeS melt can interconnect and partially segregate. To conclude, we can assert that overstepping the silicate solidus does not contribute to deformation-induced percolation; efficient core-mantle differentiation requires other mechanisms such as a large scale melting and magma ocean formation.

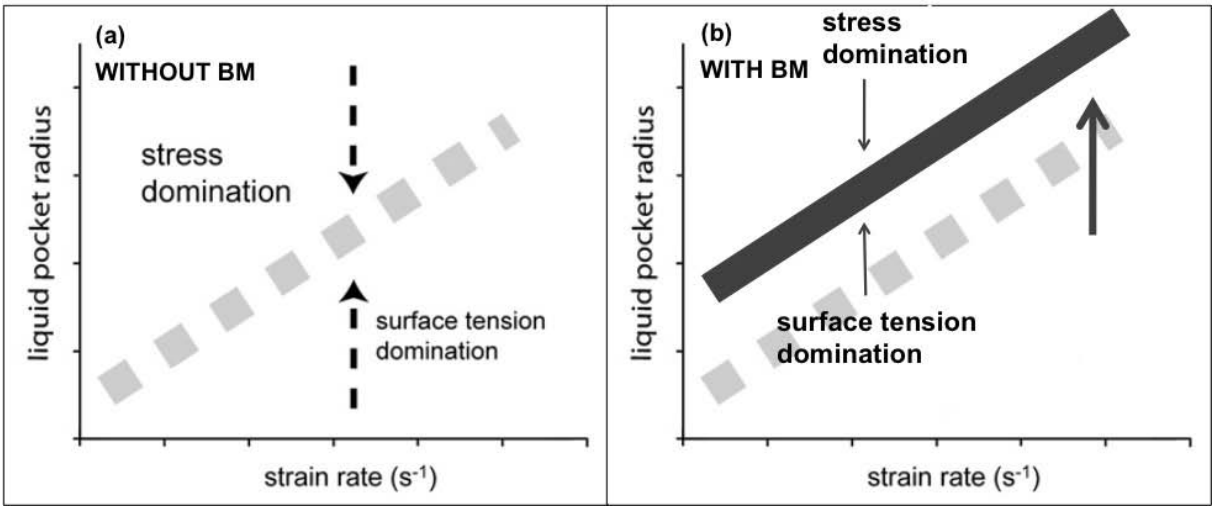

Fig. 4.6-13: Conceptual model representing the deformation regimes in olivine-FeS-silicate melt systems. The scale is logarithmic in both axes. (a) Olivine-FeS melt system. Arrows indicate the system development during progressive deformation, (b) Addition of silicate melt raises the boundary and thereby hinders FeS melt segregation (modified after Walte *et al.* 2011).

i. *The Tissint and NWA 6162 phyric shergottites: Evidence for multiple dynamic events each with distinct petrographic settings of shock-induced high-pressure mineral inventory (A. El Goresy, M. Miyahara/Sendai, E. Ohtani/Sendai, Ph. Gillet/Lausanne, S. Ozawa/Tokyo, Y.-T. Lin/Beijing, L. Feng/Beijing and S. Escerig/Lausanne)*

Tissint is a witnessed fall and a recovered Martian meteorite that fell near the town of Tissint (Morocco) on July 18th, 2011. Samples were picked up first in early October 2011. They are considered to be poorly weathered and probably with minor terrestrial contamination. NWA 6162 was also found in Morocco in 2009. Both Tissint and NWA 6162 are Al-poor ferroan basalts and are classified as shocked phyric shergottites. Tissint consists of olivine mega-crysts enclosed in a fine-grained matrix of pyroxene and maskelynite (feldspathic glass). The stone retains evidence for several dynamic episodes each with characteristic textural settings and inventory of shock-induced high-pressure assemblages.

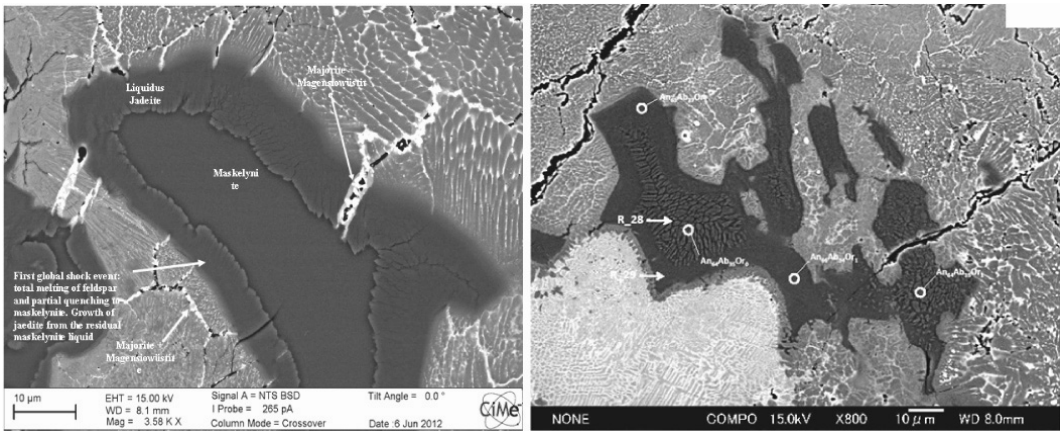

Fig. 4.6-14: **(left)** A BSE picture of a maskelynite enclave between shock-melted pyroxenes. Maskelynite is surrounded by a band of acicular liquidus jadeite crystals. Thin shock-melt veins containing the liquidus vitrified $MgSiO_3$ perovskite+ magnesiowüstite injected in pyroxene grain boundaries and also cross cut through the jadeite band indicating that they formed after solidification of both maskelynite and jadeite in a subsequent shock event. **(right)** A detail of a maskelynite enclave between pyroxene grains. Lamellar structure of jadeite inside maskelynite is well developed.

Original magmatic feldspar was quantitatively molten during the earliest shock event, quenched to both feldspathic glass and to liquidus jadeite. Pyroxene was also subjected to pervasive melting and olivine to partial phase transformation to ringwoodite. Both Tissint and NWA 6162 entirely lost their original igneous integrity during shock melting. An array of numerous thin shock-melt veins and few thick shock-melt veins of 10 micrometers in diameter pervasively intersect the Tissint stone each containing high-pressure liquidus assemblages. We decipher the shock features in Tissint and tentatively assign them to three dynamic episodes on Mars with distinct textural settings, abundance and compositions of the high-pressure inventories:

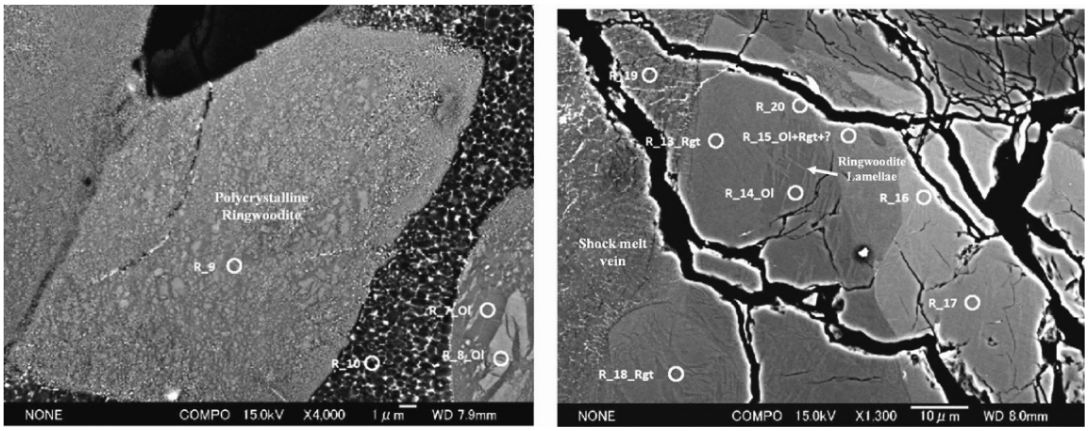

Fig. 4.6-15: **(left)** An originally olivine grain entrained in a shock-melt vein now entirely inverted to polycrystalline ringwoodite. Circle R_9 identifies the position of the Raman measurement. **(right)** Olivine inverted to ringwoodite in two sets of polycrystalline ringwoodite lamellae. Laser microRaman measurement was conducted at R_16.

(1) The first dynamic event induced total melting of feldspar and its quenching at high pressure to maskelynite glass along with liquidus jadeite is confirmed by the characteristic Raman bands at 502, 703 and 1015 cm^{-1}. Pervasive melting of pyroxene, pyrrhotite and titanomagnetite also took place at this episode as deduced from the spatial relationships. Acicular jadeite crystals grew on the pyroxene surface into the maskelynite liquid at high pressure (Fig. 4.6-14). The chemical composition of maskelynite ($An_{66}Ab_{34}Or_1$) is very similar to the composition obtained by EPMA on the jadeite crystals ($An_{64}Ab_{35}Or_1$). We hence envisage that the composition obtained from the jaedite crystals is a bulk composition of several microscopic components including jadeite as the major phase and minor silicate or silica glass. Textural and spatial relationship of the maskelynite pools and the bordering jadeite strongly suggests that jadeite was quenched from the plagioclase melt at $P < 19 > 10$ GPa and $T \approx 2000$ °C and not formed by devitrification of maskelynite glass after quenching (Fig. 4.6-14). This dynamic event entirely destroyed the original igneous texture and reset the original radiometric age.

(2) An array of thin shock-melt veins cross cut the whole Tissint stone. They penetrate Tissint along pyroxene grain boundaries and cut through the jaedite bands rimming maskelynite (Fig. 4.6-14). An assemblage of idiomorphic liquidus high-pressure $MgSiO_3$ glass and magnesiowütite fill the shock melt veins. Isotopic studies of the carbon inclusions in Tissint shergottite with NanoSIMS 50 L reveal very high δD values and isotopically light Carbon. These results are not inconsistent with an organic precursor.

(3) Another type of shock-melt veins that cross cut pyroxene contains considerably fragmented and mobilized $MgSiO_3$ glass + magnesiowüstite grains. Fragmentation and mobilization probably took place in a later dynamic or more likely a Martian tectonic event subsequent to the first vein formation episode.

(4) Fayalite-rich rims of the originally zoned olivine mega-crysts partly inverted to polycrystalline ringwoodite either in coarse ringwoodite domains in the originally fayalite-rich rims or in polycrystalline aggregate in the original olivine suggesting formation by incoherent olivine-ringwoodite phase transition (Fig. 4.6-15). Two sets of polycrystalline lamellae (Fig. 4.6-15) of ringwoodite occur in individual olivine crystals near shock-melt veins. Orientation of the two polycrystalline ringwoodite lamellae strongly suggests initial coherent nucleation of ringwoodite lamellae with their (111) parallel to the (100) planes of olivine followed by an incoherent phase transformation mechanism due to the build up of strain in the olivine crystals. Laser microRaman study revealed the main Raman bands of ringwoodite at 848 and 803cm^{-1} measured at ringwoodite lamellae at point R_16 in Fig. 4.6-15. This is also an ample evidence for erasing of the igneous texture through the young successive shock events. The Raman spectrum also shows the olivine Raman main bands at 854 and 827cm^{-1}. Several original olivine crystals adjacent to shock-melt veins were shock dissociated to a fine-grained assemblage of $MgSiO_3$ perovskite + magnesiowüstite. This strongly suggests that the olivine dissociation took place at equilibrium peak-shock pressure slightly overstepping 25 GPa and at T above 700 °C. The three tentatively deciphered dynamic events on Tissin lithology entirely erased the igneous integrity of both Tissin and NWA 6162.

4.7 Materials Science

The aims of most material science projects at Bayerisches Geoinstitut include the synthesis of new ultra-hard materials and the investigation of a wide range of physical and chemical properties of such materials. The facilities of Bayerisches Geoinstitut are ideal for pursuing these aims because of the extensive range of high-pressure equipment that is required for synthesizing ultra-hard materials. In addition, the facilities available for chemical analysis, X-ray diffraction and spectroscopic studies are ideal for characterizing sample properties. In order to investigate physical and chemical properties at pressure-temperature conditions beyond those that can be achieved experimentally, computational methods are also utilized. Results presented here cover oxides, borides, nitrides, boron and a multiferroic material $BiFeO_3$.

In the first contribution, the melting temperature of cubic boron nitride (BN) has been determined up to 1000 GPa using first-principles molecular dynamics simulations. Cubic BN is an ultra-hard material with properties approaching those of industrial diamond and it is also a potential pressure standard in diamond anvil cell experiments. Previously the melting temperature had been determined experimentally to only 10 GPa. An important conclusion is that above 500 GPa (0.5 TPa) the melting temperature decreases with increasing pressure so that the slope of the melting curve changes from positive to negative. The reason for this behaviour is that pressure-induced structural changes in liquid BN make its density greater than that of the solid at pressures above 500 GPa.

The compression behaviour of the sesquioxide V_2O_3 is reported up to 33 GPa. This compound displays a 'insulator-metal' Mott transition below 150-160 K that is associated with a strong thermodynamic instability, a structural change and a change in electrical resistivity of orders of magnitude. Results of the compression study indicate a lower bulk modulus than previously-determined values - which may have been affected by non-hydrostatic stress. The compression behaviour of corundum-structure V_2O_3 deviates from that of other sesquioxides and may be indicative of other unusual physical and chemical properties.

Borides are potential candidates for ultra-hard materials and two studies are presented here, of MnB_2 and FeB_4 respectively. Through both experiments and first-principles calculations, the structure, stability and bulk modulus of MnB_2 have been determined, with the conclusion that this is not a super-hard material. In the second study a very detailed investigation of the crystal structure of FeB_4 has been made through experiments on a single crystal and the compression behaviour has been determined up to 38 GPa. The value obtained for the bulk modulus is high compared with that of most borides and is consistent with a high hardness value for this material.

A detailed study of the Raman spectra of a single crystal of α-boron up to 36 GPa and 473 K is described below. The final two contributions present results on (1) the structural and electronic properties of OsB_2, a potentially hard material, as determined by first-principle

calculations and (2) the properties of $BiFeO_3$, a multiferroic material, using samples synthesized at various conditions up to 19 GPa and 1100 ° C.

a. *High-pressure melting of cubic boron nitride from first principles (N. de Koker)*

Due to its structural simplicity and stability over a large pressure and temperature range, cubic boron nitride (inclined structure; $F\bar{4}3m$) has been proposed as a potential pressure standard for diamond anvil cell experiments. The phase also has important industrial and manufacturing applications as a super-hard substitute for industrial diamond. Though BN is stable in a graphite-like hexagonal phase ($P6_3/mmc$) at ambient pressures, it transforms to cubic BN at pressures around 2 GPa, with the triple point on the liquidus estimated to be between 8 ± 2 GPa and 3500 ± 250 K. First-principles computations predict that cubic BN transforms to the rock salt structure ($Fm\bar{3}m$) at pressures between 0.85 - 1.11 TPa, well beyond the current limits of both experimental measurements and industrial needs. The melting temperature of cubic BN has not been determined at pressures beyond 10 GPa.

We used first-principles molecular dynamics (FPMD) simulations to construct internally consistent thermodynamic models for liquid and cubic BN, and apply them to compute the melting curve of cubic BN up to 1 TPa. Our computed melting curve (Fig. 4.7-1) reaches a maximum at 510 GPa and 6550 ± 700 K, after which it decreases to reach a value of 5570 ± 1050 K at 1 TPa. The turnover in the Clapeyron slope originates from the change in relative densities of the liquid and solid. Results from first principles simulations of the melting of diamond available in the literature show a similar turnover in the Clapeyron slope at pressures around 0.5 TPa, although the melting temperature of diamond is predicted to be around 1000-2500 K higher than that of cubic BN, consistent with measurements at lower pressures.

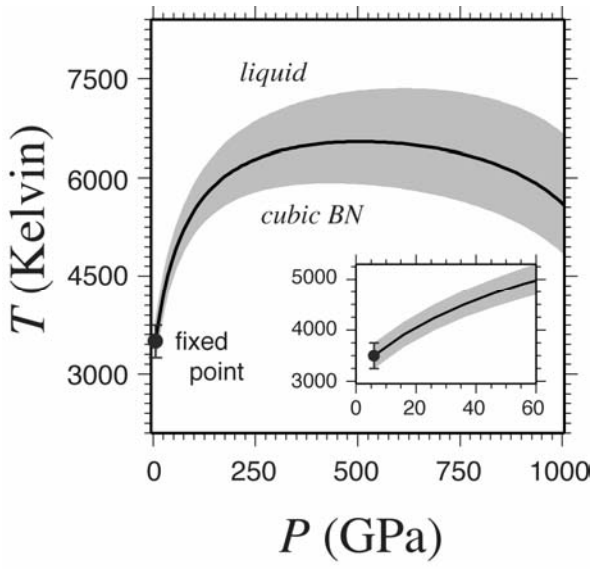

Fig. 4.7-1: Melting curve for cubic BN determined with the low-pressure experimental melting estimate at 8 GPa and 3500 ± 250 K as the integration constant.

The turnover along the melting curve and the associated density crossover between liquid and solid BN can be understood in terms of changes in the structure of the liquid relative to that of the solid as the materials are compressed. Because the lattice symmetry remains unchanged in a given solid phase (zincblende structure in this case), the only mechanism available for accommodating compression is a decrease in bond length; very large pressures (0.85-1.11 TPa) are needed to stabilize the rock salt structure, in which B and N are 6-fold coordinated. The liquid is not constrained in this way, and takes on a range of coordination species at any given volume, allowing it to accommodate compression by increasing its packing density: 5- and 6-fold coordination species are present at pressures in excess of 0.5 TPa.

b. *Compression behaviour of V_2O_3 (S.V. Ovsyannikov, D.M. Trots, A.V. Kurnosov, W. Morgenroth/Frankfurt/M. and L.S. Dubrovinsky)*

Sesquioxides M_2O_3 (M = Al, Fe, Ti, Cr, Ga, etc.) are of considerable interest in several fields, including geosciences, condensed matter physics and chemistry. At ambient conditions several of them (Al_2O_3, α-Fe_2O_3, Cr_2O_3, Ti_2O_3, V_2O_3) adopt a corundum lattice ($R\bar{3}c$ space group, #167) and several more (*e.g.*, Ga_2O_3, In_2O_3, etc.) have different ground states but may also crystallize with the corundum structure, *e.g.*, after high-pressure high-temperature treatment. Compression behaviour of most of the above sesquioxides has already been investigated. However, one interesting case has not yet attracted significant attention, namely, V_2O_3. This oxide is characterized by a fascinating 'insulator-metal' Mott transition below 150-160 K, that is accompanied by a multi-order jump in electrical resistivity values and monoclinic distortion of the crystal structure. It was found that this Mott transition is related to a very strong thermodynamic instability which can be suppressed by the application of a moderate pressure of 2 GPa. Only a few studies have examined the high-pressure behaviour of V_2O_3 beyond 2 GPa. Previous high-pressure structural studies of corundum-structured V_2O_3 have reported strongly discrepant bulk modulus values, ranging from B_0 ~ 173 GPa determined in a liquid pressure-transmitting medium, to B_0 ~ 255 GPa determined in a solid LiF pressure-transmitting medium. Recent theoretical studies have suggested that V_2O_3 should exhibit both α-Gd_2S_3-type and Th_2S_3/U_2S_3-type structures at moderate pressures.

In this work we investigated the compression behaviour of V_2O_3 powder *in situ* at high pressure. A diamond anvil cell with 250 μm culets, a rhenium gasket and a neon pressure-transmitting medium were employed. The experiment was carried out at the Petra-III beamline at DESY with a wavelength of 0.29135 Å. Examples of collected diffraction patterns are presented in Fig. 4.7-2. The high-pressure spectra above 30 GPa show additional weak peaks that should be related to a phase transition (Fig. 4.7-2). Our structural data have a good correspondance with those obtained using liquid pressure-transmitting media (Fig. 4.7-3a, b) and deviate strongly from those collected in solid NaCl/LiF media. Using the third-order Birch-Murnaghan equation of states we analyzed the data up to 32 GPa and at fixed B'=4 obtain a bulk modulus B_0 ~ 151 GPa (Fig. 4.7-3c). This value is lower than those reported earlier, B_0 ~ 214 and 255 GPa found in a NaCl/LiF pressure-transmitting medium

and B_0 ~ 173 and 195.6 GPa – in liquid ethanol-methanol medium. These results demonstrate that non-hydrostatic effects can strongly modify experimentally-obtained compression properties of V_2O_3.

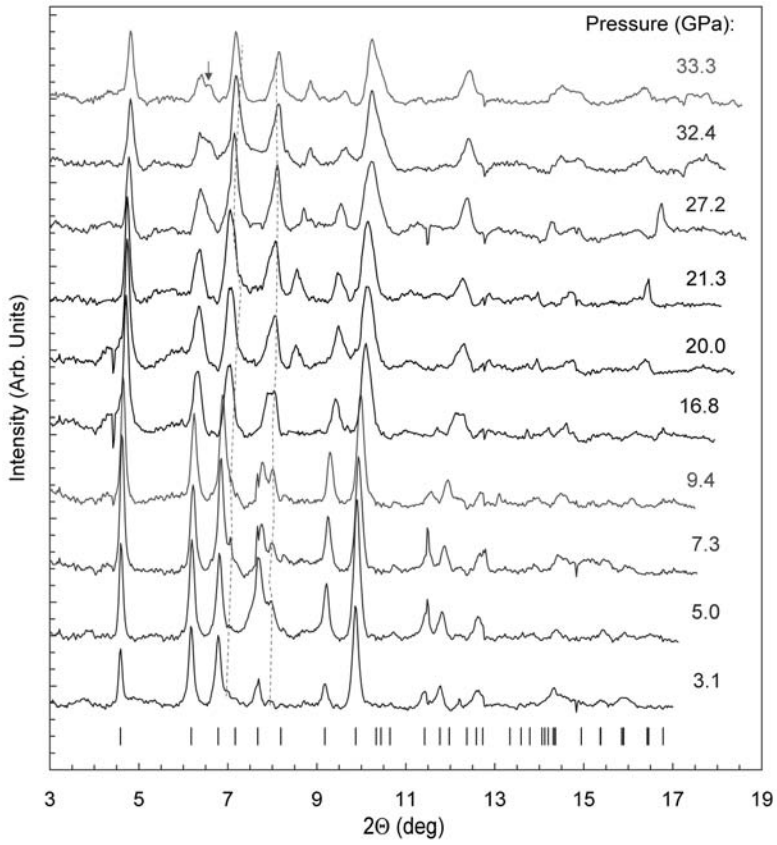

Fig. 4.7-2: Evolution of X-ray diffraction patterns of V_2O_3 at ambient temperature with increasing pressure. Pressure values are shown adjacent to each pattern. The small dashes at the bottom show the peak positions for the corundum structure. The vertical dashed lines show the positions of the main peaks originating from the Re gasket. The small arrow indicates the appearance of a new reflection at 33.3 GPa.

Based on simple 'geometrical' considerations it has been proposed that, for similar oxide compounds, the bulk modulus B_0 should be inversely proportional to the unit cell volume V_0, such that $B_0 \times V_0$ = constant. However, the strongly-correlated metallic corundum-structured phase of V_2O_3, with B_0 = 150.6 GPa, apparently deviates from results for other phases, including the narrow-band-gap corundum-type phase of Ti_2O_3 and wide-band-gap phases of Al_2O_3, Cr_2O_3, Fe_2O_3 and Ga_2O_3 (Fig. 4.7-3d). For the comparison we used the most accurate and reliable literature data that are currently available, *e.g.*, those determined in single-crystal diffraction studies in hydrostatic pressure-transmitting medium. The rather unusual compression behaviour of V_2O_3 should reflect other unconventional physical properties of this material. Probably, the lattice dynamics calculations that can account for strongly correlated effects could clarify the reasons for the low bulk modulus value of the corundum phase of V_2O_3.

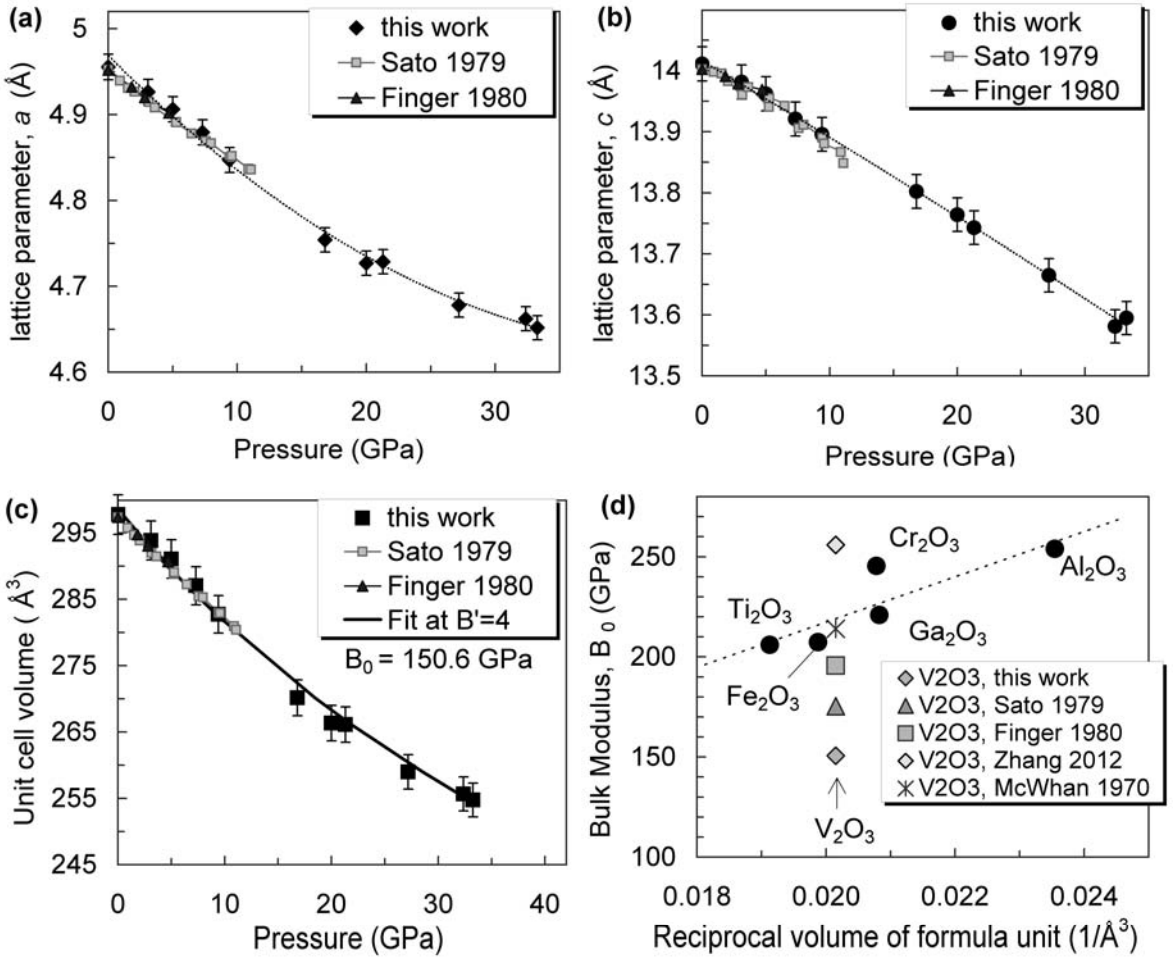

Fig. 4.7-3: Pressure dependencies of the unit cell parameters of the corundum-type V_2O_3 at ambient temperature. Plots (*a*), (*b*), and (*c*) show the pressure dependencies of the lattice parameters *a* and *c*, and the unit cell volume. Plot (*d*) shows a correlation between the bulk modulus and reciprocal volume of formula units for corundum-structure systems.

c. *Stability of MnB_2 with AlB_2-type structure revealed by first-principles calculations and experiments (H. Gou, G. Steinle-Neumann, E. Bykova, Y. Nakajima, Y. Li, S.V. Ovsyannikov, L.S. Dubrovinsky and N.A. Dubrovinskaia)*

The search for superhard materials has been the subject of active research over the past decade, with both experimental synthesis and first-principles calculations playing an active role. Despite such efforts, the identification of industrially-viable superhard materials remains difficult and often studies are misleading. Recently, manganese diboride (MnB_2) with the ReB_2-type structure was theoretically predicted to be a superhard material with hardness of ~44 GPa. According to the calculations, it is energetically favored over the AlB_2-type structured MnB_2 which can be synthesized at ambient pressure. However, the ReB_2-structure for MnB_2 has not been observed experimentally to date.

Here we performed synthesis experiments using piston-cylinder apparatus at 1.5 GPa and 3 GPa and 1150 °C, 1350 °C and 1400 °C for durations of 40 to 120 hours, and multianvil apparatus at 5 and 8 GPa and 1000 °C and 1500 °C for 1 hour. Phase analysis of recovered samples was performed by single-crystal X-ray diffraction. The morphology and chemical composition of a single crystal of MnB_2 was examined by scanning electron microscopy, transmission electron microscopy, and electron-probe micro-analysis. Vickers hardness (H_v) was measured using a microhardness tester under loads of up to 1.98 N. Structural, electronic and magnetic properties of MnB_2 candidate phases (ReB_2- and AlB_2- type structures) were calculated using the Vienna *ab initio* simulation package (VASP). Both GGA and GGA+*U* calculations using the projector augmented wave method were performed. For the GGA+*U* calculations, U =3.9 eV and J =1 eV were applied to the Mn 3*d* states.

High-pressure experiments were successful in synthesizing single crystals of MnB_2 with the previously known AlB_2-type structure. The Vickers hardness of a single-crystal of MnB_2 was measured. At a load of 0.98 N, the average hardness was found to be 7.5 GPa. As the load increased, the average hardness decreased to 5.5 GPa at 1.96 N.

Using GGA we reproduced the previous computations and found that the ReB_2-type structure was predicted stable over the AlB_2-type structure at (Fig. 4.7-4a). With a zero pressure bulk modulus of 275 GPa, the ReB_2-type MnB_2 is indeed extremely stiff; for AlB_2-structured MnB_2 the bulk modulus K_0 =230 GPa. Including on-site Coulomb interactions (GGA+*U*) for the Mn-3*d* states, the picture changes and AlB_2-type MnB_2 becomes energetically favored over the ReB_2 structure (Fig. 4.7-4b) despite the fact that Mn is now in an anti-ferromagnetic state.

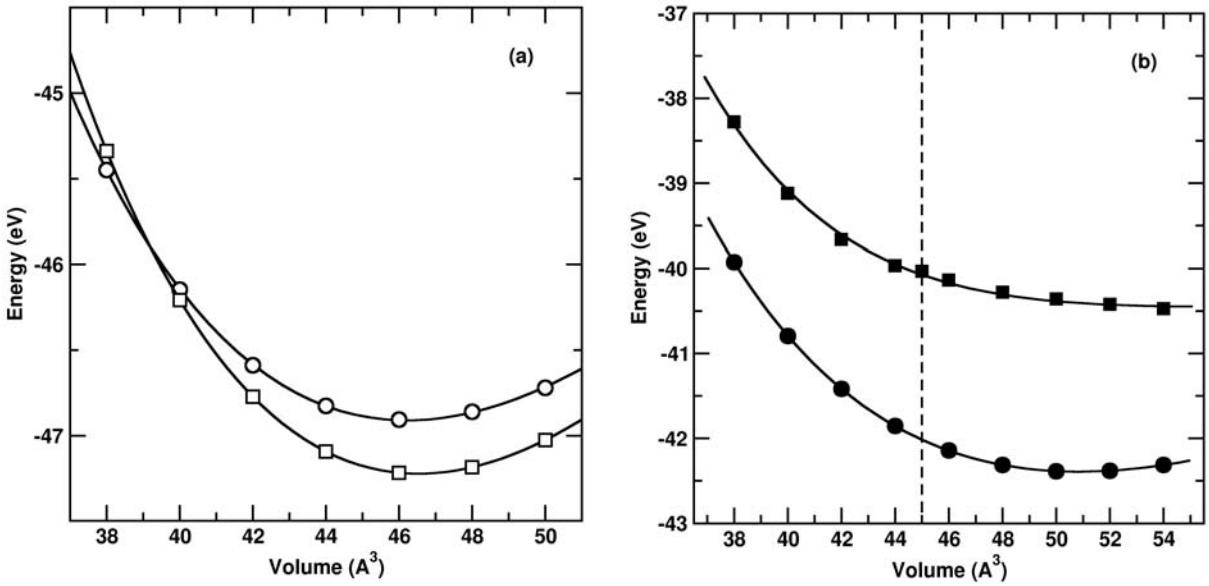

Fig. 4.7-4: Calculated total energy as a function of volume of the AlB_2-type (circles) and ReB_2-type (squares) MnB_2. (a) GGA; (b) GGA+*U* calculations, the vertical dashed line marks the location of the high-spin–low-spin transition for ReB_2-structured MnB_2 as found in the GGA+*U* calculations.

The low bulk modulus of 143 GPa for the stable AlB_2-type MnB_2 does confirm the measurements of hardness in the sense that MnB_2 is not a suitable candidate in the search for superhard materials.

d. *Compressibility of orthorhombic FeB_4 studied on a single crystal sample (E. Bykova, H. Gou, N.A. Dubrovinskaia and L.S. Dubrovinsky, in collaboration with M. Merlini and M. Hanfland/Grenoble)*

Metal borides are an important class of compounds having a number of remarkable properties such as high superconductivity (MgB_2), low compressibility (OsB_2), and high hardness (tungsten borides, for example). Therefore synthesis of novel metal borides and the investigation of their properties is of great importance for material science and technology. Theoretical calculations can help in a search for the compounds with a combination of desired properties. Recently two novel phases in the Fe-B system, FeB_2 and FeB_4, were predicted, and phonon-mediated superconductivity with T_c = 15-20 K for the latter phase was suggested theoretically. Later, the formation conditions of these borides were calculated and it was proposed that the phases are stabilized by high pressure. These predictions formed the basis of our search for novel iron borides, and a series of high-pressure and high-temperature experiments in multianvil apparatus have been undertaken. As the result a novel predicted phase of FeB_4 was synthesized. The single crystals were characterized by X-ray diffraction using an Xcalibur X-ray diffractometer (Mo K_α-radiation) equipped with a CCD detector. The data treatment (integration and absorption corrections) was performed with CrysAlis RED software. The structure was solved by the direct method and refined by a full matrix least-squares refinement using SHELXTL software.

The crystal structure of FeB_4 consists of distorted FeB_{12} polyhedra packed through sharing tetragonal faces in columns parallel to the *c* axis. Figure 4.7-5a shows that each column is connected with 4 neighbors by common edges of polyhedra and all neighbors are shifted in 1/2 *c*, forming a chess-like packing. CrB_4 has the similar structure but the CrB_{12} polyhedra are not distorted (Fig. 4.7-5b). Fe-B distances in a FeB_{12} polyhedron are 2.009(4), 2.109(4), 2.135(3) and 2.266(3) Å. According to the 3rd Pauling rule for polyhedrons sharing their faces, the Fe-B bonds tend to increase to enlarge the Fe-Fe separation. Therefore longer bonds (2.135(3) and 2.266(3) Å) are related to the boron atoms forming common tetragon faces. The Fe-B bonds located in the *a-b* plane (2.009(4), 2.109(4) Å) are the shortest among those known for iron borides. B-B distances are 1.713(6), 1.844(4), 1.894(6) Å. The shortest B-B contact, 1.713(6) Å, is that in the *a-b* plane and it is one of the shortest among those known for borides. An exception is only iron-doped β-boron ($FeB_{\sim 49}$), which has the structure of β-boron with voids occupied by Fe.

A single crystal of FeB_4 was used to study the compressibility up to 38 GPa. For generation of high pressure we used a screw-driven piston cylinder BX90 diamond anvil cell (DAC) developed at Bayerisches Geoinstitut. We used a pair of Boehler-Almax diamonds with 0.25 mm culets and a pre-indented rhenium gasket with a hole of 0.12 mm in diameter drilled in the middle of the indentation. Ne loaded at 1.2 kbar of gas pressure was used as a pressure

medium. Pressure was determined by the ruby fluorescence method. The data were collected at ID09a beam line at ESRF (λ= 0.41438 Å). The reflection intensities were measured during phi-scanning of narrow (1°) frames from phi -40 to 40° with a MAR555 flat panel detector. The sample-to-detector distance, the detector tilt, and the beam center position were calibrated using a CeO_2 standard. The data were collected between 2 and 38 GPa with a steps of ~ 3 GPa that resulted in 13 pressure points. Afterwards we decreased pressure in the cell down to ambient conditions with the same pressure step and collected data for 14 additional pressure points on decompression. The data treatment was performed with the CrysAlis RED software. No special corrections for diamond absorption were applied.

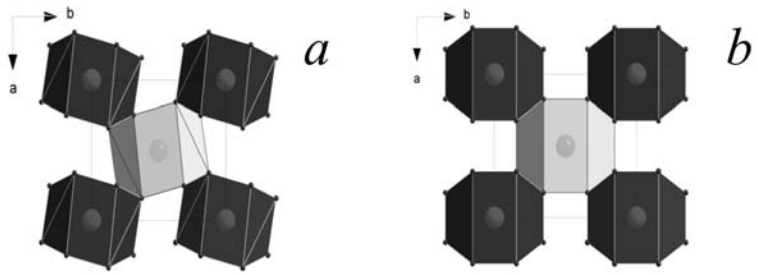

Fig. 4.7-5: Crystal structure of FeB_4 (a) and CrB_4 (b) viewed along the *c*-direction, polyhedra with the same color have the same positions in height along the *c*-direction.

Figure 4.7-6a shows the pressure dependence of the unit cell volume under compression and decompression of FeB_4. Since no significant differences between the two datasets can be observed, the combined data were fit with the 3rd order Birch-Murnaghan equation of state. The resulting bulk modulus K = 252(5) GPa is rather high among such values known for borides, which suggests a potential high hardness of FeB_4. Fig. 4.7-6b demonstrates that the unit cell parameters have different compressibilities. The largest parameter *b* is least compressible: FeB_4 in this direction is as stiff as diamond (Fig. 4.7-6b).

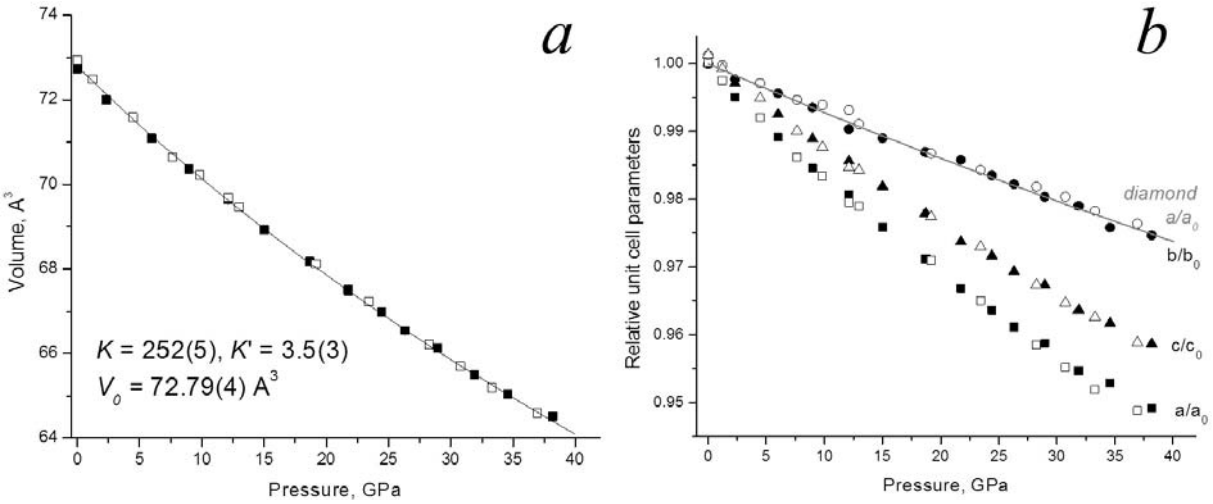

Fig. 4.7-6: Volume (*a*) and linear (*b*) compressibilities of the FeB_4 structure. Filled symbols show data points collected on compression and open ones were collected on decompression. Linear compressibility is represented in the relative change of the unit cell parameters. The linear compressibility along the *b* direction is comparable with that for diamond shown by the line.

e. *Raman spectroscopy investigation of α-boron at elevated pressures and temperatures (G. Parakhonskiy, V. Vlček, N.A. Dubrovinskaia, R. Caracas/Lyon and L.S. Dubrovinsky)*

Raman spectroscopy is recognized as a powerful non-destructive technique for characterization of boron polymorphs and their behaviour under pressure. Boron has three polymorphs (α-, β-, and γ-B), and each of these possesses its unique Raman spectrum, which can be used as a phase fingerprint.

We undertook a detailed Raman spectroscopy investigation of α-boron single crystals at ambient conditions and at pressures up to 36 GPa and temperatures up to 473 K. The crystals studied were synthesised at high pressure high temperature and their purity was carefully examined to assure the reliability of the obtained experimental results. Experimentally measured frequencies of the Raman modes of α-boron at ambient conditions agree well with those previously reported.

During isothermal compression up to 35 GPa at room temperature (298 K), a monotonous shift of the Raman peak positions of α-B toward higher wavenumbers was observed. The velocity of the shift of the frequencies is different for different lines and varies between 2.68 cm^{-1}/GPa for the 768 cm^{-1} line and 5.19 cm^{-1}/GPa for the 917 cm^{-1} line. From the acquired data the Grüneisen parameters $\gamma_i = -\partial \ln \omega_i / \partial \ln V$ were estimated. They are listed in Table 1 and are compared to the experimental and theoretical values of the Grüneisen parameters deduced from the pressure derivatives of frequences published by Vast *et al.* The monotonous pressure-induced broadening of the Raman bands is observed under compression. Exceptional behaviour of the first E_g mode was recently discussed in the literature and it was suggested that this mode corresponds to the icosahedron librational vibration that is highly harmonic. We observed that under compression up to 36 GPa, the entire Raman profile keeps its form which indicates the preservation of the icosahedral clusters in the α-B structure within the studied pressure range.

The dependence of the Raman A_{1g} mode of α-B (at 784 cm^{-1} at ambient conditions) on pressure and temperature was selected for further analysis because this line is relatively strong and sharp. Based on our experimental data (Fig. 4.7-7), we obtained an empirical equation which allows determining pressure (in GPa) if temperature and the wavenumber of the A_{1g} mode of α-B are known:

$$P = 0.293\omega + 0.03T - 239$$

where P is pressure in GPa, ω is the peak position in cm^{-1} and T is the temperature in K with estimated uncertainties of 0.5 GPa, 3 cm^{-1} and 5 K. The fitted solid line described by this equation has a slope of 0.11±0.02 $cm^{-1}K^{-1}$. The temperature shift of each point was calculated by averaging the shifts at different pressures. Estimated uncertainties in temperature and peak positions are 5 K and 3 cm^{-1} respectively.

Table 1: Mode Grüneisen parameters of α-B Raman active vibrations.

mode	E_g	E_g	A_{1g}	E_g	E_g	A_{1g}	E_g	A_{1g}	E_g
This work, γ_i	0.325	1.541	1.037	1.287	0.939	1.321	1.114	1.493	1.233
$\gamma_{exp,}$ Vast(1997)	0.130	1.260	0.973	1.139	0.756	1.186	0.904	1.306	1.040
γ_{theor}, Vast(1997)	0.077	1.215	0.889	1.077	0.656	1.155	0.834	1.229	1.083

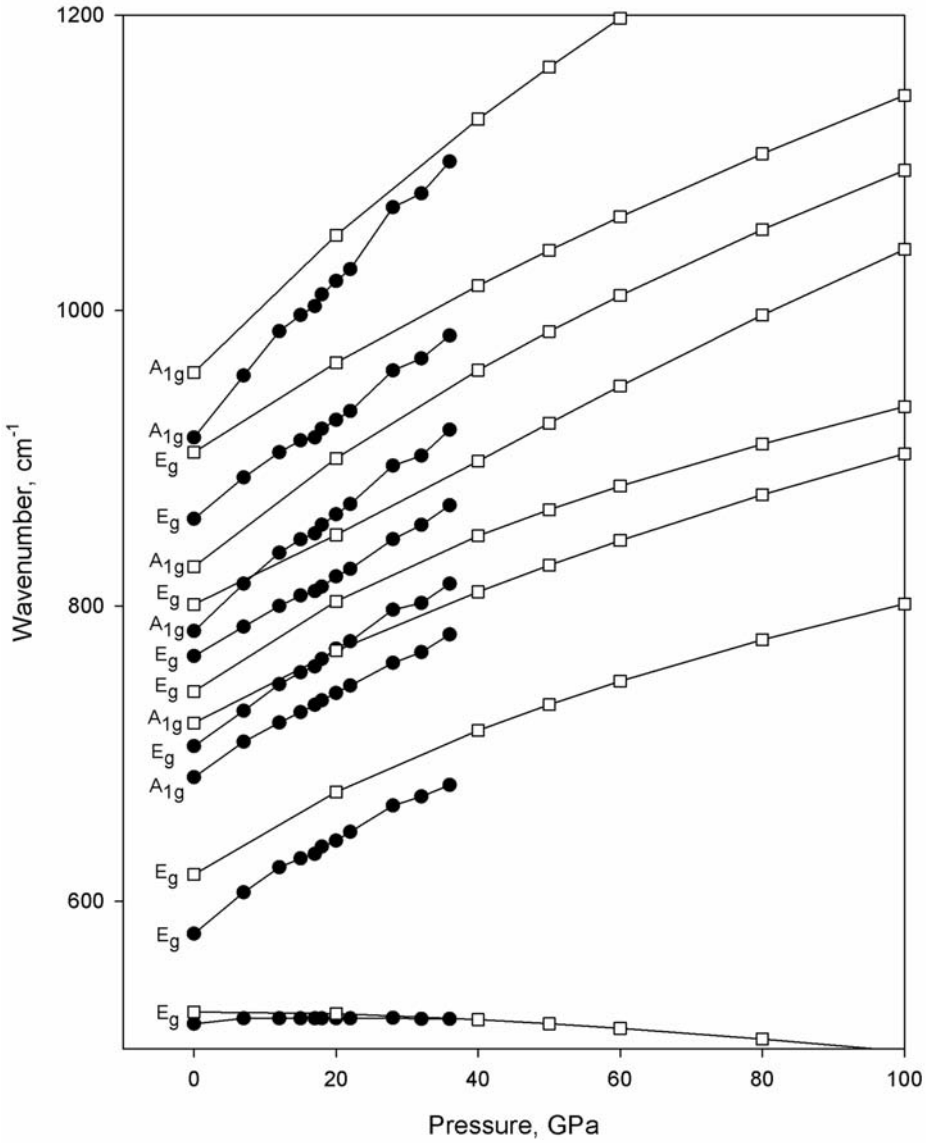

Fig. 4.7-7: The pressure dependence of the wavenumbers of the Raman modes of α-boron. Black circles are experimentally obtained values, white squares are theoretically calculated ones.

f. *Structural and relative stabilities, electronic properties and possible reactive routing of osmium and ruthenium borides from first-principles calculations (Y. Wang, T. Yao, L. Wang, J. Yao, H. Li and J. Zhang/Qinhuangdao; H. Gou)*

As likely candidates for hard or super-hard materials, transition metal borides have attracted considerable attention. The compound OsB_2 is of particular interest because of a significant enhancement of mechanical properties when the boron atom is incorporated into the osmium lattice. Recently, some tetra-boride samples were synthesized in order to investigate possible further enhancements of the mechanical properties. Osmium and ruthenium borides with high boron contents, OsB_3, OsB_4 and RuB_4, have recently been predicted to have quite different structures. Usually, neighboring metal compounds share the similar structure type; thus, questions about the lowest energy structures, especially considering the previous predictions concerning OsB_3, OsB_4 and RuB_4, remain open. If stable structures of borides change with composition, their physical properties can also completely alter.

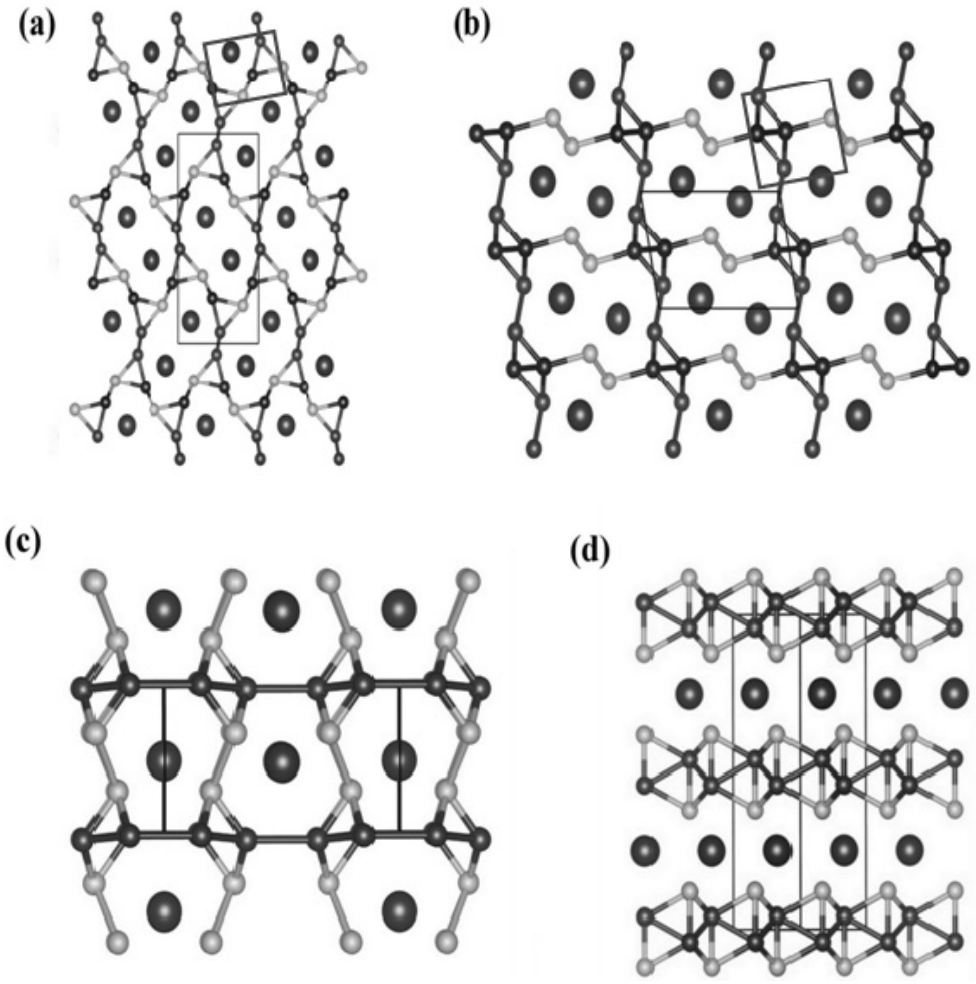

Fig. 4.7-8: Crystal structures for RuB_3 (a), OsB_3 (b), OsB_4 (c), RuB_4 (d). The large spheres represent Os or Ru atoms, and small spheres represent B atoms.

Here we perform first-principles calculations to provide a fundamental understanding of structural features and relative stability, mechanical, electronic properties and possible reactive routing of osmium and ruthenium borides. The structural searches and calculations of formation enthalpy identify a low-energy monoclinic phase for OsB_3, orthorhombic phase for OsB_4, orthorhombic phase for RuB_3 and hexagonal phase for RuB_4 (Fig. 4.7-8). Also, a structural transition at high pressure is predicted for MB_3 and MB_4 (M=Os and Ru). Moreover, among the borides, orthorhombic RuB_3 and OsB_4 phases are predicted to be potential hard materials with estimated Vickers hardness of 26.3 and 31.3GPa, respectively. The analysis of the electronic properties and crystal orbital Hamilton population shows that the directional boron-boron networks, together with strong metal-boron bonds, are responsible for their excellent mechanical properties. Relative enthalpy calculations with respect to possible constituents are also investigated to assess prospects for phase formation and attempts at high-pressure synthesis are proposed to obtain osmium and ruthenium tri- and tetra-borides.

g. *A study of thermobaric treatment effects in multiferroic $BiFeO_3$ (D.P. Kozlenko/Moscow, S.V.Ovsyannikov and L.S. Dubrovinsky)*

Multiferroic materials exhibit the coupling of electric and magnetic properties which could provide possibilities for the control of magnetic properties by an electric field and visa versa. Such materials are therefore extremely important for the development of new electronic devices and are at the current focus of scientific research in condensed matter physics.

$BiFeO_3$ is one of the most promising multiferroic materials for both fundamental and applied research, as this material exhibits both polar and magnetic order well above ambient temperature. The polar rhombohedral $BiFeO_3$ *R3c* phase is formed below the Curie temperature T_C = 1100 K. Recently, the existence of novel high-pressure phases of $BiFeO_3$ was deduced from synchrotron radiation diffraction and far infrared spectroscopy studies. The antiferroelectric orthorhombic phase of Pbam symmetry is formed at P ~ 4 GPa, and orthorhombic Pnma phase at P ~ 10 GPa.

It is well known that thermobaric treatment can stabilize novel phases of materials that are not stable at ambient conditions. In order to study thermobaric treatment effects on $BiFeO_3$, three samples were prepared at different conditions in a multianvil press: HPHT-1 at 5 GPa, 600 °C, 1h 20min, HPHT-2 at 20 GPa, 400 °C, 1 h, and HPHT-3 at 19 GPa, 1100 °C, 1 h. Images of the samples and Raman spectra are shown in Fig. 4.7-9. The Raman spectra of all samples have well-structured and narrow Raman lines in comparison to the spectrum of the initial $BiFeO_3$ powder that was used as the starting material. In addition, an extra Raman line is observed for the sample HPHT-1 at 170 cm-1, which is absent for the $BiFeO_3$ starting material. Preliminary X-ray diffraction studies have shown that observed diffraction lines can be indexed within the rhombohedral R3c space group. More detailed neutron diffraction studies of the crystal structure, which allow oxygen atomic shifts in the crystal structure to be explored with a excellent precision, are planned.

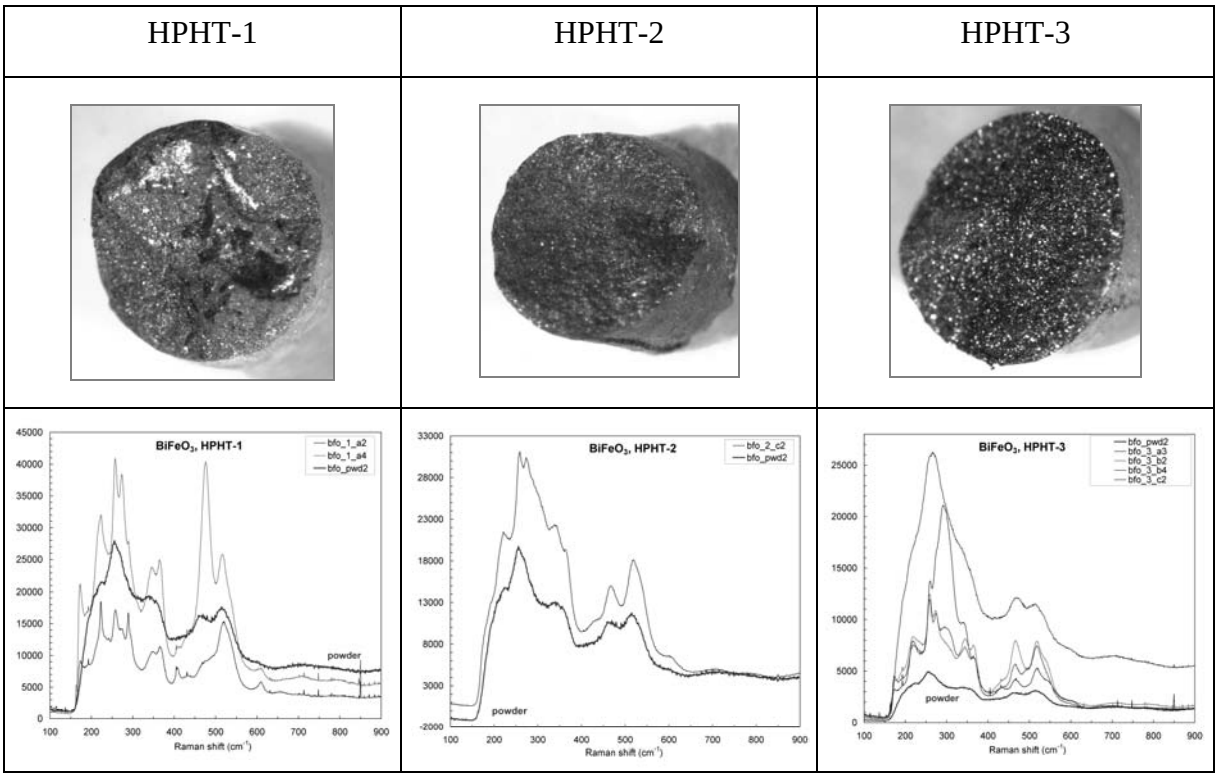

Fig. 4.7-9: Photos of the prepared $BiFeO_3$ samples and Raman spectra, recorded at several points of the sample surface and compared to the spectrum of the initial powder of $BiFeO_3$.

4.8 Methodological Developments

The development of novel theoretical and experimental techniques and the exploration of their potential are fascinating scientific challenges, which can sometimes provide unexpected pioneering results. Such innovative efforts are necessary to eventually achieve a fundamental break-through and to be at the forefront in a scientific discipline. Therefore it is worthwhile to invest the effort and expense associated with time-consuming developments. The great variety of subjects of methodological work presented this year reflects the diversity of research directions at the Bayerisches Geoinstitut.

The thermodynamic description of physical properties creates a solid basis for the analysis of processes in the Earth's deep interior. In the first contribution of this chapter a novel flexible and extensible software package structure, developed at BGI, is presented that allows the simulation of the stable phase assemblage and the thermodynamic behaviour of polycrystalline aggregates based on the properties of constituent mineral phases for a given composition.

The second computational contribution of this chapter presents a new method on how to advect a scalar field in a fluid flow, for example geodynamic simulations. The method is based on the concept of solving a second order wave-equation rather than the first order advection-equation which results in advection without numerical diffusion. Here, a multi-dimensional formulation through a splitting of the advection equation into the different directions is introduced, and the solution is analyzed. The approach is shown to be computationally efficient and remarkably successful in reproducing analytical results.

Aqueous fluids are important agents of metasomatism and chemical transport in the mantle. Solvent properties of aqueous fluid as a function of pressure are poorly known. Even basic data, such as the dielectric constant of water, the dissociation constant of water itself and the degree of dissociation of salts and acids at mantle pressures have never been determined. All these parameters are in principle accessible through measurements of electrical conductivity. A new method to investigate the electrical conductivity of fluids in a hydrothermal diamond anvil cell provides access to these properties at temperatures up to 900 °C and pressures to at least 7.5 GPa, an order of magnitude higher than in previous studies.

Accurate stress measurements are a prerequisite for the determination of rheological properties of materials, and have been a challenge for deformation experiments at elevated pressure and temperature. In the fourth contribution the piezoelectric response – charge displacement in response to stress exerted on the crystal – of marker minerals is investigated as a new approach to this long-standing problem. Initial results using quartz and $GaPO_4$ are encouraging at room temperature, but further technological development is necessary to make the method applicable at high temperature.

Similar to stress measurements in deformation experiments the exact determination of pressure is of great importance in diamond anvil cell experiments. Most conveniently pressure is measured by the fluorescence shift of a calibrant: ruby or Sm-bearing yttrium aluminium garnet (Sm:YAG) are typically used. Fluorescence shifts are secondary pressure marker as they are calibrated with the equation-of-state from shock wave experiments, and their use beyond the calibration conditions can cause large uncertainties in pressure estimates. The combination of Brillouin spectroscopy for the determination of the elastic constant tensor and X-ray diffraction for the measurement of sample density allows a calibrant-independent pressure determination that can be correlated with the fluorescence shift, making the fluorescence of Sm:YAG a primary pressure standard.

The three final contributions of this chapter deal with advances in the technical design of diamond anvil cells (DAC). The experimental setup for nuclear inelastic scattering (NIS) at the ESRF in combination with double sided laser heating requires the modification of the DAC and the laser heating setup to allow simultaneous heating and access to the beam.

The diamonds in a DAC are typically held by a metal support that traditionally has conical or polygonal shape. Here a new anvil design with a spherical crown of the diamond and a half sphere cavity in the support is presented, and it is demonstrated that this design has significant advantages in manufacturing the support system and in aligning the cell. The even support of the diamond also allows a wider angular opening of the cell for experimental probes.

Experiments conducted under static pressure play an important role for the investigation of phase transformations, chemical processes, and the effect of compression on the structure of solids. Experiments in the diamond anvil cell (DAC) have been restricted to less than ~ 400 GPa to date. In order to extend the pressure range nanocrystalline diamond was used as anvil material for the inner component of a double-stage DAC. The final contribution in this section reports on such experiments on rhenium achieving pressure in excess of 600 GPa.

a. *An object-oriented framework for thermodynamics of mantle minerals (T. Chust and G. Steinle-Neumann; H.-P. Bunge/München)*

The Earth's mantle is composed of a relatively small number of major chemical components (typically cast in terms of oxides) that, as a function of temperature and pressure, form different aggregates of crystalline phases. These are typically solid solution phases between different endmembers, *e.g.*, pyrope – grossular – majorite garnet in the transition zone.

For a variety of applications at the intersection of geodynamics, seismology, petrology and high-pressure mineral sciences it is desirable to determine elastic and thermodynamic parameters of earth materials, or to explore the composition of a mineral in a solid solution inside the Earth. Simulating the behaviour of polycrystalline aggregates requires models for the equations of state of different constituents, for the solid solution behaviour, and for the

selection of constituent minerals in a stable phase assemblage for a given chemical composition. Here we are presenting a flexible and extensible software package structure that tries to address such issues.

Questions one may pose to such a model are better dealt with in independent program modules, with a small set of well defined interfaces, than in a big monolithic model. For example, physical properties of a specific phase at given pressure-temperature (P-T) condition can be dealt with efficiently in a separate module than the computation of a phase assemblage taking into account a solid solution model. Similarly, an equation-of-state evaluation can be approached differently in a modular program structure whether experimental data in that P-T region is abundant or if an extrapolation is needed. Such a situation lends itself to an object oriented design that naturally reflects the boundaries between model subdomains in modules and allows easier replacement or addition of such modules, implementing alternative approaches for one of the problem subdomains. We tried to choose the boundaries between units of code such that the interfaces are both useful internally, when accessed by other program parts, and externally, when used directly for applications (Fig. 4.8-1). Having abstract interface boundaries also simplifies the combination of code written in different programming languages and allows us to write the performance critical numerical code in a low level language such as C while still providing a Python scripting module that makes quick experimentation and use of the framework as a toolbox much more convenient.

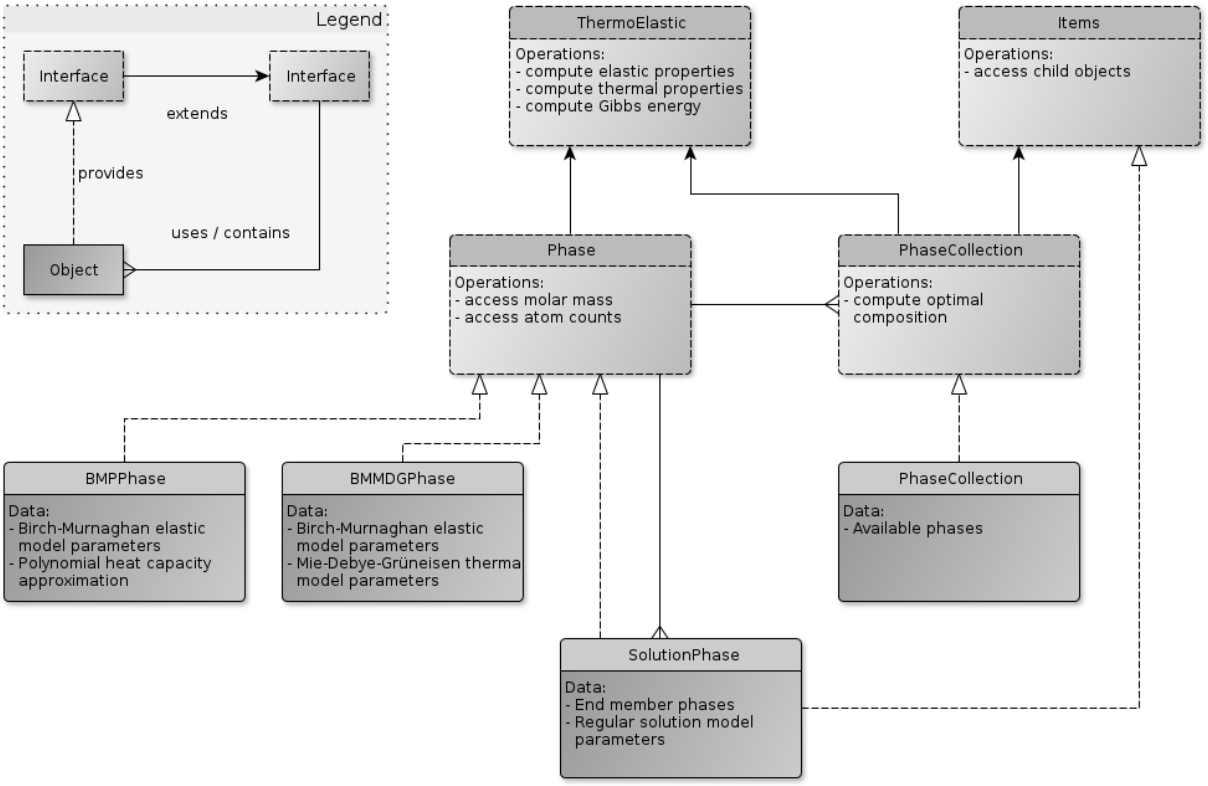

Fig. 4.8-1: Program structure of the thermodynamic software package.

In our program design “ThermoElastic” is the most important interface, which consists of methods for the computation of elastic and thermal properties including the molar Gibbs energy of the object it represents. This interface is provided by implementations of phase objects, which essentially represent an equation of state and its necessary parameter values, as well as by phase collections, which are simply containers for all available phases in a model. Container objects also provide an “Items” interface for indexed retrieval of child objects.

To make the same interfaces suitable for solutions and phase collections as well as simple phases of fixed composition, most of the operations in the “ThermoElastic” and “Phase” interfaces take composition parameters along with other necessary inputs such as pressure and temperature. The composition parameters are ignored for simple phase evaluation. To access, for example, the density or entropy of a single phase or an aggregate of phases, the client code would look precisely the same. The only difference between calls dealing with a solid solution or a simple phase is the composition vector that needs to be passed in the former case. Both “Phase” and “PhaseCollection” have specific interfaces extending “ThermoElastic” with additional methods.

Technically, function calls through interfaces are implemented slightly differently from regular function calls. Each object contains pointers to the interfaces it implements. This allows the functions to be looked up at runtime. The use of function pointers causes a slight overhead of typically one or two machine instructions. This overhead is negligible as the computationally intensive numerical operations still occur within one of the objects.

In the current code we implemented two different models for phases of fixed composition. Both compute Gibbs energy separated into an elastic and a thermal contribution

$$G(P,T)=G_0+G_{th}(P,T)+G_{el}(P,T)$$

or

$$G(P,T)=F_0+PV+F_{th}(V,T)+F_{el}(V,T).$$

In both cases, the elastic contribution is based on the Birch-Murnaghan finite strain formulation and we compute either

$$G_{el}(P,T)=\int_{P_0}^{P} V(f(P,T),T)dP$$

or

$$F_{el}(V,T)=\int_{V_0}^{V} P(f(V,T))dV.$$

Additional formulations of the equation-of-state/elastic contributions can be readily implemented through the modular structure of the code.

The thermal contributions implemented are either based on a simple polynomial approximation of heat capacity such that we can compute

$$G_{th}(P,T) = \int_{T_0}^{T} C_P(T)dT - TS(P,T)$$

or on the Mie-Debye-Grüneisen model of lattice vibrations that allows the computation of

$$F_{th}(V,T) = \int_{T_0}^{T} S(V(f(P,T)),T)dT.$$

Most of the thermoelastic parameters can then be derived from the Gibbs energy *G* and the software package contains default implementations for the interface methods using this strategy wherever possible, to simplify the implementation of a new class of phase objects.

Our implementation of solid solutions uses the regular solution model and adds statistical mixing terms of entropy as well as excess Gibbs energy terms, depending on information provided in the database.

The "PhaseCollection" interface contains an operation to determine the "optimal" composition that can then be passed on to the other operations. We implement this operation by minimizing *G* among all possible phase assemblages, compatible with a given bulk composition, for which we apply a linear programming approach.

b. *A split Wave Equation Model approach for multi-dimensional advection modeling (H. Samuel)*

The Wave Equation Model (WEM) approach has proven to be an efficient way of advecting scalar fields in one-dimensional Eulerian grids (see last year's annual report). In the case of 1D Cartesian space, the solution of the first-order ("one way") advection equation for a scalar field *C:*

$$\frac{\partial C}{\partial t} + u\frac{\partial C}{\partial x} = 0, \qquad (1)$$

is obtained by solving for the second-order (acoustic) wave equation with suitable initial and boundary conditions:

$$\frac{\partial^2 C}{\partial t^2} = u^2 \frac{\partial^2 C}{\partial x^2}. \qquad (2)$$

Using a von Neumann analysis, one can show that finite difference discretizations of the above equation are free of numerical diffusion (Fig. 4.8-2). This considerable advantage of

the WEM yields significantly higher accuracy compared to higher order discretizations of the one-way wave equation more commonly used in geodynamic modeling (Fig. 4.8-2).

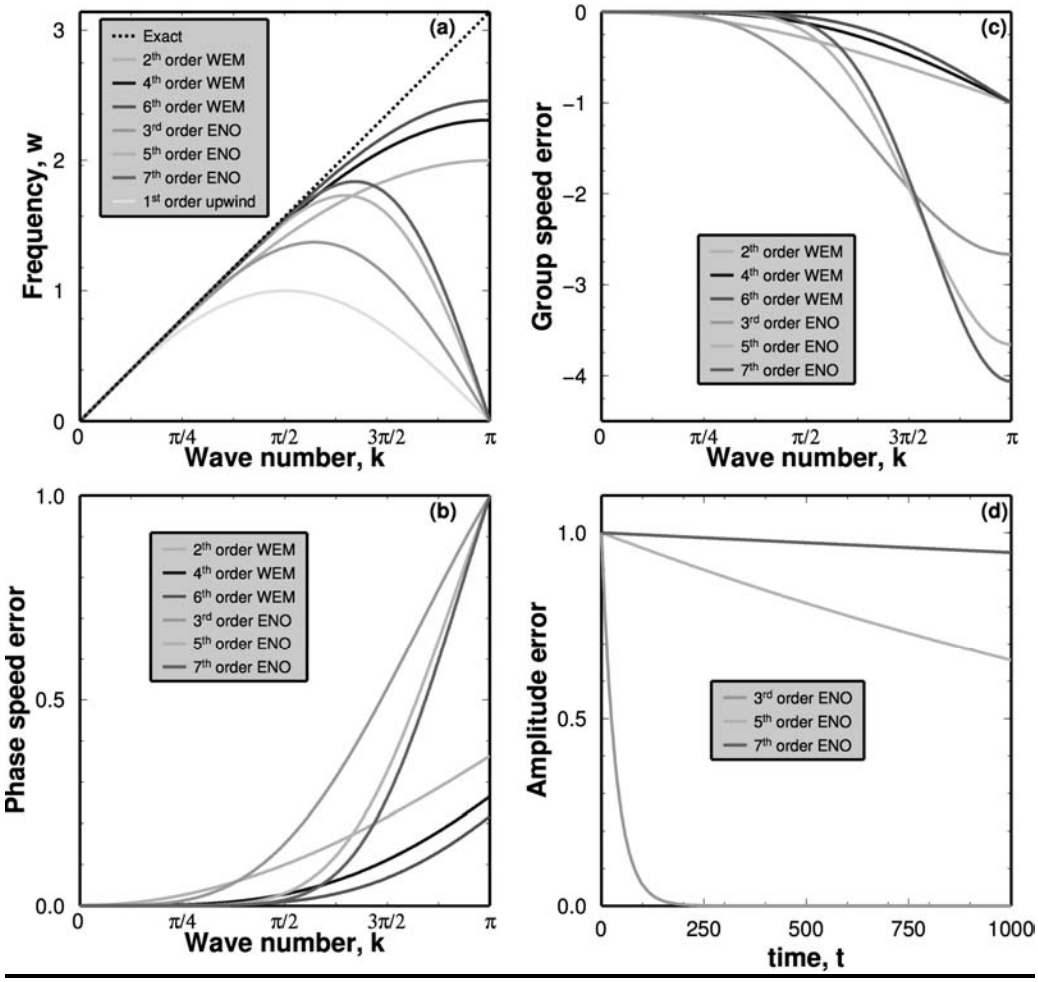

Fig. 4.8-2: Theoretical accuracy of the 1D advection solved with the WEM (Eq. 2) or with the one-way wave equation (Eq. 1). Note that the WEM method is free of amplitude errors (numerical diffusion) otherwise present in all discretizations of the one-way wave equation (Eq. 1).

While the WEM approach can be generalized to multi-dimensional advection, it has been reported that applying the WEM in 2D or 3D space yields significant directional dispersion errors. These spurious effects are mostly due to the inter-dimensional coupling due to presence of spatial cross-derivatives when solving for the WEM in 2D or in 3D space.

To circumvent this problem, one can chose to split the advection equation in each spatial direction and apply successively the 1D-WEM to each of the resulting equation. However, this requires a consistent and precise evaluation of the second-order time derivative of the advected quantity at each step of the splitting. Failure in doing so will result in the generation and the propagation of unphysical waves (*e.g.*, opposite to the direction of the local velocity

field). In order to avoid this, the use of the method of characteristics allows one to determine the value of the advected quantity at the previous (*n-1)* time step being simply (and exactly) defined as: $C_{i-\gamma}^{n-1} = C_i^n$ (where *i* is the space index, $\gamma = u/|u|$, using a time step equal to the CFL value).

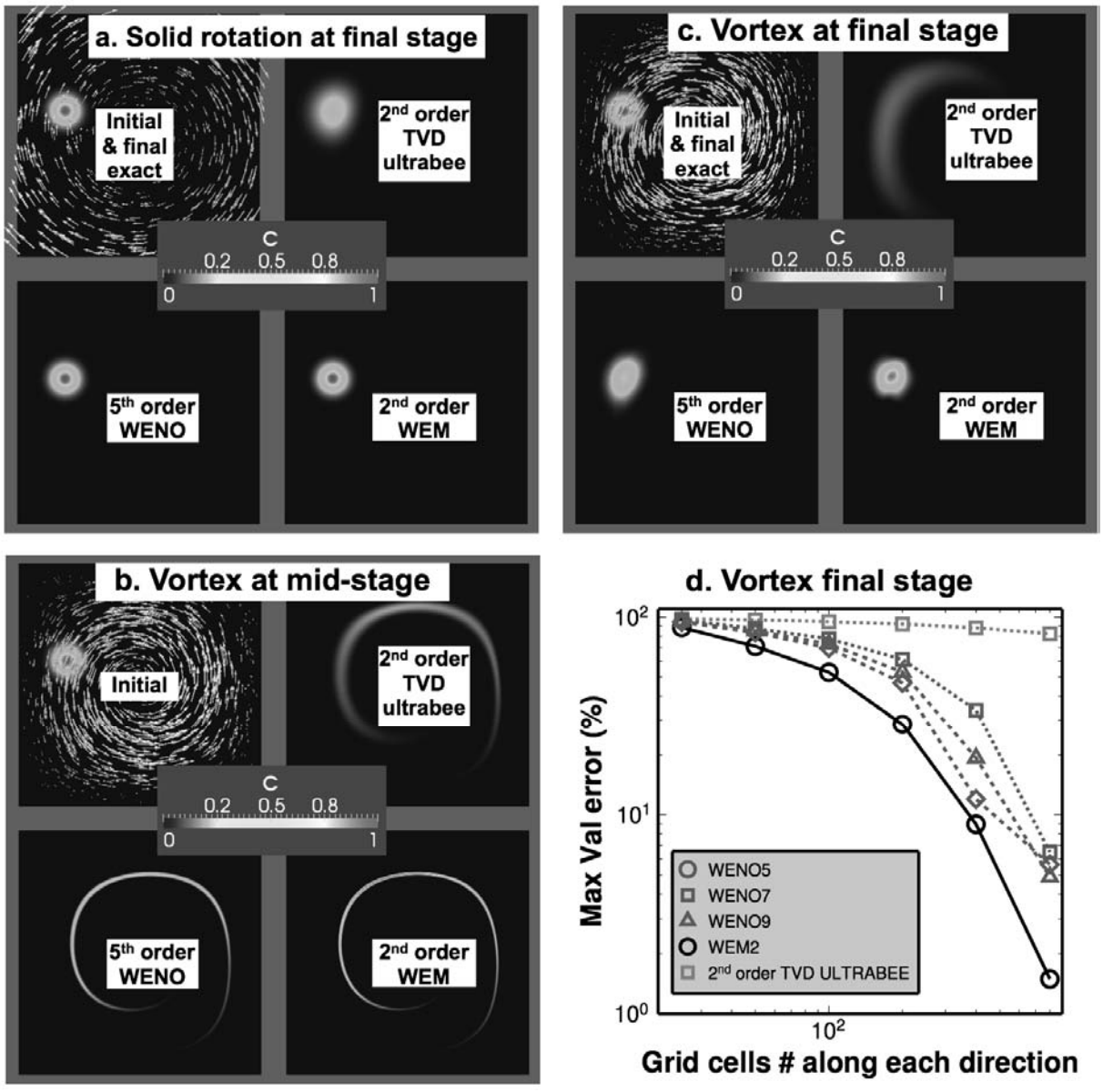

Fig. 4.8-3: Comparison of the split-WEM approach with popular first-order advection discretizations of comparable or higher truncation order (*i.e.*, fifth-order WENO and second-order TVD with an *ultrabee* limiter). Two 2D "round-trip" advection tests are considered: (a) solid rotation or vortex flow (b-d).

Embedding this in an optimally tuned three-level implicit scheme yields very accurate results for advecting smooth quantities. Although the simplest version of this scheme is only second

order in space and time, it is prone to negligible numerical diffusion, and it yields more accurate results than schemes based on higher order discretization of the first order advection equation (Eq. 1). This is illustrated in Fig. 4.8-3 that displays two advection tests for a 2D (initially Gaussian) patch in solid rotation or in vortex flows. The results clearly indicate that the second order split-WEM scheme is more accurate than TVD schemes and WENO schemes up to the ninth-order (in space).

This remarkable behaviour of the split-WEM scheme suggests that this approach is very suitable and computationally cheap to model the advection of smooth quantities in multi-dimensional space. An ideal context for this approach would therefore be the case of the *Level Set* method where the function to be advected is smooth by construction (see annual report 2010). Additionally, using flux corrections and/or flux limiters hybrid schemes, the method could be more generally applied to the advection of discontinuous quantities. These are ongoing areas of investigations.

c. *A new method for measuring electrical conductivity of fluids under pressure (H. Ni and H. Keppler)*

Aqueous fluids are important agents of metasomatism and chemical transport in the mantle. It is known that for example the composition of aqueous fluid coexisting with peridotite changes from silica-rich to more magnesia-rich with pressure, but the reason for this is poorly understood. Generally, solvent properties of aqueous fluid will change dramatically with pressure, but even basic data, such as the dielectric constant of water, the dissociation constant of water itself and the degree of dissociation of salts and acids such as NaCl or HCl at mantle pressures is missing. All these parameters are in principle accessible through measurements of electrical conductivity. Moreover, data on electrical conductivity could directly constrain fluid flow in subduction zones, as regions of high electric conductivity above subducting slabs have been related to fluid percolation.

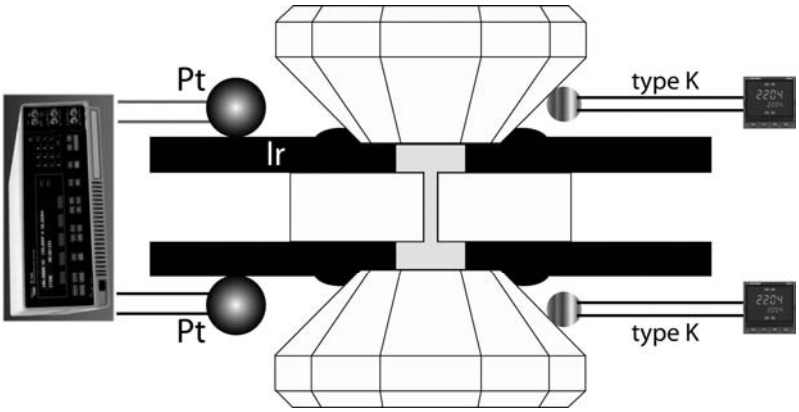

Fig. 4.8-4: Sketch of the new experimental setup for measuring electrical conductivity of fluids in a hydrothermal diamond anvil cell.

Preliminary experiments on salt (KCl) solutions have demonstrated that this novel setup is highly promising, and the conductivity measurements appear to be consistent with literature data (Fig. 4.8-5). In addition to electrical conductivity, which can be used to derive the dissociation constants of electrolytes, one may also obtain dielectric constant from acquired impedance spectra, which is a physical property describing the ionization capability of fluid. These electrical properties (electrical conductivity and dielectric constant) will significantly advance our understanding of how the nature of solvent changes with depth.

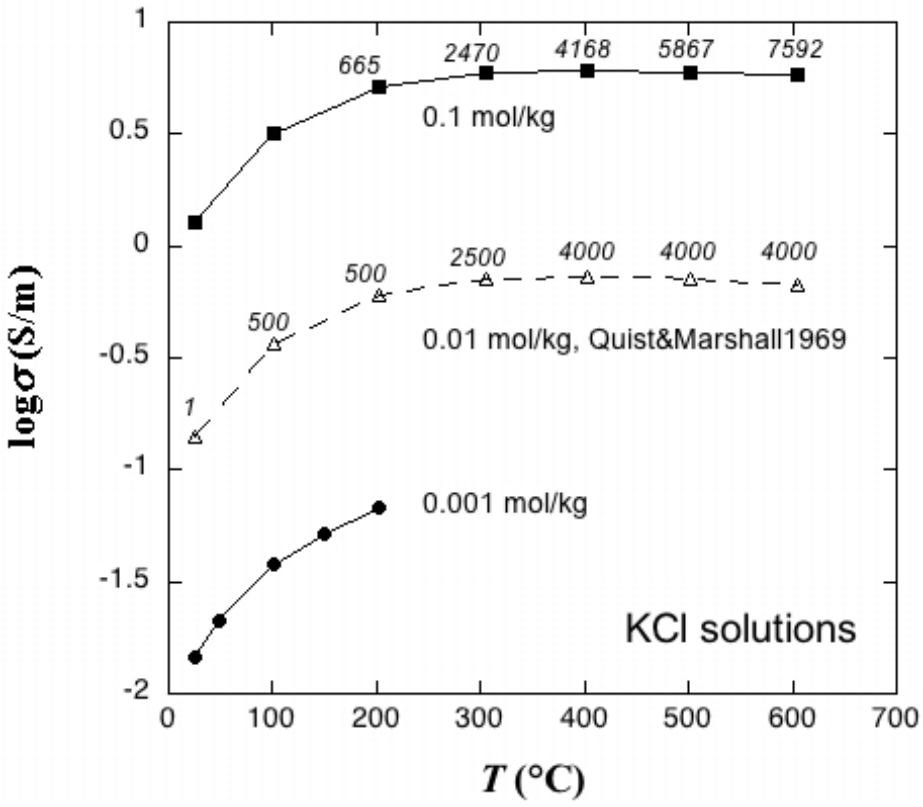

Fig. 4.8-5: Electrical conductivity of KCl solutions (0.001 mol/kg and 0.1 mol/kg) measured with the new method, compared with the literature data for 0.01 mol/kg KCl solution. The numbers close to the symbols indicate pressure in bars.

d. *Piezoelectric stress determinations at high pressures and temperatures (M.A.G.M. Manthilake and D.J. Frost)*

Quantitative rheological measurements rely on the ability to measure stresses in materials undergoing changes in strain. In room or low-pressure devices stress measurements are achieved through the use of a load cell, which resides outside of the sample environment, or high-pressure chamber, but which must be mechanically coupled to the loaded sample. In solid media multianvil high-pressure devices the need for gasketing makes this impossible

and to date only *in situ* X-ray diffraction techniques have been used to assess stresses within samples at high pressures and temperatures. The azimuthal dependence of crystallographic d spacings relative to the principal stress direction can be used to estimate sample stresses. However, due to limited resolution in the variation of the azimuthal dependence and an incomplete understanding of the directional strength within a crystal, such estimates have large uncertainties and poor stress resolution.

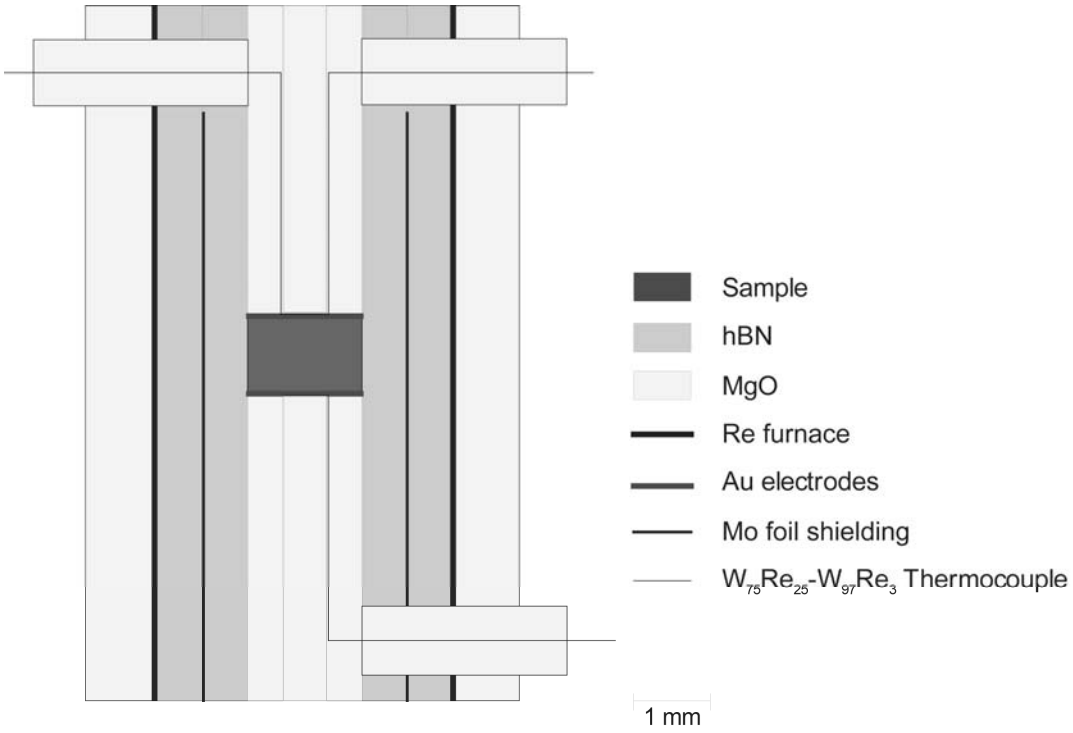

Fig. 4.8-6: A cross section of the cylindrical interior of the cubic assembly used for high-temperature piezoelectric measurements. This cylinder is placed inside a hole drilled in a 8 mm edge length cube of fired pyrophylite. The single crystal samples are also coated with 100 nm of Au. The thermocouple wires are also used to measure the charge across the crystal.

Here piezoelectric crystals of quartz and isostructural $GaPO_4$ have been deformed at room temperature and pressures up to 4 GPa such that piezoelectric charges develop that can be used to assess stresses. These crystals develop an electrical charge proportional to the applied stress that can be measured using an operational amplifier connected into the multianvil cell via electrodes. At room temperature the sample has been surrounded by Teflon to provide a highly resistive environment to prevent charge loss. Additional experiments have been performed at elevated temperature. There, Teflon is replaced with ceramic parts as shown in Fig. 4.8-6. Using the 6-ram multianvil press, the cubic assemblies are uniaxially deformed at high pressure. A high level of precision in the control of the rams allows the application of low strain rates with resolvable assembly shortening on the order of 0.3 microns.

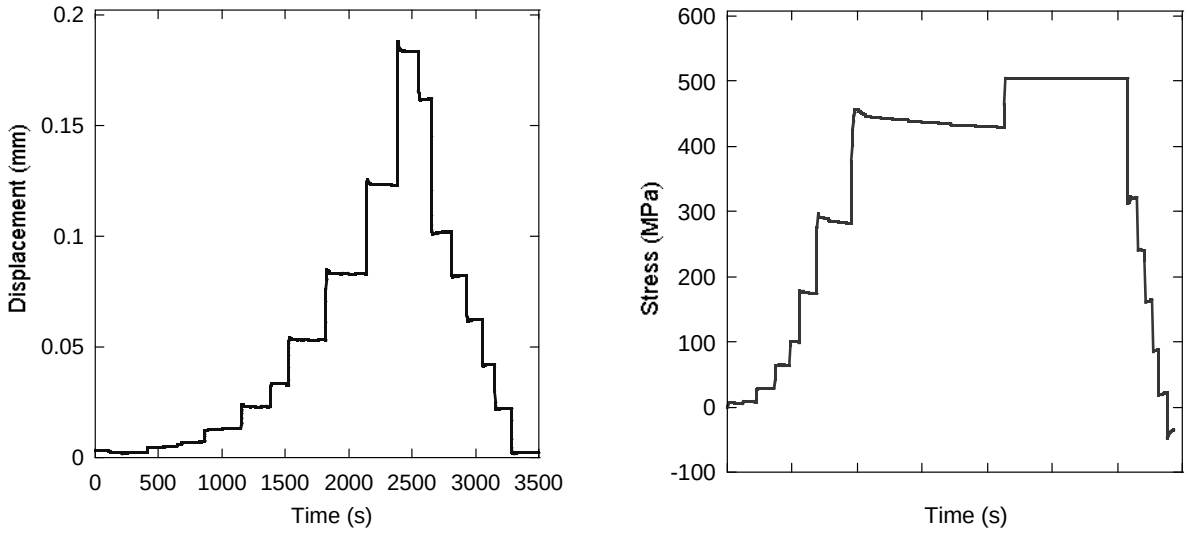

Fig. 4.8-7: Anvil displacements and corresponding stresses recorded from a sample of quartz undergoing stepwise deformation at room temperature and 3 GPa. Both uniaxial compression and decompression can be observed.

Fig. 4.8-7 shows a deformation experiment performed on quartz at room temperature and 3 GPa. The assembly was compressed uniaxially by advancing one opposing set of multianvil rams. Total displacement reached 180 microns but initial individual steps were as small as 0.5 microns. Each anvil advancement produced a stress increase determined from the charge on the crystal. The stress state was totally recoverable to the initial undeformed state. Experiments on quartz crystals at room temperature display very little drift compared to experiments using $GaPO_4$, steming from a spurious increase in background charge caused by current leaking or induction. The apparent stability of quartz may be caused by higher internal resistance.

High-temperature experiments are far more challenging as a result of the inductive current of the furnace which contributes to drift. In order to minimize this, an earthed Mo shield was placed between the sample and the furnace. The replacement of Teflon with harder ceramics leads to a strong increase in the measured stresses for a given anvil advancement. Fig. 4.8-8 shows a stress increase of approximately 500 MPa determined for a quartz crystal deformed by 60 microns at 4 GPa and 200 °C. This is much larger than that observed in Teflon bearing experiments (Fig. 4.8-7). Drift becomes a large problem at temperature when using quartz above 300 °C. As a result, it is impossible to quantitatively interpret the measured charges in terms of stress at these conditions. Nevertheless, qualitative changes in charge can still be detected upon anvil displacement even above 400 °C. In a deformation experiment where a piezoelectric crystal is used to measure stress it would be possible to place the crystal out of the hot spot of the furnace and mechanically connect it to the sample in the hot spot using hard pistons, similar to an external load cell. However, temperatures at the colder end of such a furnace are still likely to reach above 200 °C and furnace induction will become even more problematic if samples are heated above 1000 °C.

We conclude that even though quartz provides a superior piezoelectric signal than $GaPO_4$ at room temperature, the current configuration with quartz is not suitable for high-temperature measurements. Either other piezoelectric materials need to be investigated or other changes such as the use of D.C. heating need to be implemented.

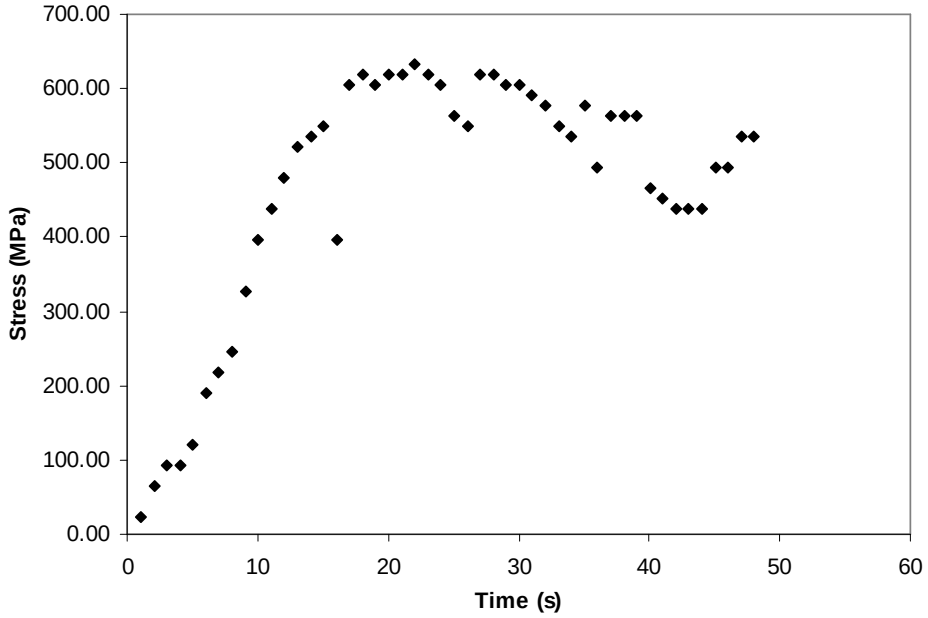

Fig. 4.8-8: Stress developed on a quartz crystal at 4 GPa and 200 °C as a result of opposed anvil advancements of 60 microns.

e. *A calibration of Sm-doped $Y_3Al_5O_{12}$ as a primary pressure standard up to 58.6 GPa (D.M. Trots, A. Kurnosov, T. Boffa Ballaran and D.J. Frost, in collaboration with S. Tkachev, K. Zhuravlev and V.B. Prakapenka/Chicago)*

In spite of major advances in high-pressure research, the accurate measurement of pressure is still a difficult task, mainly associated with the fact that one has to rely on the use of pressure calibrants. Optical pressure gauges (as for example ruby or Sm-doped $Y_3Al_5O_{12}$(Sm:YAG)) whose fluorescence shifts depend on pressure are widely used in a variety of high-pressure techniques, because their fluorescence spectra can be easily measured. Such materials are, however, secondary standards since they are calibrated using the equations of state of metals derived from shock-wave data (primary standard). Therefore, the uncertainties in pressure may be quite large, especially when such standards are used at conditions far from those at which they have been calibrated. To overcome such problems, we have performed – both at Bayerisches Geoinstitut and the Advanced Photon Source – Brillouin scattering (Fig. 4.8-9) and X-ray diffraction experiments on the same single-crystal of Sm:YAG at the same conditions in order to obtain a primary calibration of its fluorescence shift.

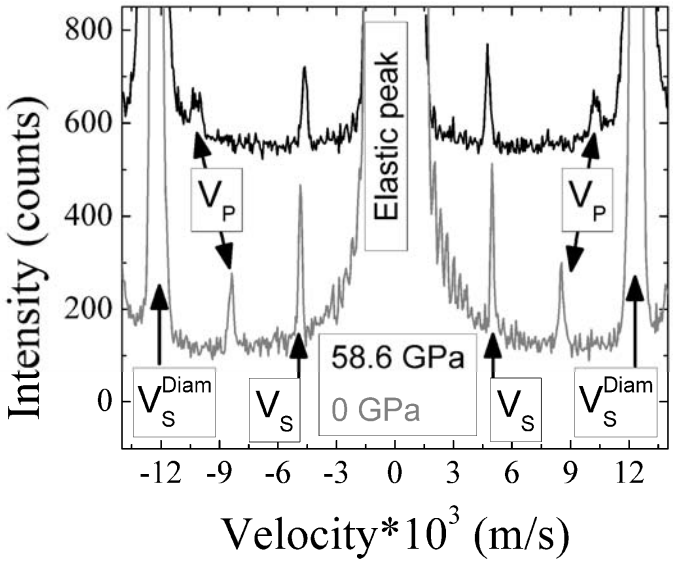

Fig. 4.8-9: Examples of Brillouin spectra at selected angles at ambient and 58.6 GPa.

Simultaneous measurements of the compliance tensor (by Brillouin spectroscopy) and specific volumes (by X-ray diffraction) in the diamond anvil cell (DAC) allows the compiliation of bulk modulus (K) vs. volume (V), *i.e.*, a compression curve. Integration K(V) yields the pressure P since the bulk modulus is defined as K= –V(dP/dV). In this way we can directly determine the pressure exerted on the sample at an observed strain, without use of any pressure calibrants. With this approach we obtained accurate and self-consistent sets of elastic parameters of Sm:YAG together with a determination of absolute pressure. At the same time the fluorescence shifts were measured at each experimental pressure and calibrated against the absolute value determined from the combination of Brillouin and X-ray measurements.

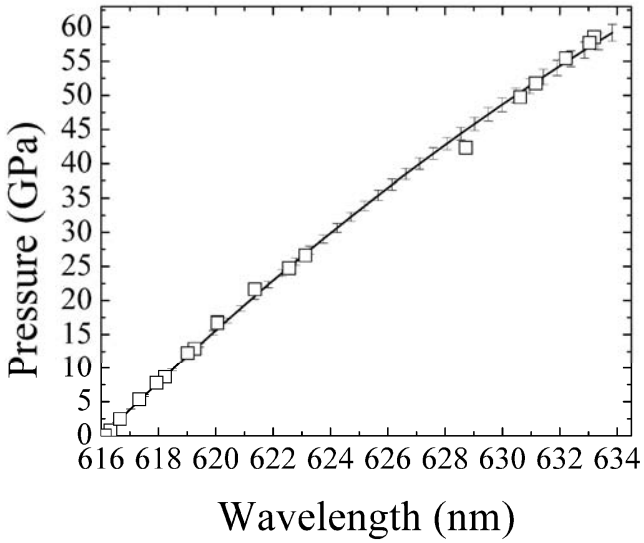

Fig. 4.8-10: Calibration of fluorescence Y2 band of Sm:YAG vs. absolute pressure (the bars in the curve demonstrate 2 % of uncertainty in pressure).

Using this approach we have, thereby, calibrated the fluorescence shift of the Y2 band of Sm:YAG (Fig. 4.8-10) vs. absolute pressure up to 58.6 GPa. To our knowledge, this is the first calibration of a fluorescence pressure sensor with respect to absolute pressure and is therefore expected to provide more accurate pressure estmates than previous calibrations of secondary fluorescence gauges. Since the fluorescense shift of Sm:YAG depend on pressure but is temperature independent, the use of this compound in combination with a temperature sensitive sensor, *e.g.*, ruby, has great potential for *in situ* measurements of sample pressure and temperature directly in the DAC.

f. *Portable double-sided laser-heating system for the nuclear inelastic and forward scattering experiments under high pressure (A.P. Kantor, L.S. Dubrovinsky and C. McCammon, in collaboration with A.I. Chumakov, R. Rüffer, J.-P. Celse, I.Yu. Kantor and I. Kupenko/ Grenoble)*

Nuclear inelastic scattering (NIS) is a valuable technique to study lattice dynamics and directly provides data on the phonon density of states. NIS measurements require synchrotron radiation of high brightness and high spectral density. Beamline ID-18 at ESRF (Grenoble, France) is dedicated to NIS measurements, also under high pressure. Since the detectors together are rather big (20x20 mm) and have to be within couple millimeters from the sample, only a special type of diamond anvil cells (DAC) with extremely wide side openings (panoramic DAC) can be used for NIS experiments. Conditions relevant to the planetary interiors require not only high pressures, but also elevated temperatures that can be achieved with the laser heating technique. The large length and significantly lower optical opening of a panoramic DAC relative to normal cell designs required modifications to both the laser heating system and the DAC. The new NIS-DAC is shorter (55 instead of 73 mm) in order to allow laser heating from both sides under an angle, which is essential for the X-rays to pass through the sample and reach the forward detectors.

The design of the NIS double-sided laser heating setup is shown in Fig. 4.8-11. Due to the length of the panoramic DAC the laser beam has to enter strictly in the coaxial direction of the cell. This requires the laser reflecting mirrors to stay in the synchrotron beam and thus to be transparent for X-ray photons; the mirrors are fabricated from fused amorphous graphite. For the same reason the focal length of the UniHead can not be less than 80 mm. Due to long working distance, low numerical aperture and imperfections of the carbon mirrors the observed sample image is not of best quality; however, it is good enough to visualize both the sample and the hot spot during heating. NIS measurements are extremely time consuming (several hours) and require absolute stability of both X-ray and laser beams. After some laboratory tests this ability was proven in an experiment on Fe_7C_3 in November 2012 at ID-18. During the experiment we managed to reached pressures of 75 GPa and temperatures of ~ 1200 K. The sample was kept for more then 6 hours under these conditions. A special water-cooled DAC holder serves as a heat sink during the high-temperature measurements.

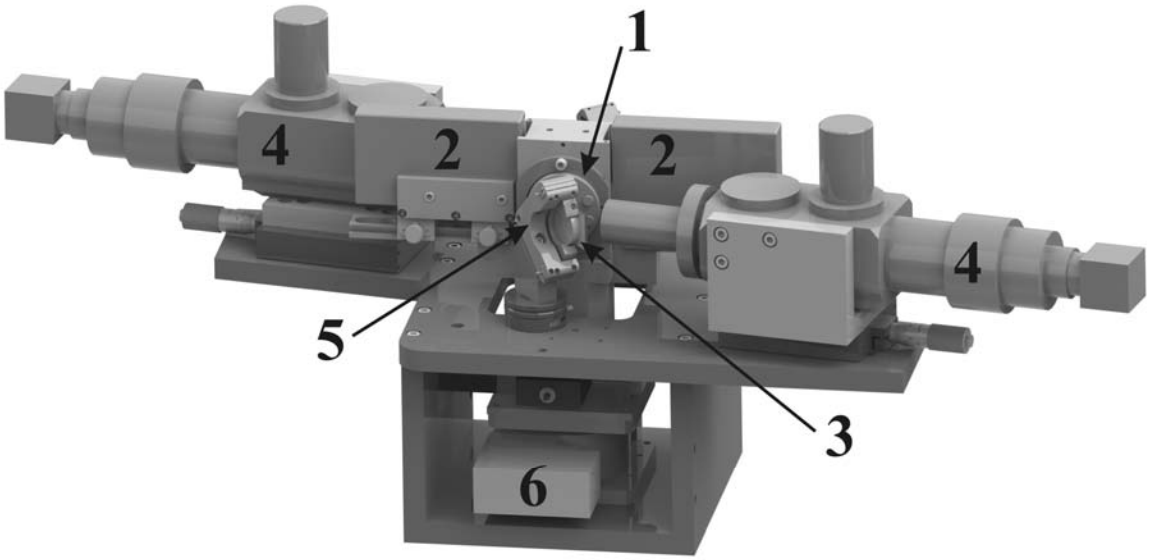

Fig. 4.8-11: Double-sided laser heating assembly for NIS measurements: 1 – DAC in a water-cooled holder; 2 – NIS-detectors' housings; 3 – glassy carbon mirror; 4 – UniHeads; 5 – piezo motorized support for mirror adjustment; 6 – x-y-z linear motors for precise DAC positioning.

ID18 beamline is capable also of nuclear forward scattering (NFS) and synchrotron Mössbauer (see BGI Annual Report 2010) experiments. These measurements can be performed utilizing standard DACs, and we made a second modification to the laser setup. For these experiments the laser optics can be brought as close as 60 mm to the sample and uses glass mirrors fixed under an angle in such a way, that they are outside the X-ray beam. This solution provides higher quality images of the sample, which we observe from both sides through the same optical UniHeads through which we pass the laser beam. Collection of NFS data was first successfully performed in July 2012, when we reached temperatures of more than 3000 K under pressures of about 80-90 GPa.

g. *Diamond anvils with a spherical support designed for X-ray and neutron diffraction experiments in DAC (N. Dubrovinskaia, L. Dubrovinsky, M. Hanfland/Grenoble and M. Hofmann/Garching)*

A wide variety of forms of the diamond anvil cell (DAC) with different forms, shapes, loading mechanisms, and sizes optimized for different measurements (see, *e.g.*, the previous contribution) are based on two basic design concepts: the piston-cylinder Mao-Bell and opposite-plate Merrill-Bassett types. Rapidly growing areas of DACs applications – single crystal and powder X-ray diffraction, *in-house* and synchrotron based spectroscopic techniques such as inelastic X-ray and nuclear scattering, Brillouin spectroscopy – require diamond anvils with a large optical aperture.

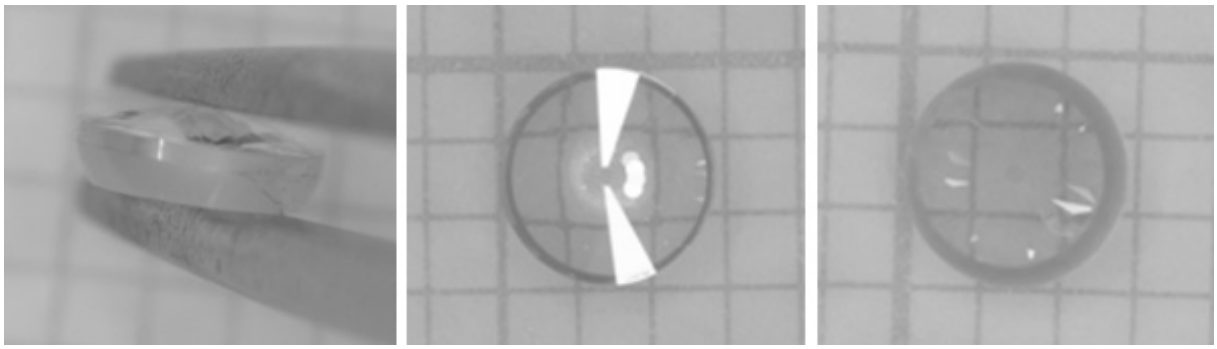

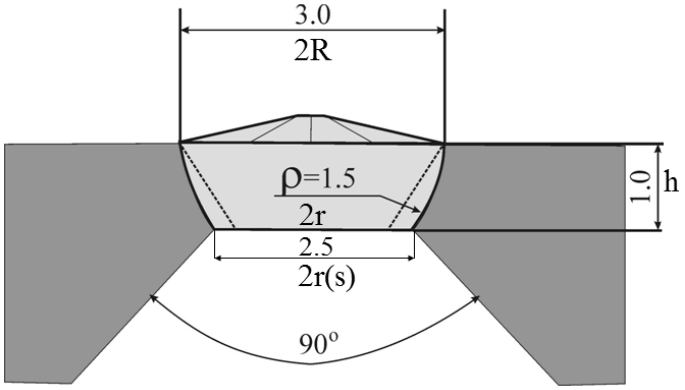

Fig. 4.8-12: The large aperture spherical diamond anvil: (a) an example of the loose spherical diamond anvils with 250 μm culets as viewed from a side, top and bottom (from left to right) ; (b) a schematic drawing of the cross-section of the anvil fixed in the spherical support of a hard metal seat. R=1.5 mm is the radius of the anvil; r(s)=1.25 mm is the radius of the table of the diamond anvil; and h=1 mm is the height; ρ=1.5 mm is the spherical radius. A cross-section of the conical anvil of the same diameter (2R) and height (h) is highlighted by the dashed line. Its table size (r) is defined by the constant angle of the cone of 60 degrees. The height of the seat is 4 mm and the diameter is 12 mm (not scaled in the figure). The spherical parts of the anvil and the seat may be ground within 1 μm tolerance.

We designed and SCIMED GmbH produced for us diamond anvils with a spherical support. The term “spherical” refers to the novel feature of the anvils’ design with a spherical crown of diamond (Fig. 4.8-12) instead of the stabdard faceted shape. This spherical diamond anvil has a larger contact area with the spherical support compared to a conical anvil. This increases the stability of the anvil and reduces stresses at the anvil-to-seat interface. Thus, making use of spherical anvils allows us to achieve higher pressures compared to those with anvils of previous design. Regarding the alignment procedure, the spherical shape provides significant advantage over any other shape of diamond support. Indeed, in contrast to supports of polygonal or conical design, a spherical anvil can not get stuck within the spherical cavity. Its position can easily be corrected and the top anvil can be aligned when the bottom one is fixed. Moreover, unlike a polygonal hole, a half-sphere cavity in seats is simple to manufacture using standard tools available in any workshop.

A DAC equipped with spherical diamonds has a large opening and even with the long-wavelength neutron radiation (on the order of 1.2-1.5 Å) reasonable diffraction data can be collected through the diamonds. The anvils showed very good performance for both high-pressure single crystal X-ray diffraction (ID-09 at ESRF Grenoble) and neutron diffraction on polycrystalline samples (Stress-Spec Spectrometer at FRMII Garching).

h. *Generation of 6 Mbar using diamond anvil cells (L. Dubrovinsky, N. Dubrovinskaia, V.B. Prakapenka/Chicago and A.M. Abakumov/Antwerp)*

The impact of high-pressure studies on fundamental physics and chemistry, and especially on Earth and planetary sciences, has been enormous. Compression of solids to 150-200 GPa may transform typical ionic, covalent, or molecular crystals into metals and even superconductors, simple metals into optically transparent insulators, and change rules governing chemical processes. Among static experiments only diamond anvil cells provide the capability of a wide range of *in situ* measurements in this pressure range, and temperatures covering conditions covering the entire Earth. The highest pressure, documented by X-ray diffraction studies based on the equation of state (EOS) of W reached about 420 GPa by means of beveled diamonds with flat tips (culets) of about 20 μm in diameter. Novel shock wave techniques can reach pressures of hundreds of gigapascals; however, by the dynamic compresson high temperatures (thousands of degrees) are generated, putting the sample into a fluid phase.

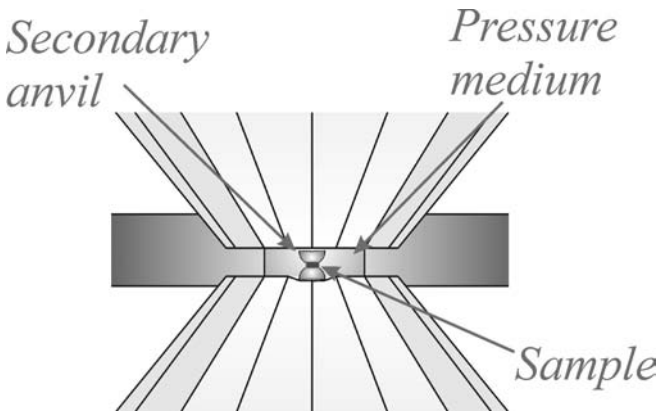

Fig. 4.8-13: Schematic diagram of the double-stage diamond anvil cell providing an enlarged view of the pressure chamber. Primary anvils are made of single crystal diamonds, while second-stage anvils are semi-balls of nanocrystalline diamond. A sample of ca. 4 microns in diameter is shown in between the secondary anvils.

In order to generate static pressures in the range not previously accessible we have combined the advantages of nanocrystalline diamond (NCD) as anvil material and the design of a double-stage high-pressure device. Mechanical properties of novel nanocrystalline diamond

materials – nanopolycrystalline diamond and aggregated diamond nanorods – are enhanced compared to single crystal diamonds due to suppressed anisotropy of hardness and missing ability for cleavage, as well as the superior fracture toughness. We realized a design of a double-stage DAC (Fig. 4.8-13) using a conventional DAC with second-stage anvils made of NCD semi-balls. The second-stage anvils are surrounded by a pressure transmitting medium and work under significant confining pressure that allowed us to reach static pressures up to 640 GPa and accurately determine the equation of state of rhenium at such extreme conditions (Fig. 4.8-14).

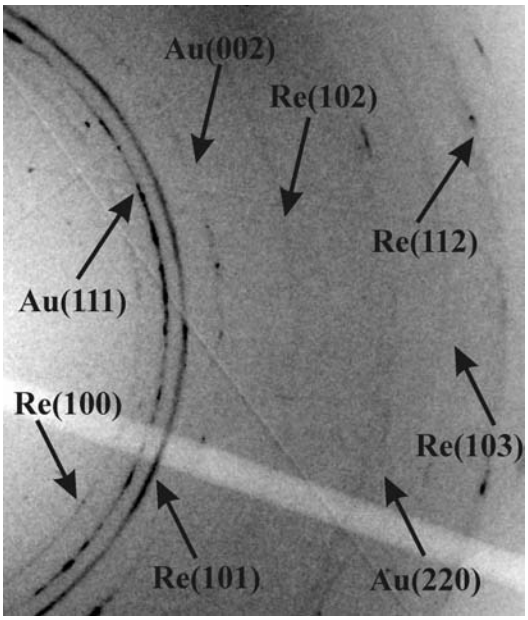

Fig. 4.8-14: The synchrotron 2D X-ray diffraction image of a mixture of Re and Au collected at 640(17) GPa (according to the gold equation of state). A mixture of Au and Re powders was compressed in a double-stage DAC using paraffin as a pressure transmitting medium. The lattice parameter of gold is a=3.303(3) Å, and rhenium are a= 2.382(1) Å and c= 3.798(2) Å.

5. International Graduate School – Elitenetzwerk Bayern/Elite Network of Bavaria "Structure, Reactivity and Properties of Oxide Materials" (OXIDES)

The interdisciplinary Graduate School is funded by the State of Bavaria and it encompasses three cooperating institutes: Bayerisches Geoinstitut (BGI), Institute of Inorganic Chemistry I (AC I), both at Bayreuth University, and the Fraunhofer Institute for Silicate Research (ISC) in Würzburg. These institutes provide their experimental and analytical facilities, complementary expertise in basic and applied research, and commitment to capitalize on synergies as well as international contacts to other leading research institutes all over the world.

The Graduate School is chaired by Prof. Dr. Hans Keppler/BGI and it includes eleven other faculty members and one coordinator. Enrollment in 2012 was eleven doctoral students on a full-time basis at all three institutes (BGI, AC I, ISC) and, in addition, sixteen doctoral students have associate status in the school which provides them with full access to all educational activities. Research projects include physical and chemical properties of oxides and mineral assemblages and mineral/melt interactions at P-T conditions of the deep Earth, synthesis and investigation of new layer silicates, polymer coatings, transition metal oxides (ceramics) and polyoxometalates as well as the development of new methods in NMR crystallography.

During 2012, seven students have graduated:

Julien Chantel (M.Sc. 2008, Clermont-Ferrand) on 19.12.2012	*Elastic properties of silicates at realistic mantle pressures and temperatures.* Supervisors: Prof. D. Frost, Prof. D. Rubie Dr. Chantel has taken a post-doctoral position at the University of Clermont-Ferrand/France.
Vasili Potapkin (M.Sc. Solid State Physics 2009, Moscow) on 22.10.2012	*Energy-domain synchrotron radiation Mössbauer source for physics under extreme conditions*. Supervisors: Prof. L. Dubrovinsky, Dr. C. McCammon Dr. Potapkin took a post-doctoral position at the *School of Physics and Astronomy* at the University of Tel Aviv/ Israel.
Thomas Lunkenbein (Dipl. Chemistry, 2009 Bayreuth) on 01.10.2012	*Mesostrukturierte Metalloxide und Polyoxometallate mittels ionogener Diblock Copolymere - Synthese, Charakterisierung und Anwendung.* Supervisor: Prof. J. Breu

	Dr. Lunkenbein took a post-doctoral position at the Fritz-Haber-Institut of the MPG at Berlin.
Linda Lerchbaumer (Mag. rer. nat. 2008, Vienna) on 06.08.2012	*The nature of fluids in hydrothermal copper and molybdenmum ore deposits*. Supervisors: Prof. H. Keppler, Dr. A. Audétat Dr. Lerchbaumer took a position with OMV (Oesterreichische Mineralölverwaltung) in Vienna.
Dunja Hirsemann (Dipl. Chemistry 2008, Bayreuth) on 16.05.2012	*Development of innovative Janus-particles based on the layered silicate kaolinite.* Supervisor: Prof. J. Senker Dr. Hirsemann took a position with BASF/Trostberg.
Dennis Harries (Dipl. Geowiss. 2008, Göttingen) on 09.05.12	*Structure and reactivity of terrestrial and extra-terrestrial pyrrhotite.* Supervisors: Prof. F. Langenhorst, Dr. K. Pollok Dr. Harries took a post-doctoral position at the University of Jena.
Sushant Shekhar (Int. M.Sc. Expl. Geophy. 2008, Kharagpur) on 27.02.2012	*Origins of olivine fabric transitions and their effects on seismic anisotropy in the upper mantle*. Supervisors: Prof. D. Frost, Prof. F. Langenhorst Dr. Shekhar returned to India.

One students has submitted his thesis in fall 2012 and and will graduate early in 2013:

Clemens Prescher (Dipl. Min. 2009, Jena)	*Iron spin crossover at high pressure and high temperature and their effects on materials relevant to the Earth's lower mantle and core.* Supervisors: Prof. L. Dubrovinsky, Prof. F. Langenhorst Clemens Prescher will take a post-doctoral position at Chicago University.

Descriptions of some of the student research projects are listed in Chapter 4 of this yearbook. Students also gave presentations at major international meetings in 2012. The list of presentations and publications may be found in Chapter 6.

As part of program requirements, all students undergo an intensive training program, in addition to their research project, that encompasses lectures, short courses, research colloquium, doctoral seminar, seminars by invited leading experts and weekend seminars on soft skills such as scientific writing, ethics and team work. Invited speakers from overseas and Europe presented novel experimental techniques and current research results.

The following courses and seminars were offered by ENB in 2012:

- Doctoral seminar, Thurnau; Graduate School "*Oxides*", 28.-29.01.2012 (Univ. Bayreuth, ISC Würzburg)
- Short course on "*High-pressure experimental techniques and applications to the Earth's interior*", 13.-17.02.2012, Bayerisches Geoinstitut;
- Industrial excursion to BASF and Wacker-Chemie at Trostberg and Burghausen, 03.-04.07.2012, Bayerisches Geoinstitut;
- Short Course on "*Introduction to polarization microscopy*", 17-19.09.2012, Bayerisches Geoinstitut;
- Soft skills short course on "*Efficient Project Management - how to plan and execute a professional research project*", 18.-19.10.2012, Bayerisches Geoinstitut, Kempkes-Gebhardt Organisationsberatung, Köln;
- During 2012 nine invited international scientists contributed to the ENB series of lectures with 18 seminars on recent research results.

Furthermore, students of the graduate school participated in several external short courses/seminars.

Four doctoral students (Tina Oertel, Veronika Schmitt (both ISC Würzburg) Mattia Giannini, Daniel Kunz) participated in the 2012 Graduation Ceremony of the Elite Network of Bavaria with the State Minister Dr. W. Heubisch in Garching on November 30, 2012.

Students and members of the graduate program received international awards for their research; these awards are listed in section 8.2.

6. Publications, Conference Presentations, Seminars

6.1 Publications (published)

a) Refereed international journals

AMTHAUER, G.; PAVIĆEVIĆ, M.; JELENKOVIĆ, R.; EL GORESY, A.; BOEV, B.; LAZIĆ, P. (2012): State of geoscientific research within the lorandite experiment (LOREX). Mineralogy and Petrology 105, 157-169

BALI, E.; KEPPLER, H.; AUDÉTAT A. (2012): The mobility of W and Mo in subduction zone fluids and the Mo-W-Th-U systematics of island arc magmas. Earth and Planetary Science Letters 351-352, 195-207

BHASKAR, A.; BRAMNIK, N.N.; TROTS, D.M.; FUESS, H.; EHRENBERG, H. (2012): In situ synchrotron diffraction study of charge-discharge mechanism of sol gel synthesized $LiM_{0.5}Mn_{1.5}O_4$ (M = Fe, Co). Journal of Power Sources 217, 464-469

BOFFA BALLARAN, T.; KURNOSOV, A.; GLAZYRIN, K.; FROST, D.J.; MERLINI, M.; HANFLAND, M.; CARACAS R. (2012): Effect of chemistry on the compressibility of silicate perovskite in the lower mantle. Earth and Planetary Science Letters 333-334, 181-190

BOLFAN-CASANOVA, N.; MUÑOZ, M.; MCCAMMON, C.; DELOULE, E.; FÉROT, A.; DEMOUCHY, S.; FRANCE, L.; ANDRAULT, D.; PASCARELLI, S. (2012): Ferric iron and water incorporation in wadsleyite under hydrous and oxidizing conditions: a XANES and SIMS study. American Mineralogist 97, 1483-1493

BULL, J.N.; TENNANT, W.C.; BALLARAN, T.B.; NESTOLA, F.; MCCAMMON, C.A. (2012): Anisotropic mean-squared-displacement tensor in cubic almandine garnet: a single crystal ^{57}Fe Mössbauer study. Physics and Chemistry of Minerals 39, 561-575

BUREAU, H.; LANGENHORST, F.; AUZENDE, A.L.; FROST, D.J.; ESTEVE, I.; SIEBERT, J. (2012): The growth of fibrous, cloudy and polycrystalline diamonds. Geochimica et Cosmochimica Acta 77, 202-214

BYKOVA, E.; PARAKHONSKIY, G.; DUBROVINSKAIA, N.; CHERNYSHOV, D.; DUBROVINSKY, L. (2012): The crystal structure of aluminum doped β-rhombohedral boron. Journal of Solid State Chemistry 194, 188-193

CAILLET-KOMOROWSKI, C.; EL GORESY, A.; MIYAHARA, M.; BOUDOUMA, O.; MA, C. (2012): Discovery of Hg-Cu-bearing metal-sulfide assemblages in primitive H-3 chondrite: Towards a new insight in early solar system processes. Earth and Planetary Science Letters 349-350, 261-271

CHANTEL, J.; FROST, D.J.; MCCAMMON, C.A.; JING, Z.; WANG, Y. (2012): Acoustic velocities of pure and iron-bearing magnesium silicate perovskite up to 25 GPa and 1200 K. Geophysical Research Letters 39, L19307, doi: 10.1029/2012GL053075

CHANTEL, J.; MOOKHERJEE, M.; FROST, D.J. (2012): The elasticity of lawsonite at high pressure and the origin of low velocity layers in subduction zones. Earth and Planetary Science Letters 349, 116-125

COCHAIN, B.; NEUVILLE, D.R.; HENDERSON, G.S.; MCCAMMON, C.; PINET, O.; RICHET, P. (2012): Iron content, redox state and structure of sodium borosilicate glasses: A Raman, Mössbauer and boron K-edge XANES spectroscopy study. Journal of the American Ceramic Society 95 (3), 962-971

COMODI, P.; KURNOSOV, A.; NAZZARENI, A.; DUBROVINSKY, L. (2012): The dehydration process of gypsum under high pressure. Physics and Chemistry of Minerals 39, 65-71

DACHRAOUI, W.; HADERMANN, J.; ABAKUMOV, A.M.; TSIRLIN, A.A.; BATUK, D.; GLAZYRIN, K.; MCCAMMON, C.; DUBROVINSKY, L.; VAN TENDELOO, G. (2012): Local oxygen-vacancy ordering and twinned octahedral tilting pattern in the $Bi_{0.81}Pb_{0.19}FeO_{2.905}$ cubic perovskite. Chemistry of Materials 24, 1378-1385

DE KOKER, N.; STEINLE-NEUMANN, G.; VLČEK, V. (2012): Electrical resistivity and thermal conductivity of liquid Fe alloys at high P and T, and heat flux in Earth's core. Proc. Nat. Acad. Science (USA) 109, 4070-4073

DE KOKER, N. (2012): Melting of cubic boron nitride at extreme pressures. Journal of Physics: Condensed Matter 24, 055401

DUBROVINSKY, L.; DUBROVINSKAIA, N.; PRAKAPENKA, V.B.; ABAKUMOV, A.M. (2012): Implementation of micro-ball nanodiamond anvils for high-pressure studies above 6 Mbar. Nature Communications 3, 1163

ESCUDERO, A.; MIYAJIMA, N.; LANGENHORST, F. (2012): Microstructure, composition and P-T conditions of rutile from diamondiferous gneiss of the Saxonian Erzgebirge, Germany. Chemie der Erde – Geochemistry 92, 25-30

ESCUDERO, A.; LANGENHORST, F.; MÜLLER, W.F. (2012): Aluminum solubility in TiO_2 rutile at high pressure and experimental evidence for a $CaCl_2$ structured polymorph. American Mineralogist 97, 1075-1082

ESCUDERO, A.; LANGENHORST, F. (2012): Aluminum incorporation in α-PbO_2 type TiO_2 at pressures up to 20 GPa. Physics of the Earth and Planetary Interiors 190-191, 87-94

ESCUDERO, A.; LANGENHORST, F. (2012): Incorporation of Si into TiO_2 phases at high pressure. American Mineralogist 97, 524-531

ESCUDERO, A.; LANGENHORST, F. (2012): Chromium incorporation into TiO_2 at high pressure. Journal of Solid State Chemistry 190, 61-67

EVONUK, M.; SAMUEL, H. (2012): Simulating rotating fluid bodies: When is vorticity generation via density stratification important? Earth and Planetary Science Letters 317-318, 1-7

FEI, H.; HEGODA, C.; YAMAZAKI, D.; WIEDENBECK, M.; YURIMOTO, H.; SHCHEKA, S.; KATSURA, T. (2012): High silicon self-diffusion coefficient in dry forsterite. Earth and Planetary Science Letters 345-348, 95-103

GALUSKIN, E.; GALUSKINA, I.; DUBROVINSKY, L.; JANECZEK, J. (2012): Thermally induced transformation of vorlanite to "protovorlanite": Restoration of cation ordering in self-irradiated $CaUO_4$. American Mineralogist 97, 1002-1004

GALUSKIN, E.; LAZIC, B.; ARMBRUSTER, T.; GALUSKINA, I.; PERTSEV, N.; GAZEEV, V.; WLODYKA, R.; DULSKI, M.; DZIERZANOWSKI, P.; ZADOV, A.; DUBROVINSKY, L. (2012): Edgrewite $Ca_9(SiO_4)_4F_2$-hydroxyledgrewite $Ca_9(SiO_4)_4(OH)_2$, a new series of calcium humite-group minerals from altered xenoliths in the ignimbrite of Upper Chegem caldera, Northern Caucasus, Kabardino-Balkaria, Russia. American Mineralogist 97, 1998-2006

GLAZYRIN, K.; MCCAMMON, C.; DUBROVINSKY, L.; SCHOLLENBRUCH, K.; MERLINI, M.; HANFLAND, M. (2012): Effect of high pressure on the crystal structure and electronic properties of magnetite below 25 GPa. American Mineralogist 97, 128-133

HUANG, R.; AUDÉTAT, A. (2012): The titanium-in-quartz (TitaniQ) thermobarometer: a critical examination and re-calibration. Geochimica et Cosmochimica Acta 84, 75-89

KANTOR, A.; KANTOR, I.; MERLINI, M.; GLAZYRIN, K.; PRESCHER, C.; HANFLAND, M.; DUBROVINSKY, L. (2012): High-pressure structural studies of eskolaite by means of single-crystal X-ray diffraction. American Mineralogist 97, No. 10, 1764-1770

KONZETT, J.; RHEDE, D.; FROST, D.J. (2012): The high PT stability of apatite and Cl partitioning between apatite and hydrous potassic phases in peridotite: an experimental study to 19 GPa with implications for the transport of P, Cl and K in the upper mantle. Contributions to Mineralogy and Petrology 163, 277-296

KUPENKO, I.; DUBROVINSKY, L.; DMITRIEV, V.; DUBROVINSKAIA, N. (2012): In situ Raman spectroscopic study of the pressure induced structural changes in ammonia borane. The Journal of Chemical Physics 137, 074506

LEPORE, G.O.; BOFFA BALLARAN, T.; NESTOLA, F.; BINDI, L.; PASQUAL, D.; BONAZZI P. (2012): Compressibility of β-As_4S_4: an *in situ* high-pressure single-crystal X-ray study. Mineralogical Magazine 76, 963-973

LERCHBAUMER, L.; AUDÉTAT, A. (2012): The quartz capsule – a new method to avoid alloying problems with noble metal capsules in hydrothermal experiments. European Journal of Mineralogy 24, 683-693

LERCHBAUMER, L.; AUDÉTAT, A. (2012): High Cu concentrations in vapor-type fluid inclusions: an artifact? Geochimica et Cosmochimica Acta 88, 255-274

LI, Y.; AUDÉTAT, A. (2012): Partitioning of V, Mn, Co, Ni, Cu, Zn, As, Mo, Ag, Sn, Sb, W, Au, Pb, and Bi between sulfide phases and hydrous basanite melt at upper mantle conditions. Earth and Planetary Science Letters 355-356, 327-340

LIEBSKE, C.; FROST, D.J. (2012): Melting phase relations in the MgO-$MgSiO_3$ system between 16 and 26 GPa: Implications for melting in Earth's deep interior. Earth and Planetary Science Letters 345, 159-170

LIN, J.-F.; ALP, E.E.; MAO, Z.; INOUE, T.; MCCAMMON, C.; XIAO, Y.; CHOW, P.; ZHAO, J. (2012): Electronic spin states of ferric and ferrous iron in the lower-mantle silicate perovskite. American Mineralogist 97, 592-597

LIU, J.; WU, G.; LI, Y.; ZHU, M.; ZHONG, W. (2012): Re-Os sulfide (chalcopyrite, pyrite and molybdenite) systematics and fluid inclusion study of the Duobaoshan porphyry Cu (Mo) deposit, Heilongjiang Province, China. Journal of Asian Earth Sciences 49, 300-312

MAIEROVA, P.; CHUST, T.; STEINLE-NEUMANN, G.; CADEK, O.; CIZKOVA, H. (2012): The effect of variable thermal diffusivity on kinematic models of subduction. Journal of Geophysical Research 117, B07202

MANG, C.; KONTNY, A.; HARRIES, D.; LANGENHORST, F.; HECHT, L. (2012): Iron deficiency in pyrrhotite of suevites from the Chesapeake Bay impact crater, USA–A consequence of shock metamorphism? Meteoritics and Planetary Science 47, 277-295

MANN, U.; FROST D.J.; RUBIE, D.C.; BECKER, H.; AUDÉTAT, A. (2012): Partitioning of Ru, Rh, Pd, Re, Ir and Pt between liquid metal and silicate at high pressures and high temperatures – implications for the origin of highly siderophile element concentrations in the Earth's mantle. Geochimica et Cosmochimica Acta 84, 593-613

MANTHILAKE, M.A.G.M.; MIYAJIMA, N.; HEIDELBACH, F.; SOUSTELLE, V.; FROST, D.J. (2012): The effect of aluminum and water on the development of deformation fabrics of orthopyroxene. Contributions to Mineralogy and Petrology, doi: 10.1007/s00410-012-0819-4

MANTHILAKE, M.A.G.M.; WALTE, N.; FROST, D.J. (2012): A new multi-anvil press employing six independently acting 8 MN hydraulic rams. High Pressure Research 32, 195-207

MAO, Z.; LIN, J.-F.; JACOBSEN, S.D.; DUFFY, T.S.; CHANG, Y.-Y.; SMYTH, J.R.; FROST, D.J.; HAURI, E.; PRAKAPENKA, V.B. (2012): Sound velocity of hydrous ringwoodite to 16 GPa and 673 K. Earth and Planetary Science Letters 331, 112-119

MERLINI, M.; CRICHTON, W.; HANFLAND, M.; GEMMI, M.; MULLER, H.; KUPENKO, I.; DUBROVINSKY, L. (2012): Structures of dolomite at ultrahigh pressure and their influence on the deep carbon cycle. Proceedings of the National Academy of Sciences 34, 13509-13514

MIKHEYKIN, A.S.; DMITRIEV, V.P.; CHAGOVETS, S.; KURIGANOVA, A.B.; SMIRNOVA, N.V.; LEONTYEV, I.N. (2012): The compressibility of nanocrystalline Pt. Applied Physics Letters 101, 173111

MISHRA, S.K.; MITTAL, R.; CHAPLOT, S.L.; OVSYANNIKOV, S.V.; TROTS, D.; DUBROVINSKY, L.; SU, Y.; BRUECKEL, Th.; MATSUISHI, S.; HOSONO, H.; GARBARINO, G. (2012): Pressure-driven phase transition in CaFeAsF at 40 and 300 K. Journal of Physics: Conference Series 377, 012034

MÜLLNER, M.; LUNKENBEIN, T.; SCHIEDER, M.; MIYAJIMA, N.; FÖRTSCH, M.; BREU, J.; CARUSO, F.; MÜLLER, A.H.E. (2012): Template-directed mild synthesis of anatase hybrid nanotubes within cylindrical core-shell-corona polymer brushes. Macromolecules 45(17), 6981-6988

MÜLLNER, M.; LUNKENBEIN, T.; MIYAJIMA, N.; BREU, J.; MÜLLER, A.H.E. (2012): A facile polymer templating route toward high-aspect-ratio crystalline titania nanostructures. small 8(17), 2636-2640

MUSSI, A.; CORDIER, P.; FROST, D.J. (2012): Crystal defects in dense hydrous magnesium silicate phase A deformed at high pressure: characterization by transmission electron microscopy. European Journal of Mineralogy 24, 429-438

NAKAJIMA, Y.; FROST, D.J.; RUBIE, D.C. (2012): Ferrous iron partitioning between magnesium silicate perovskite and ferropericlase and the composition of perovskite in the Earth's lower mantle. Journal of Geophysical Research 117, B08201, doi: 10.1029/2012JB009151

NALIBOFF, J.B.; LITHGOW-BERTELLONI, C.; RUFF, L.J.; DE KOKER, N. (2012): The effects of lithospheric thickness and density structure on Earth's stress field. Geophysical Journal International 188, 1-17

NI, H. (2012): Compositional dependence of alkali diffusivity in silicate melts: mixed alkali effect and pseudo alkali effect. American Mineralogist 97, 70-79

NI, H.; KEPPLER H. (2012): In situ Raman spectroscopic study of sulfur speciation in oxidized magmatic-hydrothermal fluids. American Mineralogist 97, 1348-1353

NISHIHARA, Y.; NAKAJIMA, Y.; AKASHI, A.; TSUJINO, N.; TAKAHASHI, E.; FUNAKOSHI, K.; HIGO, Y. (2012): Isothermal compression of face-centered cubic iron. American Mineralogist 97, 1417-1420

NIWA, K.; MIYAJIMA, N.; OHGUSHI, K.; GOTOU, H.; YAGI, T. (2012): In-situ observation of shear stress-induced perovskite to post-perovskite phase transition in $CaIrO_3$ and the development of its deformation texture in a diamond-anvil cell up to 30 GPa. Physics of the Earth and Planetary Interiors 194-195, 10-17

OVSYANNIKOV, S.V.; WU, X.; KARKIN, A.E.; SHCHENNIKOV, V.V.; MANTHILAKE, G.M. (2012): Pressure-temperature phase diagram of Ti_2O_3 and physical properties in the golden Th_2S_3-type phase. Physical Review B 86, 024106

OVSYANNIKOV, S.V.; KOROBEINIKOV, I.V.; MOROZOVA, N.V.; MISIUK, A.; ABROSIMOV, N.V.; SHCHENNIKOV, V.V. (2012): 'Smart' silicon: switching between *p*– and *n*– conduction under compression. Applied Physics Letters 101, 062107

OVSYANNIKOV, S.V.; MOROZOVA, N.V.; KARKIN, A.E.; SHCHENNIKOV, V.V. (2012): High-pressure cycling of hematite (α-Fe_2O_3): Nanostructuring, *in situ* electronic transport and possible charge disproportionation. Physical Review B 86, 205131

PALKE, A.C.; STEBBINS, J.F.; FROST, D.J.; MCCAMMON, C.A. (2012): Incorporation of Fe and Al in $MgSiO_3$ perovskite: An investigation by ^{27}Al & ^{29}Si NMR spectroscopy. American Mineralogist 97, 1955-1964

PETTKE, T.; OBERLI, F.; AUDÉTAT, A.; GUILLONG, M.; SIMON, A.C.; HANLEY, J.J.; KLEMM, L.M. (2012): Recent developments in element concentration and isotope ratio analysis of individual fluid inclusions by laser ablation single and multiple collector ICP-MS. Ore Geology Reviews 44, 10-38

POSNER, E.S.; KONZETT, J.; FROST, D.J.; DOWNS, R.T.; YANG, H.X. (2012): High-pressure synthetic $(Na_{0.97}Mg_{0.03})(Mg_{0.43}Fe_{0.17}^{3+}Si_{0.40})Si_2O_6$, with six-coordinated silicon, isostructural with *P*2/*n* omphacite. Acta Crystallographica Section E – Structure Reports Online 68(2), I18-U166 doi: 10.1107/S1600536812002966

POTAPKIN, V.; CHUMAKOV, A.I.; SMIRNOV, G.V.; CELSE, J.-P.; RUFFER, R.; MCCAMMON, C.; DUBROVINSKY, L. (2012): The ^{57}Fe synchrotron Mössbauer source at the ESRF. Journal of Synchrotron Radiation 19, 559-569

POTAPKIN, V.B.; CHUMAKOV, A.I.; SMIRNOV, G.V.; RÜFFER, R.; MCCAMMON, C.; DUBROVINSKY, L. (2012): Angular, spectral and temporal properties of nuclear radiation from the ^{57}Fe Synchrotron Mössbauer source. Physical Review A 86, 053808, doi: 10.1103/PhysRevA.86.053808

PRESCHER, C.; DUBROVINSKY, L.; MCCAMMON, C.; GLAZYRIN, K.; NAKAJIMA, Y.; KANTOR, A.; MERLINI, M.; HANFLAND, M. (2012): Structurally hidden magnetic transitions in Fe_3C at high pressures. Physical Review B 85, 140402(R)

PRESCHER, C.; MCCAMMON, C.; DUBROVINSKY, L. (2012): MossA - a program for analyzing energy-domain Mossbauer spectra from conventional and synchrotron sources. Journal of Applied Crystallography 45, 329-331

ROBINSON, P.; HARRISON, R.J.; MIYAJIMA, N.; MCENROE, S.A.; FABIAN, K. (2012): Chemical and magnetic properties of rapidly cooled metastable ferri-ilmenite solid solutions: implications for magnetic self-reversal and exchange biasuII. Chemical changes during quench and annealing. Geophysical Journal International 188(2), 447-472

SAMUEL, H. (2012): A re-evaluation of metal diapir breakup and equilibration in terrestrial magma oceans. Earth and Planetary Science Letters 313-314, 105-114

SAMUEL, H. (2012): Time-domain parallelization for computational geodynamics. G-cubed 13, doi: 10.1029/2011GC003905

SAMUEL, H.; TOSI, N. (2012): The influence of post-perovskite strength on the Earth's mantle thermal and chemical evolution. Earth and Planetary Science Letters 323-324, 50-59

SHCHEKA, S.S.; KEPPLER, H. (2012): The origin of the terrestrial noble-gas signature. Nature 490, 531-534

SHCHENNIKOV, V.V.; MOROZOVA, N.V.; OVSYANNIKOV, S.V. (2012): Similar behavior of thermoelectric properties of lanthanides under strong compression up to 20 GPa. Journal of Applied Physics 111, 112624

SMYTH, J.R.; MIYAJIMA, N.; HUSS, G.R.; HELLEBRAND, E.; RUBIE, D.C.; FROST, D.J. (2012): Olivine–wadsleyite–pyroxene topotaxy: Evidence for coherent nucleation and diffusion-controlled growth at the 410-km discontinuity. Physics of the Earth and Planetary Interiors 200-201, 85-91

SPIVAK, A.V.; LITVIN, Yu.A.; OVSYANNIKOV, S.V; DUBROVINSKAIA, N.; DUBROVINSKY, L. (2012): Stability and breakdown of $Ca^{13}CO_3$ melt combined with formation of ^{13}C-diamond in static high-pressure high-temperature experiments up to 40 GPa and 4000 K. Journal of Solid State Chemistry 191, 102-106

SUGIMURA, E.; KOMABAYASHI, T.; OHTA, K.; HIROSE, K.; OHISHI, Y.; DUBROVINSKY, L. (2012): Experimental evidence of superionic conduction in H_2O ice. Journal of Chemical Physics 137, 194505

TAN, J.; WEI, J.; AUDÉTAT A.; PETTKE, T. (2012): Source of metals in the Guocheng gold deposit, Jiaodong Peninsula, North China Craton: link to early Cretaceous mafic magmatism originating from Paleoproterozoic metasomatized lithospheric mantle. Ore Geology Reviews 48, 70-87

TERASAKI, H.; URAKAWA, S.; RUBIE, D.C.; FUNAKOSHI, K.; SAKAMAKI, T.; SHIBAZAKI, Y.; OZAWA, S.; OHTANI, E. (2012): Interfacial tension of Fe-Si liquid at high pressure: Implications for liquid Fe-alloy droplet size in magma oceans. Physics of the Earth and Planetary Interior 202-203, 1-6

TROTS, D.M.; KURNOSOV, A.; BOFFA BALLARAN, T.; FROST D.J. (2012): High-temperature structural behaviors of anhydrous wadsleyite and forsterite. American Mineralogist 97, 1582-1590

TUMANOV, N.A.; BOLDYREVA, E.V.; KOLESOV, B.A.; KURNOSOV, A.V.; QUESADA CABRERA, R. (2012): Pressure-induced phase transitions in L-alanine, revisited (Acta Cryst. B66, 458-471). Acta Crystallographica Section B – Structural Science B68, 465

VASYLECHKO, L.; BURKHARDT, U.; SCHNELLE, W.; BORRMANN, H.; HAARMANN, F.; SENYSHYN, A.; TROTS, D.; HIEBL, K.; GRIN, Y. (2012): Order/disorder in $YbNi_{1\pm X}Ga_{2\pm X}$ ($x \leq 0.08$): Crystal structure, thermal expansion and magnetic properties. Solid State Sciences 14, 746-760

VLČEK, V.; DE KOKER, N.; STEINLE-NEUMANN, G. (2012): Electrical and thermal conductivity of Al liquid at high pressures and temperatures from ab-initio computations. Physical Review B 85, 184201

WELCH, M.D.; KONZETT, J.; BINDI, L.; KOHN, S.C.; FROST, D.J. (2012); New structural features of the high-pressure synthetic sheet-disilicate Phase-X, $K_{(2-x)}Mg_2Si_2O_7H_x$. American Mineralogist 97, 1849-1857

WILLIAMS, H.M.; WOOD, B.J.; WADE, J.; FROST, D.J.; TUFF, J. (2012): Isotopic evidence for internal oxidation of the Earth's mantle during accretion. Earth and Planetary Science Letters 321, 54-63

WOODLAND, A.B.; FROST, D.J.; TROTS, D.M.; KLIMM, K.; MEZOUAR, M. (2012): In situ observation of the breakdown of magnetite (Fe_3O_4) to Fe_4O_5 and hematite at high pressures and temperatures. American Mineralogist 97, 1808-1811

YANG, X. (2012): An experimental study of H solubility in feldspars: effect of composition, oxygen fugacity, temperature and pressure and implications for crustal processes. Geochimica et Cosmochimica Acta 97, 46-57

YANG, X. (2012): Orientation-related electrical conductivity of hydrous olivine, clinopyroxene and plagioclase and implications for the structure of the lower continental crust and uppermost mantle. Earth and Planetary Science Letters 317-318, 241-250

YANG, X.; HEIDELBACH, F. (2012): Grain size effect on the electrical conductivity of clinopyroxene. Contributions to Mineralogy and Petrology 163, 939-947

YANG, X.; DUBROVINSKY, L.; MANTHILAKE, M.A.G.M.; WEI, Q. (2012): High pressure and high temperature Raman spectroscopic study of hydrous wadsleyite (b-Mg_2SiO_4). Physics and Chemistry of Minerals 39, 57-64

YANG, X.; KEPPLER, H.; MCCAMMON, C.; NI, H. (2012): Electrical conductivity of orthopyroxene and plagioclase in the lower crust. Contributions to Mineralogy and Petrology 163, 33-48

YANG, X.; MCCAMMON, C. (2012): Fe^{3+}-rich augite and high electrical conductivity in the deep lithosphere. Geology 40, No. 2, 131-134

YANG, Z.; HEIDELBACH, F. (2012): Grain size effect on the electrical conductivity of clinopyroxene. Contributions to Mineralogy and Petrology 163, 939-947

YE, Y.; BROWN, D.A.; SMYTH, J.R.; PANERO, W.R.; JACOBSEN, S.D.; CHANG, Y.-Y.; TOWNSEND, J.P.; THOMAS, S.M.; HAURI, E.H.; DERA, P.; FROST, D.J. (2012): Compressibility and thermal expansion study of hydrous Fo_{100} ringwoodite with 2.5(3) wt% H_2O. American Mineralogist 97, 573-582

YE, Y.; SMYTH, J.R.; JACOBSEN, S.D.; GOUJON, C. (2012): Crystal chemistry, thermal expansion, and Raman spectra of hydroxyl-clinohumite: implications for water in Earth's interior. Contributions to Mineralogy and Petrology, doi: 10.1007/s00410-012-0823-8

YOSHINO, T.; KATSURA, T. (2012): Re-evaluation of electrical conductivity of anhydrous and hydrous wadsleyite. Earth and Planetary Science Letters 337-338, 56-67

YOSHINO, T.; MCISAAC, E.; LAUMONIER, M.; Katsura, T. (2012): Electrical conductivity of partial molten carbonate peridotite. Physics of the Earth and Planetary Interiors 194-195, 1-9

ZHANG, L.; AUDÉTAT, A.; DOLEJS, D. (2012): Solubility of molybdenite (MoS_2) in aqueous fluids at 600-800 °C, 200 MPa: a synthetic fluid inclusion study. Geochimica et Cosmochimica Acta 77, 175-185

ZUCCHINI, A.; COMODI, P.; KATERINOPOULOU, A.; BALIC-ZUNIC, T.; MCCAMMON, C.; FRONDINI, F. (2012): Order-disorder-reorder process in thermally treated dolomite samples: a combined powder and single crystal X-ray diffraction study. Physics and Chemistry of Minerals 39, 319-328

6.2 Publications (submitted, in press)

AUDÉTAT, A.; LOWENSTERN, J.B.: Melt inclusions. – In: TUREKIAN, K.K.; HOLLAND, H.D. (Eds.): Treatise on Geochemistry, Vol. 12 (in press)

AUDÉTAT, A.; SIMON, A.: Magmatic controls on porphyry Cu genesis. – In: HEDENQUIST, J.; HARRIS, M.; CAMUS, F. (Eds.): Geology and genesis of major copper deposits and districts of the world: a tribute to Richard Sillitoe (in press)

BALI, E.; AUDÉTAT, A.; KEPPLER, H.: Water and hydrogen are immiscible in Earth's mantle. Nature (submitted)

BERNINI, D.; AUDÉTAT A.; DOLEJS, D.; KEPPLER H.: Zircon solubility in aqueous fluids at high temperatures and pressures. Geochimica et Cosmochimica Acta (submitted)

BERNINI, D.; WIEDENBECK, M.; DOLEJS, D.; KEPPLER, H.: Partitioning of halogens between mantle minerals and aqueous fluids: implications for the fluid flow regime in subduction zones. Contributions to Mineralogy and Petrology (in press)

BOFFA BALLARAN, T.: Diffraction at extreme conditions: a window into the Earth's interior. Rendiconti Lincei - Scienze Fisiche e Naturali, invited contribution for the special volume for the Centennial of X-ray diffraction (submitted)

CORDIER, P.; HEIDELBACH, F.: On the origin of twist in quartz crystals from the Alps: a transmission electron microscopy study. European Journal of Mineralogy (in press)

DE KOKER, N.; KARKI, B.B.; STIXRUDE, L.: Thermodynamics of the MgO-SiO_2 liquid system in Earth's lowermost mantle from first principles. Earth and Planetary Science Letters (in press)

DE VRIES, J.; JACOBS, M.H.G.; VAN DEN BERG, A.P.; WEHBER, M.; LATHE, C.; MCCAMMON, C.; VAN WESTRENEN, W.: Thermal equation of state of synthetic orthoferrosilite at lunar pressures and temperatures. Physics and Chemistry of Minerals (submitted)

DOMENEGHETTI, M.C.; FIORETTI, A.M.; CÁMARA, F.; MCCAMMON, C.; ALVARO, M.: Thermal history of nakhlites: a comparison between MIL03346 and its terrestrial analogue Theo's flow. Geochimica et Cosmochimica Acta (submitted)

EL GORESY, A.; GILLET, Ph.; MIYAHARA, M.; OHTANI, E.; OZAWA, S.; BECK, P.; MONTAGNAC, G.: Shock-induced deformation of shergottites: Shock pressures and perturbations of magmatic ages on Mars. Geochimica et Cosmochimica Acta (in press)

FEI, H.; WIEDENBECK, M.; YAMAZAKI, D.; KATSURA, T.: Small effect of water on upper mantle rheology. Nature (submitted)

GILLET, Ph.; EL GORESY, A.: Shock events in the solar system: The message from terrestrial planets and asteroids. Annual Review of Earth and Planetary Sciences (in press)

GLAZYRIN, K.; BALLARAN, T.B.; FROST, D.J.; MCCAMMON, C.; KANTOR, A.; MERLINI, M.; HANFLAND, M.; DUBROVINSKY, L.: Effect of iron oxidation state on the bulk sound velocity of the Earth's lower mantle. Nature Communications (submitted)

GLAZYRIN, K.; POUROVSKII, L.V.; DUBROVINSKY, L.; NARYGINA, O.; MCCAMMON, C.; HEWENER, B.; SCHÜNEMANN, V.; WOLNY, J.; MUFFLER, K.; CHUMAKOV, A.I.; CRICHTON, W.; HANFLAND, M.; PRAKAPENKA, V.; TASNÁDI, F.; EKHOLM, M.; AICHHORN, M.; VILDOSOLA, V.; RUBAN, A.V.; KATSNELSON, M.I.; ABRIKOSOV, I.A.: Importance of correlation effects in hcp iron revealed by a pressure-induced electronic topological transition. Physical Review Letters (submitted)

GOU, H.; STEINLE-NEUMANN, G.; BYKOVA, E.; NAKAJIMA, Y.; MIYAJIMA, N.; LI, Y.; OVSYANNIKOV, S.V.; DUBROVINSKY, L.S.; DUBROVINSKAIA, N.: Stability of MnB_2 with AlB_2 -type structure revealed by first-principles calculations and experiments. Physical Review B (submitted)

GROAT, L.A.; EVANS, J.; CEMPÍREK, J.; MCCAMMON, C.: As-bearing and Fe-rich vesuvianite and wiluite from Kozlov, Czech Republic. American Mineralogist (submitted)

GU, T.; WU, X.; QIN, S.; MCCAMMON, C.; DUBROVINSKY, L.: Mössbauer spectroscopic study of pressure-induced phase transition of Fe_2P. Journal of Physics: Condensed Matter (submitted)

HARRIES, D.; BERG, T.; LANGENHORST, F.; PALME, H.: Structural clues to the origin of refractory metal alloys as condensates of the solar nebula. Meteoritics and Planetary Science (in press)

HEIDELBACH, F.; TERRY, M.P.: Inherited fabric in an omphacite symplectite: reconstruction of plastic deformation under ultra-high pressure conditions. Microscopy and Microanalysis (submitted)

HERMANNSDÖRFER, J.; FRIEDRICH, M.; MIYAJIMA, N.; ALBUQUERQUE, R.Q.; KÜMMEL, S.; KEMPE, R.: Synergistic catalysis with cavity-conform Ni/Pd nanoparticles. Angewandte Chemie (in press)

HOWELL, D.; PIAZOLO, S.; DOBSON, D.P.; WOOD, I.G.; JONES, A.P.; WALTE, N.; FROST, D.J.; FISHER, D.: Quantitative characterization of plastic deformation of single diamond crystals: a High Pressure High Temperature (HPHT) experimental deformation study combined with Electron Backscatter Diffraction (EBSD). Diamond and Related Materials (in press)

KUPENKO, I.; DUBROVINSKY, L.; DUBROVINSKAIA, N.; MCCAMMON, C.; GLAZYRIN, K.; BYKOVA, E.; BOFFA BALLARAN, T.; SINMYO, R.; CHUMAKOV, A.I.; POTAPKIN, V.; KANTOR, A.; RÜFFER, R.; HANFLAND, M.; CRICHTON, W.; MERLINI, M.: Portable double-sided laser-heating system for Mössbauer spectroscopy and X-ray diffraction experiments at synchrotron facilities with diamond anvil cells. Review of Scientific Instruments (in press)

LEONTYEVA, D.V.; LEONTYEV, I.N.; AVRAMENKO, M.V.; YUZYUK, Yu.I.; KUKUSHKINA, Yu.A.; REVENKO, R.; SMIRNOVA, N.V.: Electrochemical dispergation as simple and effective route toward preparation NiO based nanocomposit for supercapacitor application. Journal of Materials Chemistry (submitted)

LERCHBAUMER, L.; AUDÉTAT, A.: The metal content of silicate melts and aqueous fluids in sub-economically Mo-mineralized granites: implications for porphyry Mo genesis. Economic Geology (submitted)

LI, Y.; AUDÉTAT, A.: Gold solubility and partitioning between sulfide liquid, monosulfide solid solution and hydrous mantle melts: Implications for crust–mantle differentiation and the formation of Au-rich magmas. Geochimica et Cosmochimica Acta (submitted)

MANTHILAKE, M.A.G.M.; MIYAJIMA, N.; HEIDELBACH, F.; SOUSTELLE, V.; FROST, D.J.: The effect of aluminum and water on the development of deformation fabrics in orthopyroxene. Contributions to Mineralogy and Petrology (in press)

MORISHIMA, R.; GOLABEK, G.; SAMUEL, H.: N-body simulations of oligarchic growth of Mars: Implications for Hf-W chronology. Earth and Planetary Science Letters (submitted)

NI, H.; KEPPLER H.: Carbon in silicate melts. Review in Mineralogy and Geochemistry 75 (in press)

NI, H.; XU, Z.; ZHANG Y.: Hydroxyl and molecular H_2O diffusivity in a haploandesitic melt. Geochimica et Cosmochimica Acta (in press)

NI, H.; HUI, H.; STEINLE-NEUMANN, G.: Transport properties of silicate melts: methods, models, and geophysical implications. Reviews of Geophysics (submitted)

OTSUKA, K.; LONGO, M.; MCCAMMON, C.A.; KARATO, S.-I.: Ferric iron content of ferropericlase as a function of composition, oxygen fugacity, temperature and pressure: Implications for redox conditions during diamond formation in the lower mantle. Earth and Planetary Science Letters (in press)

OVSYANNIKOV, S.V.; ABAKUMOV, A.M.; TSIRLIN, A.A.; SCHNELLE, W.; EGOAVIL, R.; VERBEECK, J.; VAN TENDELOO, G.; GLAZYRIN, K.; HANFLAND, M.; DUBROVINSKY, L.: Perovskite-like Mn_2O_3: a path to new manganites. Angewandte Chemie International Edition (submitted)

OVSYANNIKOV, S.V.; GOU, H.; MOROZOVA, N.V.; TYAGUR, I.; TYAGUR, Y.; SHCHENNIKOV, V.V.: Raman spectroscopy of ferroelectric $Sn_2P_2S_6$ under high pressure up to 40 GPa: phase transitions and metallization. Journal of Applied Physics (submitted)

POTAPKIN, V.; MCCAMMON, C.; GLAZYRIN, K.; KANTOR, A.; KUPENKO, I.; PRESCHER, C.; SINMYO, R.; SMIRNOV, G.V.; CHUMAKOV, A.I.; RÜFFER, R.; DUBROVINSKY, L.: Effect of iron oxidation state on the electrical conductivity of the Earth's lower mantle. Nature Communications (submitted)

PRESCHER, C.; WEIGEL, C.; MCCAMMON, C.; NARYGINA, O.; POTAPKIN, V.; KUPENKO, I.; GLAZYRIN, K.; SINMYO, R.; CHUMAKOV, A.I.; DUBROVINSKY, L.: Iron spin state in silicate glass at high pressure: implications for melts in the Earth's lower mantle. Earth and Planetary Science Letters (submitted)

ROBINSON, P.; FABIAN, K.; MCENROE, S.A.; HEIDELBACH, F.: Influence of lattice-preferred orientation with respect to magnetizing field on intensity of remanent magnetization in polycrystalline hemo-ilmenite. Geophysical Journal International (in press)

SINMYO, R.; HIROSE, K.: Iron partitioning in pyrolitic lower mantle. Physics and Chemistry of Minerals (accepted)

SOUSTELLE, V.; TOMMASI, A.; DEMOUCHY, S.; FRANZ, L.: Effect of fluid-rock interactions on deformation and seismic properties of the oceanic sub-arc mantle: Microstructural study of mantle xenoliths from seamounts near Lihir Island, Papua-New-Guinea. Tectonophysics (submitted)

STAGNO, V.; OJWANG, D.O.; MCCAMMON, C.A.; FROST, D.J.: The oxidation state of the mantle and the extraction of carbon from Earth's interior. Nature (in press)

TSUJINO, N.; NISHIHARA, Y.; NAKAJIMA, Y.; TAKAHASHI, E.; FUNAKOSHI, K.; HIGO, Y.: Equation of state of γ-Fe: reference density for planetary cores. Earth and Planetary Science Letters (submitted)

TSUNO, K.; FROST, D.J.; RUBIE, D.C.: Simultaneous partitioning of silicon and oxygen into the Earth's core during early Earth differentiation. Geophysical Research Letters (submitted)

VAN MIERLO, W.L.; LANGENHORST, F.; FROST, D.J.; RUBIE, D.C.: Slow diffusion in the Earth's transition zone as a factor in slab stagnation. Nature Geoscience (submitted)

ZHANG, Q.; WU, X.; OVSYANNIKOV, S.V.; SHAN, Q.; DUBROVINSKY, L.: High-pressure high-temperature synthesis of a monoclinic Y_2O_3 phase. Zeitschrift für Anorganische und Allgemeine Chemie (submitted)

6.3 Presentations at scientific institutions and at congresses

AUDÉTAT, A.; HUANG, R.; ZHANG, L.: 28.-29.01.2012, ENB weekend seminar, Schloss Thurnau, Germany: "Thermobarometry of silicic igneous rocks"

AUDÉTAT, A.; ZHANG, L.: 04.-07.03.2012, EMPG XIV, Kiel, Germany[*1]: "Partitioning of vanadium between hydrous rhyolite melt and magnetite"

AUDÉTAT, A.: 15.-20.07.2012, Gordon Research Conference on Geochemistry of Mineral Deposits, Proctor Academy, Andover, USA *(invited)*: "The roles of vapor, brine and magmatic sulfides in the formation of porphyry-type ore deposits"

BALI, E.; KEPPLER, H.; AUDÉTAT, A.: 04.-07.03.2012, EMPG XIV, Kiel, Germany[*1]: "The mobility of W and Mo in subduction zone fluids" Abstract Volume, 38

BOBROV, A.; DYMSHITS, A.; BINDI, L.; LITVIN, Y.; DUBROVINSKY, L.: 05.-10.08.2012, 34th International Geological Congress, Brisbane, Australia: "Na-majorite $Na_2MgSi_5O_{12}$: phase relations, structural peculiarities and solid solutions (experiments at 7-25 GPa)"

BOFFA BALLARAN, T.: 08.-09.05.2012, International Conference 'Centennial of X-ray Diffraction', Accademia Nazionale dei Lincei, Roma, Italy: "Diffraction at extreme conditions: a window into the Earth's interior"

BOFFA BALLARAN, T.: 04.-05.08.2012, Satellite Workshop 'Methods of High-Pressure Single-Crystal X-ray Diffraction' at the European Crystallographic Meeting, Bergen, Norway *(invited)*: "Equations of State"

BYKOVA, E.; GLAZYRIN, K.; GREENBERG, E.; BOFFA BALLARAN, T.; PRAKAPENKA, V.; HANFLAND, M.; DUBROVINSKAIA, N.; DUBROVINSKY, L.: 12.-15.03.2012, 20th Annual Meeting of the German Crystallographic Society (DGK), Munich, Germany: "Crystal structure of α-FeOOH under high-pressure"

CAILLET-KOMOROWSKI, C.; EL GORESY, A.; MIYAHARA, M.; BOUDOUMA, O.; MA, C.: 12.-17.08.2012, 75th Annual Meeting of the Meteoritical Society, Cairns, Australia *(invited)*: "Hg-Cu-bearing metal-sulfide assemblage in the H3 chondrite Tieschitz: Important carriers of pristine Hg and possibly Cd isotopic signatures in the early solar system"

CERNOK, A.; DUBROVINSKY, L.: 04.-07.03.2012, EMPG XIV, Kiel, Germany*1: "Development of electrically heated diamond anvil cell for optical spectroscopy measurements"

CERNOK, A.; BYKOVA, E.; DUBROVINSKY, L.; MIYAJIMA, N.; LIERMANN, H.-P.: 01.07.-10.08.2012, CIDER 2012 Summer Program 'Deep Time: How did early Earth become our modern world?', KITP, Santa Barbara, USA: "High-pressure behavior of coesite"

DE KOKER, N.; STEINLE-NEUMANN, G.; VLČEK, V.: 10.01.2012, Universität Rostock, Quantum and Statistical Physics Seminar, Rostock, Germany *(invited)*: "Thermal conductivity of Earth's liquid outer core from first-principles calculations"

DOMENEGHETTI, M.; FIORETTI, A.; CÁMARA, F.; MCCAMMON, C.; ALVARO, M.: 02.-06.09.2012, European Mineralogical Conference, Frankfurt/M., Germany: "Thermal history of nakhlites: a comparison between MIL03346 and its terrestrial analogue Theo's flow", Abstract EMC2012-396, 2012

DUBROVINSKY, L.S.: 07.-08.02.2012, ESRF User Meeting, Grenoble, France (*invited*): "Ultra-high pressure crystallography"

DUBROVINSKY, L.S.; BYKOVA, E.; PRESCHER, C.; GLAZYRIN, K.; KANTOR, A.; MCCAMMON, C.; MOOKHERJEE, M.; NAKAJIMA, Y.; DUBROVINKSKAYA, N.; MERLINI, M.; HANFLAND, M.: 16.-21.09.2012, 50th EHPRG Meeting, Thessaloniki, Greece: "Structure and electronic properties of novel iron carbides up to 160 GPa from single crystal X-ray and Mössbauer spectroscopy data"

DUBROVINSKY, L.; DUBROVINSKAIA, N.: 13.-15.12.2012, CECAM Workshop on 'New insights on metals under extreme conditions', Paris, France (*invited*): "Transition metals at multimegabar pressures"

EL GORESY, A.: 04.04.2012, Chinese Academy of Sciences, Institute of Geology, Geophysics and the Lithosphere, Beijing, China: "EL-3 chondrites MS-17 and MS-177 from Almahata Sitta TC3 asteroid: Two primitive EL-chondrites probably from different primordial asteroids?"

EL GORESY, A.: 20.-25.05.2012, Japan Geoscience Union Meeting 2012, Chiba, Japan *(invited)*: "Shock-induced deformation of shergottites: Shock-pressures and perturbations of magmatic ages on Mars"

EL GORESY, A.: 01.06.2012, Tohoku University, Institute of Mineralogy, Petrology and Mineral Deposits, Sendai, Japan: "Mineralogical, chemical and isotopic study of the earliest solarcondensates in unequilibrated enstatite chondrites from EL-3 fragments MS-17 and MS-177 of Almahata Sitta TC_3 asteroid"

EL GORESY, A.; LIN, Y.; FENG, L.; BOYET, M.; HAO, J.; ZHANG, J.; DUBROVINSKY, L.: 12.-17.08.2012, 75th Annual Meeting of the Meteoritical Society, Cairns, Australia: "Almahata Sitta El-3 chondrite: Sinoite, graphite and oldhamite (CaS) assemblages, C- and N-isotope compositions and REE patterns"

EL GORESY, A.; LIN, A.; FENG, L.; BOYET, M.; HAO, J.; ZHANG, J.; MIYAHARA, M.; OHTANI, E.; DUBROVINSKY, L.: 09.-12.10.2012, Joint meeting 'Paneth Kolloquium', 'The first 10 million years of the solar system' (DFG SPP 1385) & 'MEMIN', Nördlingen, Germany: "Earliest condensate assemblages in EL3 fragments of Almahata Sitta TC_3 asteroid: REE patterns of oldhamite and C- and N- isotopic compositions of Si_2N_2O and graphite by NanoSIMS 50 L"

FEI, H.; HEGODA, C.; YAMAZAKI, D.; CHAKRABORTY, S.; DOHMEN, R.; WIEDENBECK, M.; YURIMOTO, H.; SHCHEKA, S.; KATSURA, T.: 04.-07.03.2012, EMPG XIV, Kiel, Germany[*1]: "High silicon self-diffusion coefficient in dry forsterite"

FEI, H.; WIEDENBECK, M.; YAMAZAKI, D.; KATSURA, T.: 03.-07.12.2012, AGU Fall Meeting, San Francisco, USA[*2]: "Small effect of water on upper mantle rheology based on silicon self-diffusion coefficients", Abstract DI13D-2448, 2012

FROST, D.J: 26.-28.02.2012, Scoping Study Workshop on 'The mantle control on a habitable planet: The importance of volatiles and fluids', Oxford, U.K.: "The redox state of the mantle and its relationship with volatile speciation"

FROST, D.J.; SHEKHAR, S.; MANTHILAKE, G.: 04.-07.03.2012, EMPG XIV, Kiel, Germany[*1]: "The use of piezoelectric crystals to measure stress in high pressure deformation experiments"

FROST, D.J.; RUBIE, D.C.: 01.-06.07.2012, SEDI 2012, Leeds, U.K.: "The composition of the base of the mantle and reactions with the outer core"

FROST, D.J.; CHANTEL, J.; KURNOSOV, A.; TROTS, D.; BOFFA BALLARAN, T.; WANG, W.: 24.-29.06.2012, Goldschmidt 2012, Montréal, Canada: "The composition of the lower mantle constrained by experiments on the elasticity of magnesium silicate perovskite", Mineralogical Magazine 76, 1721

FUJI-TA, K.; KATSURA, T.; ICHIKI, M.; SEKI, M.: 18.-21.03.2012, Joint Symposium of Misasa-2012 and Geofluid-2 'Dynamics and Evolution of the Earth's Interior: special emphasis on the role of fluids', Misasa, Tottori, Japan: "Variation in electrical conductivity of hydrous rock and mineral"

GLAZYRIN, K.; BOFFA BALLARAN, T.; FROST, D.J.; MCCAMMON, C.A.; KANTOR, A.; MERLINI, M.; HANFLAND, M.; DUBROVINSKY, L.S.: 03.-07.12.2012, AGU Fall Meeting, San Francisco, USA[*2]: "Spin state of iron and elastic properties of $(MgFe)(SiAl)O_3$ under conditions of the lower mantle", Abstract MR43B-2305, 2012

GOU, H.; STEINLE-NEUMANN, G.; BYKOVA, E.; NAKAJIMA, Y.; MIYAJIMA, N.; LI, Y.; OVSYANNIKOV, S.V; DUBROVINSKAIA, N.; DUBROVINSKY, L.: 08.-10.10.2012, High-Pressure Symposium, Freiberg, Germany: "Understanding crystal structure, hardness and electronic structure of MnB_2 from single-crystal synthesis and first-principle calculations"

GREENBERG, E.; ROZENBERG, G.K.; XU, W.; PASTERNAK, M.P.; DUBROVINSKY, L.; MCCAMMON, C.: 16.-21.09.2012, 50th EHPRG Meeting, Thessaloniki, Greece: "New insights into the high-pressure phase transitions of $CaFe_2O_4$ and Fe_2O_3"

HEIDELBACH, F.; WALTE, N.: 04.-07.03.2012, EMPG XIV, Kiel, Germany[*1]: "Deformation fabrics at the aragonite-calcite phase transition"

HEIDELBACH, F.: 17.-20.06.2012, 10th EMAS Regional Workshop, Padua, Italy *(invited)*: "Looking into the Earth's mantle deformation microstructures"

HEMPEL, S.; LIU, X.; RAINEY, E.S.; ULVROVA, M.; WANG, Y.; YE, L.; SHI, C.Y.; SRAMEK, O.; CARACAS, R.; GARNERO, E.J.; RUBIE, D.C.; WILLIAMS, Q.: 03.-07.12.2012, AGU Fall Meeting, San Francisco, USA[*2]: "On the possibility of a thin, molten silicate basal magma layer at the base of Earth's mantle", Abstract DI33A-2419, 2012

KATSURA, T.; YAMAZAKI, D.; CHAKRABORTY, S.; DOHMEN, R.; SHATSKIY, A.; XU, J.-S.; FEI, H.-Z.; HEGODA, C.; YURIMOTO, H.; WIEDENBECK; M.: 04.-07.03.2012, EMPG XIV, Kiel, Germany[*1]: "Si and Mg self-diffusion in stishovite, Mg-perovskite and forsterite"

KATSURA, T.; YAMAZAKI, D.; CHAKRABORTY, S.; DOHMEN, R.; SHATSKIY, A.; XU, J.-S.; FEI, H.-Z.; HEGODA, C.; YURIMOTO, H.; WIEDENBECK, M.: 18.-21.03.2012, Joint Symposium of Misasa-2012 and Geofluid-2 'Dynamics and Evolution of the Earth's Interior: special emphasis on the role of fluids', Misasa, Tottori, Japan: "Self-diffusion coefficients of mantle minerals and its applications to mantle rheology"

KATSURA; T.: 11.-13.06.2012, Graduate University of the Chinese Academy of Sciences, Beijing, China: "Physics and chemistry of the Earths interior" part 1 - part 6

KATSURA, T.; FEI, H.-Z.; YAMAZAKI, D.; XU, J.-S.; SHATSKIY, A.; HEGODA, C.; CHAKRABORTY, S.; DOHMEN, R.; YURIMOTO, H.; WIEDENBECK, M.: 09.-13.07.2012, Joint 2012 COMPRES Annual Meeting and High-Pressure Mineral Physics Seminar-8, Lake Tahoe, USA: "Self-diffusion coefficients of the mantle minerals"

KATSURA, T.: 10.09.2012, 2nd Workshop for Extreme Conditions Research in a Large Volume Press at PETRA III, Hamburg, Germany: "Possible high-energy X-ray diffraction studies at the LVP beam line in PETRA III Extension"

KATSURA, T.: 26.09.2012, China University of Geosciences, Wuhan, China: "Electrical conductivity of the deep mantle"

KATSURA, T.: 27.09.2012, China University of Geosciences, Wuhan, China: "Si self-diffusion coefficient of mantle minerals and its implication for the mantle rheology"

KATSURA, T.; FEI, H.; HEGODA, C.; YAMAZAKI, D.; WIEDENBECK, M.; YURIMOTO, H.; SHCHEKA, S.: 03.-07.12.2012, AGU Fall Meeting, San Francisco, USA[*2]: "High silicon self-diffusion coefficient in dry forsterite", Abstract MR31A-02, 2012

KING, S.; SAMUEL, H.: 22.-27.04.2012, European Geophysical Union General Assembly, Vienna, Austria: "Combine effects of plate motions and small-scale convection on mantle stirring efficiency"

KUPENKO, I.; DUBROVINSKY, L.; DUBROVINSKAIA, N.; CHUMAKOV, A.I.; POTAPKIN, V.; KANTOR, A.; RÜFFER, R.; MCCAMMON, C.; GLAZYRIN, K.; BYKOVA, E.; SINMYO, R.; HANFLAND, M.; CRICHTON, W.; MERLINI, M.: 04.-07.03.2012, EMPG XIV, Kiel, Germany[*1]: "Portable double-sided laser-heating system for diamond anvil cells"

KURNOSOV, A.; BOFFA BALLARAN, T.; GLAZYRIN, K.; TROTS, D.M.; FROST, D.J.; MERLINI, M.; HANFLAND, M.: 09.-13.07.2012, Joint 2012 COMPRES Annual Meeting and High-Pressure Mineral Physics Seminar-8, Lake Tahoe, USA: "Single-crystal elasticity and structural behavior of $MgSiO_3$ perovskite at pressure of the lower mantle"

LEONTYEV, I.; CHAGOVETS, S.; KURIGANOVA, A.; SMIRNOVA, N.: 28.-31.10.2012, 13th European Powder Diffraction Conference, Grenoble, France: "The compressibility of carbon supported Pt nanoparticles", Book of Abstracts, 107

LI, Y.: 02.-06.09.2012, European Mineralogical Conference, Frankfurt/M., Germany: "Nitrogen solubility in upper mantle minerals"

MCCAMMON, C.: 27.01.2012, Ludwig Maximilians Universität München, Germany: "Pushing the limits of Mössbauer spectroscopy"

MCCAMMON, C.: 26.-29.02.2012, 'Progress in Nuclear Resonance Scattering: from Methods to Materials', Bad Honnef, Germany: "NRS applications in geophysics"

MCCAMMON, C.; DUBROVINSKY, L.; GLAZYRIN, K.; PRESCHER, C.; KUPENKO, I.; POTAPKIN, V.; CHUMAKOV, A.; RÜFFER, R.; KANTOR, A.; KANTOR, I.; SMIRNOV, G.; POPOV, S.L.: 04.-07.03.2012, EMPG XIV, Kiel, Germany[*1]: "Development of a synchrotron Mössbauer source for measurements at extreme P,T conditions"

MCCAMMON, C.: 13.-15.03.2012, Biologie et Sciences de la Terre, Ecole Normale Supérieure de Lyon, France: "Oxygen Fugacity: Lecture and Practical"

MCCAMMON, C.; DUBROVINSKY, L.; POTAPKIN, V.; GLAZYRIN, K.; KANTOR, A.; KUPENKO, I.; PRESCHER, C.; SINMYO, R.; SMIRNOV, G.; CHUMAKOV, A.; RÜFFER, R.: 22.-27.04.2012, European Geophysical Union General Assembly, Vienna, Austria: "Iron spin transitions in the lower mantle"

MCCAMMON, C.: 01.05.2012, COMPRES Graduate Course 2012 – Mineral Physics, Las Vegas, USA: "Mössbauer Spectroscopy"

MCCAMMON, C.; DUBROVINSKY, L.; POTAPKIN, V.; GLAZYRIN, K.; KANTOR, A.; PRESCHER, C.; SINMYO, R.; SMIRNOV, G.; CHUMAKOV, A.; RÜFFER, R.: 02.-06.09.2012, European Mineralogical Conference, Frankfurt/M., Germany: "Advances in synchrotron-based methods of Mössbauer spectroscopy", Abstract EMC2012-702, 2012

MCCAMMON, C.: 24.-26.09.2012, CentralSync School on Synchrotron Radiation Methods and their Applications in Earth Science, Mátrafüred, Hungary: "Applications of nuclear resonance at high pressure and high temperature: Measurements at conditions of the deep Earth's interior"

MCCAMMON, C.: 25.-28.09.2012, 5th Berichtskolloquium of the SPP1236 'Structures and characteristics of crystals at extremely high pressures and temperatures', Bad Salzschlirf, Germany: "High P,T nuclear resonance studies of lower mantle phases: New insights into lower mantle properties and processes"

MCCAMMON, C.; POTAPKIN, V.; GLAZYRIN, K.; KANTOR, A.; KUPENKO, I.; PRESCHER, C.; SINMYO, R.; PESCE, G.; SMIRNOV, G.; CHUMAKOV, A.; RÜFFER, R.; DUBROVINSKY, L.: 03.-07.12.2012, AGU Fall Meeting, San Francisco, USA[*2]: "Spin transitions in $(Mg,Fe)(Si,Al)O_3$ perovskite and the electrical conductivity of the lower mantle"

MIYAJIMA, N.; SHEKHAR, S.; FROST, D.J.; LANGENHORST, F.; HEIDELBACH, F.: 04.-07.03.2012, EMPG XIV, Kiel, Germany[*1]: "Suzuki segregation on (001) stacking faults in an experimentally deformed olivine"

MIYAJIMA, N.; IRIFUNE, T.: 24.-29.06.2012, Goldschmidt 2012, Montréal, Canada: "Dislocation microstructures of ferropericlase at high pressures"

MIYAJIMA, N.: 09.-13.07.2012, Joint 2012 COMPRES Annual Meeting and High-Pressure Mineral Physics Seminar-8, Lake Tahoe, USA: "Dislocation textures and aluminum diffusion in majoritic garnet. ATEM study"

MIYAJIMA, N.; KATSURA, T.: 02.-06.09.2012, European Mineralogical Conference, Frankfurt/M., Germany: "Transmission electron microscopy of large $MgSiO_3$ perovskite single crystals", Abstract EMC2012-699, 2012

MIYAJIMA, N.: 19.-23.11.2012, MinTEM 2012, Graduate and PhD Course, Villeneuve-d'Ascq, France: Lecture and practical on "EELS for Mineralogy"

MORBIDELLI, A.; RUBIE, D.C.: 24.-29.06.2012, Goldschmidt 2012, Montréal, Canada: "Dynamical and chemical modeling of terrestrial planet accretion"

MROSKO, M.; KOCH-MÜLLER, M.; MCCAMMON, C.A.; RHEDE, D.; WIRTH, R.: 04.-07.03.2012, EMPG XIV, Kiel, Germany[*1]: "Water, iron, redox environment: Effects on the wadsleyite-ringwoodite phase transition"

NAKAJIMA, Y.; FROST, D.J.; RUBIE, D.C.: 09.-13.07.2012, Joint 2012 COMPRES Annual Meeting and High-Pressure Mineral Physics Seminar-8, Lake Tahoe, USA: "Ferrous iron partitioning between magnesium silicate perovskite and ferropericlase"

NI, H.; KEPPLER H.: 04.-07.03.2012, EMPG XIV, Kiel, Germany[*1]: "A new method for measuring electrical conductivity of fluids under pressure", Abstract Volume, 13

NI, H.: 06.06.2012, University of Science and Technology of China, School of Earth and Space Sciences, Hefei, China: "Electrical conductivity of silicate melts and hydrothermal fluids: measurements and application"

OUSSADOU, M.; MOOKHERJEE, M.; STEINLE-NEUMANN, G.: 04.-07.03.2012, EMPG XIV, Kiel, Germany[*1]: "Structural properties of FeO-, Fe_2O_3- and Al_2O_3-bearing $MgSiO_3$ post perovskite from ab-initio calculations"

OVSYANNIKOV, S.V.; ABAKUMOV, A.M.; TSIRLIN, A.A.; EGOAVIL, R.; VERBEECK, J.; VAN TENDELOO, G.; GLAZYRIN, K.; HANFLAND, M.; DUBROVINSKY, L.: 25.-27.07.2012, XV-th 'High Pressure in Semiconductor Physics': HPSP-15, Montpellier, France: "New high-pressure high-temperature polymorphs in simple sesquioxides", p. 34

OVSYANNIKOV, S.V.; ABAKUMOV, A.M.; TSIRLIN, A.A.; EGOAVIL, R.; VERBEECK, J.; VAN TENDELOO, G.; GLAZYRIN, K.; HANFLAND, M.; DUBROVINSKY, L.: 16.-21.09.2012, 50^{th} EHPRG Meeting, Thessaloniki, Greece: "Unusual perovskite structures in binary sesquioxides", p. 57

OVSYANNIKOV, S.V.; ABAKUMOV, A.M.; TSIRLIN, A.A.; EGOAVIL, R.; VERBEECK, J.; VAN TENDELOO, G.; GLAZYRIN, K.; HANFLAND, M.; DUBROVINSKY, L.: 08.-10.10.2012, High-Pressure Symposium, Freiberg, Germany: "Unusual perovskite structures in binary sesquioxides"

POTAPKIN, V.; CHUMAKOV, A.I.; SMIRNOV, G.V.; CELSE, J.-P.; RÜFFER, R.; MCCAMMON, C.; DUBROVINSKY, L.: 11.-15.06.2012, 'Mössbauer Spectroscopy in Materials Science', Olomouc, Czech Republic: "The ^{57}Fe Synchrotron Mössbauer source at the ESRF"

POTAPKIN, V.; DUBROVINSKY, L.S.; MCCAMMON, C.A.; KANTOR, A.; KUPENKO, I.; GLAZYRIN, K.; CHUMAKOV, A.; RÜFFER, R.; KANTOR, I.; PRESCHER, C.; SMIRNOV, G.V.: 16.-21.09.2012, 50th EHPRG Meeting, Thessaloniki, Greece: "No spin transition of ferric iron in the lower mantle"

PRESCHER, C.; DUBROVINSKY, L.; MCCAMMON, C.; BOFFA-BALLARAN, T.; GLAZYRIN, K.; NAKAJIMA, Y.; KANTOR, A.; HANFLAND, M.: 04.-07.03.2012, EMPG XIV, Kiel, Germany[*1]: "Structurally hidden magnetic transitions in Fe_3C at high pressures"

RUBIE, D.C.; FROST, D.J.; VOGEL, A.; O'BRIEN D.P.; MORBIDELLI, A.; NIMMO, F.; PALME, H.: 04.-07.03.2012, EMPG XIV, Kiel, Germany[*1]: "Core formation in the terrestrial planets: Constraints from metal-silicate partitioning of siderophile elements"

RUBIE, D.C.: 31.07.2012, University of California, Santa Cruz, USA: "Core formation in terrestrial planets"

RUBIE, D.C.: 01.07.-10.08.2012, CIDER 2012 Summer Program 'Deep Time: How did early Earth become our modern world?', KITP, Santa Barbara, USA: "Experimental studies related to the early differentiation of the Earth"

RUBIE, D.C.: 01.07.-10.08.2012, CIDER 2012 Summer Program 'Deep Time: How did early Earth become our modern world?', KITP, Santa Barbara, USA: "Models of core formation in terrestrial planets"

RUBIE, D.C.: 25.10.2012, ETH Zürich, Switzerland: "Accretion and early differentiation of the terrestrial planets"

RUBIE, D.C.; NIMMO, F.; MORBIDELLI, A.; FROST, D.J.: 03.-07.12.2012, AGU Fall Meeting, San Francisco, USA[*2]: "Extent of metal-silicate disequilibrium during accretion and early differentiation of the Earth", Abstract V53G-03, 2012

RUBIE, D.C.; NAKAJIMA, Y.; WESTON, L.A.; VOGEL, A.; FROST, D.J.: 03.-07.12.2012, AGU Fall Meeting, San Francisco, USA[*2]: "Effects of light elements, Si, O and S, on siderophile element partitioning between liquid Fe alloy and silicate liquid at high pressure", Abstract V31E-06, 2012

RUBIE, D.C.: 08.12.2012, Post-AGU 2012 CIDER Workshop, Berkeley, USA: "Evolution of the light element content of the Earth's core and implications for reactions at the CMB"

SAMUEL, H.: 25.01.2012, Universität Münster, Germany (*invited*): "Core formation and its consequences on the early thermo-chemical state of terrestrial planets"

SAMUEL, H.: 17.02.2012, Deutsches Zentrum für Luft- und Raumfahrt (DLR), Berlin, Germany (*invited*): "Core formation in solid proto-mantles and in terrestrial magma oceans"

SAMUEL, H.; TOSI, N.: 22.-27.04.2012, European Geophysical Union General Assembly, Vienna, Austria: "The influence of post-perovskite rheology on mantle convective stirring efficiency"

SAMUEL, H.: 22.-27.04.2012, European Geophysical Union General Assembly, Vienna, Austria: "Time-domain parallelization for geodynamic modeling"

SAMUEL, H.: 25.10.2012, Institut des Sciences de la Terre, Grenoble, France (*invited*): "The breakup and chemical equilibration of metal diapirs in terrestrial magma oceans"

SAMUEL, H.: 12.-14.11.2012, International Workshop on Deep Earth Mantle, Paris, France: "The split-WEM method"

SAMUEL, H.: 03.-07.12.2012, AGU Fall Meeting, San Francisco, USA[*2]: "Modeling advection in geophysical flows with wave equation models", Abstract DI13C-2433, 2012

SAMUEL, H.; EVONUK, M.: 03.-07.12.2012, AGU Fall Meeting, San Francisco, USA[*2]: "Simulating rotating fluid bodies: When is vorticity generation via density-stratification important?", Abstract GP21A-1153, 2012

SHATSKIY, A.; LITASOV, K.D.; KATSURA, T.; BORZDOV, Y.M.; YAMAZAKI, D.; OHTANI, E.: 18.-21.03.2012, Joint Symposium of Misasa-2012 and Geofluid-2 'Dynamics and Evolution of the Earth's Interior: special emphasis on the role of fluids', Misasa, Tottori, Japan: "Silicate diffusion in alkali-carbonatite and hydrous melt at 16.5 and 24 GPa, with implications for mass transfer in the deep mantle"

SHCHEKA, S.; KEPPLER, H.: 02.-06.09.2012, European Mineralogical Conference, Frankfurt/M., Germany: "Noble gas solubility in $MgSiO_3$ perovskite and the terrestrial noble gas signature"

SHCHEKA, S.; KEPPLER, H.: 25.-28.09.2012, 5th Berichtskolloquium of the SPP1236 'Structures and characteristics of crystals at extremely high pressures and temperatures', Bad Salzschlirf, Germany: "$MgSiO_3$-perovskite and the terrestrial noble gas signature"

SHCHENNIKOV, V.V.; MOROZOVA, N.V.; OVSYANNIKOV, S.V.; TYAGUR, I.; TYAGUR, Y.: 25.-27.07.2012, XV-th 'High Pressure in Semiconductor Physics': HPSP-15, Montpellier, France: "Semiconductor-metal transition at ferroelectric $Sn_2P_2S_6$ at high pressure", p. 78

SHCHENNIKOV, V.V.; MOROZOVA, N.V.; OVSYANNIKOV, S.V.; TYAGUR, I.; TYAGUR, Y.: 16.-21.09.2012, 50th EHPRG Meeting, Thessaloniki, Greece: "Thermoelectric properties of ferroelectric $Sn_2P_2S_6$ at high pressure", p. 158

SHCHENNIKOV, V.V.; MOROZOVA, N.V.; OVSYANNIKOV, S.V.: 16.-21.09.2012, 50th EHPRG Meeting, Thessaloniki, Greece: "Thermoelectric properties of rare-earth elements at high pressures", p. 157

SHUSHAKOVA, V.; FULLER, E.R.; HEIDELBACH, F. SIEGESMUND, S.: 22.-27.04.2012, European Geophysical Union General Assembly, Vienna, Austria: "Marble decay due to microcracking"

SHUSHAKOVA, V.; FULLER, E.R.; HEIDELBACH, F. SIEGESMUND, S.: 22.-26.10.2012, 12th International Congress on Deterioration and Conservation of Stone, New York: "Fabric influences on microcrack degradation of marbles"

SINMYO, R.; DUBROVINSKY, L.; MCCAMMON, C.; BYKOVA, E.; GLAZYRIN, K.; KUPENKO, I.; POTAPKIN, V.; CHUMAKOV, A.; SMIRNOV, G.; RÜFFER, R.: 09.-13.07.2012, Joint 2012 COMPRES Annual Meeting and High-Pressure Mineral Physics Seminar-8, Lake Tahoe, USA: "Cation distribution in Fe^{3+} bearing $(Mg,Fe)SiO_3$ perovskite determined using single-crystal X-ray refinements and the synchrotron Mössbauer spectroscopy"

SOUSTELLE, V.; MANTHILAKE, G.; WALTE, N.; MIYAJIMA, N.; FROST, D.; HEIDELBACH, F.: 02.-06.09.2012, European Mineralogical Conference, Frankfurt/M., Germany (*keynote*): "Interaction between deformation and reactive melt percolation in the upper mantle: Deformation-Dia and 6-ram multi-anvil experiments at high pressure and temperature", Abstract EMC2012-738, 2012

SPECKBACHER, R.; STIPP, M.; HEIDELBACH, F.; BEHRMANN, J.H.: 28.-30.03.2012, TSK 14, Kiel, Germany: "Deformation fabrics of quartz- and calcite-rich mylonites from the Moresby Seamount detachment, Woodlark Basin (offshore Papua New Guinea)"

STAGNO, V.; FEI, Y.; MCCAMMON, C.A.; FROST, D.J.: 02.-06.09.2012, European Mineralogical Conference, Frankfurt/M., Germany: "Redox equilibria within eclogite assemblages as function of pressure and temperature: implications for the deep carbon cycle", Abstract EMC2012-670, 2012

STEINLE-NEUMANN, G.; DE KOKER, N.; VLČEK, V.: 04.-07.03.2012, EMPG XIV, Kiel, Germany[*1]: "Electrical and thermal conducticity of metallic liquids at high pressure"

STEINLE-NEUMANN, G.: 17.-19.04.2012, Workshop on Magnetic Mineral Identification, Paleomagnetic Laboratory, Niederlippach, Germany: "The death of magnetism with pressure from a theoretical perspective"

STEINLE-NEUMANN, G.; VLČEK, V.; DE KOKER, N.: 23.-26.09.2012, 3rd Colloquium of the SPP 1488 'Planetary Magnetism', Rostock, Germany: "Electrical and thermal conductivity of Fe-alloys at high pressure and temperature from ab-inito computations"

STEINLE-NEUMANN, G.: 13.12.2012, Ghent University, Centre for Molecular Modeling, Ghent, Belgium (*invited*): "Electrical and thermal conducticity of metallic liquids at high pressure from ab-initio computations"

STEINLE-NEUMANN, G.: 14.12.2012, Royal Observatory of Belgium, Brussels, Belgium (*invited*): "Electrical and thermal conducticity of liquid iron and iron alloys at high pressure: Implications for planetary evolution"

TROTS, D.M.; KURNOSOV, A.; TKACHEV S.; ZHURAVLEV K.; PRAKAPENKA, V.; BOFFA BALLARAN, T.; FROST D.J.: 04.-07.03.2012, EMPG XIV, Kiel, Germany[*1]: "Calibration of Sm-doped $Y_3Al_5O_{12}$ pressure sensor with an independent absolute pressure scale"

TROTS, D.M.; KURNOSOV, A.; TKACHEV S.; ZHURAVLEV K.; PRAKAPENKA, V.; BOFFA BALLARAN, T.; FROST D.J.: 12.-15.03.2012, 20th Annual Meeting of the German Crystallographic Society (DGK), Munich, Germany: "Elasticity of Sm-doped $Y_3Al_5O_{12}$ with an independent absolute pressure scale and its calibration as a primary pressure standard"

VLČEK, V.; DE KOKER, N.; STEINLE-NEUMANN, G.: 02.-05.10.2012, 17th ETSF Workshop on Electronic Excitations, Coimbra, Portugal: "Electrical and thermal conductivity of liquid Al at high pressures and temperatures from ab-initio computations: lesson for geophysics"

VLČEK, V.; DE KOKER, N.; STEINLE-NEUMANN, G.: 06.-09.11.2012, CECAM Workshop on 'Vibrational coupling: most important, often ignored, and a challenge for ab-initio theory', Lausanne, Switzerland "Electrical and thermal conductivity of liquid Al at high pressures and temperatures from ab-initio computations: lesson for geophysics"

VOGEL, A.K.; RUBIE, D.C.; FROST, D.J.; PALME, H.: 04.-07.03.2012, EMPG XIV, Kiel, Germany[*1]: "The partitioning of volatile elements between metal and silicate at high pressures and temperaturs"

VOGEL, A.K.; RUBIE, D.C.; FROST, D.J.; AUDÉTAT, A.; PALME, H.: 09.-12.10.2012, Joint meeting 'Paneth Kolloquium', 'The first 10 million years of the solar system' (DFG SPP 1385) & 'MEMIN', Nördlingen, Germany: "New Metal / Silicate Partitioning Data for the Siderophile Elements Ag, Pb, Sn, Au and Cu in S-free and S-bearing compositions"

WALTE, N.; KEPPLER, H.; FROST, D.: 04.-07.03.2012, EMPG XIV, Kiel, Germany[*1]: "The new multianvil facility for neutron diffraction and radiography at FRM II"

ZHANG, B.H.; YOSHINO, T.; KATSURA, T.; WU, X. P.: 18.-21.03.2012, Joint Symposium of Misasa-2012 and Geofluid-2 'Dynamics and Evolution of the Earth's Interior: special emphasis on the role of fluids', Misasa, Tottori, Japan: "Electrical conductivity of hydrous orthopyroxene: Implications for the electrical structure in the upper mantle"

ZUCCHINI, A.; COMODI, P.; PRENCIPE, M.; FRONDINI, F.; MCCAMMON, C.; KATERINOPOULOU, A.; ZUNIC, T.B.: 17.-20.06.2012, European Microbeam Analysis Society, Padua, Italy: "Cation distribution in dolomite structure: theory and experiments"

[*1] **14 International Conference on Experimental Mineralogy Petrology Geochemistry, 04.-07.03.2012, Kiel, Germany**

[*2] **AGU: American Geophysical Union Fall Meeting, 03.-07.12.2012, San Francisco, USA**

6.4 Lectures and seminars at Bayerisches Geoinstitut

ANGEL, R., Università degli Studi di Padova, Dipartimento di Geoscienze, Padova, Italy: "Elasticity of materials I", 19.03.2012

ANGEL, R., Università degli Studi di Padova, Dipartimento di Geoscienze, Padova, Italy: "Elasticity of materials II", 20.03.2012

BERCOVICI, D., Yale University, Department of Geology & Geophysics, New Haven, USA: "Generation of plate tectonics on Earth and other planets via grain-damage and pinning", 01.10.2012

BERCOVICI, D., Yale University, Department of Geology & Geophysics, New Haven, USA: "Volcanological physics", 02.10.2012

BOSSAK, A., European Synchrotron Radiation Facility, Grenoble, France: "Diffraction studies of ice from Lake Vostok (Antarctica)", 22.10.2012

CAMPBELL, A., University of Chicago, Department of Geophysicsl Sciences, Chicago, USA: "Composition of Earth's core", 31.05.2012

CAMPBELL, A., University of Chicago, Department of Geophysicsl Sciences, Chicago, USA: "Advances in experimental high pressure, high temperature research", 01.06.2012

CERANTOLA, V., Bayerisches Geoinstitut, Bayreuth, Germany: "Deformation of a crystalline system with two immiscible liquids: Implications for early core-mantle differentiation", 02.08.2012

DALOU, C., Carnegie Institution of Washington, Geophysical Laboratory, Washington DC, USA: "The behavior of F and Cl in the upper mantle: fractionation, solubility and solution mechanisms", 20.12.2012

DE KOKER, N., Bayerisches Geoinstitut, Bayreuth, Germany: "Thermal conductivity of Earth's liquid outer core from first-principles calculations", 26.01.2012

DE VRIES, J., Utrecht University, Faculty of Geosciences, Utrecht, The Netherlands: "Combining high pressure, high temperature experiments and convection models in a study of lunar evolution", 09.05.2012

DORFMAN, S., École Polytechnique Fédéral de Lausanne, Physics Department, Earth and Planetary Science Laboratory, Lausanne, Switzerland: "Iron-rich perovskite and post-perovskite in the deep lower mantle", 09.02.2012

FARLA, R., Yale University, Department of Geology & Geophysics, New Haven, USA: "Weakening in the ductile lithosphere caused by dynamic recrystallization and the strength of wadsleyite in the transition zone", 02.10.2012

GLAßMEIER, K.-H., Technische Universität Braunschweig, Institut für Geophysik und extraterrestrische Physik, Braunschweig, Germany: "The elusive magnetic field of planet Mercury", 03.05.2012

HARRIES, D., Bayerisches Geoinstitut, Bayreuth, Germany: "Nanomineralogical processes in materials of the early solar system", 23.02.2012

HUANG, R., Bayerisches Geoinstitut, Bayreuth, Germany: "Sulfur partitioning between silicate melts and aqueous fluid", 16.08.2012

IIZUKA, R., University of Tokyo, Graduate School of Science, Geochemical Laboratory (Laboratory for Earthquake Chemistry), Tokyo, Japan: "Pressure-induced phase transition in $Ca(OH)_2$ and technical development of high pressure neutron experiments", 12.07.2012

KAWAZOE, T., Ehime University, Geodynamics Research Center, Matsuyama, Japan: "Experimental rheology of the mantle transition zone", 02.10.2012

KEMPL, J., VU University Amsterdam, Department of Petrology (FALW), Amsterdam, The Netherlands: "Planetary core formation: constraints from experimentally determined Si isotope analyses on a MC-ICPMS", 23.10.2012

KUPENKO, I., Bayerisches Geoinstitut, Bayreuth, Germany: "Portable double-sided laser-heating system for diamond anvil cells", 24.05.2012

LAURENZ, V., Universität Bonn, Steinmann-Institut für Geologie, Mineralogie und Paläontologie, Bonn, Germany: "The effect of Fe and S on HSE solubility in silicate melts", 10.05.2012

LERCHBAUMER, L., Bayerisches Geoinstitut, Bayreuth, Germany: "The metal content of melts and fluids in Mo-mineralized granites", 19.06.2012

MASOTTA, M., Università degli Studi di Roma "La Sapienza", Roma, Italy: "Magma differentiation in shallow, thermally zoned magma chambers: the example of Sabatini of Volcanic District", 05.06.2012

MERKEL, S., Université Lille 1, UMET - Unité Matériaux et Transformation, CNRS, Villeneuve d'Ascq, France: "High pressure studies of texture and rheology of deep Earth minerals", 07.05.2012

MERKEL, S., Université Lille 1, UMET - Unité Matériaux et Transformation, CNRS, Villeneuve d'Ascq, France: "In situ 3D X-ray diffraction at high pressure: tracking grains and microstructures inside the diamond anvil cell", 08.05.2012

MERLINI, M., Università degli Studi di Milano, Dipartimento di Scienze della Terra, Milano, Italy: "New structures of carbonates at the Earth's mantle conditions determined by single crystal diffraction and their relevance for deep carbon cycle", 11.10.2012

MEZGER, K., Universität Bern, Institut für Geologie, Bern, Switzerland: "Evolution of the early solar system", 05.07.2012

MEZGER, K., Universität Bern, Institut für Geologie, Bern, Switzerland: "Early Earth and Moon", 06.07.2012

MIYAHARA, M., Tohoku University, Institute of Mineralogy, Petrology and Economic Geology, Sendai, Japan: "Nature and origin of diamond in Asteroid Almahatta Sitta Ureilite Ms-170", 16.10.2012

MIZUKAMI, T., Kanazawa University, Department of Earth Science, Graduate School of Environmental Studies, Kanazawa, Japan: "Field observations on hydration and deformation of the shallowest part of mantle wedge: an example from SW Japan", 13.12.2012

MOJZSIS, S., Université Lyon 1 - Claude Bernard & École Normale Supérieure, Villeurbanne, France: "The primordial crust on Earth and its transformation", 21.05.2012

MOJZSIS, S., Université Lyon 1 - Claude Bernard & École Normale Supérieure, Villeurbanne, France: "Reduced, reused and recycled: Detrital zircons in the ca. 3750-3780 Ma Nuvvuagittuq supracrustal belt (Québec, Canada)", 22.05.2012

NAKAMURA, T., Tohoku University, Department of Earth & Planetary Materials, Sendai, Japan: "How asteroids formed in the early solar system? - message from the Hayabusa spacecraft -", 14.06.2012

O'NEILL, H., The Australian National University, Research School of Earth Sciences, Canberra, Australia: "The global pattern of trace-element distributions in Ocean Floor Basalts", 13.08.2012

OVSYANNIKOV, S., Bayerisches Geoinstitut, Bayreuth, Germany: "Complex perovskite structure in simple oxide", 13.09.2012

PALME, H., Forschungsinstitut und Naturmuseum Senckenberg, Frankfurt/M., Germany: "Meteorites, the oldest rocks of the solar system", 19.01.2012

PALME, H., Forschungsinstitut und Naturmuseum Senckenberg, Frankfurt/M., Germany: "The age of the Earth", 20.01.2012

PARAKHONSKIY, G., Universität Bayreuth, Lehrstuhl für Kristallographie, Bayreuth, Germany: "Synthesis and investigation of boron phases at high pressures and temperatures", 15.11.2012

PESCE, G., Bayerisches Geoinstitut, Bayreuth, Germany: "Electrical conductivity measurements of $(Mg,Fe)(Al,Si)O_3$ perovskite in laser-heated DAC at lower mantle conditions", 26.07.2012

PETITGIRARD, S., European Synchrotron Radiation Facility, Grenoble, France: "Partitioning of Pd and Ru between silicate and iron-rich melts at high pressure and temperature", 04.06.2012

POSNER, E., University of Arizona, Department of Geosciences, Tucson, USA: "Planetary applications of cation diffusion in mantle minerals: Cr in spinel and W in diopside", 09.03.2012

PRESCHER, C., Bayerisches Geoinstitut, Bayreuth, Germany: "The effect of Fe spin crossovers on its partitioning behavior and oxidation state in a pyrolitic Earth's lower mantle", 08.11.2012

RICHET, P., Institut de Physique du Globe de Paris, France: "Thermal properties of crystalline and liquid silicates", 29.11.2012

RICHET, P., Institut de Physique du Globe de Paris, France: "Vibrational vs. configurational properties of silicate melts: interplays and subtle distinctions", 30.11.2012

ROSENTHAL, A., Bayerisches Geoinstitut, Bayreuth, Germany: "Creation and modification of upper mantle heterogeneities and the consequences for magmatism", 22.11.2012

SHABESTARI, A., Bayerisches Geoinstitut, Bayreuth, Germany: "Electrical resistivity and thermal conductivity of liquid Fe-C alloy at high P and T", 23.08.2012

SINMYO, R., Bayerisches Geoinstitut, Bayreuth, Germany: "Nuclear resonance inelastic X-ray scattering (NRIXS) measurements of lower mantle minerals", 26.04.2012

SORBADERE, F., Université Blaise Pascal, Observatoire de Physique du Globe de Clermond-Ferrand, Aubière, France: "Heterogeneous sources involved in the genesis of nepheline-normative primitive magmas in island arcs: Evidence from primary melt inclusions and high-pressure experiments", 06.06.2012

SOUSTELLE, V., Bayerisches Geoinstitut, Bayreuth, Germany: "Interaction between deformation and reactive melt percolation in the upper mantle: experiment at high T & P", 30.08.2012

SPIEKERMANN, G., GeoForschungsZentrum Potsdam, Germany: "Vibrational properties of silica species in SiO_2-H_2O liquids and glasses from ab initio molecular dynamics", 21.06.2012

STEINLE-NEUMANN, G., Bayerisches Geoinstitut, Bayreuth, Germany: "Cores of terrestrial planets", 12.01.2012

WALTE, N., Bayerisches Geoinstitut, Bayreuth, Germany: "Deformation under transition zone conditions with the big press", 02.02.2012

WU, Y., China University of Geosiences, Wuhan, China: "The fate of subducted continental crust from experimental perspective", 08.02.2012

XIONG, X., Guangzhou Institute of Geochemistry, Guangzhou, China: "The role of rutile in fractionation of Nb/Ta during partial melting", 28.06.2012

YANG, X., Bayerisches Geoinstitut, Bayreuth, Germany: "H in feldspars and implications for crustal processes", 09.08.2012

YANG, Y., University of Science & Technology, Department of Earth & Space Science, Hefei, China: "In situ FTIR investigation of NAMs at varying temperatures", 27.02.2012

YOUNG, E., University of California, Earth & Space Sciences, Los Angeles, USA: "Stable isotopes as tracers of planetary differentiation", 24.09.2012

YOUNG, E., University of California, Earth & Space Sciences, Los Angeles, USA: "The provenance of meteorite parent bodies and the history of the asteroid belt", 25.09.2012

6.5 Conference organization

04.-07.03.2012, EMPG XIV, Kiel, Germany: Session S06 "Deformation processes, transport properties, reaction mechanisms and kinetics: combining experimental (HP/HT) and numerical aspects" (B. JOACHIM; R. MILKE; P. CORDIER; F. HEIDELBACH)

04.-07.03.2012, EMPG XIV, Kiel, Germany: Session S11 "Computational Mineralogy and Geochemistry" (G. STEINLE-NEUMANN)

04.-07.03.2012, EMPG XIV, Kiel, Germany: Session S12 "Frontiers and new developments in experimental methods and high pressure technologies" (D.J. FROST)

09.-13.07.2012, Joint 2012 COMPRES Annual Meeting and High-Pressure Mineral Physics Seminar-8, Lake Tahoe, USA (T. KATSURA, co-convener)

02.-06.09.2012, European Mineralogical Conference 2012, Frankfurt/M., Germany: Session "Earth's Deep Volatile Cycle" (H. KEPPLER; S. DEMOUCHY; G. BROMILEY)

02.-06.09.2012, European Mineralogical Conference 2012, Frankfurt/M., Germany: Session 5c "Advances in Spectroscopy of Earth Materials" (C. MCCAMMON; R. STALDER; M. WILKE)

03.-07.12.2012, American Geophysical Union Fall Meeting, San Francisco, USA: Session T12D "Melt Extraction through the Lithosphere: Interactions among Melt Evolution, Deformation, and Migration" (S. MISRA; L. MONTESI; V. SOUSTELLE; R. WEINBERG)

03.-07.12.2012, American Geophysical Union Fall Meeting, San Francisco, USA: Session P002 "Accretion, Core-Mantle Differentiation and Early Planetary Evolution" (H. SAMUEL; G. GOLABEK)

7. Visiting scientists

7.1 Visiting scientists funded by the Bayerisches Geoinstitut

AUSUBEL, J., The Rockefeller University, Program for the Human Environment, New York, USA: 07.-08.11.2012

BALI, E., Universität Göttingen, Experimentelle und Angewandte Mineralogie, Göttingen, Germany: 03.-06.06.2012

CIAZELA, J., Adam-Michiewicz-University, Poznan, Poland: 25.-26.06.2012

DE VRIES, J., Utrecht University, Faculty of Geosciences, Utrecht, The Netherlands: 07.-11.05.2012

DOLEJŠ, D., Charles University, Institute of Petrology and Structural Geology, Prague, Czech Republic: 13.-17.02.2012

DORFMAN, S., École Polytechnique Fédéral de Lausanne, Physics Department, Earth and Planetary Science Laboratory, Lausanne, Switzerland: 08.-11.02.2012

FARLA, R., Yale University, Department of Geology & Geophysics, New Haven, USA: 30.09.-05.10.2012

GLAßMEIER, K.-H., Technische Universität Braunschweig, Institut für Geophysik und extraterrestrische Physik, Braunschweig, Germany: 03.-04.05.2012

JIN, Z., China University of Geosiences, Wuhan, China: 08.-09.02.2012

KEMPL, J., VU University Amsterdam, Department of Petrology (FALW), Amsterdam, The Netherlands: 21.-25.10.2012

KAWAZOE, T., Ehime University, Geodynamics Research Center, Matsuyama, Japan: 30.09.-05.10.2012

MASOTTA, M., Università degli Studi di Roma "La Sapienza", Roma, Italy: 03.-06.06.2012

MIYAHARA, M., Tohoku University, Institute of Mineralogy, Petrology and Economic Geology, Sendai, Japan: 13.-18.10.2012

MOOKHERJEE, M., Cornell University, Earth and Atmospheric Sciences, Ithaca, USA: 02.08.-29.09.2012

NAKAMURA, T., Tohoku University, Department of Earth & Planetary Materials, Sendai, Japan: 14.-15.06.2012

O'NEILL, H., The Australian National University, Research School of Earth Sciences, Canberra, Australia: 12.-14.08.2012

POSNER, E., University of Arizona, Department of Geosciences, Tucson, USA: 08.-12.03.2012

SORBADERE, F., Université Blaise Pascal, Observatoire de Physique du Globe de Clermond-Ferrand, Aubière, France: 04.-06.06.2012

SPIEKERMANN, G., GeoForschungsZentrum Potsdam, Germany: 19.-22.06.2012

WANG, L., China University of Geosiences, Wuhan, China: 08.-09.02.2012

WU, Y., China University of Geosiences, Wuhan, China: 08.-09.02.2012

YANG, Y., University of Science & Technology, Department of Earth & Space Science, Hefei, China: 25.02.-02.03.2012

7.2 Visiting scientists supported by other externally funded BGI projects

ANGEL, R., Università degli Studi di Padova, Dipartimento di Geoscienze, Padova, Italy: 16.-22.03.2012 (ENB [*A])

BERCOVICI, D., Yale University, Department of Geology & Geophysics, New Haven, USA: 30.09.-03.10.2012 (ENB [*A])

BOSSAK, A., European Synchrotron Radiation Facility, Grenoble, France: 21.-23.10.2012 (DFG [*B])

CAMPBELL, A., University of Chicago, Department of Geophysicsl Sciences, Chicago, USA: 29.05.-03.06.2012 (ENB [*A])

FISCHER, R., University of Chicago, Department of Geophysicsl Sciences, Chicago, USA: 29.05.-09.06.2012 (ERC [*C])

LAURENZ, V., Universität Bonn, Steinmann-Institut für Geologie, Mineralogie und Paläontologie, Bonn, Germany: 08.-11.05.2012 (ERC [*C])

MERKEL, S., Université Lille 1, UMET - Unité Matériaux et Transformation, CNRS, Villeneuve d'Ascq, France: 06.-09.05.2012 (ENB [*A])

MERLINI, M., Università degli Studi di Milano, Dipartimento di Scienze della Terra, Milano, Italy: 10.-12.10.2012 (DFG [*B])

MEZGER, K., Universität Bern, Institut für Geologie, Bern, Switzerland: 04.-06.07.2012 (ENB [*A])

MOJZSIS, S., Université Lyon 1 - Claude Bernard & École Normale Supérieure, Villeurbanne, France: 20.-24.05.2012 (ENB [*A])

PALME, H., Forschungsinstitut und Naturmuseum Senckenberg, Frankfurt/M., Germany: 19.-20.01.2012 (ENB [*A])

PETITGIRARD, S., European Synchrotron Radiation Facility, Grenoble, France: 03.-05.06.2012 (ERC [*C])

POTAPKIN, V., European Synchrotron Radiation Facility, Grenoble, France: 21.-26.10.2012 (DFG [*B])

RICHET, P., Institut de Physique du Globe de Paris, France: 28.-30.11.2012 (ENB [*A])

SPIVAK, A., Institute of Experimental Mineralogy, Chernogolovka, Moscow region, Russia: 20.06.-30.07.2012, 04.09.-28.11.2012 (DFG [*B])

YOUNG, E., University of California, Earth & Space Sciences, Los Angeles, USA: 23.-26.09.2012 (ENB [*A])

[*A)] ENB: International Graduate School under the Elitenetzwerk Bayern

[*B)] DFG: Deutsche Forschungsgemeinschaft

[*C)] ERC: European Research Council

7.3 Visitors (externally funded)

AKSENOV, S., Russian Academy of Sciences, Crystallography Institution, Moscow, Russia: 23.10.-30.11.2012

BOBROV, A., Moscow State University, Petrological Department, Moscow, Russia: 04.06.-25.07.2012, 10.-21.11.2012

BUREAU, H., Institut de Minéralogie et de Physique des Milieux Condensés, Paris, France: 20.-26.05.2012

CARACAS, R., Laboratoire de Sciences de la Terre, CNRS UMR5570, Ecole Normale Supérieure de Lyon, France: 20.02.-03.03.2012

CHANTEL, J., European Synchrotron Radiation Facility, Grenoble, France: 23.01.-16.02.2012, 13.-21.06.2012, 03.-11.10.2012

CHEMIA, Z., Geological Survey of Norway, Trondheim, Norway: 12.-17.08.2012

DALOU, C., Carnegie Institution of Washington, Geophysical Laboratory, Washington DC, USA: 20.-21.12.2012

DOBSON, D., University College London, Department of Earth Sciences, London, U.K.: 14.-17.05.2012, 06.-16.08.2012

DOLEJŠ, D., Charles University, Institute of Petrology and Structural Geology, Prague, Czech Republic: 06.-17.08.2012, 23.-24.11.2012

DZIVENKO, D., TU Darmstadt, Material- und Geowissenschaften, Darmstadt, Germany: 09.-11.10.2012

GARBEV, K., Karlsruher Institut für Technologie, Institut für Technische Chemie, Karlsruhe, Germany: 03.-05.12.2012

GASHAROVA, B., Karlsruher Institut für Technologie, Institut für Photonenforschung und Synchrotronstrahlung, Karlsruhe, Germany: 03.-05.12.2012

GOTOU, H., University of Tokyo, Institute for Solid State Physics, Chiba, Japan: 28.-29.09.2012

GREENBERG, E., Tel Aviv University, Israel: 24.09.-23.10.2012

HOPP, J., Universität Heidelberg, Institut für Geowissenschaften, Heidelberg, Germany: 28.-29.11.2012

HUMPHREYS, M., University of Oxford, Department of Earth Sciences, Oxford, U.K.: 10.-16.09.2012

IRIFUNE, T., Ehime University, Geodynamics Research Center, Matsuyama, Japan: 12.-15.09.2012

ISMAILOVA, L., Moscow State University, Petrological Department, Moscow, Russia: 10.10.-10.11.2012

JACOBSEN, S., Northwestern University, Department of Earth and Planetary Sciences, Evanston, USA: 29.03.-10.04.2012

KEMPL, J., VU University Amsterdam, Department of Petrology (FALW), Amsterdam, The Netherlands: 08.-21.01.2012, 16.-27.04.2012

KESHAV, S., Université Montpellier 2, Géosciences, Montpellier, France: 15.11.-31.12.2012

KING, S., Virginia Polytechnic Institute and State University, Department of Geosciences, Blacksburgh, USA: 16.-20.04.2012

KOZLENKO, D., Frank Laboratory of Neutron Physics, Joint Institute for Nuclear Research, Dubna, Russia: 21.02.-06.03.2012

LAUMONIER, M., UMR 7327 – CNRS/Université d'OrléansInstitut des Sciences de la Terre d'Orléans, France: 08.-09.03.2012

LEONTYEV, I., Rostov State University, Physics Department, Rostov, Russia: 20.09.-06.12.2012

LITVIN, Y., Institute of Experimental Mineralogy, Chernogolovka, Moscow region, Russia: 25.-31.08.2012

LIU, X., Chinese Academy of Sciences, Guangzhou Institute of Geochemistry, Guangzhou, China: 10.04.-10.10.2012

LUKIN, E., Frank Laboratory of Neutron Physics, Joint Institute for Nuclear Research, Dubna, Russia: 08.-11.07.2012

MCSCORLEY, A., Cornell University, Department of Chemistry and Chemical Biology, Ithaca, USA: 10.01.-10.07.2012

MIZUKAMI, T., Kanazawa University, Department of Earth Science, Graduate School of Environmental Studies, Kanazawa, Japan: 02.-31.12.2012

NISHIYAMA, N., Deutsches Elektronen Synchrotron DESY, Photon Science (FS-DO), Hamburg, Germany: 22.-29.08.2012, 18.-19.09.2012

ROBERGE, M., Institut de Minéralogie et de Physique des Milieux Condensés, Paris, France: 20.-27.05.2012, 04.-11.10.2012

SMYTH, J.R., University of Colorado at Boulder, Department of Geological Sciences, Boulder, USA: 30.04.-30.06.2012

STONEBRAKER, J., University of Colorado at Boulder, Department of Geological Sciences, Boulder, USA: 20.-23.06.2012

TRØNNES, R., University of Oslo, Natural History Museum, Oslo, Norway: 08.05.-16.06.2012, 12.09.-17.10.2012

WOODLAND, A., Johann Wolfgang Goethe-Universität, Physikalisch-Chemische Mineralogie, Frankfurt/M., Germany: 16.-17.02.2012, 19.-23.03.2012

XIONG, X., Chinese Academy of Sciences, Guangzhou Institute of Geochemistry, Guangzhou, China: 10.04.-10.07.2012

ZAKHARCHENKO, E., Institute of Experimental Mineralogy, Chernogolovka, Moscow region, Russia: 20.06.-30.07.2012, 04.09.-28.11.2012

ZAKHAROV, B., Novosibirsk State University, Russia: 13.08.2012

8. Additional scientific activities

8.1 Theses

Ph.D. theses

CHANTEL, Julien: Elastic properties of silicates at realistic mantle pressures and temperatures.
HARRIES, Dennis: Structure and reactivity of terrestrial and extraterrestrial pyrrhotite
LERCHBAUMER, Linda: The nature of fluids in hydrothermal copper and molybdenum ore deposits.
POTAPKIN, Vasily: Energy-domain synchrotron radiation Mössbauer source for physics under extreme conditions.
SHEKHAR, Sushant: The origins of olivine fabric transitions and their effects on seismic anisotropy in the upper mantle.

M.Sc. theses

CERANTOLA, Valerio: Deformation of a crystalline system with two immiscible liquids: Implications for early core-mantle differentiation.
HASSANI SHABESTARI, Asiye Sadat: Electrical and thermal conductivity of liquids in the Fe-C system at high pressure and temperature from ab-initio simulations.
HUANG, Ruifang: Sulfur partitioning between silicate melts and aqueous fluid.
PESCE, Giacomo: Electrical conductrivity measurements of $(Mg,Fe)(Al,Si)O_3$ perovskite in laser-heated DAC at lower mantle conditions.

8.2 Honours and awards

DUBROVINSKY, Leonid	Visiting Professor ("Postes Rouges"), CNRS, Toulouse, France March-April, 2012)
HARRIES, Dennis	received the Paul Ramdohr Prize of the German Mineralogical Society at the European Mineralogical Conference, Frankfurt, 2012
KEPPLER, Hans	Fellow of the Geochemical Society and European Association of Geochemistry
SEIFERT, Fritz	was awarded the Walter Kerz Medal for 2012 of the German Geophysical Society at the annual meeting of the Society in Hamburg
SOLOPOVA, Natalia	Young Scientist Travel Award of the European Mineralogical Union for presentations at the European Mineralogical Conference, Frankfurt, 2012

STAGNO, Vincenzo	received the 2012 prize of the Italian Association of Mineralogy and Petrology (SIMP) for his outstanding PhD thesis at the European Mineralogical Conference, Frankfurt, 2012
TROTS, Dmytro	Visiting Professor at LSPM-CNRS, University Paris Nord, France: "Surface Brillouin scattering on opaque samples in diamond anvil cell"

8.3 Editorship of scientific journals

HEIDELBACH, Florian	Associate Editor "American Mineralogist"
KATSURA, Tomoo	Associate Editor "Reviews of Geophysics"
KEPPLER, Hans	Editorial Advisory Board "Elements" Editorial Board "Contributions to Mineralogy and Petrology"
MCCAMMON, Catherine	Chief Editor "Physics and Chemistry of Minerals" Advisory Editor "Springer Briefs in Earth Sciences"
RUBIE, David	Editorial Board "Physics of the Earth and Planetary Interiors"

8.4 Membership of scientific advisory bodies

BOFFA BALLARAN, Tiziana	Member of the Peer Review Panel 5 for beamlines I15 and I16 of Diamond Light Source
DUBROVINSKY, Leonid	Chair of SIG "Crystallography at extreme conditions" of the European Crystallography Union Member, Editorial Board of the Journal of High Pressure Research Member, Review Panel of Canadian Light Source Member, Review Panel of SPRING8 Chair, Subcomission on Spectroscopy, Diffraction, and new Instrumentations in Mineral Physics of the International Mineralogical Association Scientific expert for the Research Council of Lithuania Member, Deep Carbon Observatory Scientific Steering Committee
FROST, Dan	Member of the council of the European Association of Geochemistry (EAG)
KEPPLER, Hans	Member, Research Council of the German Mineralogical Society (Forschungskollegium Mineralogie der DMG)

	Member, Abraham Gottlob Werner Medal Committee, German Mineralogical Society (DMG) Chair, American Geophysical Union Fellow Committee (VGP section) Member, Commission for Research of Bayreuth University (Präsidialkommission für Forschung und wissenschaftlichen Nachwuchs) Member, German National Academy of Sciences (Leopoldina) Member, Bavarian Academy of Sciences Member, Deep Carbon Observatory Scientific Steering Committee Member, Alexander von Humboldt Foundation Selection Panel for Humboldt Awardees Member, Commision for Research Infrastructures, Wissenschaftsrat (German Council of Science and Humanities)
MCCAMMON, Catherine	President Elect, Volcanology, Geochemistry & Petrology Section of the American Geophysical Union Member, Council of the American Geophysical Union Chair, Sub-committee “Earth’s Deep Interior” of the Commission of the Physics of Minerals, International Mineralogical Association Co-Chair, Theme 22 “The Cutting Edge in Mineralogy and Mineral Physics”, Goldschmidt 2013 IAVCEI representative, Inter-Association Commission for Physics and Chemistry of Earth Materials
RUBIE, David	Member of Houtermans Award Committee, European Association of Geochemistry

8. Scientific and Technical Personnel

Name		Position	Duration in 2012	Funding source
ALEKSANDROV, Vladislav	M.Sc.	Wiss. Mitarbeiter	to 14.12.	DFG
AUDÉTAT, Andreas	Dr.	Akad. Rat z.A.		BGI
BEYER, Christopher	M.Sc.	Wiss. Mitarbeiter		EU
BLAHA, Stephan	M.Sc.	Wiss. Mitarbeiter		BGI/IGS
BÖHM, Ulrich		Mechaniker		BGI
BOFFA BALLARAN, Tiziana	Dr.	Akad. Oberrätin		BGI
BROCKMANN, Nicolas	Dipl.-Chem.	Wiss. Mitarbeiter		BGI/IGS[1]
BUCHERT, Petra		Fremdsprachen-sekretärin		BGI
BUTTERHOF, Christian	M.Sc.	Wiss. Mitarbeiter	from 01.06.	BGI/IGS[3]
CERANTOLA, Valerio	B.Sc.	Stud. Hilfskraft	to 30.09.	DFG/BGI
	M.Sc.	Wiss. Mitarbeiter	from 01.11.	EU
CERNOK, Ana	M.Sc.	Wiss. Mitarbeiterin	from 11.07.	BGI/IGS
CHUST, Thomas	Dipl. Geophys.	Wiss. Mitarbeiter		DFG
DE KOKER, Nico	Dr.	Wiss. Mitarbeiter	to 31.01.	DFG
DE VRIES, Jellie	Dr.	Wiss. Mitarbeiterin	from 01.07.	EU
DINIUS, Ganna	Mag.	Außenreferat	from 29.05.	BGI
DUBROVINSKY, Leonid	Apl. Prof. Dr.	Akad. Direktor		BGI
EL GORESY, Ahmed	Prof. Dr.			BGI/VP[2]
EVONUK, Martha	Dr.	Wiss. Mitarbeiterin		DFG
FEI, Hongzhan	B.Sc.	Wiss. Mitarbeiter		BGI/VP
FISCHER, Heinz		Mechaniker		BGI
FISCHER, Nicole	ROI	Verwalt. Beamtin		BGI
FRIGO, Corinne	B.Sc.	Stud. Hilfskraft		DFG
FROST, Daniel	Dr.	Akad. Direktor	to 30.09.	BGI
		Universitätsprofessor	from 01.10.	BGI
GIANNINI, Mattia	M.Sc.	Wiss. Mitarbeiter		DFG
GOLLNER, Gertrud		Chem.-Techn. Assistentin		BGI
GOU, Huiyang	Dr.	Forschungsstipendiat		AvH
GUTIERREZ, Xochilt	B.Sc.	Stud. Hilfskraft	from 01.12.	BGI
HASSANI SHABESTARI, Asiye Sadat	B.Sc.	Stud. Hilfskraft	to 30.08.	DFG
			01.09.-30.09.	SG[5]
HEIDELBACH, Florian	Dr.	Wiss. Mitarbeiter	to 30.09.	BGI/IGS
HUANG, Ruifang	B.Sc.	Stud. Hilfskraft	to 30.09.	DFG
IIZUKA, Riko	M.Sc.	Forschungsstipendiatin	01.06.-16.11.	AvH

KANTOR, Anastasia	Dr.	Wiss. Mitarbeiterin		BMBF
KATSURA, Tomoo	Prof. Dr.	Stellvertr. Leiter	to 30.09.	BGI
		Leiter	from 01.10.	BGI
KEPPLER, Hans	Prof. Dr.	Leiter	to 30.09.	BGI
		Stellvertr. Leiter	from 01.10.	BGI
KEYSSNER, Stefan	Dr.	Akad. Oberrat		BGI
KISON-HERZING, Lydia		Sekretärin		BGI
KLASINSKI, Kurt	Dipl.-Ing. (FH)	Techn. Angestellter		BGI
KRAUßE, Detlef	Dipl.-Inform. (FH)	Techn. Angestellter		BGI
KRIEGL, Holger		Haustechniker		BGI
KULARATNE, Kanchana	B.Sc.	Stud. Hilfskraft		DFG
KUNZ, Daniel	Dipl.-Chem.	Wiss. Mitarbeiter		BGI/IGS[3]
KUPENKO, Ilya	Dipl.-Phys.	Wiss. Mitarbeiter	to 31.07.	BMBF
KURNOSOV, Alexander	Dr.	Wiss. Mitarbeiter		EU
LAURENZ, Vera	Dr. rer. nat.	Wiss. Mitarbeiterin	from 01.10.	EU
LERCHBAUMER, Linda	Mag. rer. nat.	Wiss. Mitarbeiterin	to 30.06.	DFG
LI, Yuan	M.Sc.	Wiss. Mitarbeiter		BGI/IGS
LINHARDT, Sven		Elektrotechniker		BGI
LUNKENBEIN, Thomas	Dipl.-Chem.	Wiss. Mitarbeiter	to 31.05.	BGI/IGS[3]
MANTHILAKE, Geeth	Dr.	Wiss. Mitarbeiter	to 30.09.	BGI/VP
MASOTTA, Matteo	Dr.	Wiss. Mitarbeiter	from 10.09.	BGI/VP
MCCAMMON, Catherine	Dr.	Akad. Oberrätin		BGI
MIYAJIMA, Nobuyoshi	Dr.	Akad. Rat		BGI
MOHSENI AHOUEI, Hoda	B.Sc.	Stud. Hilfskraft	from 15.07.	DFG
MOOKHERJEE, Mainak	Dr.	Wiss. Mitarbeiter	to 15.01.	BGI
MYHILL, Robert	Dr.	Wiss. Mitarbeiter	from 01.10.	BGI/VP
NAKAJIMA, Yoichi	Dr.	Wiss. Mitarbeiter	to 14.12.	BGI/VP
NI, Huaiwei	Dr.	Wiss. Mitarbeiter	to 29.02.	DFG
			from 01.03.	BGI/VP
NJUL, Raphael		Präparator		BGI
NOVELLA, Davide	M.Sc.	Wiss. Mitarbeiter		BGI/IGS
OERTEL, Tina	Dipl.-Ing.	Wiss. Mitarbeiterin		BGI/IGS[1]
OJWANG, Dickson	B.Sc.	Stud. Hilfskraft	to 31.05.	DFG
			from 01.06.	BGI
OUSSADOU, Mezhoura	M.Sc.	Gastwissenschaftlerin		DFG
OVSYANNIKOV, Sergey	Dr.	Wiss. Mitarbeiter		DFG
PAMATO, Martha	M.Sc.	nebenberufliche wiss. Hilfskraft		DFG u. UB e.V.
PESCE, Giacomo	B.Sc.	Stud. Hilfskraft	to 05.01.	BGI/HiWi
			06.01.-30.09.	DFG
POTZEL, Anke		Chem.-Techn. Assistentin		BGI

PRESCHER, Clemens	Dipl.-Min.	wiss. Mitarbeiter		BGI/IGS
RAMMING, Gerd		Elektroniker		BGI
RAUSCH, Oliver		Mechaniker		BGI
ROSENTHAL, Anja	Dr.	Wiss. Mitarbeiterin	from 10.09.	EU
RUBIE, David C.	Prof. Dr.			EU
SAMUEL, Henri	Prof. Dr.	Juniorprofessor		Stiftung[4]
SAVCHUK, Oles	B.Sc.	Stud. Hilfskraft	to 30.09.	DFG
			from 01.10.	SG[5]
SCHMITT, Veronika	Dipl.-Min.	Wiss. Mitarbeiterin		BGI/IGS[1]
SCHULZE, Hubert		Präparator		BGI
SHCHEKA, Svyatoslav	Dr.	Wiss. Mitarbeiter	to 30.09.	DFG
			from 01.10.	BGI/IGS
SHEKHAR, Sushant	M.Sc.	Wiss. Mitarbeiter	20.01.-01.03.	BGI/VP
SINMYO, Ryosuke	Dr.	Wiss. Mitarbeiter		BGI/VP
SOLOPOVA, Natalia	M.Sc.	Wiss. Mitarbeiterin	from 23.04.	DFG
SOUSTELLE, Vincent	Dr.	Forschungsstipendiat		AvH
STEINLE-NEUMANN, Gerd	Dr.	Akad. Rat		BGI
TRENZ, Ulrike		Biol.-Techn. Assistentin		BGI
TROTS, Dmytro	Dr.	Wiss. Mitarbeiter		EU
ÜBELHACK, Stefan		Mechaniker		BGI
VLCEK, Vojtech	M.Sc.	Wiss. Mitarbeiter		DFG
VOGEL, Antje	Dipl.-Min.	Wiss. Mitarbeiterin		DFG
WACK, Julia	Dipl.-Chem.	Wiss. Mitarbeiterin		BGI/IGS[3]
WALTE, Nicolas	Dr.	Wiss. Mitarbeiter		BMBF
YAGI, Takehiko	Prof.	Forschungspreisträger	01.06.-30.08.	AvH
YANG, Xiaozhi	Dr.	Wiss. Mitarbeiter	to 31.08.	BGI

Abbreviations/explanations:

AvH	Alexander von Humboldt Foundation
BGI	Staff Position of Bayerisches Geoinstitut
BGI/HiWi	Hilfskraftmittel BGI
BGI/VP	Visiting Scientists' Program of Bayerisches Geoinstitut
BMBF	Federal Ministry of Education and Research
DFG	German Science Foundation
EU	European Union
IGS	International Graduate School under the Elitenetzwerk Bayern "Structure, Reactivity and Properties of Oxide Materials"
UB e.V.	Universität Bayern e.V.

[1] Fraunhofer ISC Würzburg

[2] partially funded by the Visiting Scientists' Program of Bayerisches Geoinstitut

[3] Chair of Inorganic Chemistry I, Prof. Breu

[4] Juniorprofessorship for Geodynamic Modeling funded by Stifterverband für die Deutsche Wissenschaft

[5] Studiengebühren

Index